UNIVERSIDADE ESTADUAL PAULISTA
"JÚLIO DE MESQUITA FILHO"
CAMPUS DE GUARATINGUETÁ

RUBENS COUTINHO TOLEDO

Technical analysis of Calcium Looping process applied to natural gas power plant

Guaratinguetá
2026

Rubens Coutinho Toledo

Technical analysis of Calcium Looping process applied to natural gas power plant

Thesis presented to the Faculty of Engineering and Sciences at the Guaratinguetá Campus, State University of São Paulo, for obtaining the title of Doctor in Engineering - Mechanical.

Supervisor: Profº Dr. João de Andrade de Carvalho Júnior
Co-supervisor: Profª Drª. Ivonete Ávila

Guaratinguetá
2026

Toledo, Rubens Coutinho
T649t Technical analysis of Calcium Looping process applied to natural gas power plant / Rubens Coutinho Toledo - Guaratinguetá, 2026.
180 f : il.
Bibliografia: f. 148-163

Tese (Doutorado) – Universidade Estadual Paulista, Faculdade de Engenharia e Ciências de Guaratinguetá, 2026.

Orientador: Prof. Dr. João de Andrade de Carvalho Júnior
Coorientadora: Prof.ª Drª. Ivonete Ávila

1. Dióxido de carbono. 2.Termogravimetria. 3. Dolomita. I. Título.

CDU 662.767(043)

Luciana Máximo
Bibliotecária/CRB-8 3595

POTENTIAL IMPACT OF THIS RESEARCH

This research aligns with SDG 7 (Clean and Affordable Energy) by supporting low-carbon power generation through calcium looping in natural gas plants. It contributes to SDG 9 (Industry, Innovation and Infrastructure) by advancing technological pathways for industrial decarbonization, and to SDG 13 (Climate Action) by enabling CO_2 emissions reduction and supporting climate mitigation strategies in Brazil.

IMPACTO POTENCIAL DESTA PESQUISA

Esta pesquisa está alinhada ao ODS 7 (Energia Limpa e Acessível) ao promover geração de energia de baixo carbono via looping de cálcio em usinas a gás natural. Contribui para o ODS 9 (Indústria, Inovação e Infraestrutura) ao avançar soluções tecnológicas para descarbonização industrial, e para o ODS 13 (Ação contra a Mudança do Clima) ao viabilizar a redução de emissões de CO_2 e apoiar estratégias de mitigação no Brasil.

RUBENS COUTINHO TOLEDO

Technical analysis of Calcium Looping process applied to natural gas power plant.

Tese apresentada à Universidade Estadual Paulista (UNESP), Faculdade de Engenharia e Ciências de Guaratinguetá, para obtenção do título de Doutor em Engenharia.

Data da defesa: 27/02/2026

Banca Examinadora:

gov.br Documento assinado digitalmente
JOAO ANDRADE DE CARVALHO JUNIOR
Data: 10/03/2026 10:16:50-0300
Verifique em https://validar.iti.gov.br

Prof. Dr. JOÃO ANDRADE DE CARVALHO JÚNIOR
Orientador - UNESP

gov.br Documento assinado digitalmente
RODRIGO FERNANDO COSTA MARQUES
Data: 05/03/2026 15:12:50-0300
Verifique em https://validar.iti.gov.br

Prof. Dr. RODRIGO FERNANDO COSTA MARQUES
UNESP

Einara Blanco Machin
Firmado digitalmente por Einara Blanco Machin
DN: cn=Einara Blanco Machin, c=CL, o=Universidad de Concepción, ou=Departamento de Ingeniaria Mecánica, email=eblanco@udec.cl
Fecha: 2026.03.04 10:50:57 -03'00'

Profa. Dra. EINARA BLANCO MACHIN
University of Conception

gov.br Documento assinado digitalmente
THIAGO AVERALDO BIMESTRE
Data: 09/03/2026 17:03:17-0300
Verifique em https://validar.iti.gov.br

Prof. Dr. THIAGO AVERALDO BIMESTRE
UNESP

gov.br Documento assinado digitalmente
NESTOR PROENZA PEREZ
Data: 10/03/2026 08:44:50-0300
Verifique em https://validar.iti.gov.br

Prof. Dr. NESTOR PROENZA PÉREZ
UNESP

To the boy who one day dreamed of being a scientist and my dear wife.

ACKNOWLEDGEMENTS

I would like to thank my supervisor, Prof. João Andrade de Carvalho Jr., for the many inspiring meetings and pieces of advice over the years, which helped refine this thesis. You always asked the best questions and made me reflect more deeply on my work.

I would like to thank my co-supervisor, Prof. Ivonete Ávila, for her constant support and active involvement throughout my PhD. and I am especially grateful for opening the doors of her laboratory (LC3 - Laboratory of Combustion and Carbon Capture), for her constructive criticism, trust and patience, and for going out of her way to support the development of my work despite my stubbornness. I also thank her for believing in and encouraging my ideas, and for supporting my experiments and teachings regarding scientific writing.

I would like to thank the University of Naples "Federico II" for accepting and contributing to this work through the expertise of Professors Fabrizio Scala and Fabio Montagnaro, as well as for providing the experimental apparatus used in this study. I also express my gratitude to Dr. Antonio Coppola and Dr. Fiorella Massa for their guidance, teaching, and assistance during the development of part of this work in their laboratory. Finally, I would like to thank my laboratory colleagues in Naples for their care, friendship, coffee, and Italian language lessons: Vincenzo Del Duca, Elshaday Mulu, Eduardo Arango, Felipe Rezende da Costa, Marco Marshall Marciani, Stefano Scognamiglio, Antonio Capasso, and Renata Migliaccio.

I also thank the members of the LC3 for their collaboration, technical support, parties, and chaos: Ana Laura Scapin Ortiz, Abigail Cardoso Paes de Barros, David Vieira Valim, Fábio Roberto Vieira, Fernando Manente Perrella Balestieri, Jane Rose Dias Dionísio Rodrigues, Luis Augusto Alves de Oliveira, Maristela Ribeiro de Oliveira, Miriam Ricciulli de Oliveira, Mônica Valéria dos Santos Machado, Naiara Firmiano Fabiano da Silva, Saif Aladawi, Tadakadzwa Pswarayi, Vinoth Thangarasu, and Yasmin Mirai Kaneda Paes. Special thanks are extended to Fernando Manente Perrella Balestieri for his help during the experiments, the thoughtful discussions, and the music we made.

I would like to thank Thereza Magnussen Fortes, Caio Leandro de Moraes, Luis Fernando L. de Campos, and Vitor P. Ribeiro for actively contributing to this work. I apologize for asking you to work beyond normal hours, your dedication was essential to this work. I hope you have learned from me as much as I have learned from you.

I thank Dr. Rogério Hein for the friendship and for contributing to this work, both directly and indirectly.

I am grateful to the UNESP staff for their support throughout this work: José Alberto, Rizzato, Rodolfo, Maria Inês, Joice, Aislilian, José Claudio, Formiga, Joel, Emilia, Cristovão, and others whose names I may have unintentionally forgotten.

I would like to thank Calcário Diamante for donating the dolomite used in this work, which made this research possible.

I would like to thank my family and friends, whose support and number has grown over the years. I am especially grateful to my wife, Maísa, for her continuous support throughout this PhD. Your support reached every part of this work, and this achievement is also yours. We both have grown so much during these year and I am more happy than ever to share this with you.

I thank Carlos D. Maciel and Graça A. Oliveira for their guidance, care, and loving support during this journey. Without you, I would not have made it this far.

Finally, I thank João Pedro, Juliana, Fábio, Marlei, Orlando, and Vanuza for believing in and supporting my dream from the very beginning. The sacrifices you made made this achievement possible.

The following institutions supported this work:
Support from the Coordination for the Improvement of Higher Education Personnel - Brazil (CAPES) - financing code 001.
Financial support: (1) National Agency for Petroleum, Natural Gas and Biofuels (ANP), the Financier of Studies and Projects (FINEP) and from the Ministry of Science, Technology and Innovation (MCTI), through the ANP Human Resources Training Program for the Sector Oil and Gas (PRH) - ANP/MCTI, through the PRH 34.1 FEG/UNESP program;
(2) Financial support from FAPESP (Proc. 2019/16966-8).
(3) CNPq (Proc. 406351/2023-6).

ABSTRACT

The global effort to mitigate greenhouse gas emissions has intensified the development of carbon capture technologies compatible with low-carbon energy systems. In this context, the growing role of natural gas–fired (NG) power plants in the Brazilian energy matrix poses specific challenges for carbon capture due to the low concentration of carbon dioxide (CO_2) in their flue gases. Calcium looping (CaL) emerges as a promising alternative; however, no experimental studies addressing Brazilian limestone under NG combustion conditions have been reported to date. This thesis aims to develop a technical assessment of the CaL process applied to natural gas power plants using a Brazilian dolomite as a CaO-based sorbent. The study investigates whether laboratory-scale experimental approaches can establish operational criteria and demonstrate the technical feasibility of CaL under low CO_2 concentration conditions. N_2 adsorption porosimetry was employed to correlate sorbent pore structure with process performance. An integrated methodology combining thermogravimetric analysis (TGA) and a bench-scale Dual Interconnected Fluidized Bed (DIFB) reactor was adopted. A Rotatable Central Composite Design (RCCD) method was used to optimize and evaluate key experimental parameters in both TGA and DIFB systems. The results demonstrate that Brazilian dolomite exhibits promising carbon capture performance under low CO_2 partial pressures, provided that appropriate operational windows are applied. Pore structure analysis revealed a critical pore size range between 30 and 100 Å, governing both initial capture efficiency and cyclic degradation. TGA experiments showed that most of the fast carbonation occurs within the first 2.5 min, whereas longer carbonation times are dominated by diffusion-controlled regimes. Carbonation temperature was identified as the dominant operational parameter, with optimal conditions at 580 °C for 7.5 min and 550 °C for 10 min, yielding IEC$10, c$ values of 1.34 and 1.20, respectively. In the DIFB system, increased elutriation and thermal degradation resulted in lower capture efficiencies, with maximum values on the order of 0.0177 kg CO_2/kg $CaCO_3$, indicating that scale-up introduces additional degradation mechanisms not observed in fixed-bed systems. The originality of this thesis lies in the integrated experimental evaluation of CaL under conditions representative of NG combustion using a Brazilian dolomite, a context that remains scarcely addressed in the literature. The combined use of pore structure analysis, TGA, and DIFB provides novel insights into the relationship between sorbent microstructure, operational conditions, and performance degradation, demonstrating that the limitations observed in fluidized bed systems are primarily associated with intrinsic sorbent properties rather than low CO_2 concentration. These findings constitute a key contribution of this thesis, as they demonstrate that performance limitations in fluidized bed systems are mainly related to intrinsic sorbent properties rather than low CO_2 concentration, while providing a comprehensive analysis of parameter impacts on carbon capture performance and a realistic basis for future studies in pilot-scale reactors and sorbent development.

KEYWORDS: Calcium looping; Natural gas; Dolomite; CO_2 capture; Thermogravimetry;

Fluidized bed; Pore blockage.

RESUMO

O esforço global para a mitigação das emissões de gases de efeito estufa tem impulsionado o desenvolvimento de tecnologias de captura de carbono compatíveis com sistemas energéticos de baixo carbono. Nesse contexto, a crescente participação das usinas termelétricas a GN na matriz energética brasileira impõe desafios específicos à captura de carbono, em razão da baixa concentração de dióxido de carbono (CO_2) nos gases de exaustão. O CaL surge como uma alternativa promissora; entretanto, ainda não há estudos experimentais que abordem o uso de calcários brasileiros sob condições de combustão de GN. Esta tese tem como objetivo desenvolver uma análise técnica do processo CaL aplicado a usinas a gás natural, utilizando uma dolomita brasileira como sorvente à base de CaO. O estudo investiga se abordagens experimentais em escala de laboratório são capazes de estabelecer critérios operacionais e demonstrar a viabilidade técnica do CaL sob condições de baixa concentração de CO_2. A porosimetria por adsorção de N_2 foi empregada para correlacionar a estrutura dos poros do sorvente com o desempenho do processo. Adotou-se uma metodologia integrada combinando análises de TGA e um DIFB em escala de bancada. O método de RCCD foi utilizado para otimizar e avaliar os principais parâmetros experimentais tanto nos ensaios de TGA quanto no sistema DIFB. Os resultados demonstram que a dolomita brasileira apresenta desempenho promissor na captura de carbono sob baixas pressões parciais de CO_2, desde que adotadas condições operacionais adequadas. A análise da estrutura dos pores revelou uma faixa crítica de tamanho de poros entre 30,0 e 100,0 Å, a qual governa tanto a eficiência inicial de captura quanto a degradação cíclica do sorvente. Os experimentos em TGA indicaram que a maior parte da carbonatação rápida ocorre nos primeiros 2,5 min, enquanto tempos de carbonatação mais longos são dominados por regimes controlados por difusão. A temperatura de carbonatação foi identificada como o principal parâmetro operacional, com condições ótimas em 580 °C por 7,5 min e 550 °C por 10,0 min, resultando em valores de IEC$10, c$ de 1,34 e 1,20, respectivamente. No sistema DIFB, o aumento da elutriação e da degradação térmica resultou em menores eficiências de captura, com valores máximos da ordem de 0,0177 kg CO_2/kg $CaCO_3$, indicando que a ampliação de escala introduz mecanismos adicionais de degradação não observados em sistemas de leito fixo. A originalidade desta tese reside na avaliação experimental integrada do CaL sob condições representativas da combustão de GN, utilizando uma dolomita brasileira, um contexto ainda pouco explorado na literatura. O uso combinado da análise da estrutura porosa, TGA e DIFB fornece novos insights sobre a relação entre a microestrutura do sorvente, as condições operacionais e a degradação de desempenho, demonstrando que as limitações observadas em sistemas de leito fluidizado estão principalmente associadas às propriedades intrínsecas do sorvente, e não à baixa concentração de CO_2. Esses resultados constituem uma contribuição relevante desta tese, ao evidenciar que as limitações de desempenho em sistemas de leito fluidizado estão majoritariamente relacionadas às propriedades intrínsecas do sorvente, além de fornecer uma análise abrangente do impacto

dos parâmetros operacionais na captura de carbono e uma base realista para estudos futuros em reatores em escala piloto e no desenvolvimento de novos sorventes.

PALAVRAS-CHAVES: Calcium looping; Gás Natural; Dolomita; Captura de CO_2; Termogravimetria; Leito fluidizado; Bloqueio de poros.

LIST OF FIGURES

LIST OF TABLES

CONTENTS

1 INTRODUCTION

1.1 PROBLEM DESCRIPTION AND JUSTIFICATION

Greenhouse gas (GHG) emissions constitute a central challenge for contemporary society, as climate change increasingly affects daily life through alterations in land use, lifestyle transformations, and evolving patterns of consumption and production across regions and among individuals (FILONCHYK *et al.*, 2024; SHAH *et al.*, 2024; LEE; ROMERO, 2023).

The increase in GHG emissions into the atmosphere causes an increase in the average temperature of the oceans, causing changes in the amount and periods of rain, an increase in periods of drought, a decrease in glaciers, the incidence of storms and rising ocean levels with devastating consequences for biomes and living beings (ALFONSO; GESTO; SADOUL, 2021; ISIAKA; NDUKWE; CHIBUIKE, 2021; MUGWANYA *et al.*, 2022; STRAUSS *et al.*, 2021). Also, temperature increases affect various aspects of crop growth, such as flowering, fruiting, fruit size, quality, and ripening, ultimately leading to reduced productivity and lower costs (SHAH *et al.*, 2024). Furthermore, the variation in the concentrations of certain gases that make up GHGs is the main factor attributed to the increase in temperature, with anthropogenic CO_2 considered the main responsible for global warming (FILONCHYK *et al.*, 2024; MOKHOV, 2022; STIPS *et al.*, 2016).

The escalation in global energy consumption and the associated rise in carbon dioxide (CO_2) emissions to the atmosphere have prompted the scientific community to develop and implement technological strategies aimed at mitigating the contribution of CO_2 to climate change. In this context, substantial investments have been directed toward projects focused on improving energy efficiency, expanding the deployment of renewable energy sources, and advancing low-carbon technologies (ARCE *et al.*, 2017; COSENSE4CLIMATE PROJECT, 2024; CLEVER PROJECT, 2024; CLEANKER, 2017; NATURAL RESOURCES CANADA, 2022; SOCRATCES, 2018). Concurrently, the reduction of anthropogenic CO_2 emissions is recognized as a key measure to attenuate the adverse impacts of climate change (LEE; ROMERO, 2023; MIKHAYLOV *et al.*, 2020).

The energy and industrial sectors are the largest contributors to global greenhouse gas emissions, accounting for approximately 34% and 24% of total emissions, respectively (LAMB *et al.*, 2021). Although policies targeting the phase-out of fossil fuels have intensified, future scenarios such as the Net Zero 2050 pathway still project that about 15% of total primary energy supply will be derived from oil and approximately 5% from coal and natural gas (INTERNATIONAL ENERGY AGENCY (IEA), 2023). Currently, fossil fuels remain the dominant energy sources, supplying around 80–85% of global energy demand. This predominance is associated with several advantages, including abundant reserves, high energy density, operational flexibility, ease of storage, extensive existing infrastructure and relatively low cost (INTERNATIONAL

ENERGY AGENCY (IEA), 2023).

International projections indicate that, during the initial stages of the transition toward a predominantly renewable energy matrix, the use of non-renewable energy sources will temporarily increase to support and enable the structural changes required for this transition, before a sustained decline in their consumption is realized (INTERNATIONAL ENERGY AGENCY (IEA), 2023). National statistics for Brazil show that, in 2024, oil and oil derivatives accounted for 40.7% of the total primary energy supply in the domestic energy mix, while natural gas contributed 7.5%, representing increases of 7.6 and 1.2 percentage points, respectively, compared with the 2023 report (EPE, 2024).

In 2024, Brazil's natural gas consumption was substantial, reaching 77 million m^3/day; of this volume, 36.5% was consumed by the industrial sector and 18.3% by the energy sector (EPE, 2024). In the context of the continued exploration and development of Brazil's "pré-sal" offshore reserves, public policies have been oriented toward expanding natural gas utilization across multiple sectors, with a particular emphasis on industry. Projections indicate that industrial natural gas demand alone could increase to 80 million m^3/day by 2040 (BRAZILIAN DEVELOPMENT BANK (BNDES), 2021).

The Calcium Looping (CaL) process consists of a reversible carbonation-calcination reaction of a CaO-based sorbent (DIEGO; ARIAS, 2020a), mostly using limestone even though many CaO-based substitutes have been researched as replacement to natural limestone (ANTZARA *et al.*, 2018; CHAI *et al.*, 2022; DONG *et al.*, 2020; LI; WANG; LI, 2022). Limestone is an abundant low-cost material suitable for an economically viable process, being natural limestone largely utilized (ANTZARA *et al.*, 2018; BLAMEY *et al.*, 2016; ZHANG *et al.*, 2016).

The main advantages of this CO_2 capture technology, relative to alternative approaches, include its suitability as a short- to medium-term mitigation option due to its compatibility with retrofitting in existing plants; the use of low-cost, naturally occurring sorbents that are abundantly available (e.g., calcitic and dolomitic limestones); the relatively minor efficiency penalty imposed on the combustion process; the possibility of exploiting commercially mature fluidized bed technologies; and its applicability to CO_2 capture in both pre-combustion and post-combustion configurations (CHAMPAGNE *et al.*, 2016; DEAN *et al.*, 2011; VALVERDE; SANCHEZ-JIMENEZ; PÉREZ-MAQUEDA, 2015).

For CaL systems applied to natural gas-fired power plants, the techno-economic feasibility is still under active investigation. Most modeling studies consider several process configurations in which CaL could serve as a substitute for coal-based systems. Previous study (SCHAKEL *et al.*, 2018) reported improved performance in natural gas applications, mainly attributable to the lower sulfur content of the fuel, which decreases sorbent purge requirements. Other study (PILLAI *et al.*, 2022) observed that Natural Gas Combined Cycle (NGCC) plants integrated with CaL can be further enhanced by coupling with renewable energy sources, although economic concerns related to natural gas price volatility remain (MOORE; CRISTINA; KULAY, 2019). Numerous studies have sought to achieve NGCC–CaL efficiencies comparable to those of coal-fired plants;

however, they frequently lack a detailed characterization of the carbonator gas atmosphere and, in some cases, adopt flue gas parameters derived from coal combustion instead of those specific to natural gas. (HU; AHN, 2017) suggested that regenerating the calciner outlet stream to increase CO_2 concentration could reduce the thermal energy demand of the process.

From the limited number of experimental studies available (SYMONDS *et al.*, 2016), a natural gas combustor was employed to supply CO_2 (8.59 vol.% wet) to the carbonator. However, the primary objective of that work was the comparison between synthetic pellets and natural limestone, rather than the investigation of the effects of low CO_2 concentrations. In another study (HAAF *et al.*, 2020a), Solid Recovered Fuel (SRF) was tested in the calciner, while lignite and natural gas–derived flue gases were used in the carbonator. A CO_2 concentration of 9.5 vol.% in the flue gas was reported, with no observable adverse impact on CO_2 capture efficiency. Additional experiments were performed at different pressures using simulated coal and natural gas flue gases in a TGA system, with a CO_2 concentration of 16.7 vol.% wet during carbonation cycles (DUHOUX *et al.*, 2020). Although natural gas was considered in these studies, the specific influence of low CO_2 concentrations on the CaL process was not systematically examined. In practical applications, natural gas flue gases typically exhibit substantially lower CO_2 concentrations (approximately 4.0 vol.% wet), which may significantly affect CaL performance.

Fluidized bed reactors are widely employed for gas–solid reactions owing to the excellent gas–solid contact within the bed, the efficient heat and mass transfer between gas and particles, and the high heat transfer coefficients at the bed walls and internal surfaces (WERTHER, 2000). Calcium-looping processes are particularly noteworthy because they are associated with superior sorbent conversion performance (HAAF *et al.*, 2020b; TREGAMBI *et al.*, 2018). At the industrial scale, numerous studies have implemented experimental configurations consisting of two independent reactors (ALONSO *et al.*, 2018; ARIAS *et al.*, 2018; DIEGO; ARIAS, 2020a; HAAF *et al.*, 2020b; HILZ *et al.*, 2018; HILZ *et al.*, 2019). Furthermore, several studies have sought to improve the techno-economic feasibility of calcium looping through the integration of solar energy (TREGAMBI *et al.*, 2018), the development of CaO-based laboratory-fabricated pellets with enhanced properties (MA *et al.*, 2021), the design of high-capacity carbonators (DIEGO; ARIAS, 2020a), and the application of indirect heating strategies (HOFMANN *et al.*, 2024).

One of the most critical milestones in the advancement of calcium looping (CaL) technology is the demonstration and optimization of the process at industrial scale (ERANS; MANOVIC; ANTHONY, 2016; DIETER *et al.*, 2014; HOFMANN *et al.*, 2024). Although the technology can be implemented in various process configurations, it remains unclear which specific configuration is best suited for a given application, industrial sector, or scale of operation (TAN *et al.*, 2024; PAPALAS *et al.*, 2024). Furthermore, sorbent materials still do not exhibit sufficiently robust performance, primarily due to their progressive deactivation over multiple carbonation–calcination cycles (HOFMANN *et al.*, 2024; PEREJÓN *et al.*, 2024). In this context, the design and con-

struction of fluidized bed reactors equipped with advanced particle classification systems should be prioritized in laboratories working on CaL processes, in order to accurately characterize and demonstrate the complete decay behavior of CO_2 sorbents under conditions representative of industrial-scale CaL operation (JAYARATHNA *et al.*, 2019).

In this context, the present study is motivated by the need to mitigate the environmental impacts associated with climate change through research on carbon capture and storage (CCS) technologies, as recognized by the Intergovernmental Panel on Climate Change (IPCC), thereby providing a potential pathway for reducing CO_2 emissions. Accordingly, the central research question guiding this work is: *How can laboratory-scale experimental investigations support the establishment of operational criteria and demonstrate the technical feasibility of the calcium looping process, employing Brazilian dolomite as a sorbent, for carbon dioxide capture under conditions representative of natural gas–fired power plants?*

1.2 OBJECTIVES

The general objective of this thesis is to conduct a comprehensive technical assessment of the calcium looping (CaL) process, employing a domestically sourced dolomite, through experimental investigations based on thermogravimetric analysis (TGA) and a laboratory-scale fluidized bed reactor, specifically a Dual Interconnected Fluidized Bed (DIFB) system. The aim is to define suitable operating criteria and evaluate the feasibility of CO_2 capture under conditions representative of a natural gas-fired power plant.

To achieve that, these objectives will follow:

1. To characterize the nationally sourced dolomite used as a CO_2 sorbent in the CaL process and to assess the effects of CO_2 concentration in the reaction atmosphere and bed compaction on the thermodynamic and kinetic behavior of the calcination and carbonation stages, as well as to evaluate pore structure blockage and sorbent deactivation during carbonation.

2. To study the CaL process via thermogravimetric analysis, employing a rotatable central composite design to identify key response variables, optimize operating conditions, and evaluate sorbent behavior over multiple calcination–carbonation cycles;

3. To compare the behavior of the CaL process in TGA and in a downer-interconnected fluidized bed reactor, identifying performance differences associated with distinct reaction dynamics, sorbent degradation mechanisms, and the representativeness of each experimental system.

1.3 RESEARCH DELIMITATION

The CaL technique is based on the cyclic sequence of calcination and carbonation, corresponding to Equations 1.1 and 1.2, respectively. In the calcination step, calcium carbonate ($CaCO_3$) thermally decomposes into calcium oxide (CaO) and CO_2 in an endothermic reaction. Conversely, the carbonation step is the reverse process, in which CaO reacts with CO_2 to form $CaCO_3$ in an exothermic reaction (ÁVILA; CRNKOVIC; MILIOLI, 2007).

$$\mathrm{CaCO_{3(s)}} \longrightarrow \mathrm{CaO_{(s)}} + \mathrm{CO_{2(g)}} \quad \Delta H_r = -178\,\mathrm{kJ/mol} \tag{1.1}$$

$$\mathrm{CaO_{(s)}} + \mathrm{CO_{2(g)}} \longrightarrow \mathrm{CaCO_{3(s)}} \quad \Delta H_r = +178\,\mathrm{kJ/mol} \tag{1.2}$$

The process was originally conceived for integration with conventional power plants, whereby a CO_2-rich flue gas stream, instead of being discharged directly into the atmosphere, is routed to a carbonator reactor. CaL can be implemented in several configurations; however, the most widely adopted arrangement consists of a dual-reactor system with a dedicated reactor for each principal reaction. Figure 1 illustrates a representative dual configuration comprising a carbonator (blue) and a calciner (red).

In this configuration, the flue gas is introduced into the carbonator, where CaO reacts with the CO_2 contained in the flue gas, as described in Equation 1.2. The resulting CO_2-depleted (lean) flue gas stream can subsequently be subjected to additional purification steps, employed as a heat-transfer medium, and ultimately discharged to the atmosphere. The $CaCO_3$ formed in the carbonator is continuously transferred to the calciner.

Within the calciner, an external heat source is utilized to attain the elevated temperatures required for the calcination step. While laboratory-scale reactors frequently employ alternative heating strategies, such as electrical or solar heating, fuel combustion remains the predominant heating method at the industrial scale. Upon completion of calcination, a high-purity CO_2 stream is obtained for compression and geological storage (or other forms of long-term sequestration), whereas the regenerated CaO is recirculated to the carbonator, thus establishing a closed-loop system.

A CaL reactor at larger scales can exhibit substantial design and operational complexity. Figure 2 depicts a 200 kW CaL pilot facility equipped with the main components required for continuous operation (HAWTHORNE *et al.*, 2011). The carbonator and regenerator (B, C) each have a height of approximately 10 m, whereas the combustor (A) has a height of 6 m. Mass flow measurement units (F) are installed in each solid circulation line to accurately determine the solids circulation rate and, consequently, the solid looping ratio. High-pressure blowers (G) provide the primary gas supply either via the gas distributors of all reactors or through staged injection. Storage vessels (H) are used for the provision and handling of fuel and limestone.

The dense bed regions of both the combustion reactor and the carbonator are equipped with water-cooled heat exchangers (I) for heat removal and temperature control. In the lean bed region,

bayonet-type coolers (J) are employed for additional heat extraction. Gas coolers (K) reduce the flue gas temperature to approximately 150 °C, whereas a water quench (L) provides further cooling where required. Bag filters (M) are used to remove particulate matter from the flue gases. Pressure control valves (N), located upstream of the induced draft (ID) fan, regulate the pressure in each of the three process trains. The ID fan (O) extracts the flue gases from the system. A 400 kW excess-air gas burner (P) is used to preheat the reactors to the desired operating temperature. Bed discharge units (Q) are supplied with process or purge gas to ensure controlled withdrawal of solids.

Figure 1 – A common dual fluidized bed schematic detail used for CaL in lab scale: a) Carbonator, b) Calciner, c) and e) Carbonator cyclone, d) and f) Calciner cyclone, and h) and g) Temperature measuring point.

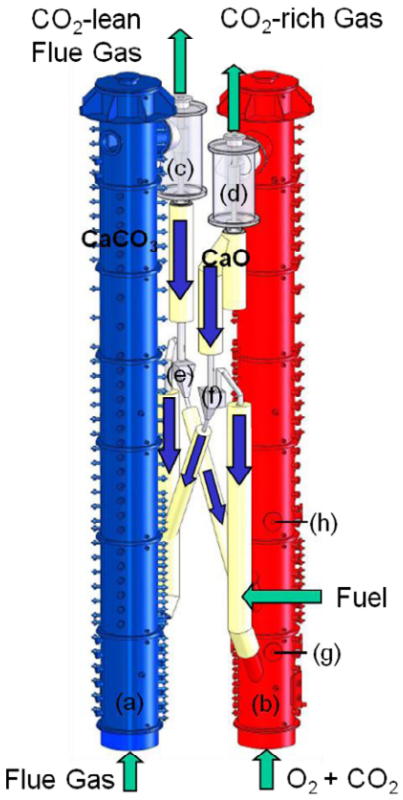

Source: (HAWTHORNE *et al.*, 2011)

It should be emphasized that, as CaL is still an emerging technology, multiple reactor and plant configurations are under development, and the specific layout illustrated here is subject to further optimization and modification.

In this work, a simulated gas mixture based on compositions reported in the literature will be employed as the reference atmosphere for the CO_2 concentration supplied to the carbonator. A Brazilian dolomite will be used as the sorbent material for CO_2 capture from this simulated flue gas.

Due to the high capital expenditure and large footprint associated with fluidized-bed reactors,

numerous researchers have opted to conduct fundamental investigations, such as sorbent characterization, in smaller laboratory-scale reactors (TOLEDO *et al.*, 2023), with much research being conducted on TGAs) operated as fixed-bed reactors (SALAUDEEN *et al.*, 2018; VALVERDE *et al.*, 2013; VALVERDE; SANCHEZ-JIMENEZ; PEREZ-MAQUEDA, 2014). When scaling up a CaL process, it is essential to understand how differences in reactor scale and hydrodynamics influence key parameters, including CO_2 capture capacity, sorbent deactivation behavior, calcination and carbonation temperatures, as well as elutriation and fragmentation phenomena.

Figure 2 – A dual fluidized bed complete schematic used for CaL in industrial scale

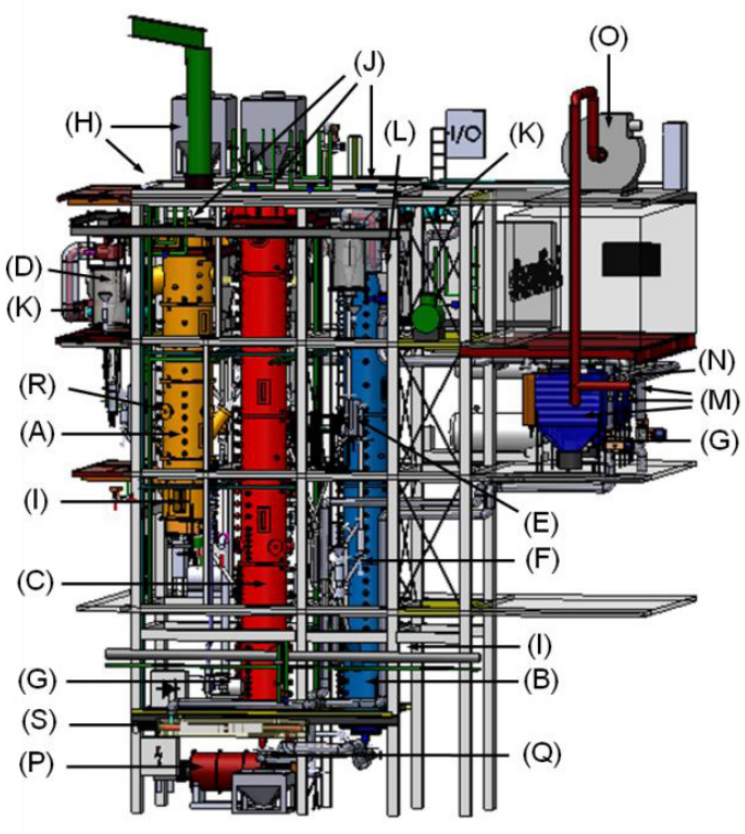

Source: (HAWTHORNE *et al.*, 2011)

To this end, a systematic characterization and performance evaluation of the Brazilian dolomite will first be carried out, followed by preliminary small-scale tests in a fixed-bed configuration. In these tests, a thermogravimetric furnace will be employed as a fixed-bed reactor for both the carbonator and calciner, with the operating temperature adjusted according to the reaction step under investigation.

Experiments under fluidized-bed conditions were conducted in a Dual Interconnected Fluidized Bed (DIFB) system located in Naples, Italy. This system comprises two identical fluidized-bed reactors, one operated as the calciner and the other as the carbonator, allowing continuous circulation of the sorbent between the two units.

A comprehensive understanding of the performance of the Brazilian dolomite was thus developed by integrating the results obtained from both TGA and DIFB experiments. Based

on the outcomes of this study, recommendations were be made regarding the suitability and future application of this dolomite in calcium looping processes for CO_2 capture from natural gas combustion flue gases.

1.4 CLASSIFICATION OF THE RESEARCH

This thesis is restricted to experimental tests and statistical methods involving limestone rocks. It is therefore classified as applied research employing a quantitative methodological approach. The study is configured as laboratory-scale experimental research with an explanatory objective, insofar as it seeks, based on observed phenomena, to elucidate the causal factors that affect process efficiency and CO_2 capture (MIGUEL *et al.*, 2010). This experimental design examines the relationships between two or more variables within a system under conditions rigorously controlled by the investigator, who is responsible for the manipulation and regulation of these variables. The changes induced in the phenomenon under investigation as a consequence of such manipulations constitute the empirical results of the research (MIGUEL *et al.*, 2010).

1.5 RESEARCH CONTRIBUTION AND ORIGINALITY

1.5.1 Scientific contributions

Brazil has maintained a longstanding commitment to mitigating CO_2 emissions and has established ambitious GHG reduction targets for the coming decades. By 2025, the country planned to reduce its GHG emissions by 37% relative to 2005 levels, followed by a further reduction to 43% below 2005 levels by 2030 (TOLMASQUIM *et al.*, 2021). In 2022, national emissions totaled 1.69 $GtCO_2$, of which 18% originated from the energy sector (TSAI *et al.*, 2023).

Natural gas exhibits substantial potential as an energy source and is frequently employed as a complementary input in thermoelectric power plants to support electricity generation and mitigate the risk of blackouts associated with reduced hydropower availability during periods of low rainfall and depleted reservoir levels. In the Brazilian energy matrix, natural gas accounts for 7.5% of total electricity generation (EPE, 2024).

Figure 3 presents nationwide natural gas utilization for the years 2015, 2019, and 2024, disaggregated by geographic region. The data indicate that the Southeast, Northeast, and South regions account for the predominant share of total natural gas consumption, with contributions of 66.4%, 18.1%, and 11%, respectively. In the state of São Paulo, industrial activities are responsible for up to 80% of total natural gas demand (SãO PAULO STATE PUBLIC UTILITIES REGULATORY AGENCY (ARSESP), 2023). In Rio de Janeiro, the current industrial consumption profile corresponds to a demand exceeding 2.38 million m^3/day (RIO DE JANEIRO STATE FEDERATION OF INDUSTRIES (FIRJAN), 2024). In the state of Bahia, natural gas use is also primarily directed to industrial applications: 53.3% of the volume is consumed by fuel industries,

followed by 30.2% allocated to cogeneration processes (BAHIA STATE FEDERATION OF INDUSTRIES (FIEB), 2024). The increasing nationwide incorporation of natural gas-fired power plants into Brazil's energy matrix represents a critical opportunity to achieve substantial emission reductions from the power sector.

Figure 3 – Total annual natural gas consumption in Brazil (m^3/year) by region for the years 2015, 2019, and 2024.

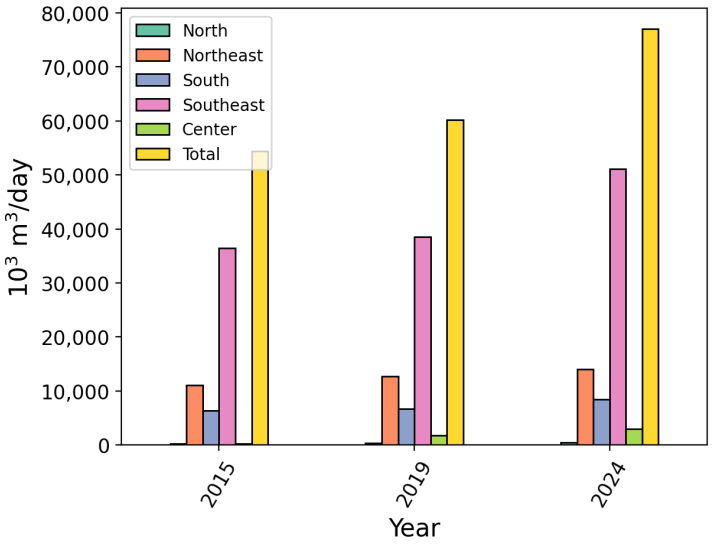

Source: Adapted from (EPE, 2024)

Most Brazilian research on CaL is still primarily focused on the physicochemical characterization of sorbents (both naturally occurring minerals and newly synthesized materials), with the objective of determining sorbent cyclic performance and the decay in CO_2 capture capacity over multiple carbonation–calcination cycles. These characterization studies are typically carried out at laboratory scale and employ particle size ranges that do not reflect industrial operating conditions, most often using finely divided powders. This situation reveals a significant gap in knowledge regarding the modeling, sizing, and design of interconnected circulating fluidized bed reactors under more realistic process conditions, including the use of larger particle sizes and the explicit consideration of reactor fluid dynamics and sorbent sintering phenomena in such regimes.

Although the CaL process is considered one of the most promising options among Carbon Capture and Storage (CCS) technologies, primarily due to its comparatively straightforward scalability and integration into existing industrial infrastructures, it still faces several significant challenges. These include the need to enhance the CO_2 capture capacity of Ca-based sorbents, to improve their performance over an increased number of repetitive carbonation–calcination cycles, and to mitigate performance deterioration associated with limestone particle sintering and elutriation phenomena.

Given the current level of technological maturity associated with the process under investiga-

tion, it is evident that its implementation involves a complex and comprehensive set of stages that still demand the development of novel methodologies suitable for deploying the CaL process at more realistic scales. In this context, the present thesis is expected to generate critical information to advance the technological development of CaL at scales closer to industrial application and, additionally, to support the formulation and strengthening of Brazilian public policies aimed at controlling pollutant emissions from energy generation, with potential positive impacts on society from an environmental standpoint.

A bibliometric review was performed using the SCOPUS database on 18 July 2024 to identify the state of research on calcium looping (CaL) applied to natural gas-fired power plants. The primary search terms used were “Natural gas” and “Calcium looping,” including their common abbreviations and variations, namely “NG,” “CaL,” “CLP,” and “NGCC.”

The initial search returned 134 documents. From this set, all publications that did not meet the following criteria were excluded: (i) document type classified as “article,” (ii) written in English, (iii) published in a journal, and (iv) in the final stage of publication. After applying these filters, the dataset was reduced to 77 documents.

A subsequent manual screening was then conducted to retain only those articles explicitly addressing natural gas-fired power plants using non-synthetic natural sorbents and some form of calcium looping technology. Following this manual selection, 22 articles remained. These were then processed using dedicated bibliometric analysis software, as described in Section 2.1.

Figure 4 indicates that the countries most actively engaged in this research topic are the United Kingdom, Romania, Norway, the United States, and China. The field reached its peak activity in 2020, as shown in Figure 5, and has exhibited a declining trend since then, although the annual number of publications remains comparable to earlier years. Brazil shows only a modest level of participation despite its extensive use of natural gas.

Moore *et al.* (2019) evaluated four different scenarios for the Brazilian energy matrix: the current configuration, CaL applied to coal-fired power plants, CaL applied to natural gas-fired power plants, and a hybrid configuration combining both applications. The authors identify the additional energy demand associated with the implementation of CaL as a major barrier to its deployment in conjunction with natural gas, together with methane (CH_4) emissions. These findings underscore the need for a more detailed understanding of the CaL process when applied specifically to natural gas combustion conditions.

Although the keywords used to retrieve the articles (Figure 6) were expected to be prominently represented in this analysis, only “calcium looping” appears among the five most frequently cited keywords. “Carbon capture” and “CO_2 capture” are broad terms encompassing multiple technological approaches, which is consistent with the discussion presented in Section 2.1. The remaining three keywords—“techno-economic assessment,” “NGCC power plant,” and “chemical absorption/adsorption”—are directly associated with the specific characteristics of this research area.

Among the 22 articles considered in this analysis—a relatively small sample size that

reinforces the presence of selection bias—19 focus on modeling studies addressing either techno-economic feasibility or purely economic viability. Consequently, only three publications are based on experimental investigations of the process. While feasibility studies are an essential step in technology development, calcium looping under low CO_2 partial pressures remains insufficiently explored, despite its specific features, which are examined in detail throughout this thesis.

Figure 4 – Bibliometric study of natural gas used in calcium looping – Country publication

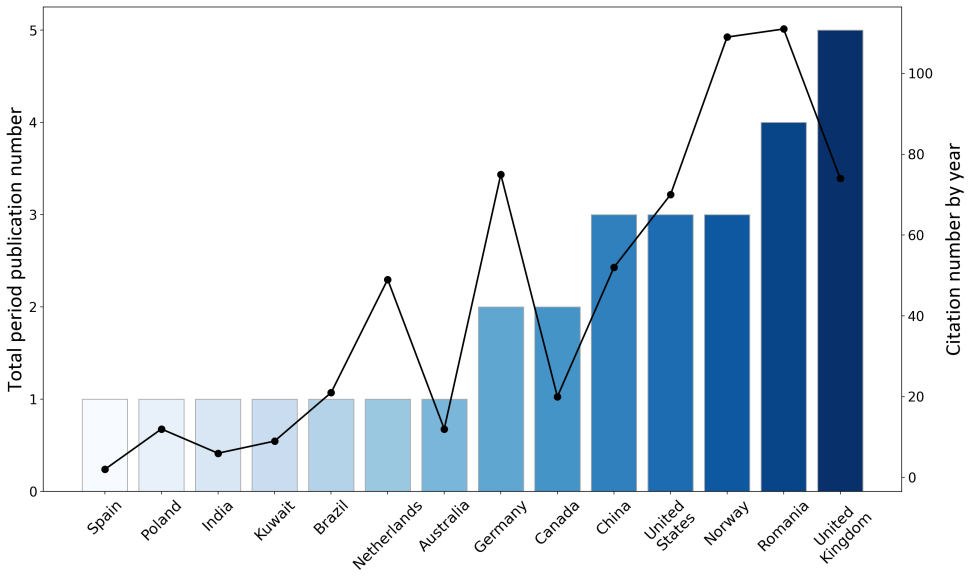

Source: Author

Figure 5 – Bibliometric study of natural gas used in calcium looping – Field publication by year

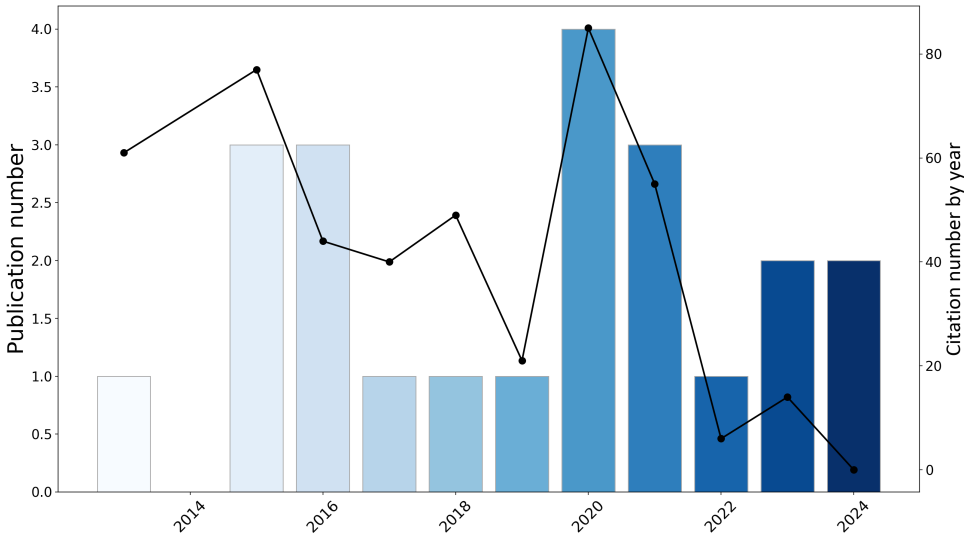

Source: Author

Most of the modelling studies evaluated describe alternative configurations in which CaL

can be implemented to replace coal combustion. (SCHAKEL *et al.*, 2018) reported superior performance for natural gas relative to coal, primarily due to its lower sulphur content and reduced impurity levels, which diminish the purge requirements and consequently decrease both fuel and limestone consumption. These findings are supported by a comprehensive life cycle assessment. (PILLAI *et al.*, 2022) demonstrated that the performance of NGCC systems integrated with CaL can be further enhanced through the incorporation of renewable energy sources. Nevertheless, the cost of natural gas has been identified as a significant concern (MOORE; CRISTINA; KULAY, 2019).

An alternative application was proposed by RAMEZANI *et al.* (2015), who modeled the use of CaL to regulate CO_2 flows for greenhouse crop cultivation. The majority of studies in this area have focused on adjusting NGCC–CaL system efficiencies to approach those of conventional coal-fired power plants; however, many of these works omit critical process information, such as the gas atmosphere employed in the carbonator. In some cases, inconsistencies have been reported, for example, in the assumed flue gas composition of coal-fired plants, despite natural gas actually being used as the fuel.

HU; AHN (2017) proposed a modification of the calciner outlet stream in order to both increase the CO_2 concentration from 4.0% to 6.8% and reduce the energy required to heat the fluidized bed.

Figure 6 – Bibliometric study of natural gas used in calcium looping – Keywords usage

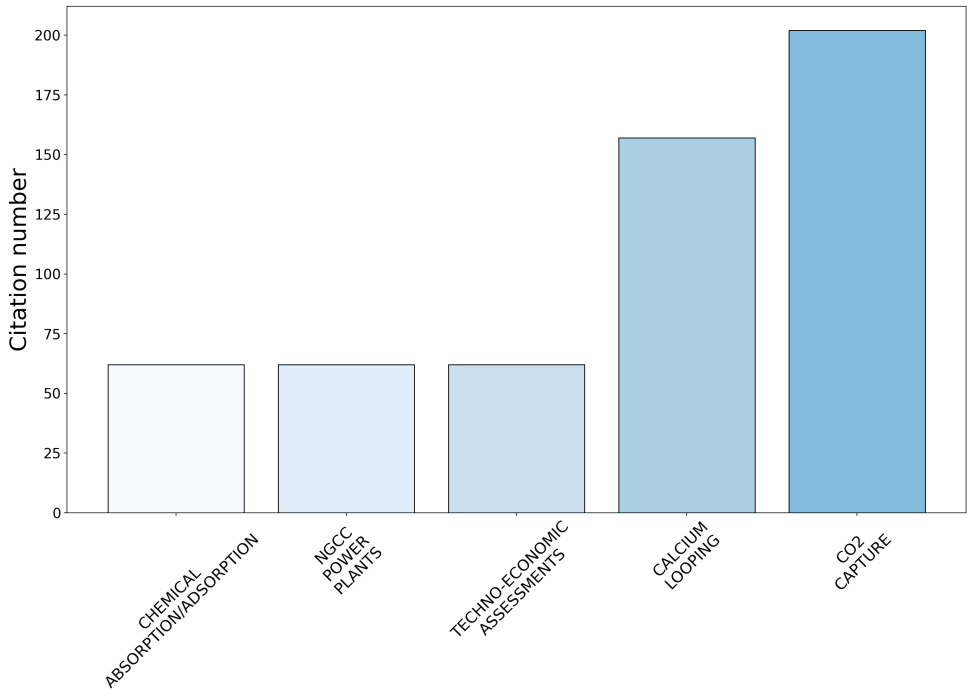

Source: Author

The pool of experimental studies is restricted to only three publications which, despite methodological differences, constitute an important step in the development of CaL systems

applied to natural gas fields. SYMONDS *et al.* (2016) is the earliest contribution identified in this bibliometric review. In that work, the authors employed a natural-gas-fired combustor to supply a CO_2-rich flue gas, with a concentration of 8.59 vol.% under wet conditions, to the carbonator. However, their primary objective was to compare the performance of synthetic Ca-based pellets with that of natural limestone, rather than to investigate the impact of low CO_2 concentration on the carbonator performance.

HAAF *et al.* (2020a) examined the use of Solid Recovered Fuel (SRF) in the calciner and its influence on the CaL process, while employing lignite- and natural-gas-derived flue gases in the carbonator. They reported an adjusted flue gas CO_2 concentration of 9.5 vol.%, which, according to the authors, is typical of waste-to-energy plants. Their results indicate that the incorporation of SRF into the process does not adversely affect CO_2 capture efficiency.

DUHOUX *et al.* (2020) investigated the effect of different pressures in a TGA setup under simulated coal- and natural-gas-derived flue gas atmospheres. Nonetheless, their carbonation experiments were conducted at a CO_2 concentration of 16.7 vol.% (wet basis).

Overall, although these studies incorporate natural gas in some aspect of their experimental configurations, none explicitly addresses the influence of low CO_2 concentrations on CaL reaction performance. Furthermore, actual natural-gas-based flue gases typically exhibit substantially lower CO_2 levels (on the order of 4.0 vol.% wet, as discussed in section 2.4.3), which may significantly affect the CaL process due to reduced CO_2 availability for reaction with CaO. Based on the SCOPUS database search conducted with the specified keywords, it can be concluded that no experimental work has yet systematically examined the effect of low CO_2 concentrations in natural-gas flue gas on the CaL reaction, nor has any study attempted to determine optimal process parameters (such as carbonation temperature, residence time, fluidization velocity, and particle size) for this specific configuration, either at TGA laboratory scale or in fluidized-bed systems.

1.5.2 Research alignment with the Sustainable Development Goals (SDGs)

The data generated in this project will be unprecedented and of broad relevance to society, particularly for applied research, targeting CCS technologies with enhanced performance and reduced costs. The project also investigates the CaL process under conditions representative of natural gas combustion, which is highly desirable for the Brazilian government given the increasing use of natural gas at the industrial scale. Furthermore, most of the data obtained for the DIFB system under these conditions, using Brazilian dolomite as sorbent, are unprecedented.

In this context, the project has substantial potential to advance innovation and originality in the field. The results will be extensively disseminated through national and international scientific conferences and in peer-reviewed journals, thereby providing objective indicators for assessing both the scientific quality of the work and the progress of the project.

The United Nations (UN) formulated the Sustainable Development Goals (SDGs), comprising 17 objectives that address the principal development challenges affecting populations worldwide,

including those in Brazil. This study is understood to be aligned with three of the 17 objectives established by the UN, which are listed below:

SDG 7 – Lean and affordable energy

SDG 9 – Industry, innovation and infrastructure

SDG 13 – Action against global climate change

1.5.3 Research originality

The originality of this thesis resides in the comprehensive and integrated experimental assessment of the CaL process employing Brazilian dolomite under operating conditions representative of natural gas-fired power plants, a scenario that remains relatively underexplored in the scientific literature. By combining TGA analysis, bench-scale DIFB experiments, and detailed pore structure characterization, this study establishes a robust basis for comparing fixed-bed and fluidized-bed reactor configurations, thereby enabling the formulation of operational criteria and the performance of realistic techno-feasibility evaluations.

A key contribution of this work is the elucidation of pore-blocking mechanisms and the identification of a critical pore-size window (30–100 Å) that governs both the initial CO_2 capture efficiency and the cyclic performance degradation, thereby establishing a direct correlation between sorbent microstructure and performance under low CO_2 partial pressures. Furthermore, the use of a rotatable central composite design (RCCD) enabled the determination of optimal carbonation conditions that simultaneously balance energy demand, capture efficiency, and long-term sorbent stability.

Overall, this thesis presents original experimental evidence indicating that performance constraints in fluidized bed systems are predominantly governed by the intrinsic physicochemical properties of Brazilian dolomite, rather than by the relatively low CO_2 concentrations employed. These findings establish a robust and realistic foundation for subsequent pilot-scale investigations and for the rational design and optimization of CO_2 sorbents tailored to the Brazilian energy sector.

1.6 STRUCTURE OF THE THESIS

This thesis is organized into five chapters. Chapter 1 provides an introduction. Chapter 2 presents a bibliometric review, the identification and development of scientific gaps, a review of CO_2 capture technologies, and an analysis of the Brazilian natural gas utilization profile. Chapter 3 describes the materials and methods employed to obtain the results reported in Chapter 4, which presents and discusses the findings. Finally, Chapter 5 offers the conclusions of this thesis, highlighting the main results and providing suggestions for future research.

2 LITERATURE REVIEW

2.1 BIBLIOMETRIC ANALYSIS

To quantitatively assess scientific production, as well as determine scientific gaps, a bibliometric review was conducted. Bibliometric analysis makes it possible to examine trends and patterns within a given field of inquiry, thereby facilitating the detection of underexplored or emerging topics. This approach typically relies on the major scientific databases to generate a systematic meta-analysis of the relevant literature.

Given that this study has already been published, the analytical scope is confined to data collected up to 2023 in order to preserve the originality and distinctiveness of the contribution.

2.1.1 Database formation

To start compiling the database, the topic should be well outlined. In this context, the database search should reveal works related to experimental data and setups for CaL utilization. A total of ten manuscripts from relevant paper references were selected, while a manual check was conducted to ensure that works had experimental data, an experimental apparatus description, a material description and that they were conducted in the context of CaL processes using a fluidized bed reactor. The previous requirement was used to lay down the following eligibility criteria:

1. It should not be classified as a conference, abstract, or be under consolidation;
2. It must be focused on CaO and $CaCO_3$, regardless of whether it has undergone a procedure to enhance its properties or not;
3. The research scope must be within experimental carbon capture using fluidized beds, which should be bubbling or circulating;
4. The primary focus of the paper must be the development, specific details, phenomena, and limitations of the technique used for CaL carbon capture using fluidized bed reactors;
5. In order to validate experiments and analyses, CaO and $CaCO_3$ conversion processes must be observed in at least one complete cycle.

They were used to reveal that the whole database has been filtered in accordance with such criteria.

Keywords were collected from ten papers and listed in order of frequency. The most frequent keywords were “calcium looping”, “co2 capture”, and “fluidized bed” with eight occurrences each, followed by “attrition” with four occurrences and “limestone” with three. An additional 13 keywords were also found; however, they were disregarded since they were found only once on

the list. The remaining keywords were “attrition” and “limestone”, which restricted the search only to natural limestone; therefore, they were also disregarded.

An online search for recent publications was performed on 14 February 2023 on the Scopus and Web of Science databases in an attempt to find the words “calcium looping”, “co2 capture” and “fluidized bed” in the title, abstract, or keywords of papers.

A total of 133 results from the Scopus database were obtained after inputting the selected keywords. Only final editions of research papers published in English were retrieved. Ultimately, 103 manuscripts remained, and 98 of them could be accessed. The results were manually narrowed down to the topic of ’experimental CaL technique applied to fluidized bed’ using the eligibility criteria. Similarly to the process conducted in papers to establish criteria, database papers were downloaded, and the information present on the criteria was sought manually. Only papers containing all these items of information were selected. Based on these criteria, only 37 items satisfied the requirements. These papers were then organized by author names, title, journal title, author keywords, indexation keywords, abstract, addresses, references, number of citations, year of publication, DOI, database source, country, and affiliation on a data frame.

The same procedure described above for the Scopus database was used for the Web of Science database, and it yielded 71 results. A total of 65 items remained after applying the filters. The result of a comparison between the two databases found 19 duplicate articles, which were then removed from the list to result in 51 papers, but access was only granted to 49 of them. After applying eligibility criteria, only five papers remained. They were separated into a new data frame combining the Scopus and Web of Science databases. The final data frame comprised a total of 42 articles.

2.1.2 Data analysis methodology

Documents were extracted in a CSV (comma-separated values) format from the Scopus and Web of Science databases. Due to variances in the structure of both files, it was necessary to standardize data collection. The Scopus database was used as standard. Data columns inconsistent with the current analysis were removed. Then, documents were arranged according to their year of publication and included the following details: authors’ names, document title, source title, keywords, abstract, affiliations, and DOI (digital object identifier). The information provided was used to carry out a variety of bibliometric analyses. This paper regards that publication relevance entails a large number of citations; therefore, the year of publication served as a weighted indicator of significance. In this case, a study published four or ten years ago might have had a similar amount of citations, but, due to the time required to compile a paper, there was insufficient time for research published to receive citations.

This analysis assessed the relevance of articles using the number of citations as the criteria. A publication with a great number of citations is believed to provide a distinctive viewpoint on a subject or offer solutions to problems.

In order to classify authors, the citations must be attributed in a structured way. Citations were attributed through two steps. Firstly, for each paper, the authors were arranged, and the total number of paper citations was assigned to the first author. Secondly, after assigning the citation for every paper, the authors were organized in descending order by summing citations.

The dataframe assessment process made it possible to identify research trends, key results over the years, experimental setup dimensions, materials, sizing, and scientific gaps that might not have been filled yet. Additionally, an international overview of research development was performed by assessing the number of articles published by different nations and authors. Furthermore, a correlation between keywords used to create our database and those which generated a greater number of citations by database was examined.

2.1.3 Co-citation analysis methodology

This analysis was restricted to the Scopus database (37 articles), since it was impossible to export citation information through the WoS database.

There was a list of references associated with every input. Citation information is composed of authors names, paper name, year, journal name, and page number. For this analysis, information was filtered using only authors' names. For every author cited, their name was attributed to each collaborator of an input paper.

Two new lists were compiled: one only with authors based on publication and citation and the other having a relation between publishing author and cited author, in which each author of a published paper received all author citations. Every link with equal names was then removed from the list.

A list containing only one author's publications and citations was vast and contained a large amount of non-critical information. It was found that many citations were not correlated with the remaining publishing authors, and the list was filtered so that only authors included on the lists of publications and citations were selected.

A list of unique authors was used as the central node of the analysis. In order to define the strength of peer cooperation, the number of times an author cited another was counted, and, the larger the number, the wider the bar and the greener the color of names was.

2.1.4 Analyses of publication and citation tendencies

The number of documents and citations per year that reveal publication patterns are displayed in Figure 7. Three periods are the most relevant: 2008, 2010–2012, and 2018. A rising trend in the number of publications can be observed, starting from papers published in 2008. In the following years, there was a continuous increase in the number of documents published until 2013, after which the annual production remained constant until 2017. Compared to earlier years, 2018 showed a significant increase in the number of documents published, which might be related to the Paris Agreement being concluded in 2016. In 2019, there was a decline in

production, which was expected, given the results of 2018. 2020 also had larger numbers of above-average documents, which indicated a steady growth in the amount of knowledge on the subject. There was a small number of articles published between 2021 and 2022, possibly due to the COVID-19 pandemic, which might have halted scientific research.

An examination of the most frequently cited authors was performed to more precisely indicate essential research in Figure 7. This analysis can assist in the discussion, once the author and research receiving the majority of a given year's citations can be identified. Figure 8 shows the five most cited authors from the data frame, along with their respective publications over the years.

Figure 7 – Evolution of database citations and publications over the years

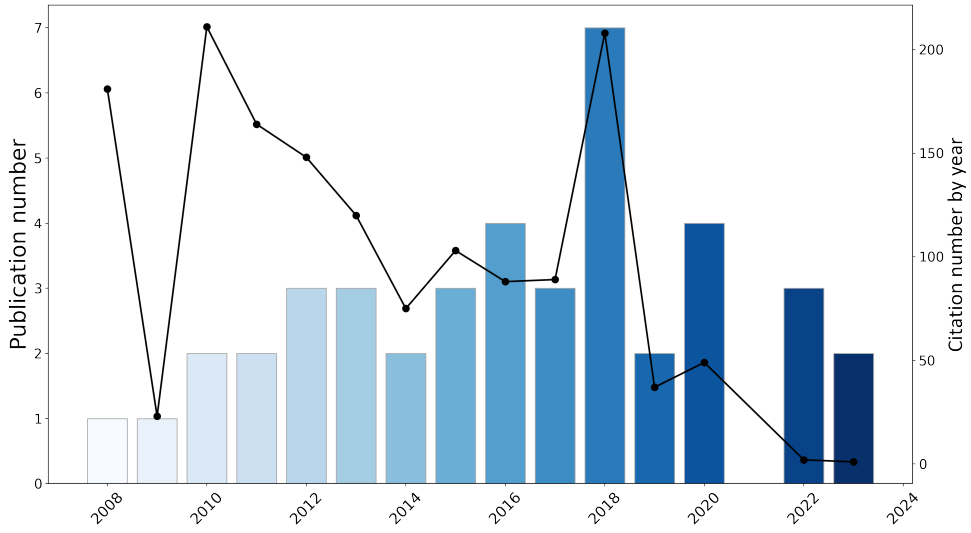

Source: Author

Lu *et al.* 2008 appeared first on Figure 8, and they introduced a dual fluidized bed reactor setup, with each bed being responsible for a single reaction in the CaL process. This investigation revealed recent research complications, such as the attrition of particles (COPPOLA *et al.*, 2019; HILZ *et al.*, 2019). Moreover, the authors clearly stated that several processes were happening on the sorbent surface, which could be seen in other experimental setups, e.g., using fixed bed reactors. The number of gaps and the novelty of works might be a reason for greater interest in this specific technology. 2008 was the year during which there was the highest number of citations on the current analysis, with Lu *et al.* (2008) being the only 2008 work.

Charitos *et al.*(2010) investigated the effects of carbonator space-time, carbonator temperature, and the CaL ratio on a dual fluidized bed reactor plant. Its relevance might be related to parameter denomination and experimental measurement range. Carbon capture efficiency was firstly reported on the data frame as being 90%, and the experimental temperature ranges of maximum CO_2 capture efficiency were provided (600–660 °C). Carbon capture efficiency is related to the CaL ratio and space-time. Furthermore, the effects of sintering were presented and its aggravation with higher cycling, which also impacted CO_2 carrying capacity, pore volume

reduction, and a decrease in particle surface area. Finally, data on the dolomite attrition ratio were 2 wt%/h of total mass. This paper received about 69% of the 2010 total citations, which was quite likely considering the information and measurement reference.

Figure 8 – Current data frame arranged from the most cited to the least authors

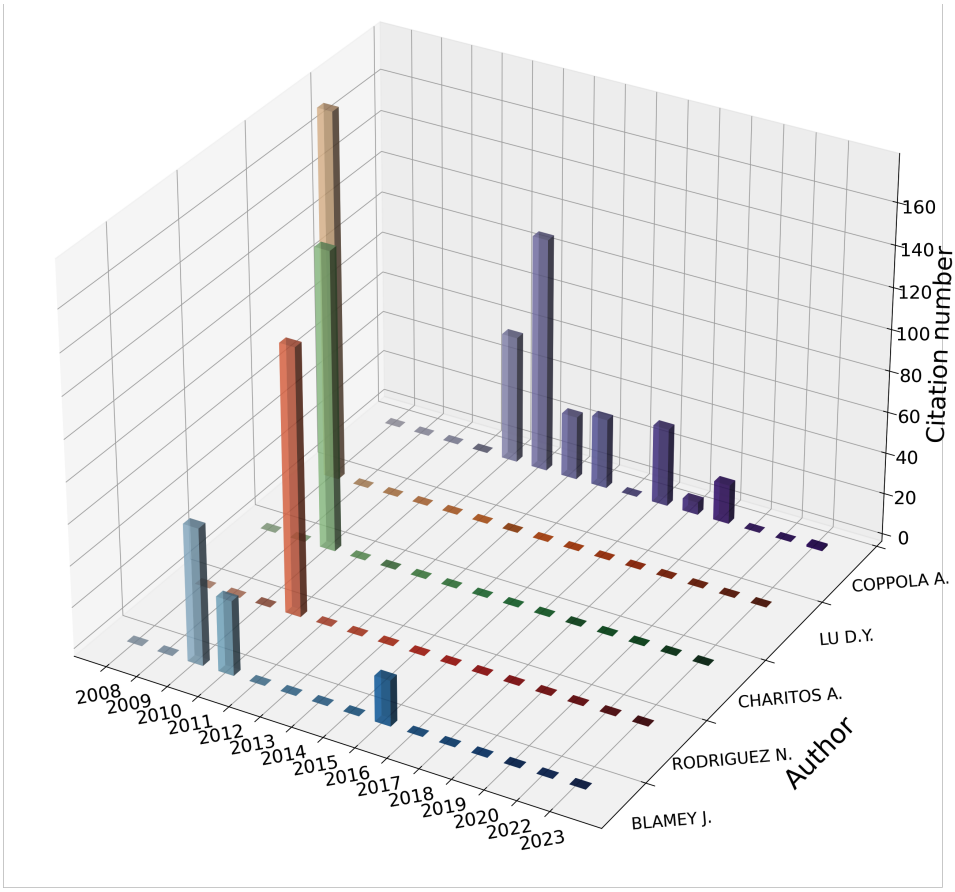

Source: Author

A paper published by Blamey *et al.* ((BLAMEY *et al.*, 2010c)) had 31% of all citations in 2010. The authors investigated the hydration effect of a CO_2 sorbent during the CaL process using a fluidized bed reactor with the aim to mitigate sorbent inactiveness after a few cycles. A higher efficiency was found after a hydration pretreatment of the sorbent, although greater particle fragmentation was also observed due to the stronger sintering effect caused by cycles. Within the evaluation period, this is the very first work on using a pretreatment of sorbent hydration to reactivate it. In addition, they introduced new issues regarding sorbent hydration in a fluidized bed reactor.

A study carried out by Rodríguez *et al.* (2011) received 78% of all citations in 2011, wherein they studied constant CaO flux on the carbonator, and their work was the first of its kind in our database. Due to deactivated particle accumulation inside the carbonator, it presented the cycling of active particles in order to ensure a constant and minimum quantity of activate material inside the fluidized bed reactor. Furthermore, the authors suggested that the efficiency of a sorbent with

a larger number of cycles can be improved by keeping it on the fluidized bed for longer than the newer sorbent, thus enhancing carbon capture efficiency.

Coppolla achieved a total of four publications between 2012 and 2013, among which Coppola et al. ((COPPOLA *et al.*, 2012b; COPPOLA *et al.*, 2013a)) were the ones receiving the largest number of citations. Coppola *et al.* (2012b) was the first work performed by Coppolla and collaborators to be found in our database. It offers an analysis of the effect of SO_2 on carbonation, which was evidenced to be present and harmful to the process (CHEN *et al.*, 2021; COTTON; PATCHIGOLLA; OAKEY, 2013; HOMSY *et al.*, 2020). Furthermore, the authors reported that SO_2 concentrations between 100 and 1800 ppm produced similar results, thereby demonstrating that the SO_2 in flue gas greatly reduced the sorbent CO_2 capture capacity. Additionally, a small increase in attrition was caused by SO_2 during particle carbonation. An interaction between the degree of calcium sintering and the sulphate layer properties generated on the sorbent surface regulated the propensity of limestone to undergo attrition. The SO_2 ratio found in fixed beds was also related to fluidized beds and elutriation results. Coppola *et al.* ((COPPOLA *et al.*, 2013a)) verified the elutriation effect on six different types of limestone using a fluidized bed reactor. The study presents the effect of sintering during the first cycles and found that SO_2 affected the process and presented an average elutriation of 0.5%/h. There was a weak relation of SO_2 to elutriation, in addition to the fact the SO_2 effect on elutriation was introduced therein and is still under discussion recently (COPPOLA *et al.*, 2019).

2018 was the year that achieved the highest number of articles, and it also had a large number of citations. To better understand 2018 (the column presented in Figure 7), an in-depth analysis was conducted, which can be seen in Figure 9, so as to enhance visualization of each individual author's impact on a given year. Among the most cited papers, it can be seen that 28.8% (60) of the total citations were to Antzara *et al.* (2018), 26.9% (56) were to Tregambi *et al.* (2018), and 18.3% (38) were to Arias *et al.* (2018). Together, these authors were responsible for 74% (154) of the total citations in 2018.

Figure 9 – Percentage distribution of author citations in 2018

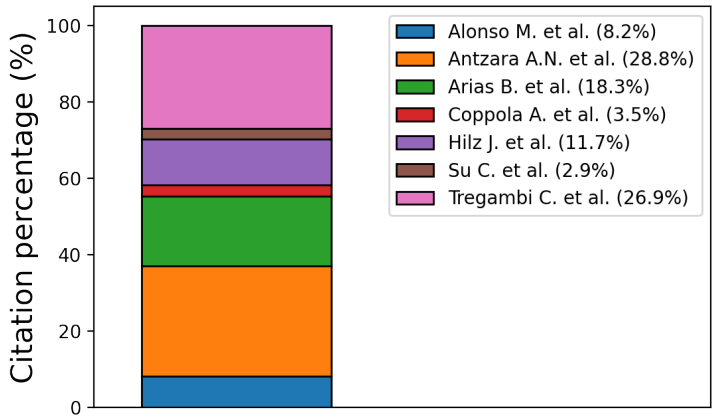

Source: Author

Antzara *et al.* (2018) investigated Zr-promoted CaO-based CO_2 sorbents under various conditions using a fluidized bed reactor with the aim to analyze the decay properties of a sorbent material. The proposed material showed superior properties compared to natural limestone in all aspects. Its larger number of citations might be due to the excellent performance of the proposed material. A hydration analysis was also conducted, and a conversion rate of 85% was found; thus, the capacity of this synthetic material was 5.6 times greater than natural limestone. Its higher performance allows a better use of this hybrid material in the future as the amount of material is reduced, and, consequently, its cost is also reduced due to higher efficiency.

Tregambi *et al.* (2018) used solar energy and a solar concentrator to heat up a CaL reactor. The authors reported a successful CaL cycle, although there was some temperature heterogeneity. Using solar power to conduct the heating might have been the reason for its large number of citations, given that it used clean energy to aid the process and reduce emission rise chances even further, in addition to enhancing the efficiency of CaL technology.

Arias *et al.* (2018) investigated the feasibility of an ultra-rich oxygen condition on a calciner used in La Pereda CaL pilot plant. After a few modifications of their experimental setup, it was possible to perform tests using a max concentration of 75% O_2. The results confirmed the efficacy of its operational condition, which was attributed to the endothermic nature of calcination and the large glow of solids circulating within the carbonator.

After an in-depth analysis of the most relevant years in Figure 7, it can be assumed that its high citation number might be related to the novelty of the experimental setup (LU; HUGHES; ANTHONY, 2008; TREGAMBI *et al.*, 2018), the measurement methods and new experimental data (ARIAS *et al.*, 2018; CHARITOS *et al.*, 2010; COPPOLA *et al.*, 2012b; COPPOLA *et al.*, 2013a), and the novel techniques and methods used to solve known problems (ANTZARA *et al.*, 2018; RODRÍGUEZ; ALONSO; ABANADES, 2011). However, the stage of technology development might have affected the way such information was perceived in the literature. Furthermore, once this data frame is restricted to experimental research investigation, the topics pointed out above might not be true for different areas.

2.1.4.1 Total publication by nation

Figure 10 illustrates the total number of papers published by nation within the years 2008–2023 that were compiled in our database. A total of 12 nations appeared on this list, including 8 members of the EU. The western hemisphere is represented by Canada, and the eastern one by China and New Zealand. The fact that many countries are not included in this list is possibly due to a lack of incentive for CCS technologies. Another point worth mentioning is the absence of developing countries, which indicates a divergent global contribution to carbon emission mitigation technologies.

The large number of EU publications might be due to specific investments. Recently, under project Horizon 2020, two projects have been focused on CaL technology (CLEANKER, 2017; SOCRATCES, 2018). They were developed from 2017 to 2021, which might have affected the

number of publications in 2018. Both projects had a total cost of 14,213,254 EUR and were coordinated by research groups in Spain and Italy. In addition, both projects involved twelve countries, many of which are included in Figure 10. The relationship between nations' numbers of publications and their citation or paper relevance can also be observed in Figure 10. Italy also had the largest number of citations in our database, with a ratio (publication/paper) of 29.9. The lowest ratio was represented by the nations having only one publication. The highest ratio belonged to Canada with 44.7. Canada has invested CAD 319 million in carbon capture, utilization, and storage technologies according to Natural Resources Canada (NATURAL RESOURCES CANADA, 2022). Even though its funding is divided among different technologies, it seems as though a large sum of investment contributed to achieving more paper citations.

Figure 10 – Data frame classifying countries according to their number of publications and total citations

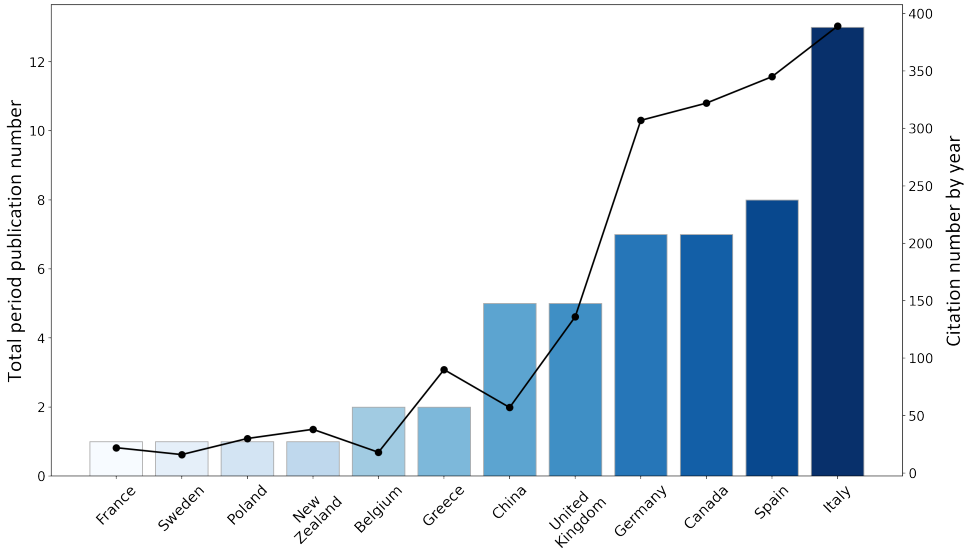

Source: Author

2.1.4.2 Journal analysis

Journals were been investigated based on their number of citations and publications. Although every journal had their cite score and impact factor, such parameters might differ for a specific topic as the one explored herein. Figure 11 presents the number of publications and total sum of citations from the data frame. It can be seen that powder technologies had the highest number of papers for this current topic, although it achieved a low number of citations (109), which suggests that this topic might not be in the scope of this specific journal. By observing the ratio between the amount of publications and the number of documents, the rankings changed as follows: the AICHE Journal (63.5) was ranked first, followed by the International Journal of Greenhouse Control (63), Fuel Processing Technology (46.7), the Chemical Engineering

Journal (45.7), Energy and Fuels (45), Industrial and Engineering Chemistry Research (40.5), Proceedings of The Combustion Institute (29.5), Fuel (27.8), and Powder Technologies (18.2)

For this particular subject, in order to optimize exposition and citation, selecting one of the three journals achieving a higher ratio of publication number/number of documents seemed appropriate.

Figure 11 – Most cited journals by number of documents and citation

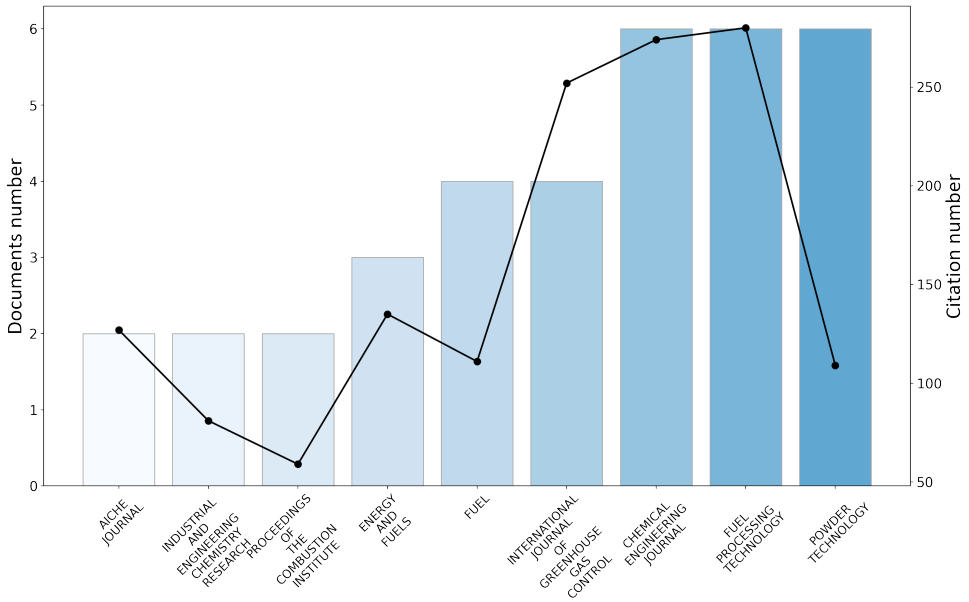

Source: Author

2.1.4.3 Keyword analysis on citation

Figure 12 shows the top five cited keywords, among which 'co2 capture' and 'calcium looping' were the first two keywords on the list. The most cited ones, representing the main subject of this analysis, were also used in the data frame. However, the third keyword, 'attrition', was used differently, as it is an intrinsic characteristic of the process. Even though 'carbonatation' appeared on the list as the main keyword on the topic of calcium looping, it was observed that keyword choice might have reached a higher number of citations to a given work if it was related to the main barriers and gaps found about it. Furthermore, associating the main subject with a keyword is essential to include the work in a given subject, but not addressing gaps and conclusions while selecting keywords could restrict views and citations. This result reveals that two or three keywords addressing the main subject were enough to delimit a topic, and all remaining keywords should be used to highlight gaps to be filled and barriers to be faced. Nonetheless, an analysis of Figure 12 clearly evidences the fact that keyword use reached a maximum number of citations. Therefore, it is important to investigate other databases and themes so as to verify coverage of this statement, given that this result is only valid to this specific theme and data.

Figure 12 – Five most-cited keywords

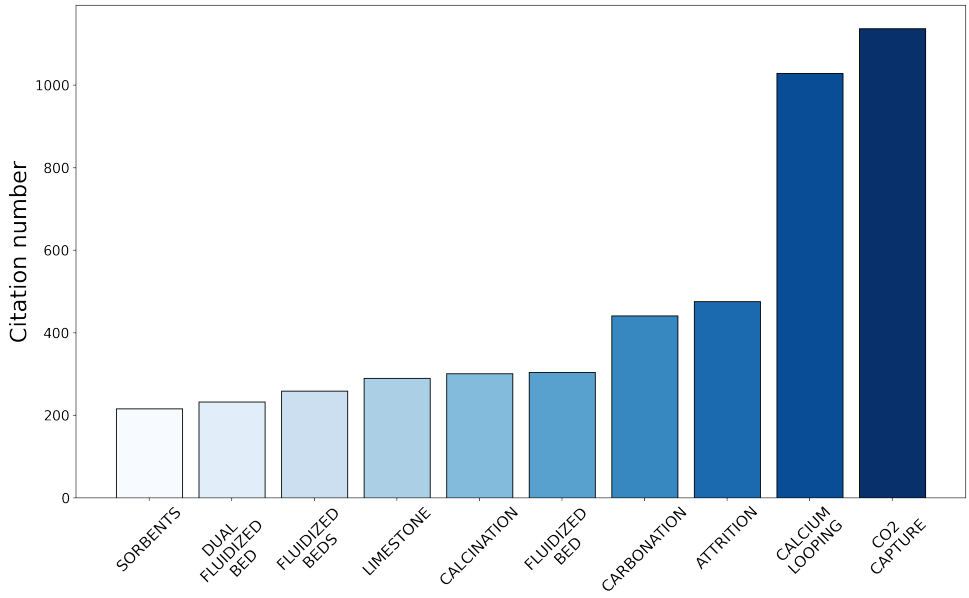

Source: Author

2.1.4.4 Co-citation analysis

Figure 13 presents the analysis of citations between the data frame authors and their citations. Two main clusters of data can be observed: one of strong interconnected names and a peripheral one with many weak connections pairs. A central node (a node with many different connections) is understood as a diverse author with extensive cooperation with different group or individuals and a strong connection (wide dark green bar) entails a strong cooperation between the two names.

The most-cited authors in Figure 8 (COPPOLA A., LU D.Y., CHARITOS A., RODRIGUEZ N., and BLAMEY J.) can be found at different places as central or peripheral nodes; nonetheless, many names have a stronger connection and wider range than all of them, which implies that the citation number does not directly translate into research cooperation. However, while seeking the other names on their publication (which is usually used by the project manager/coordinator of the work), names such as SCALA F., SALATINO, P., ANTHONY E. J., and ABANADES J.C. are not uncommon but are extensively interconnected and have many strong connections on the central cluster. Even though the analysis in Figure 8 initially returned authors having the largest number of citations, Figure 13 shows that citation number did not directly translate into a cooperative researcher, even though it is likely that the paper contained a strong cooperative author.

2.1.5 Manual verification significance

Bibliometric analysis is a meta-data analysis of main scientific Databases. This type of analysis is dependent of search word quality to find exact papers. Figure 14 illustrate the

difference between the analysis of a raw export to a manual filtered export used for bibliometric.

Figure 13 – Data frame co-citation analysis

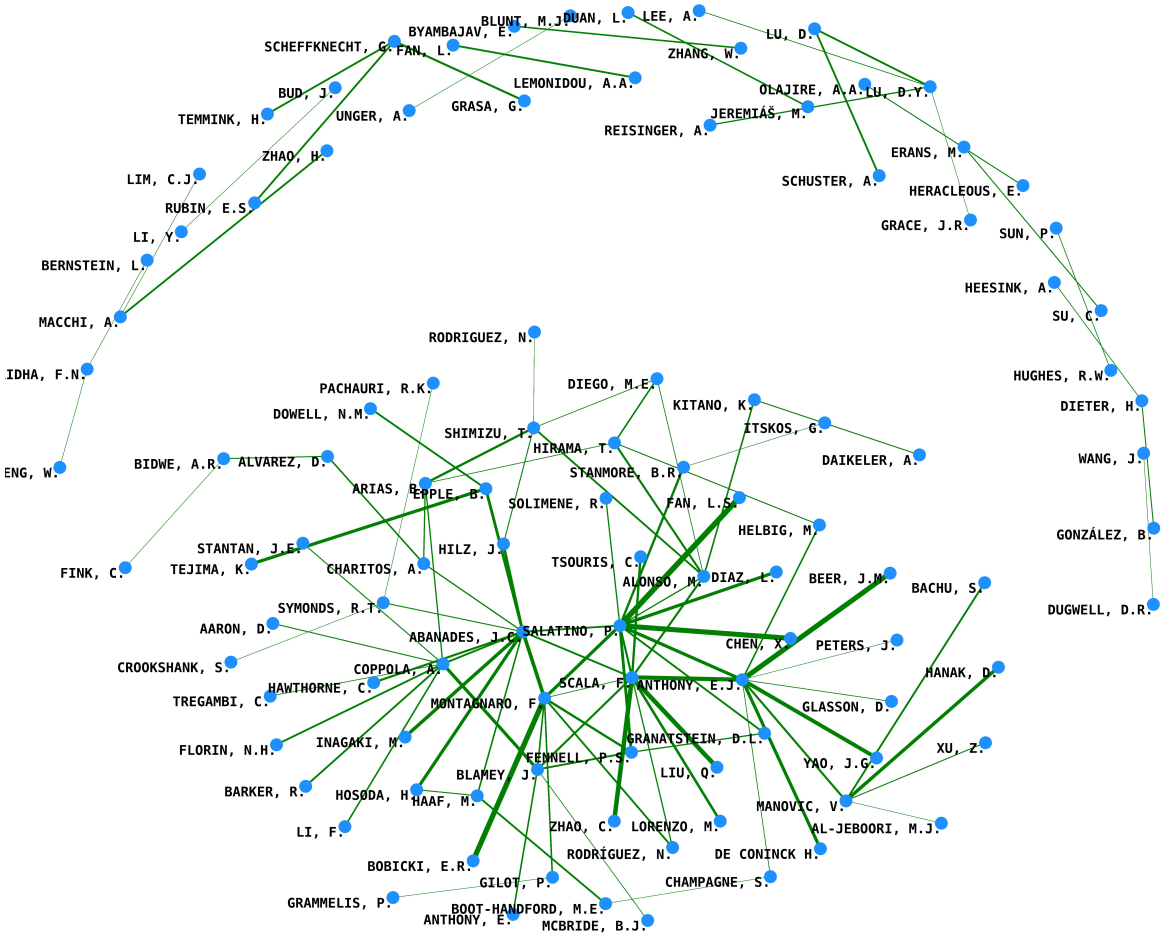

Source: Author

Non relevant works are the majority of papers retrieved from the Databases. In this case, care should be take when using this type of analysis to avoid false conclusions.

2.1.6 Comparative analysis of experimental setups

Table 1 present a comprehensive analysis of relevant experimental data from the Dataframe. Table 1 was compiled with the purpose of presenting the main parameters used in experimental setups of fluidized bed reactors used in CaL processes. It shows that experimental setups are unique, as there are different sizes, sorbents, heating methods and conversion atmospheres.

2.1.6.1 Sorbents of CO_2

Limestone was the most common CaO-based sorbent used, as 77% of total sorbent usage was found. Most experimental setups use raw limestone or in pellets with additions of cement

and clay. Given the fact that it is a natural component, its composition is usually associated with its source due to different compositions. For the present DataFrame, it was found that 25.4% is from Germany, 14.3% from Poland, 12.7% are not mentioned, 12.7% from Italy and Canada, 6.3% from China, Greece and Spain, and 3.2% from the UK. Other works used dolomite and lab-grade CaO, either with or without doping.

Figure 14 – Comparison between raw and manual filtered data used for bibliometric analysis: (a) manual filtered data; (b) raw data

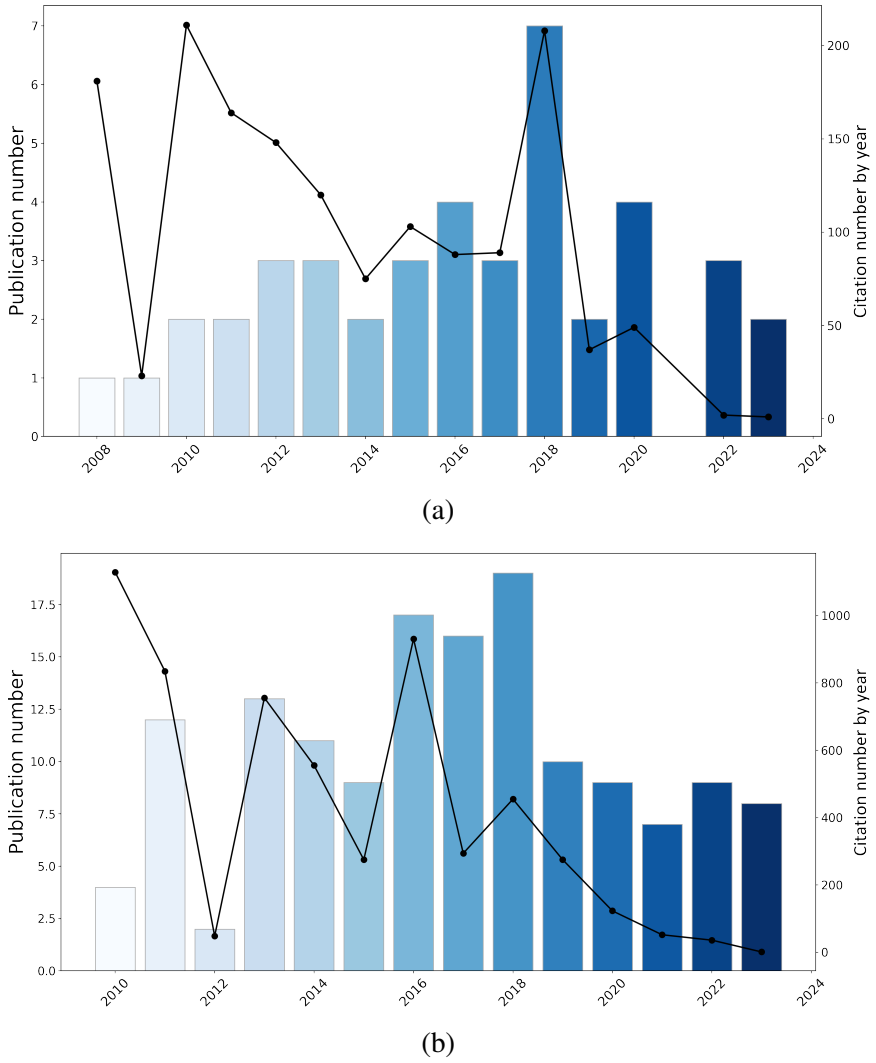

Source: Author

Sorbent were found to be the most widely used, as its particle size might range from 25 µm to 800 µm. Also, many studies use sand inside the reactor to enhance the thermal inertia of its bed. Sand was reported as inactive in the reaction and had a vastly different particle size from that of the sorbent for later sieving. Hydration was used to recover spent limestone due to loss of efficiency, where 37% of works make use of some method of hydration to investigate its effects or enhance capture efficiency.

2.1.6.2 Fluidized bed reactors

Fluidized bed are applied to solid-gas flow reactor due to the higher area of contact between solid and gas improving process efficiency. Fluidized bed can be used as a single unit, where calcination and carbonation takes place on the same reactor, or dual unit where the first reactor control the calcination process while the other controls the carbonation. Most reactors are insulated to have a higher thermal inertia.

Fluidized bed reactors were classified by their flow regime, i.e. circulating or bubbling fluidized beds. 54.8% were configured as bubbling and 26.2% are Circulating, and 11.9% uses both flow regimes, however 7.1% had no clear information about their configurations.

Fluidized bed for calcium looping have different setups, while more studies are necessary to identify which setup suits better an application (TAN *et al.*, 2024), they all follow a similar build structure. Figure 15 present an example of calcium looping lab scale reactors.

Figure 15 – An schematic of a pioneer fluidized bed reactor and research used in CaL

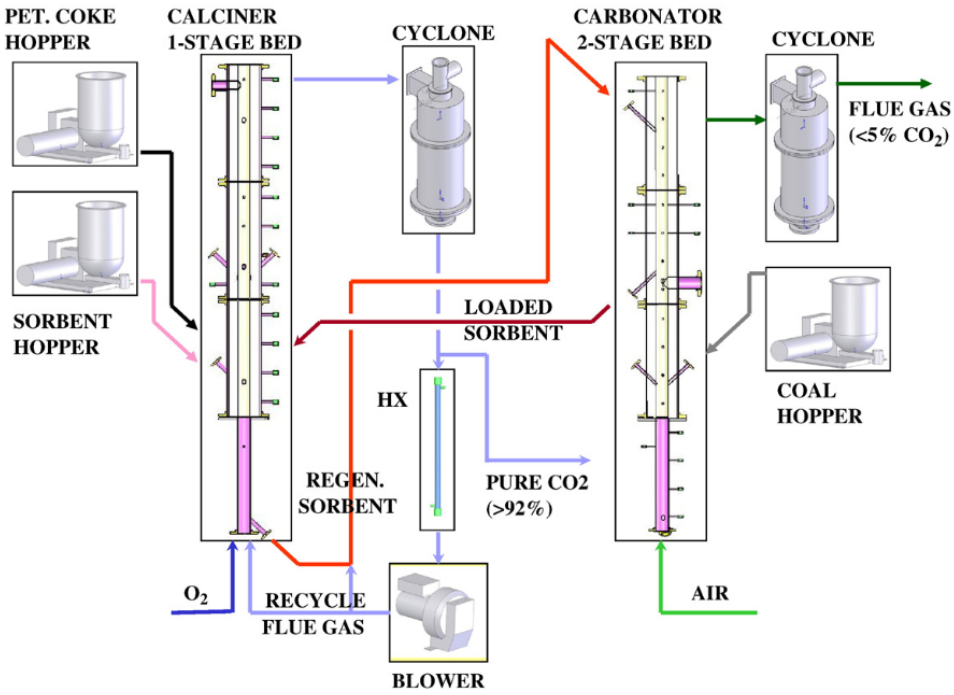

Source: (LU; HUGHES; ANTHONY, 2008)

The main structure of a reactor is composed by a bed reactor where the sample sits above the perforated plate which creates the fluidizing of solid samples. Bed reactor and perforated plates combination can have many setups, including height, diameter, number and types of holes, and material. Below the bed, there is the plenum. The plenum is responsible to even distribute the flow before it passes trough the perforated plate. Before the plenum is the equipment responsible for the flow. A common scenario is to use a blower to inject air at a controlled speed inside the bed. This particular case is common for bed that burn fuel to heat sample. Figure 15 shows an

example of this case where air is blown through coal to capture CO_2 in the carboantor and a mixture of flue gas and O_2 to heat up the calciner.

As discussed earlier, there is two main ways of heating on those setups: Electrical heating or burning. Even though there is some studies evaluating novelty techniques of heating (HOFMANN *et al.*, 2024; TREGAMBI *et al.*, 2018) they are a small quantity if compared to the other two. Electrical heating are used mostly for small lab scale fluidized bed due to its easier control of temperature and lack of corrosive gases as SO_2. For larger scale, usual fuels are coal, hard coal, lignite, and natural gas. Sample are inserted on bed before test start or after flow through a hopper. Where the Hhpper is a structure that inject samples from top to the perforated plate.

The cyclone is used most on circulating fluidized bed, it is a structure which an helicoidal screw that separate fine particle (which are blown up from the cyclone) from the particle that are going to still be used. Particle that are not finer enough to be blown up are caught by the helocoidal screw driving particle back to bed or to another part of the process. Is not uncommon to measure CO_2 content on calcium looping process through a filter plus analyzer installed at the top part of a cyclone.

The majority of studies use two fluidized beds for each reaction represented by Equation (1.2), although lab-scale studies present a single bed configuration usually on a smaller scale. On the Dataframe, 52.4% of data presents a dual bed configuration where two reactors are used and 47.6% consist in using a single reactor.

Heating method of reactors is divided into two main topics, one being electrical resistance and the other by fuel combustion. 66.7% of data is on using the electrical resistance method while 16.7% used calciner run by the fuel type are coal, hard coal, lignite, natural gas and biomass. TREGAMBI *et al.* (2018) was the only study to use a solar/infrared heating method. 14.3% makes use of a combination of a calciner and an electrical resistance to heat reactors.

Regarding the sizing of reactors, minimum height reported on Dataframe is 0.1 m while the highest height reaches 15 m, reaching a value of 5.5 m on average. Diameter follows a similar pattern, once values of minimum and maximum diameter are 0.018 m and 0.75 m, respectively, being 0.22 m on average. 16.7% of works used carbonators and calciners of different sizes.

Calcination and carbonatation operation temperatures and vary widely. Calcination temperatures are in a total range of 750-1000 °C and carbonatation temperature ranges between 550-715 $^{\circ}$ C

Velocity reported on fluidized bed reactors are defined differently. Velocity is commonly referred to as the ratio of superficial velocity required to start fluidization using the minimum velocity. This relation defines non-dimensional parameters which can be used to scale-up the design. On the DataFrame, velocities are reported as minimum fluidization (0.06-2.5 m/s), average velocities (0.8-2.8 m/s), superficial velocities (0.5 - 5.9 m/s), times of minimum fluidisation (2-7 (-)).

2.2 SCIENTIFIC GAPS DEVELOPMENT

Table 1 offers a concise overview of gaps in each article. Five primary gaps were detected in the majority of works: the use of pellets rather than raw materials, attrition and sintering, temperature effects, CO_2 capture capacity mechanism and reactivation of sorbent and steam effects. Despite the fact that these categories are listed separately, these effects are frequently intertwined.

CO_2 capture capacity improvements and its effects were the most widely reported and discussed, in addition to the fact sorbent capacities on fluidized beds are lower than those reported through thermogravimetric analyses (HUGHES *et al.*, 2009). This affirmation was further ascertained by many works attributing such difference to a lack of similarities between fixed bed and fluidized bed tests (SYMONDS *et al.*, 2012), not to mention the distinct fluid dynamics affecting heating and reaction rates (COPPOLA *et al.*, 2013). Another indirect fact worth mentioning also contributes to the affirmation that particle sizes affect fluidization due to segregation (ALONSO *et al.*, 2014), in addition to the fact that fuel quality and inert material within the bed influence sorbent inactiveness (HILZ *et al.*, 2017). However some studies found that bed inventory using inert material, like sand, might have a negative impact on limestone porosity/carbon capture capacity (LAURO *et al.*, 2023; TREGAMBI *et al.*, 2023).

CO_2 capture capacity was found to be susceptible to multiple parameters, such as the presence of SO_2 reducing effectiveness (ACHARYA; DUTTA; BASU, 2012; COPPOLA *et al.*, 2012b) which could greatly affect efficiency, even in negligible amounts (COPPOLA *et al.*, 2012b). Soon afterwards, it was found that high temperatures and CO_2 concentration could affect CO_2 capture capacity (COPPOLA *et al.*, 2013b). The effect of temperature was further explored and it was found that combustion leads to higher heat transfer, although it was also detected that it causes local high temperature spots which in turn increases sintering and decay of activities (CHARITOS *et al.*, 2010; DUELLI *et al.*, 2015b; KONG *et al.*, 2024; TREGAMBI *et al.*, 2018). Moreover, some researchers have reported that not only high temperature causes damage in long-term carbon capture, but thermal shocks might have an effect on particles (COPPOLA; SCALA; SALATINO, 2018). It was also reported that these damages might be irreversible once the thermal history of sorbent seems to affect CO_2 carbon capacity (COPPOLA *et al.*, 2017; COPPOLA; SCALA; SALATINO, 2018). However, recent studies found higher temperature of carbonation have shown an increase surface resistance of limestone that led to reduced fragmentation (COPPOLA *et al.*, 2023).

A hindrance to the CaL technology is a reduction in CO_2 carbon capacity with a greater number of cycles due to sintering and pore pluggage (ACHARYA; DUTTA; BASU, 2012). Sintering processes are directly linked to attrition and sorbent loss during fludized bed reactions (LU; HUGHES; ANTHONY, 2008), which are higher to calcinated samples and often linked to orifice velocity (ASIEDU-BOATENG *et al.*, 2023). Notwithstanding the fact that effects of elutriation are greater with a large number of cycles, high attrition regimes, as those found

while using bubbling fluidized beds, have been reported to worsen the effect (BLAMEY *et al.*, 2011). Multiple works have attempted to mitigate the effect of elutriation and sintering in order to improve CO_2 capture capacity. Increasing the presence of MgO using dolomite have proved to achieve higher CO_2 capture capacity (COPPOLA *et al.*, 2013b). Furthermore, counterbalancing loss of efficiency with larger number of fresh particles (COPPOLA *et al.*, 2023a; RODRÍGUEZ; ALONSO; ABANADES, 2011) and pelletization of limestone and CaO (BLAMEY *et al.*, 2016) have showed a few advantageous effects. Pellets are an alternative in CaL research due to achieving better performance than raw limestone (BLAMEY *et al.*, 2016; HILZ *et al.*, 2018). Although some works have pointed out that the cost of pellets could be reduced on a larger scale (SYMONDS *et al.*, 2016), others express disagreement with (RIDHA *et al.*, 2016).

Hydration of new and spent limestone is deemed as solution to the decay effect after a large number of carbon capture cycles (COPPOLA *et al.*, 2017; COPPOLA *et al.*, 2019). The most commonly reported reactivation method is water soaking or using steam, and the latter is reported as the most efficient (COPPOLA *et al.*, 2015). Steam seems to increase carbon capture capacity, up to a threshold temperature and if a higher temperature is used, sintering effect decrease carbon uptake (COPPOLA *et al.*, 2023) due to embrittlement caused by the temperature, as appears to have no direct correlation to combined effect of steam use and carbonation temperature (MASSA *et al.*, 2024). Studies on salt water doping are being conducted, but it should be harmful to CO_2 capture capacity if overdoped (GONZÁLEZ; KOKOT-BLAMEY; FENNELL, 2020). Even though steam is beneficial to CO_2 uptake (COPPOLA *et al.*, 2017; COPPOLA *et al.*, 2019), there seems to be a lack of understanding about its effect, as some authors reported that hydration increases particle breakage at higher temperatures (BLAMEY *et al.*, 2010b), nevertheless, it depends on steam concentration (DONG *et al.*, 2020).

Table 1 – DataFrame experimental setup parameters and conditions

Reference (year)	Sorbent: type/ pretreatment / origin / particle size	Fluidized-bed: type / dual or single / heating method / height x diameter	Process: calciner x carbonator atmosphere / calciner x carbonator temperature / Investigated velocity / Wattage / Capture efficiency	Gaps
COPPOLA *et al.* (2023a)	Limestone / no / Italy, Poland, Germany / 600-400 μm	Bubbling / Dual / Resistance / n.i. x 0.04 m	calc 10%CO_2-air, carb 10%CO_2N_2 / 950 x 650 °C / $U_{carb} = U_{calc}$ = 0.5 m/s / n.i / 85-15%	(1) Materials, pre-processed in Dual Interconnected Fluidized Beds, underwent impact fragmentation following a chipping/splitting pattern as a function of an increase in impact velocity.
COPPOLA *et al.* (2023)	Limestone / hydration / Italy / 600-400 μm	Bubbling / Dual / Resistance / n.i. x 0.04 m	calc 10%CO_2-Air carb 10%CO_2-0-10%H_2O-N_2 / 850 x 700-600 ° C / $U_{carb} = U_{calc}$ = 0.5 m/s / n.i / 0.23-0.03 g/g	(1) Optimal carbonation temperature of 650 °C is suggested for this limestone once it both satisfies CO_2 uptake of N number of carbonation stages and slight tendency to attrition/fragmentation.
CHAI *et al.* (2022)	Limestone + doped CaO / no / China / 180-125 μm	Bubbling / Single / Resistance / 0.9 x 0.032 m	CO_2-CO-NO-O_2-N_2 balance carb, 20%$O_2 - CO_2$ calc / 950 x 650 °C / U_{carb} = 0.018 m/s / n.i / n.i	(1) the Ce ($(CH_3CO_2)_3Ce\dot{x}H_2$ + limestone mixture) doping is more advantageous for N_2 formation and CO_2 adsorption than that of Mn doping on the CaO surface.
LI; WANG; LI (2022)	Limestone + pellets / no / Canada / 850-600 μm	n.i / Single / Resistance / n.i x 0.0254 m	17%CO_2-N_2 / 850 x 675 °C / n.i / n.i / 0.5-0.1 g/g	(1) Synthetic sorbents showed an uptake capacity of 0.4–0.45 g/g after 5 cycles in the reactor system, much greater than the uptake capacity of Cadomin limestone (0.15 g/g after 5 cycles). (2) MgO-promoted sorbent indicated a higher uptake capacity than $CaZrO_3$-promoted sorbent due to the higher mass ratio of CaO in the sorbent. (3) SEM images indicated formation of cracks in post-cycling samples, as a result of expansion and contraction of sorbent grains going through carbonation and calcination.
HASHEMI; ZHOU; MAHINPEY (2022)	Limestone / no / China / 1250-150 μm	Bubbling / Single / Resistance / n.i x 0.028 m	17%CO_2-N_2 / 920-750 x 650 °C / 3xU_{mf} / n.i / 0.5-0.1 g/g	(1) The effect of particle size on limestone calcination kinetics presents three-zone characteristics of the reaction controlling mechanism. In Zone I, particle size is < 80 μm, which has little effect on consumption rate, and calcination is mainly controlled by the chemical reaction. In Zone III, particle size is > 450 μm, the calcination process is mainly controlled by gas diffusion, and the effect of particle size is significant. In Zone II, particle size ranges between 80–450 μm and calcination is controlled by both gas diffusion and the chemical reaction.

* n.i means nothing informed or it was not possible to find the information

Table 1 continued

Reference (year)	Sorbent: type/ pretreatment / origin/ particle size	Fluidized-bed: type / dual or single / heating method / height x diameter	Process: calciner x carbonator atmosphere / calciner x carbonator temperature / Investigated velocity / Wattage / Capture efficiency	Gaps
GONZÁLEZ KOKOT-BLAMEY; FENNELL (2020)	Limestone / hydration / Canada, United Kingdom, Spain / 710-500 μm	n.i / Single / Resistance / 0.5 x 0.021 m	15%CO_2-0-10%steam-N_2 / 900 x 700-650 °C / 8xU_{mf} / n.i / n.i	(1) Calculation results reveal that it is likely that other researchers investigating seawater and $NaCl$ doping of limestone in CaL processes reported reductions in reactivity while overdoping their sorbents.
HAAF *et al.* (2020b)	Limestone / no / Germany / 500-25 μm	Circulating / Dual / Calciner (Fueled by Natural Gas) / 8.6 m carb and 11 m calc x 0.59 m carb and 0.4 m calc	Flue gas 9.5%CO_2 / 920-750 °C x 690-610 °C / U_{carb}=3.5-2.5 m/s x U_{calc} = 5.5-4.5 m/s / 1 MW/ 92-42 %	(1) Attention should be placed upon the hydrodynamics of coupled fluidized bed systems with regard to coarse inert ash fractions. (2) Further works are required to assess the influence of Solid Recovered Fuel during the solid phase and gaseous emission generation by the calciner.
DONG *et al.* (2020)	Lab grade CaO / Hydration / n.i / 850-430 μm	Bubbling / Single / Resistance / 0.6 m x 0.06 m	carb = 20%CO_2-0-40%steam-N_2, calc = 10-40%steam - N_2/ 900 x 650 °C / n.i / n.i/ dry = 15-20.5%, hydrated = 15-21.7%	(1) The effect of steam during calcination was influenced by steam concentration. While carbonation conversion efficiency increased by adding 10 vol.% steam after 10 CaL cycles, a concentration of 20 and 40 vol.% led to a negative impact on sorbent reactivity due to sintering acceleration leading to smaller surface area and larger pore size.
DIEGO; ARIAS (2020a)	Limestone / no / n.i / 130-80 μm	Circulating / Dual / Calciner (n.i) / 15 m x 0.65 m carb and 0.75 m calc	14%CO_2 carbonator / n.i x 670-660 °C / U_{carb} = 5.5-2.0 m/s and U_{calc} = 5.9-2.6 m/s / 1.7 MW/ 100-50 %	(1) Modifications to the make-up flow might be needed in a few cases to counterbalance the hydrodynamic changes occurring in flexible CaL systems to ensure high CO_2 capture efficiencies.
HILZ *et al.* (2019)	Limestone / no / n.i/ n.i	Circulating / Dual / Calciner / 8.6 m carb and 11 m calc x 0.6 m carb and 0.4 m calc	carb = 13%CO_2 x n.i / 900 x 700-630 °C / U_{carb} = 2.2 m/s and U_{calc} = 5.5-5.0 m/s / 1 MW / 88-70 %	(1) Conservative parameters, such as specific carbonator inventory > 700 $kg/m2$, make-up ratio > 0.15 mole Ca/mole CO_2 and looping rate of 10–15 mole Ca /mole CO_2 were identified as the basis to scale-up the process.

* n.i means nothing informed or it was not possible to find the information

Table 1 continued

Reference (year)	Sorbent: type/ pretreatment / origin/ particle size	Fluidized-bed: type / dual or single / heating method / height x diameter	Process: calciner x carbonator atmosphere / calciner x carbonator temperature / Investigated velocity / Wattage / Capture efficiency	Gaps
COPPOLA *et al.* (2019)	Limestone / Hydration/ Germany / 600-400 μm	Bubbling / Dual / Resistance / 1 x 0.04 m	calc = 70%CO_2-air and carb = 15%CO_2-Air, 15%CO_2-10%H_2O-Air / 940 x 650 °C / $U_{carb} = U_{calc}$= 0.5 m/s / n.i/ dry = 0.05-0.20 hydrated = 0.07-0.20 gCO_2/g Initial sorbent	(1) Steam exerts a beneficial effect on CO_2 uptake, which can be even great enough to counterbalance the detrimental effect of SO_2 when concentration of the latter is small. (2) As regards sorbent mechanical properties, attrition is very limited under all operating conditions. The presence of H_2O and/or SO_2 leads to a slight increase of sorbent fragmentation which, however, is not likely to significantly affect the operation of a CaL process.
SU; DUAN; ANTHONY (2018)	Limestone, cement, spent bleaching clay / no / China / 600-250 μm	Bubbling / Single / Resistance / 1.1 x 0.025 m	carb = 15-20%CO_2-N_2 calc = 80%CO_2-N_2 / 920 x 650 °C / U_{carb} = 0.05 m/s / n.i/ 10-44 g CO_2/100 g calcined sorbent	(1) The prepared pellets demonstrated lower elutriation rates as they had greater sphericity than limestone particles. (2) doped limestone-based pellets showed superior cyclic CO_2 capture capacity and attrition resistance.
ALONSO *et al.* (2018)	Limestone / no / n.i / 600-0 μm	Circulating / Dual / Resistance / 6.3 m carb, 6.1 m calc x 0.1 m	air + coal fumes / 780 °C x n.i/ n.i/ 30 kW / n.i	(1) Neither the Attrition Index defined by Gwyn nor that proposed by Forsythe and Hertwig are able to account for the changes observed in Power Spectral Density (PSD) curves sufficiently well. However, the Total Particle Generated Index and the maximum particle size generated during attrition, which require a re-construction of PSDs of elutriated and non-elutriated solids, provided a more accurate description of attrition phenomena as for this methodology, in addition to distinguishing different attrition mechanisms and ranking the materials
ARIAS *et al.* (2018)	n.i/ no / n.i / n.i	Circulating / Dual / calciner (Fueled by coal) / 15 m x 0.65 carb m and 0.75 calc m	carb = 12-14%CO_2 and calc = 70%CO_2 / 950-830 x 715-620 °C / U_{carb} = 4.5-2.5 m/s and U_{calc} = 5.0 - 3.5 m/s / 1.7 MW / 95 - 40 %	(1) Results confirm that it is possible to operate the calciner of a CaL system under oxygen-rich conditions due to the endothermic nature of a calcination reaction and the large flow of solids circulating within the carbonator. The axial temperature profiles measured along the calciner during these tests showed that no hot spots are found as long as there is sufficient circulation and bed inventory of solids in the calciner.

* n.i means nothing informed or it was not possible to find the information

Table 1 continued

Reference (year)	Sorbent: type/ pretreatment / origin/ particle size	Fluidized-bed: type / dual or single / heating method / height x diameter	Process: calciner x carbonator atmosphere / calciner x carbonator temperature / Investigated velocity / Wattage / Capture efficiency	Gaps
COPPOLA; SCALA; SALATINO (2018)	Limestone / no / Germany / 600-400 μm	Bubbling / Dual / Resistance / 1 m x 0.04 m	Carb = 70%CO_2-air, Calc = 15%CO_2-air / 940 x 650 °C / $U_{carb} = U_{calc}$= 0.5 m/s / n.i / 0.02-0.22 g co2/ g sorbent	(1) The larger thermal shocks experienced by the sorbent in single bed system tests appear to be detrimental in terms of CO_2 capture and attrition tendency. (2) The thermal history has non-trivial effects on sorbent fragmentation, largely associated with the tendency of limestone sintering. (3) Sintering strengthens particle structure which hampers secondary fragmentation on the one hand, but intensifies the effects of thermal shock (primary fragmentation) on the other.
ANTZARA *et al.* (2018)	CaO-based, limestone / hydration / Greece / 500-355 μm	Bubbling / Single / Resistance / n.i x 0.018 m	dry carb = 10CO_2-N_2-3.2O_2-N_2, hydr carb = 10%CO_2-20%H_2O-3.2%O_2-N_2 dry calc = N_2 hydr calc = 20%H_2O-N_2 / 920-800 x 680-650 °C / $U_{carb} = U_{calc}$=3.8-2.5 m/s / n.i / hydr = 88-14 %	(1) The addition of steam led to higher conversion rates, especially during pre-breakthrough, due to decreased CO_2 diffusion resistance through the formed layer of $CaCO_3$. (2) In addition, steam significantly enhanced sorbent stability, leading to < 16% deactivation after 20 consecutive cycles. (3) When the sorbent was tested in tests at slightly different temperatures for carbonation (680 °C) and calcination (750 °C), it exhibited similar carbonation conversion but higher deactivation. (4) Compared to a natural limestone that was used as reference material, the final capacity of $CaO/CaZrO_3$ was almost 5.6 times greater.
HILZ *et al.* (2018)	Limestone / no / Germany / Mean 175 μm	Circulating / Dual / Calciner (Fueled by hard coal and Lignite) / 8.6 m carb 11 m calc x 0.6 m carb 0.4 m calc	n.i / 935-840 x 711-642 °C / n.i / 1 MW / 85-45%	(1) Demonstration of a successful semi-industrial pilot testing of the CaL process on a scale of 1 MWth under realistic operating conditions.
TREGAMB *et al.* (2018)	Limestone / no / Italy / 590-420 μm	n.i / Single / Solar-infrared / 0.1 m x 0.102 m	carb = 15%CO_2 and calc = 70%CO_2 / 950-940 x 650 °C / 2x$U_{sand,mf}$/ 3.2 kW/ 0.025 - 0.085 g CO_2 / g sobernt	(1) It is inferred that local and occasional higher peak temperatures experienced by sorbent particles in solar CaL result in more extensive thermal sintering and loss of CO_2 capture capacity.

* n.i means nothing informed or it was not possible to find the information

Table 1 continued

Reference (year)	Sorbent: type/ pretreatment / origin/ particle size	Fluidized-bed: type / dual or single / heating method / height x diameter	Process: calciner x carbonator atmosphere / calciner x carbonator temperature / Investigated velocity / Wattage / Capture efficiency	Gaps
HILZ *et al.* (2017)	Limestone / no / Germany / mean 175 μm	Circulating / Dual / Calciner (Fueled by hard coal and lignite) / 8.6 m carb 11 m calc x 0.6 m carb 0.4 m calc	carbonator 11-16%CO_2 / 940-850 x 700-639 / U_{carb} = 2.5-2.3 m/s, U_{calc} = 5.5-4.5 m/s / 1 MW / 95-45%	(1) An accumulation of inert material shows the dependency on ash and sulphur fractions of fuel combusted in the calciner. (2) High-grade fuel reduces the inactive sorbent share in comparable operation conditions from around 20 to 8 wt%.
COPPOLA *et al.* (2017)	Limestone / hydration / Germany / 600-400 $/mum$	Bubbling / Single / Resistance / 0.95 m x 0.040 m	calc = 70%CO_2-30%air, carb = 15%CO_2-85%air hydr calc = 10%H_2O-70%CO_2-air hydr carb = 10%H_2O-15%CO_2-air / 940 x 650 / $U_{carb} = U_{calc}$ = 2.5-2 m/s / n.i/ dry = 0.17 - 0.05 and hydrated = 0.19 - 0.07 g co2/g sorbent	(1) Synergistic effects were observed when steam was added, both during calcination and carbonation, resulting in a very pronounced increase of sorbent CO_2 capture capacity if compared to a no-steam case. (2) A characterization of fragmentation propensity of samples in light of morphological features assessed via microscopy showed that exposure to steam during calcination induces a more resistant external particle structure.
COPPOLA *et al.* (2017)	Limestone / no / Germany/ 600-400 μm	Bubbling / Dual / Resistance / 1 m x 0.04 m	100 - 15%CO_2air / 850 x 650 °C / U_{mf} = 0.06 m/s / n.i / 0.05-0.20 g CO_2 / g sorbent	(1) CO_2 capture capacity results exhibited a typical decay trend with respect to the number of cycles, as expected in CaL processes. Interestingly enough, a comparison of these results with those previously obtained using the same limestone and under similar operating conditions for single-bed apparatuses has revealed that capture capacity values were higher than those for single bed reactors. This finding seems to emphasize a non-negligible role of sorbent thermal history in Cal CO_2 capture performance

* n.i means nothing informed or it was not possible to find the information

Table 1 continued

Reference (year)	Sorbent: type/ pretreatment / origin/ particle size	Fluidized-bed: type / dual or single / heating method / height x diameter	Process: calciner x carbonator atmosphere / calciner x carbonator temperature / Investigated velocity / Wattage / Capture efficiency	Gaps
PENG; XU; ZHAO (2016)	$CaO + Al_2O_3$ / no / China / 300-200 μm	Bubbling / Single / Resistance / 0.892 m x 0.026 m	carb = 10%CO_2-N_2, calc = 100%N_2 / 900 x 700 °C / $U_{carb} = U_{calc}$= 5.0-3.0 m/s / n.i / 0.45-0.82 mol CO_2 / mol CaO	(1) In addition, results of ESEM proves its high sintering resistance to maintain abundant available surface area and stable textural structure for CO_2 capture reactions, which evidences the advantage of novel SATS method. In addition to addressing the loss-in-capacity of CaO-based CO_2 sorbents, attrition resistance is another important parameter worth being considered, especially in fluidized bed environments.(2) Pore size distribution and mechanical durability results show that the CaO/TiO_2–Al_2O_3 sorbent exhibits high mechanical strength, long-lasting anti-attrition performance and favourable long-life stability. Finally, a raw material analysis shows that CaO/TiO_2–Al_2O_3 sorbent has competitive advantage for further continuous long-term large-scale industrial operations.
RIDHA *et al.* (2016)	Cadomin and Limestone Pellet / no / Canada, Spain / 600-212 μm	Mixed / Dual / Resistance and calciner (natural gas carbonator and calcined biomass wood pellets) / 5.1 m calc, 3 m carb x 0.1 m	80%CO_2 / 900 x 650 °C / U_{carb} = 0.8-0.5 m/s, U_{calc} = 2.6-2.0 m/s / 0.1 MW / 90-80%	(1) Batch and continuous injection of pellets into the system revealed that the injection method exerted an insignificant effect on the attrition of pellets. The similarity of particle size distribution patterns of pellets is indicative of similar attrition tendencies, and it appears to be a characteristic of these pellets, regardless of limestone type and injection method. (2) It was found that pelletization of CaO-based sorbents using limestone and 10% cement results in a marginal improvement in the mechanical strength of resultant pellets. Therefore, pelletization of sorbent for CaL CO_2 capture is considered inadequate for sorbent attrition reduction
SYMONDS *et al.* (2016)	Cadomin and Limestone Pellet / no / Canada, Spain / 600-250 μm	Mixed / Dual / Resistance and Calciner (natural gas carbonator and biomass pellets calciner) / 5.1 m calc, 3 m carb x 0.1 m	80%CO_2 / U_{carb} = 0.8-0.5 m/s, U_{calc} = 2.6-2.0 m/s / 0.1 MW / 100-82 %	(1) In accordance with published works on CO_2 capture performance of synthetic/modified CaO-based sorbents at bench-scale, this work aims to highlight the fact that such sorbents could have had a more significant and enhanced performance when tested in a pilot-scale system. This suggests that the assessment of such relatively expensive sorbents should be performed under pilot-scale testing conditions to evaluate their performance with respect to their production cost.

* n.i means nothing informed or it was not possible to find the information

Table 1 continued

Reference (year)	Sorbent: type/ pretreatment / origin/ particle size	Fluidized-bed: type / dual or single / heating method / height x diameter	Process: calciner x carbonator atmosphere / calciner x carbonator temperature / Investigated velocity / Wattage / Capture efficiency	Gaps
BLAMEY *et al.* (2016)	Limestone and cement pellets / hydration / n.i / 710-500 μm	Bubbling / Single / Resistance / n.i x 0.021 m	15%CO2-N2 and 10%H2O13.5%CO2N2 / 900 x 700-600 °C / U_{carb} = 7.2-5.8 m/s, U_{calc} = 9.8-7.9 m/s / n.i/ 0.32-0.08 g CO_2 / g calcined sorbent	(1) Bubbling bed reactor tests were carried out using up to 20 CO_2 capture cycles on limestone-based pellets produced using calcium aluminate as binder. These tests show that pellets exhibit a similar or slightly more enhanced behaviour in terms of attrition resistance to its parent limestone, in addition to showing superior CO_2 capture performance altogether
COPPOLA *et al.* (2015)	Limestone / hydration / Germany / 600-400 μm	Bubbling / Single / Resistance / n.i x 0.04 m	Calc = 70%CO_2-air, carb = 15%CO_2-Air, Hydration = 50%H_2ON_2 / 940 x 650 °C / $U_{carb} = U_{calc}$ = 2.5-2.0 m/s / n.i / spent = 0.10 - 0.48 and hydrated = 0.11-0.51 mol/mol	(1) The effectiveness of sorbent hydration using steam as means to reactivate CO_2 uptake potential of limestone for CaL applications has been demonstrated. Steam hydration followed by dehydration of reactivated sorbent in a hot fluidized bed reactor leads to increased porosity, hence an improved rate and length of CO_2 uptake. (2) Furthermore, attrition and fragmentation propensity of reactivated sorbent is increased. (3) For the aforementinoed limestone, optimal trade-off between sorbent reactivity/uptake and mechanical strength is achieved after 60 min of hydration of spent sorbent, but it is expected that such a result cannot be generalised, since it is critically dependent upon sorbent texture. A comparison between water and steam hydration of spent sorbents as means of reactivation indicated that steam hydration is more favourable. (4) Albeit liquid water hydration gives rise to greater water uptake, prolonged soaking of liquid water makes the reactivated sorbent more susceptible to attrition and fragmentation.
DUELLI *et al.* (2015b)	Limestone / hydration / Germany / 375 μm	Mixed / Dual / Resistance / 12.4-0.5 x 0.15-0.071 m	calc = 0-75%$CO_2$0-35%H_2O-N_2, carb = 10-16$CO_2$0-10H_2O N_2 / 930-880 x 680-600 / U_{carb} = 5.5-4.5 m/s U_{calc} = 2.0-0.3 m/s / 10 kW / dry = 60-20% hydr = 95-40 %	(1) Combustion may lead to faster calcination due to better heat transfer; however, local high temperatures may cause pronounced sintering, thus further decay of activity as recorded herein and there might be sorbent hardening.

* n.i means nothing informed or it was not possible to find the information

Table 1 continued

Reference (year)	Sorbent: type/ pretreatment / origin/ particle size	Fluidized-bed: type / dual or single / heating method / height x diameter	Process: calciner x carbonator atmosphere / calciner x carbonator temperature / Investigated velocity / Wattage / Capture efficiency	Gaps
DUELLI *et al.* (2015a)	Limestone / no / Germany / n.i	Bubbling / Dual / Resistance / 12.4 m x 0.114 m	calc = 0-65%CO_2-N_2, carb = 14%CO_2-N_2 / 920-905 x 630/ n.i / 10 kW / 18-9% mol $CaCO_3$/mol Ca	(1) Full sorbent regeneration could not be achieved primarily due to the bubbling fluidization regime of the bed and the quality of heat provided by electric heaters through the walls to the bed. These limitations impose solid residence times up to 8 min for a calcination of solids instead of seconds, as it is in TGA investigations as well as industrial applications such as clinker production. This is not the case for process scale-up where these limitations are not found due to the fast fluidization regime and combustion atmosphere, thus the data presented herein is suggested to be treated qualitatively, not quantitatively
COPPOLA *et al.* (2014)	Limestone / hydration / Italy / 600-400 μm	Bubbling / Single / Resistance / n.i x 0.04 m	70%CO_2-Air / 940 x 650 °C / U_{mf} = 0.7 m/s / n.i / hydr = 0.03-0.35 gg-1, dry = 0.03 gg-1	(1) optimal hydration time depends on pore size.
ALONSO *et al.* (2014)	Limestone / no / Spain, Germany / 348-87 μm	Circulating / Dual / Calciner (biomass pellets) / 12 m x 0.4 m	n.i / 950-800 x 720-630 °C / $U_{carb} = U_{calc}$ = 2.8-0.8 m/s / 300 kW / 85-5%	(1) Large discrepancies were detected in experiments conducted with large particles, probably due to segregation effects of denser and coarser particles in the reactor bed inventory.
COPPOLA *et al.* (2013)	Dolomite, Limestone / no / Italy, Germany, Greece, Poland / 600-400 μm	Bubbling / Single / Resistance / 0.95 m x 0.04 m	calc = 70%CO_2N_2, carb = 15%CO_2N_2 / 940 x 650 °C / $U_{carb} = U_{calc}$ = 0.7-0.6 m/s / n.i / 0.02 - 0.14 g CO_2 / g Ca	(1) TG and FB devices are characterized by quite different fluid-dynamic and mass transfer conditions, which result in different sample heating and reaction rates. However, as far as CO_2 capture capacity is concerned, the results suggest that the type of reactor has a lower influence than calcination environment on sorbent performance. Factors enhancing sintering (e.g. high temperature and CO_2 concentration) severely impact the sorbent CO_2 capture capacity. On the other hand, factors slowing down sintering (e.g. the presence of MgO, as in dolomite) improve sorbent performance.

* n.i means nothing informed or it was not possible to find the information

Table 1 continued

Reference (year)	Sorbent: type/ pretreatment / origin/ particle size	Fluidized-bed: type / dual or single / heating method / height x diameter	Process: calciner x carbonator atmosphere / calciner x carbonator temperature / Investigated velocity / Wattage / Capture efficiency	Gaps
COPPOLA *et al.* (2013b)	Dolomite, Limestone / no / Italy, Germany, Greece, Poland / 600-400 μm	Bubbling / Single / Resistance / 0.95 m x 0.04 m	calc = 70%$CO_2$30%N_2, Carb = 15%$CO_2$85%N_2 / 940 x 650 °C / $U_{carb} = U_{calc}$ = 0.7-0.6 m/s / n.i / 80-18% mol/mol	(1) The CO_2 capture capacity of the dolomite was always greater than that of limestone, and remained relatively high along cycles, despite the lower calcium content of the sorbent.
COPPOLA *et al.* (2013a)	Limestone / no / Italy, Germany, Greece, Poland / 500-30 μm	Bubbling / Single / Resistance / 0.95 m x 0.04 m	calc = 70%$CO_2$30%N_2, carb = 15%$CO_2$85%N_2 / 940 x 650 °C / $U_{carb} = U_{calc}$ = 0.7-0.6 m/s / n.i / capture capacity = 0.02 - 0.21 g CO_2 /g $CaCO_3$	(1) The measured fines elutriation rate was only moderately large during the first cycle, but it reduced along the cycles, since a combined chemical thermal treatment significantly hardened the particle structure. (2) A high SO_2 concentration had a detrimental effect on CO_2 capture capacity of all limestones, while a low SO_2 concentration had a more limited effect.
COPPOLA *et al.* (2012b)	Limestone / no / Italy / 600-400 μm	Bubbling / Single / Resistance / 1 m x 0.04 m	Calc = 20CO_2N_2, Carb = 16CO_2N_2 / 850 x 700 °C / $U_{carb} = U_{calc}$ = 0.7-0.6 m/s / 4.4 kW / 60-10%	(1) Results showed that the presence of SO_2 in the flue gas significantly decreased the sorbent CO_2 capacity, quite possibly due to the formation of an impervious $CaSO_4$ layer at the periphery of particles. (2) Even a small quantity of SO_2 is sufficient to significantly hinder the sorbent CO_2 capture capacity. (3) An analysis of particle size distribution of bed material over repeated calcination/carbonation cycles indicated that particle fragmentation was very limited in all investigated conditions. (4) Results obtained using 1800 ppm SO_2 showed divergences from other conditions as regards: cumulative particle size distribution of fragments, cumulative elutriated material over five repeated cycles, and degree of SO_2 uptake over repeated cycles.

* n.i means nothing informed or it was not possible to find the information

Table 1 continued

Reference (year)	Sorbent: type/ pretreatment / origin/ particle size	Fluidized-bed: type / dual or single / heating method / height x diameter	Process: calciner x carbonator atmosphere / calciner x carbonator temperature / Investigated velocity / Wattage / Capture efficiency	Gaps
ACHARYA; DUTTA; BASU (2012)	Limestone / n.i / n.i / 325-135 μm	Mixed / Dual / Resistance / n.i x 0.101 m	Calc = Steam+Air Carb = 22-25%CO_2-N_2 / 900 x 600-550 °C / n.i / 100-10% (air) and 100-25% (steam)	(1) The CO_2 absorbing capacity of CaO decreases progressively as it goes through alternating cycles of carbonation and calcination. Such a reduction is due to several factors, including sintering and pore pluggage. (2) Calcination of $CaCO_3$ in the presence of different media shows that the degree of calcination of $CaCO_3$ in the presence of H_2O is similar to that of N_2. (3) Kinetic rates of calcination are much higher when measured using H_2O and N_2 than CO_2. (4) Sintering leading to sorbent agglomeration cannot be avoided during calcination at higher temperatures, even while using steam.
SYMONDS *et al.* (2012)	Limestone / hydration / Canada, Poland / 612-512 μm	Circulating / Single / Resistance + Calciner (Pure fiber hardwood blend) / 5 m x 0.1 m	Calc = 1%CO7.5%O_2 35%CO_2 or 1%CO6%O_2 35%CO_2 and Carb = 8%CO_2 19.3%O_2 72.7%N_2 or 8%CO_2 15.7O_2 17%H_2O 59.3%N_2 / 920-860 x 690-610 / n.i / 49 - 11 %	(1) Results suggest that CO_2 capture cycles in TGA experiments should encompass as many factors present during FBC operation as possible (i.e. higher calcination temperatures/CO_2 concentrations, and the presence of steam and other gases such as SO_2) so as to avoid rather misleading results and conclusions regarding sorbent performance.
RODRÍGUEZ; ALONSO; ABANADES (2011)	Limestone / no / n.i / <350 μm	Circulating / Dual / Resistance / calc = 6 m, carb = 6.5 m x 0.1 m	Calc = 5-3%$O_2$7-22%CO_2, Carb = 15-2%CO_2 17%O_2 / 850-800 x 722-568 °C / n.i / 30 kW/ 92-30%	(1) When there are enough active CaO particles inside the reactor, the low-carrying capacity of highly cycled CaO particles can be counterbalanced by sufficiently large inventories of solids in the carbonator, which can increase the carbonation conversion achieved by CaO to values close to the maximum capture capacity of the material by increasing the average residence time of particles in the reactor.
BLAMEY *et al.* (2011)	Limestone / hydration / Canada / 710-500 μm	Bubbling / Single / Resistance / 0.33 m x 0.026 m	15%CO_2N_2 / 950-850 x 700 °C / U_{mf} = 8 / n.i / 70-10% fresh, 35-0% hydr after 13 cycles	(1) Severe temperatures in calcination causes particles to become friable and increases elutriation process. (2) Results indicated that reactivation would be unsuitable for a bubbling fluidised bed CO_2 capture process, though it may be suitable for a moving or fixed bed reactor.

* n.i means nothing informed or it was not possible to find the information

Table 1 continued

Reference (year)	Sorbent: type/ pretreatment / origin/ particle size	Fluidized-bed: type / dual or single / heating method / height x diameter	Process: calciner x carbonator atmosphere / calciner x carbonator temperature / Investigated velocity / Wattage / Capture efficiency	Gaps
BLAMEY *et al.* (2010b)	Limestone / hydration / United Kingdom, Canada, Spain / 710-500 μm	Bubbling / Single / Resistance / 0.33 m x 0.026 m	15%CO_2N_2 / 1000-840 x 700 °C / U_{mf} = 7 / n.i / 78-2 g/100g and 58-18 g/100g hydrated	(1) Significant expansion and break-up of particles was observed in the hydration for particles cycled at higher temperatures, and it is proposed that this is due to a significant densification of particles
CHARITOS *et al.* (2010)	Limestone / no / Germany / n.i	Bubbling / Dual / Resistance and calciner (Natural gas) / 12.4 m x 0.071 m calc 0.114 m carb	15%CO_2air / n.i x 700-630 °C / n.i / 10 kW/ 97-90%	(1) The degree of sorbent particle sintering increased along carbonation–calcination cycles and resulted in smaller values of average CO_2 capture capacity, reduction in small pore volume (<200 nm) and a decrease in particle surface area.
HUGHES *et al.* (2009)	Limestone / no / Poland, Canada / n.i	Mixed / Dual / Resistance and Calciner (Wood pellets) / 5 m x 0.1 m	Calc = 46%N_2O_2 Carb = 8%CO_2Air or 8%$CO_2$17%H_2OAir / 910-860 x 600 °C / n.i / 75 kW /n.i	(1) Sorbent capacity was significantly lower than that expected based on previous thermogravimetric analyses. It is believed to be at least partially captured due to the formation of a thin, low-porosity shell around the sorbent enhanced by the deposition of ash from the solid fuel under oxygen-fired conditions
LU; HUGHES; ANTHONY (2008)	Limestone / no / Canada / 800-400 μm	Circulating / Dual / Resistance and Calciner (biomass or coal) / 5 m x 0.1 m	15%CO_2air / 950-850 x 720-580 °C / $U_{carb} = U_{calc}$ = 0.8-0.4 m/s / 75 kW / 85-70%	(1) An examination of sorbent surface characteristics suggests that a number of complicated processes are occurring on the particle surface as a consequence of the number of reaction cycles. Issues of sorbent loss through attrition, impact of sulphation and process optimization require further investigation

* n.i means nothing informed or it was not possible to find the information

Source: Author

2.3 CARBON DIOXIDE CAPTURE

CaL was first proposed as carbon capture technology by SHIMIZU *et al.* (1999). The technique was first proposed as a solution for global warming and emission reduction, thought to be used with Coal power plants which produces flue gases with high CO_2 concentration. First industrial scale demonstration pilot plant was reached (La Pereda plant), through two projects between 2009 and 2015 (ARIAS *et al.*, 2017).

2.3.1 Kinetics of calcination and carbonation reactions

The carbonator usually operates from 550-715 °C and with atmosphere containing according to Table 7. The carbonation reaction is a function of equilibrium vapor pressure and temperature, Equation 2.1 proposed by Baker (1962), which model its behavior.

$$logP(atm) = 7.079 - 38.000/4,574T(K) \tag{2.1}$$

Carbonation reaction is known to occurs in two stages. The first stage is relatively fast and is governed by the chemical reaction kinetics. Molecules of CO_2 interact with CaO pores and surface creating a $CaCO_3$ layer outside the particle. The second stage is much slower and is limited by the diffusion of reactants through the $CaCO_3$ product layer. As CaO keep reacting with CO_2 the $CaCO_3$ layer thicken from pore to outside, when this layer reaches a critical value the mechanism changes to the CO_2 diffusion through the layer to a CaO nucleus. This layer is believed to reach a critical level when the mechanism change, which occurs when its thickness approaches approximately 50 nm (ALVAREZ; ABANADES, 2005) which is said to be a constant characteristic. Figure 16 present a schematic of the saturation process.

Figure 16 – Schematic representation of the carbonation process over time in a CaO particle, showing the evolution across regions I, II, and III

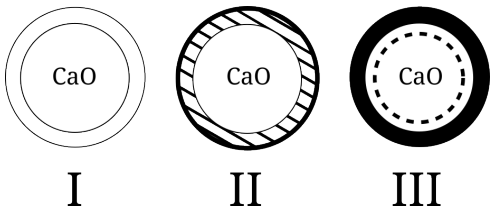

Source: Author

After carbonation, the recent carbonated sorbent is directed to the calciner (or the condition is changed inside the same reactor when using single bed reactors) where temperature is increased to start calcination reaction. This calcination reaction typically occurs at temperatures between 1000-780 °C, which can varry with the sorbent used and due to process utilization. Calcination temperature is linked to sintering and elutriation problems on CaL (ASIEDU-BOATENG *et al.*, 2023; MANOVIC *et al.*, 2009). Calciners usually require additional heat to compensate the

endothermic reaction, for which industrial scale fuel burning is a common approach. On the other hand, lab scale reactor usually use electrical heating. After regeneration, the sorbent is returned to the carbonator to begin a new cycle.

CaL technique is sought to undergo many cycles as possible before new sorbent is needed. The lost of efficiency for high cycles has been a concern of CaL, for which research have been addressing for some time (AMGHAR *et al.*, 2023; CHAMPAGNE *et al.*, 2016; MOGHTADERI; SEYFAEE, 2024; VALVERDE; SANCHEZ-JIMENEZ; PEREZ-MAQUEDA, 2014a). Is postulated that multi cycles of carbonation-calcination reduces limestone ability to capture CO_2. This effect is mostly due to sintering, Figure 17. After first calcination, recent CaO particle will break or fracture due to decrepitation and fragile properties of CaO oxide. Sintering also plays a major role in this case, which reduces the total surface area. When the next carbonation cycle occurs, the reduced surface area causes the diffusion mechanism to take effect, which leads to CaO nuclei not forming $CaCO_3$. Although a large loss of efficiency can be observed from the first to the second cycle, the efficiency remains relatively constant until the combination of these effects reduces the capture properties to a very low level (LYSIKOV; SALANOV; OKUNEV, 2007).

Figure 17 – Limestone effect after many cycle where it loses its effect of carbon capture efficiency. This effect if remarked by the breakage and sintering of particles

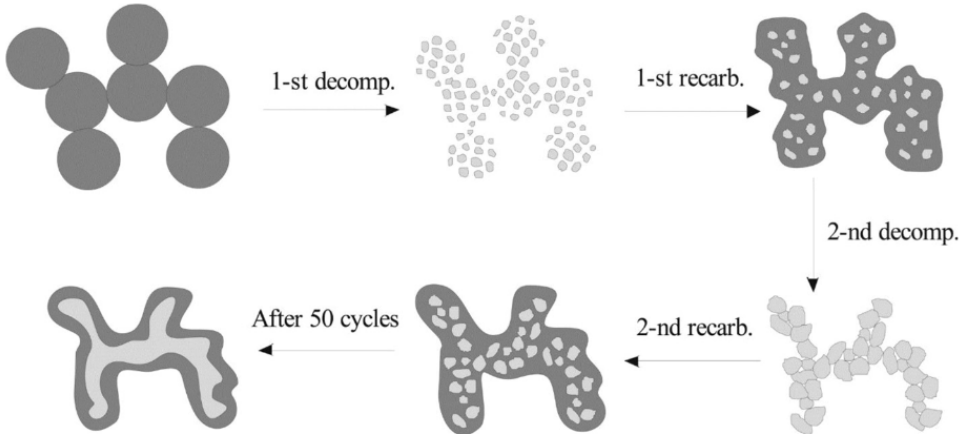

Source: (LYSIKOV; SALANOV; OKUNEV, 2007)

2.3.1.1 Accounting of capture efficiency

Regarding capture efficiency, it is important to note that different authors have employed various approaches to evaluate it. The analysis revealed a set of equations that can be grouped according to their similarities, despite minor differences among them. These equations are presented below in chronological order.

Blamey (2010c), Equation (2.2): α_∞ is an asymptote constant; C_N is capture capacity; RMM_x molar mass of species x; F_x fraction of species x in the original limestone; k decay

constant; N cycle number.

$$C_N = 100 \cdot \left[\frac{1}{(1/(1-\alpha_\infty)) + kN} + \alpha_\infty \right] \cdot \left[\frac{RMM_{CaCO_3} F_{CaCO_3}}{RMM_{CO_2} \left(\left(\frac{F_{CaCO_3} RMM_{CaO}}{RMM_{CaCO_3}} \right) + (1 - F_{CaCO_3}) \right)} \right] \tag{2.2}$$

Blamey (2011), Equation (2.3): α_∞ is an asymptote constant; k decay constant; N cycle number.

$$C_N = 100 \cdot \left[\frac{1}{(1/(1-\alpha_\infty)) + kN} + \alpha_\infty \right] \tag{2.3}$$

Rodriguez; Alonso; Abanades (2011), Equation (2.4):

$$E_{carb} = \frac{\text{CO}_2 \text{ reacting with CaO in the bed}}{\text{CO}_2 \text{ entering the bed in the flue gas}} \tag{2.4}$$

Coppola *et al.* (2013a), Equation (2.5): $F^{in}_{CO_2}$, $F^{out}_{CO_2}$ are inlet and outlet CO_2 mass flow rates, respectively; m_0 is the initial mass of sorbent on the system.

$$\text{CO}_2 \text{ Capture Capacity} = \frac{\int_0^t \left[F^{in}_{CO_2} - F^{out}_{CO_2}(t) \right] dt}{m_0} \tag{2.5}$$

Alonso *et al.* (2014), Equation (2.6): $F_{CO_2,comb}$,$F_{CO_2,out}$ are the molar flow rate of CO_2 (mol/m^2s) generated by combustion and in equilibrium, respectively.

$$E_{carb} = \frac{F_{CO_2,comb} - F_{CO_2,out}}{F_{CO_2,comb}} \tag{2.6}$$

Duelli *et al.* (2015a), Equation (2.7): F_{Ca}, F_{CO_2} are molar flow rates of Ca and CO_2 entering and leaving the carbonator, respectively; X_{calc}, X_{carb} are contents of CO_2 on Ca particles before and after the reaction.

$$E_{CO2} = \frac{F_{Ca}(X_{carb} - X_{calc})}{F_{CO2}} \tag{2.7}$$

Duelli *et al.* (2015b), Equation (2.8): Carbonator efficiency (E_{carb}) is defined as the moles of CO_2 captured by the solids with respect to moles introduced into the reactor.

$$E_{carb} = 1 - \frac{F_{CO2,out}}{F_{CO2,in}} \tag{2.8}$$

Sysmonds *et al.* (2016), Equation (2.9): where F_{CO_2} represents the molar flow rate of CO_2 entering the carbonator ($kmol/h$) and F_{carb} represents the molar flow rate of CO_2 leaving the carbonator ($kmol/h$).

$$E_{carb} = \frac{F_{CO2} - F_{carb}}{F_{CO2}} \tag{2.9}$$

Hilz *et al.* (2018), Equation (2.10): $F_{CO_2,carb,in}$, $F_{CO_2,coal}$, $F_{CO_2,0}$, $F_{CO_2,calc,out}$ refer to the CO_2 fed into the carbonator, CO_2 formed by oxy-fuel combustion, CO_2 from calcinated fresh

limetone and CO_2 at the calciner outlet, respectively.

$$E_{total} = \frac{F_{CO2,calc_out}}{F_{CO2,carb,in} + F_{CO2,0} + F_{CO2,coal}} \tag{2.10}$$

Antzara *et al.* (2018), Equation (2.11):

$$CO_2 capture, \% = \frac{\text{moles of } CO_{2,in} \text{ - moles of } CO_{2,out}}{\text{moles of } CO_{2,in}} \tag{2.11}$$

Blamey *et al.* (2016), Equation (2.12): t means carbonation time; X_{in} the inlet fraction of CO_2; X_{out} the outlet fraction of CO_2 and η_{in} the total molar flow rate of gas fed into the reactor

$$\eta_{CO_{2,carb}} = \int_0^t \left(\frac{\eta_{in}(X_{in} - X_{out})}{(1 - X_{out})} \right) dt \tag{2.12}$$

Diego; Arias (2020a), Equation (2.13): E_{carb} is the CO_2 capture efficiency achieved by the carbonator; K_s is the reaction rate constant; φ represents the gas-solid contact factor; ν_{CO2} is the molar fraction of CO_2 and $\nu_{CO2,eq}$ is the molar fraction in equilibrium conditions; τ_{active} is active space time; f_a is active particle fraction; W_{ca} is the molar bed inventory of calcium in the carbonator; $F_{CO2,in}$ is the molar flow of CO_2 at the reactor inlet; X_{ave} is average CO_2 capture capacity; t^* is the characteristic reaction time.

$$\begin{aligned} E_{carb} &= K_s \varphi \tau_{active} (\overline{\nu_{CO2} - \nu_{CO2,eq}}) \\ \tau_{active} &= f_a \frac{W_{ca}}{F_{CO2,in}} X_{ave} \\ f_a &= 1 - e^{-\frac{t^*}{W_{ca}/F_{ca}}} \\ t^* &= \frac{X_{ave} - X_{calc}}{k_s \varphi X_{ave} (\overline{\nu_{CO2} \nu_{CO2,eq}})} \end{aligned} \tag{2.13}$$

Dong *et al.* (2020), Equation (2.14): $m1, m0$ are final and initial mass of loaded samples, respectively; M_{CaO}, M_{CO_2} are molar masses of CaO and CO_2, respectively.

$$CCE(\%) = \frac{m_1 - m_0}{m_0} \frac{M_{CaO}}{M_{CO_2}} \cdot 100 \tag{2.14}$$

Coppola *et al.* (2023a), Equation (2.15): $W^{in}_{CO_2}$ is the mass flow rate of CO_2 at the carbonator inlet, $W^{out}_{CO_2}(t)$ is the mass flow rate of CO_2 at its outlet, t is carbonation time, MW is molecular weight and f_{CaCO_3} is the mass fraction of $CaCO_3$.

$$X_{Ca} = \frac{\int_0^t W^{in}_{CO_2} - W^{out}_{CO_2}(t)}{m_0 f_{CaCO_3}} \frac{MW_{CaCO_3}}{MW_{CO_2}} \tag{2.15}$$

Carbon capture efficiency has been evaluated using a wide range of distinct methodological approaches. Although these formulations can be further categorized into overall, carbonator, and

calciner carbon capture efficiencies—each considered either with or without accounting for fuel consumption—their primary governing parameters are generally consistent. These parameters include the residence time within the bed, the quantity of CO_2 introduced or generated in the bed, the reaction rate, the fraction of active particles, the mass flow rate of reactive particles entering the bed, the mass flow rate of particles exiting the bed, the CO_2 mass flow rate within the bed, and the number of operating cycles.

The extensive range of available equations is beneficial for scaling up the technology, as it reflects the validation of multiple independent methodological approaches. However, establishing correlations among these studies remains challenging because the equations are highly diverse, indicating a lack of consensus within the academic community. Moreover, to the best of current knowledge, no study has systematically compared these equations in the literature; therefore, such a comparative analysis is proposed as a topic for future research.

2.3.2 Compaction effect

Compaction is associated with the bed voidage or porosity, which is influenced by particle size, particle shape, and the method of compaction (PATANKAR; MANDAL, 1980).

The calcium looping (CaL) reaction is significantly affected by the particle size of the sorbent. It is well established that smaller particles can enhance carbon capture performance by increasing the surface area available for reaction with CO_2 (BORGWARDT; BRUCE, 1986; CHANG *et al.*, 1982; LUO *et al.*, 2010). Additionally, bed compaction strongly influences both carbon conversion and pressure drop within the reactor (TEIXEIRA *et al.*, 2012). However, excessive reduction in particle size may lead to the obstruction of the available superficial area. This phenomenon occurs because smaller particles tend to establish a greater number of contact points with neighboring particles, thereby blocking regions that would otherwise be accessible for gas–solid reactions. In contrast, although larger particles also experience interparticle contact, the ratio between total surface area and the surface area obstructed by contact points is considerably lower.

This effect has been observed in various gas–solid reaction systems and is not exclusive to calcium looping. Voge (1972), while investigating the dehydrogenation of butene using catalysts in a fixed-bed reactor, reported that reducing particle size below 1.1 mm did not improve reactor performance and, in some cases, resulted in a slight decline in efficiency. Furthermore, increased compaction has been associated with improved thermal equilibrium between the gas and solid phases (LOWE; GREENAWAY, 2005).

2.4 BRAZILIAN INDUSTRIAL NATURAL GAS UTILIZATION

2.4.1 Extraction of natural gas used in Brazil

Brazilian natural gas production is mostly based on sea extraction, being 86.5% of February 2024 production based on offshore. The extraction is controlled by the Brazilian National

Petroleum company, Petrobras, which controls 88.69% of all natural gas produced (BRAZIL NATIONAL AGENCY OF PETROLEUM, NATURAL GAS AND BIOFUELS (ANP), 2024a).

Brazilian petroleum production is largely driven by the Pré-sal development, a highly successful offshore deep- and ultra-deep-water oil and natural gas exploration initiative in Brazil. In February, a total of 148 wells were in operation, producing 113.5 million m³/day of natural gas. This volume accounted for 76.1% of the country's total oil and natural gas production (BRAZIL NATIONAL AGENCY OF PETROLEUM, NATURAL GAS AND BIOFUELS (ANP), 2024a).

The term Pré-sal refers to hydrocarbon reservoirs located beneath a thick salt layer. As exploration technologies advanced, Brazil developed the capability to exploit reservoirs beyond this interval, known as the Pós-sal. National production is approximately distributed as 76.30% from the Pré-sal, 18.73% from the Pós-sal, and 4.97% from onshore fields. While production from the Pré-sal shows notable month-to-month variability, the contributions from Pós-sal and onshore extraction remain comparatively stable (BRAZIL NATIONAL AGENCY OF PETROLEUM, NATURAL GAS AND BIOFUELS (ANP), 2024a).

A total of 14 sedimentary basins are currently under exploration, of which 13 produce natural gas. The most productive is the Santos Basin, with 29 wells in operation and a production of 114,033 million m^3/day in February 2024. The second most productive basin is the Solimões Basin, where seven wells produced 13,114 million m^3/day during the same period. The Santos Basin is the most important basin for both oil and natural gas production, accounting for approximately 74.0% of total national output in February 2024 (BRAZIL NATIONAL AGENCY OF PETROLEUM, NATURAL GAS AND BIOFUELS (ANP), 2024a).

This sedimentary basin covers approximately 350,000 km^2 and extends from Cabo Frio, in the state of Rio de Janeiro, to Florianópolis, in the state of Santa Catarina. Initial investments aimed at exploring the Santos Basin date back to the 1970s. During the 1990s and 2000s, several discoveries were made in post-salt reservoirs, contributing significantly to the development of Brazil's offshore petroleum sector (BRAZIL NATIONAL AGENCY OF PETROLEUM, NATURAL GAS AND BIOFUELS (ANP), 2024b).

2.4.2 Natural gas utilization

The national scenario assumes equal competitiveness between natural gas and fuel oil in the short term. Other factors include industrial preference for natural gas in processes requiring high product purity, such as glass and certain ceramics manufacturing, as well as in the fertilizer sector, where it is used for energy and raw material (EPE, 2024).

Table 2 shows natural gas utilization in the country in 2015, 2019, and 2024 by region. It can be seen Southeast, Northeast, and South region uses the large majority of all gas utilization with 66.4%, 18.1%, and 11%, respectively.

São Paulo's industries uses up to 80% of state total consumption of natural gas (SãO PAULO STATE PUBLIC UTILITIES REGULATORY AGENCY (ARSESP), 2023). Rio de Janeiro current industrial gas consumption scenario, over 2.38 million m³/day is demanded, with 85%

Table 2 – Natural gas consumption in Brazil by region from 2015 to 2024 in thousand m³/day, including absolute and annual percentage variation for each period

Year	North	Northeast	South	Southeast	C.West	Brazil
	Thousand m^3 per day					
2015	271	11,117	6,393	36,446	231	54,428
2019	386	12,683	6,718	38,562	1,811	60,159
2024	461	13,972	8,459	51,134	3,011	77,037
Period	Period variation (Thousand m^3 per day)					
2014-2024	202	3,369	2,892	15,702	2,796	24,961
Period	Variation (% year)					
2014-2019	8.4	3.6	3.8	1.7	53.1	2.9
2019-2024	3.6	2	4.7	5.8	10.7	5.1
2014-2024	6	2.8	4.3	3.7	30.2	4

Note: Co-generation, thermomeletric, and E&P (Humid gas) consumption not included

Source: (EPE, 2024)

used by steel, 6% by chemicals, and 5% by glass. The remaining 4% is spread across sectors like food, ceramics, construction, textiles, and printing (RIO DE JANEIRO STATE FEDERATION OF INDUSTRIES (FIRJAN), 2024). Bahia has most of natural gas usage concentrated on industrial facilities with 53.3% of total usage in industry fuel, followed by 30.2% used in co-generation (BAHIA STATE FEDERATION OF INDUSTRIES (FIEB), 2024).

A crucial aspect in assessing natural gas use in the industry is its direct competition with fuel oil, as seen before. Therefore, for projection purposes, assumptions regarding the price relationship between these energy sources are essential.

Natural gas also has a strong relation with energy production and it is often used as bolster, through thermal plant, the power generation system during years with low rainfall and prevent blackouts due to water shortages in reservoirs. Its use represents 7.5% of all Brazilian energy matrix usage (EPE, 2024).

To calculate total natural gas demand, usage for electricity generation, crucial for infrastructure planning, are included. Where expected gas consumption for the decade is based on expected thermal generation, without considering operational system factors or external planning models. This create a over design of gas use in the energy matrix, which in case of shortage of other energy supply could be used to maintain the system. That being said, for 2024, 170.6 million m^3/day is the maximum demand, where 53.2% is used on energy generation, 22.2% industrial utilization, 11.2% used by refineries to produce energy, and 6.6% used as supplies on production line of many industries (EPE, 2024). Table 3 gives a detail description of 2024 national usage of natural gas.

Natural gas is also closely linked to electricity generation and is frequently used to support the power system during periods of low rainfall, when hydroelectric reservoir levels are reduced

and the risk of blackouts increases. In such situations, thermal power plants fired by natural gas help stabilize the grid. Natural gas accounted for approximately 7.5% of Brazil's total energy matrix in 2024, reflecting its role in the country's overall energy supply mix (EPE, 2024).

To estimate total natural gas demand, consumption for power generation—an essential factor for infrastructure planning—is included. Expected gas use over the coming decade is based on projected thermal generation without accounting for system operation factors or external planning models. This results in a design that tends to overestimate gas requirements, providing additional capacity that can be relied upon if other energy sources are insufficient. Based on these projections, maximum natural gas demand for 2024 is estimated at 170.6 million m³/day, with 53.2% of that used for electricity generation, 22.2% for industrial consumption, 11.2% by refineries for energy production, and 6.6% as feedstock in various industrial processes (EPE, 2024). Table 3 gives a detailed description of the 2024 national usage of natural gas.

Table 3 – Natural gas consumption in Brazil by use category for the years 2015, 2019, and 2024, in thousand m³/day, including expected and maximum demand scenarios

Consumption	2015	2019	2024
	Thousand m^3 per day		
Expected energy generation	22.3	11.2	24.4
Co-generation(1)	2.6	2.6	2.8
Material(2)	7.3	9.5	11.2
Industry	0.8	0.8	0.9
FAFEN's and UFN's	1.6	2.9	4.4
Refinary	4.9	5.7	5.9
Energy sector(3)	9.8	11.5	19.1
Residential	1.1	1.4	1.9
Commercial/Public/Agro	0.7	0.8	1.1
Transport	5.2	5.4	5.7
Industrial(4)	30.4	31.6	38
General industry	29.2	30.2	36.3
FAFEN's and UFN's	1.3	1.4	1.7
Total expected demand	79.3	74	104.2
Additional energy generation	29.3	53	66.4
Maximum demand	108.6	127	170.6

(1) Industrial and commercial Co-generation. E&P not included.
(2) Natural gas used as input product by refinaries, fertilazion and general industries.
(3) Input to refinaries, not included hidrogen production. Not consided inputo to E&P (humid gas).
(4) Fertilization energy share included.

Source: (EPE, 2024)

2.4.3 Natural gas composition and combustion emissions

Natural gas is predominantly made up of hydrocarbons, with over 95% typically belonging to the paraffin series. The main hydrocarbons found in natural gas are methane (CH_4), followed by

ethane (C_2H_6), propane (C_3H_8), and butanes (C_4H_{10}), along with some heavier components. The proportion of heavier hydrocarbons decreases due to their higher molecular weights. Additionally, natural gas may contain non-hydrocarbon gases like nitrogen, carbon dioxide, and sometimes small amounts of hydrogen sulfide or mercaptans (KHILYUK *et al.*, 2000).

Natural gas is used in many industries and equipment such as furnaces and turbines. Those emit a flue gas with a concentration ranging from 3.8% to 5% vol. of CO_2 in wet condition (AMROLLAHI; ERTESVÅG; BOLLAND, 2011; CAMPANARI; MANZOLINI; CHIESA, 2013; COLORADO; HERRERA; AMELL, 2010; DÍAZ-HERRERA *et al.*, 2020; DUTTA; NORD; BOLLAND, 2017; FRIEDMAN; LI, 2005; LOTT *et al.*, 2023; QURESHI; ALI; SHER, 2021; SIPÖCZ; TOBIESEN, 2012).

3 MATERIALS AND METHOD

Figure 18 presents a schematic diagram of the methodology adopted in this chapter, designed to facilitate the understanding of the experimental procedures, given that the methodological framework is complex and encompasses multiple experimental configurations. The diagram synthesizes the logical sequence and the interrelationships among the techniques and systems employed, thereby serving as a reference guide for the reading and interpretation of the subsequent sections.

Figure 18 – Experimental methodology flow chart of the thesis

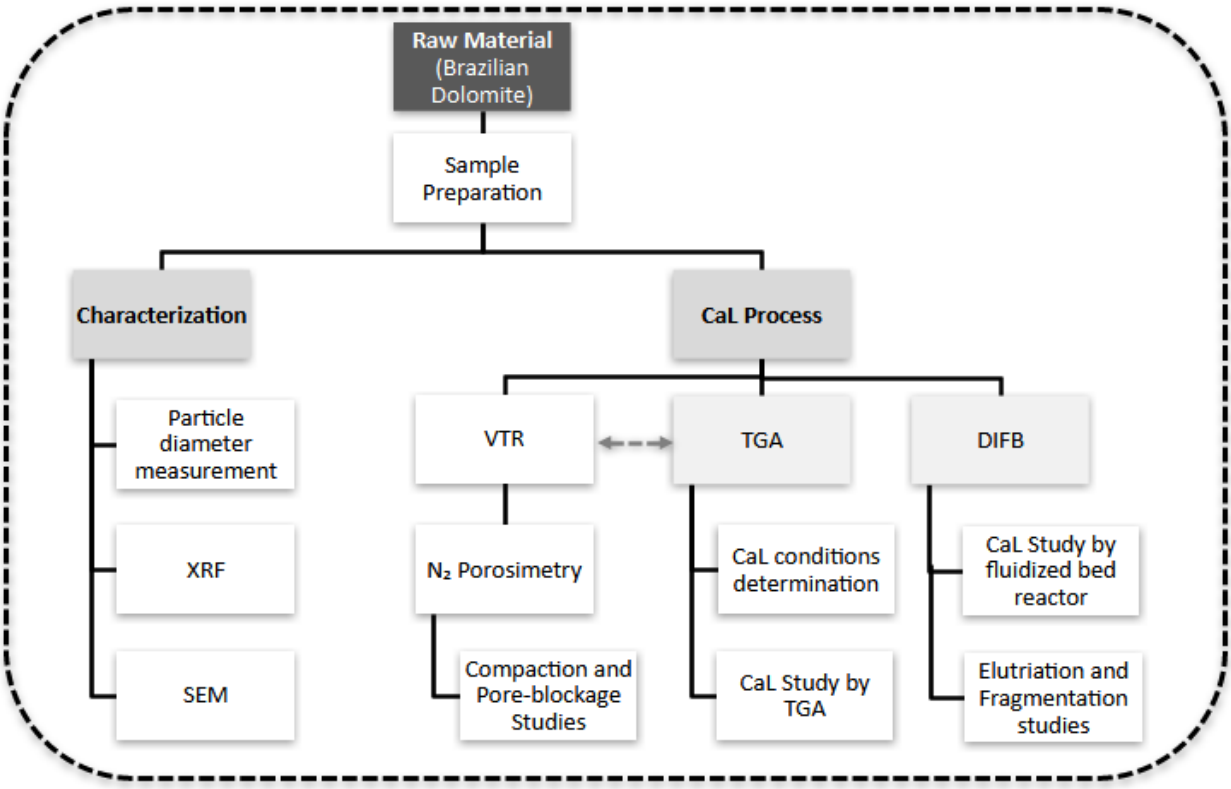

Source: Author

Initially, a nationally sourced raw material, Brazilian dolomite, was selected and employed as the sorbent throughout the investigation. The material underwent systematic preparation and granulometric classification, including the selection of specific particle size ranges, in order to ensure controlled and reproducible experimental conditions, as well as compatibility with the various analytical techniques and experimental setups utilized in the study.

Subsequently, a comprehensive physicochemical and geometrical characterization of the sorbent was conducted. Determination of particle diameter is particularly critical in the context of fluidized bed investigations, as it exerts a direct influence on fluidization hydrodynamics, particle elutriation, and reaction kinetics. X-ray fluorescence (XRF) spectroscopy was employed

to quantify the elemental composition, with particular emphasis on the CaO content, whereas scanning electron microscopy (SEM) was utilized as a complementary technique to assess surface morphology and microstructural features.

A Vertical Tubular Reactor (VTR) was employed to produce larger quantities of calcined and carbonated materials required for N_2 adsorption porosimetry. These experiments were conducted subsequent to the calcium looping investigations performed via TGA. The optimal calcination and carbonation parameters identified in the TGA were replicated in the VTR to generate sufficient sample mass for subsequent structural characterization.

The calcium looping investigations performed using a TGA and a Dual Interconnected Fluidized Bed (DIFB) reactor constitute the central focus of this thesis. In the TGA system, the process was examined under well-controlled conditions, which enabled a detailed assessment of CO_2 conversion, the cyclic performance of the sorbent, and, in conjunction with porosimetric analyses, the influence of sample compaction and pore-blockage phenomena. In contrast, the DIFB system facilitated the investigation of the process under fluidized-bed operating conditions, thereby incorporating relevant hydrodynamic and mechanical phenomena, such as attrition, fragmentation, and elutriation, which more closely simulate industrial-scale environments.

Thus, the diagram underscores that the adopted methodology is not linear but rather integrated and complementary, thereby enabling (i) the definition of operational criteria, (ii) the identification of intrinsic limitations of the sorbent, and (iii) the evaluation of the technical feasibility of the calcium looping process for its application in natural gas–fired power plants. Collectively, these elements directly contribute to addressing the central research question of this thesis.

3.1 RAW MATERIAL

Figure 19 presents the location of the material source on the official Mineral Resources Map of the State of São Paulo (GEOLOGICAL SURVEY OF BRAZIL (SGB/CPRM), 2006), close to the city of Piracicaba. The raw material is supplied by the company Calcário Diamante (indicated on the map), consisting of a dark-colored rock identified as dolomite from Piracicaba, São Paulo, Brazil. The material is obtained by comminution of dolomitic rock with, according to the supplier, has a general chemical composition of 25 wt% CaO and 17 wt% MgO. The reported particle size distribution is 100% retained on the ASTM No. 10 sieve, 93% on the ASTM No. 20 sieve, and 68% on the ASTM No. 50 sieve.

In Figure 19, three distinct regions surrounding the mine can be observed, each identified by a specific code: P1tt, represented in brown; P2i, represented in light brown; and P3tic, represented in light green. The map describes these regions as follows:

- P3tic – Corumbataí Formation: Clayey siltstone, siltstone, shale and rare sandstone, as well as micritic and microsparitic limestone, occurring in massive or laminated facies; overlain by heterolithic successions with sandstone interlaminated with sandstone, siltstone and

mudstone, siltstone and sandy siltstone, micritic limestone and marl. Deposited in a marine setting, ranging from offshore to a transitional zone between offshore and shoreface.

- P2i – Irati Formation: Shale, siltstone and dark gray mudstone, interbedded with limestone, marl and bituminous shale bearing mesosaurid reptile fossils. Interpreted as a marine environment, with fine-grained sedimentation by decantation below effective wave base, under conditions that included periods of water-column stratification and intervals influenced by storm activity.

- P1tt – composite stratigraphic unit comprising three formations: (i) Palermo Formation: Siltstone, sandy siltstone, fine to very fine sandstone and shale, with lenses of thick sandstone and conglomerate containing discoid pebbles; predominantly gray to greenish gray in color, locally weathering to yellowish; interpreted as deposited in shallow marine environments. (ii) Rio Bonito Formation: Arkosic sandstone, gray to dark gray and carbonaceous siltstone, white quartz sandstone, dark gray to black carbonaceous shale, coal, diamictite with a carbonaceous matrix and marl; associated with fluvio-deltaic, shallow marine shelf and coastal depositional environments. (iii) Tatuí Formation: Gray siltstone and sandy siltstone; fine quartzose sandstone, medium- to coarse-grained immature greenish-gray sandstone, limestone and silexite, with occasional coal fragments and coal-bearing horizons, as well as pyrite nodules; interpreted as representing a shallow marine environment.

P31c, P2i, and P1tt all belong to the Permian–Triassic interval of the Paleozoic era.

Figure 19 – DOL mine location and geology composition

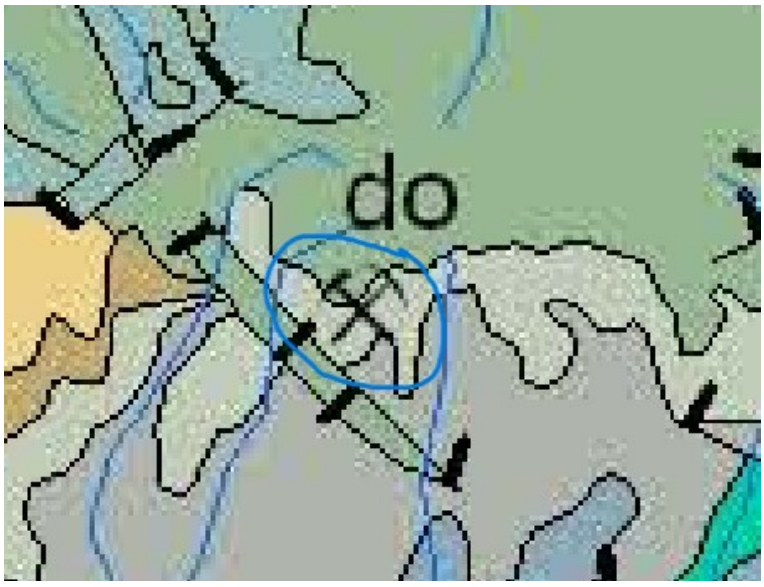

Source: Adapted from (GEOLOGICAL SURVEY OF BRAZIL (SGB/CPRM), 2006)

3.2.1 Particle diameter measurement

For the determination of particle size distribution, a mechanical sieving procedure was conducted using a mechanical siever (Bertel). A commercial batch of material, provided as a donation by Calcário Diamante, served as the primary sample. This material was initially subjected to a quartering procedure to obtain smaller, representative subsamples.

A bulk sample with a total mass of 356.5 g was subsequently subdivided into seven subsamples of approximately 50 g each by means of quartering. These subsamples were employed to determine the mean particle diameter and the associated standard deviation. For each sieve fraction, the characteristic particle diameter was defined as the arithmetic mean of the nominal aperture sizes of the current sieve and the preceding sieve. During the sieving procedure, the vibration intensity was maintained at 50%, and the total sieving time was 3 min.

Each 50 g sample was subjected to mechanical sieving using a stack of 18 sieves arranged in consecutive order. For each sieve fraction, seven replicate measurements were performed to determine the mass percentage retained within the corresponding particle size fraction. The initial sample mass was normalized to 100%, and, for each sieve, the reported mass percentage and associated standard deviation describe the measurement range for that size fraction.

Further methodological details pertaining to the particle size determination procedure are presented in Appendix A.

3.2.1.1 Particle diameter and circularity measurements using microscope

Given the substantial variability observed in the conventional sieving method, a correction correlation is proposed to adjust the results obtained by standard sieving and thereby derive a more accurate estimate of the mean particle size. For this purpose, a small amount of each sieved fraction is mounted on microscope slides for image-based particle analysis using a ZEISS SteREO Discovery microscope. Subsequently, 30 images in .tif format are acquired from distinct regions of each slide, ensuring that no individual particle is imaged more than once in the analysis.

Subsequently, the images were processed in ImageJ. All files were converted to 8-bit format, followed by individual evaluation of different thresholding methods and the application of filters to remove particle agglomerates and background noise. Thereafter, particle circularity and mean diameter were quantified using ImageJ's circularity analysis algorithm.

A correlation was created through a linear regression fitted on data of both circularity and mean diameter as follow:

$$\text{Circularity} = \text{A} \cdot (\text{Mean diameter}) + \text{B}$$

$$\text{Adjusted Mean diameter} = \text{A} \cdot (\text{Mean diameter}) + \text{B}$$

where A and B are slope and intersect, respectively.

3.2.2 Mean particle diameter determined by analysis

For the tests described below, narrow particle size fractions with well-defined mean diameters were employed. These fractions correspond to particles retained between two consecutive sieves. In this context, the mean particle diameter is determined as the arithmetic average of the apertures of the upper and immediately lower sieves, thereby yielding a relatively narrow and uniform particle size distribution. The particle size ranges adopted in the following analyses are specified as follows:

1. XRF analysis was performed using a mean particle size of 327.5 μm for the determination of the general composition. For the assessment of the specific color fractions, a larger mean particle diameter of 925 μm was employed, as this particle size range facilitated more reliable visual discrimination of color by the naked eye.

2. Surface area analysis was conducted using samples with particle size fractions of 780 μm, 390 μm, 231 μm, 98 μm, 82.5 μm, 69 μm, and 58 μm.

3. CO_2 atmosphere analyses were conducted using a particle size of 231 μm. Pore blockage analyses employed particle size fractions corresponding to mesh apertures between 500 and 425 μm. Compaction behavior was evaluated for particle sizes >1000 μm, 780 μm, 550 μm, 390 μm, 296 μm, 137.5 μm, 115.5 μm, 98 μm, 69 μm, 58 μm, 49 μm, 41.5 μm, and 31.5 μm. Surface area analyses of the compaction samples were conducted only for particle sizes of 780 μm, 390 μm, 98 μm, 82.5 μm, 69 μm, and 58 μm.

4. Thermogravimetric analysis (TGA) under a natural gas flue gas atmosphere was performed on samples with particle sizes ranging from 840 μm to 210 μm. Within this particle size range, a Design of Experiments (DoE) matrix was implemented, the effect of multiple reaction cycles was evaluated, and scanning electron microscopy (SEM) imaging was conducted on the same sample set.

5. In the DIFB experiments, particles with sizes in the range of 600–400 μm were employed, corresponding to the operational constraints of the reactor. For the impact tests, DIFB samples were subsequently sieved to a maximum particle size of 400 μm prior to analysis.

3.2.3 X-ray fluorescence (XRF) analysis

The samples were sent to the Central de Análises Químicas Instrumentais - CAQI of the Chemistry Institute (EESC/USP) in São Carlos - SP to perform XRF tests. Sample were stored in eppendorfs tubes, labeled and sent through couriers. CAQI lab conducted the test through their own protocol (brand PANalytical - Model: MiniPaI4).

In molecular fluorescence analyses, molecules present in solid compounds or in solution are excited by radiation of a specific wavelength, and the radiation emitted by the molecules as a result of the excitation is recorded using fluorescence emission spectra. These spectra can be used in qualitative and quantitative analyzes of fluorescent substances.

This technique was mainly used in this work to verify the different composition throughout raw and processed limestone samples.

3.2.4 Scanning electron microscopy (SEM)

Morphological observations were made using a ZEISS EVO LS-15 SEM manufactured by Carl Zeiss Microscopy GmbH in Oberkochen, Germany. Samples were sent to the Laboratório de Imagens de Materiais (LAIMAT) at the Materials department (FEG/UNESP) in Guaratinguetá—SP for analyses. Morphological analyses were conducted, to assess the impact of the process on the surface integrity of the samples.

3.3 THERMOGRAVIMETRIC ANALYSIS (TGA)

To perform a comprehensive evaluation of the calcium looping process employing dolomite as the sorbent, TGA experiments were carried out under various operating conditions using a simultaneous thermal analysis system (SDT TG-DSC Q600, TA Instruments), equipped with an alumina crucible (⌀6 mm × 2.5 mm), as schematically illustrated in Figure 20.

Prior to the experimental measurements, the thermogravimetric analyzer was thoroughly calibrated. Subsequently, CO_2 was introduced via the lateral gas inlet using an Aalborg mass flow controller (model GFC-17). Detailed specifications regarding the accuracy and resolution of the measurements are summarized in Table 4.

Table 4 – Instruments used in Figure 20 technical information showing range, accuracy and resolution

Instrument	Measurement	Range	Accuracy	Resolution
SDT Q600	Mass (mg)	0-200	± 1 %	0.1 μg
	Gas flow (mL/min)	20-1000	± 2 %	1
GFC-17	Gas flow (mL/min)	0-50	± 1 % f.s	0.1

Source: Author

Figure 20 – TGA schematic setup used in this work: Main Air/N_2 supply connect direct to the equipment, CO_2 supply connected to a flow controller connected to lateral TGA entrance for gas mixtures, TGA furnace connect to TA Instruments software for data acquisition

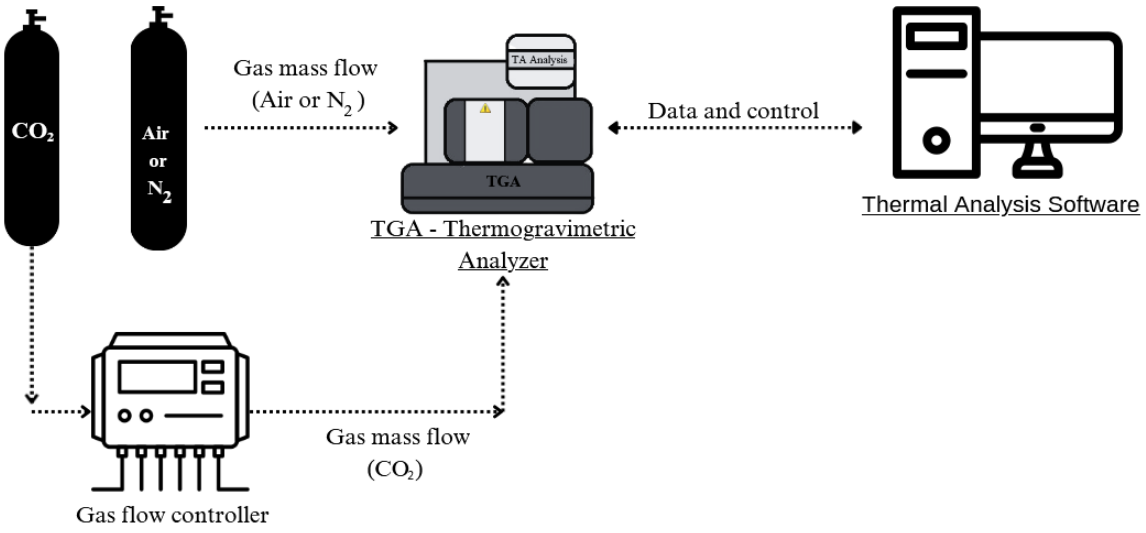

Source: Author

3.3.1 Experimental Conditions for Calcium Looping by TGA

TGA tests were applied during the analysis to verify the processing of the sample, which involves reversible reactions (calcination / carbonation), (Equation 3.1) (DIEGO; ARIAS, 2020b; YUAN; ZHAO, 2018).

$$\mathrm{CaCO_{3(s)}} \longleftrightarrow \mathrm{CaO_{(s)}} + \mathrm{CO_{2(g)}} \tag{3.1}$$

In the carbonation stage, experiments were conducted in a synthetic atmosphere representative of flue gases from natural gas combustion, given Brazil's high natural gas consumption for power generation (EPE, 2024). A literature survey of experimental studies on natural-gas-fired exhaust streams (AMROLLAHI; ERTESVÅG; BOLLAND, 2011; CAMPANARI; MANZOLINI; CHIESA, 2013; COLORADO; HERRERA; AMELL, 2010; DÍAZ-HERRERA *et al.*, 2020; DUTTA; NORD; BOLLAND, 2017; FRIEDMAN; LI, 2005; LOTT *et al.*, 2023; QURESHI; ALI; SHER, 2021; SIPÖCZ; TOBIESEN, 2012) was performed to estimate the CO_2 concentration at combustion exhaust conditions, yielding an average value of 4.2% vol. (wet basis) CO_2. Owing to limitations of the mass flow controllers, an approximate value of 4.0% vol. CO_2 was adopted, with N_2 or synthetic air employed as the balance gas.

Additionally, different CO_2 concentrations were investigated to evaluate the effect of CO_2 partial pressure on the carbonation behavior. For the condition with 4.0% CO_2, carbon dioxide was supplied at a flow rate of 4.0 mL/min, whereas the balance gas (N_2 or synthetic air) flow rate was set to 96 mL/min, thereby maintaining a constant total gas flow rate. Moreover, the

isothermal holding times were systematically varied to assess the influence of gas–solid residence time on the distinct phenomena associated with the carbonation process.

3.3.2 Effect of CO_2 Concentration in calcination step

TGA were conducted using samples with a total mass of (10.0 ± 0.5) mg placed in alumina crucibles. The experiments were initiated by stabilizing the furnace temperature at 30 °C, after which the samples were heated to 1000 °C at a constant heating rate of 20 °C/min. A volumetric gas flow rate of 100 mL/min was employed, with CO_2 concentrations ranging from 5% to 30%, the balance being synthetic air.

3.3.3 Effect of CO_2 concentration in carbonation step

A total sample mass of (12.0±0.5) mg contained in an alumina crucible was used in the analyses. The test was initiated by stabilizing the furnace temperature at 30 °C, after which the samples were heated to 1000 °C at a heating rate of 10 °C/min under a synthetic air atmosphere with a volumetric gas flow rate of 100 mL/min. After completion of the calcination step, cooling was initiated and continued until the temperature stabilized at 550 °C. Subsequently, the atmosphere was switched to a mixture of synthetic air and CO_2 with CO_2 concentrations ranging from 5% to 50%, and the samples were maintained isothermally under these conditions for 10 min.

3.3.4 Sorbent conversion in CO_2 sorption process

The sorption capacity of the sorbents was determined on the basis of a conversion parameter, defined as the ratio between the mass of the calcined reactant introduced into the process and the mass of the solid reactant that effectively participates in the reaction. The conversion (X) is calculated using Equation 3.2, where M_{Calc} denotes the mass of the sample after calcination and M_{Carb} represents the change in the mass of the sample during CO_2 injection, as measured by thermogravimetric analysis.

$$X(\%) = \frac{M_{Carb} - M_{Calc}}{M_{Calc}} \cdot 100 \tag{3.2}$$

3.4 POROSIMETRY BY NITROGEN GAS ADSORPTION

The Brunauer-Emmett-Teller (BET) surface area and Barrett-Joyner-Halenda (BJH) pore size distribution were determined by gas adsorption of nitrogen (N_2). This technique allows the evaluation of changes in the dolomite surface and in the available reactive surface area, which is critical for gas–solid reactions.

The characterization of the pore structure was performed by N_2 gas adsorption porosimetry using a Micromeritics ASAP system (Accelerated Surface Area and Porosimetry - ASAP 2020).

Prior to the experiments, the instrument was calibrated in accordance with the manufacturer's specifications, and the amount of liquid N_2 was quantified to ensure uninterrupted operation throughout all experiments.

Before the degassing step, the prepared samples were dried in an oven for approximately $12\,\mathrm{h}$ at a temperature of 110 ºC. Samples of (0.6±0.05) g were used in all experiments. The conditions used to degas the samples and analyze them in the porosimeter are described as follows:

1. Degas conditions were applied for vacuum restricted 10 ºC/min up to 150 ºC; 10 mmHg to 1 mmHg) and non-restricted vacuum (10 mmHg/s until 10 μHg), remaining under these conditions for 30 min. The heating was continued (10 ºC/min) until 300 ºC for raw dolomite or 350 ºC for calcined and carbonated samples, remaining under these conditions for 240 min.

2. Analysis conditions: the analysis of samples was started under vacuum restricted at an evacuation rate of 5 mmHg/s until 5 mmHg; the evacuation was changed to non-restricted vacuum at the same evacuation rate until 10 μHg, remaining under these conditions for 6 min. Then a P/P_0 programming was applied for 37 points (24 points for adsorption and 13 points for desorption). P/P_0 is the ratio between applied pressure (P) and saturation vapor pressure of adsorbed gas (P_0), that is, N_2.

The porosity was measured for the raw, calcined, and carbonated samples of dolomite. According to Webb and Orr (WEBB; ORR, 1997), convention has established that the quantity of gas adsorbed is expressed as its volume under standard conditions of temperature and pressure (0 ºC and 760 torr represented by STP), while the pressure is expressed as a relative pressure, which is the actual gas pressure (P) divided by the vapor pressure (P_0) of the adsorbing gas at the temperature at which the test is conducted.

3.4.1 Pore volume calculation

The experimental data were interpolated using a cubic spline, which provided a good fit to the measured values. The pore distribution analysis was limited to diameters up to 100 nm for all conditions, since the majority of the pore volume was concentrated within this range, and larger diameters did not show significant variation.

The total pore volume was calculated by numerical integration of the pore volume distribution using the composite trapezoidal rule, as shown in Equation 3.3:

$$V_{total} = \int_{D_{min}}^{D_{max}} \left(\frac{dV}{dD} \right) dD \tag{3.3}$$

where V_{total} is the cumulative pore volume from the minimum diameter (D_{min}) to 100 nm (D_{max}), D is the pore diameter, and $\frac{dV}{dD}$ represents the differential pore volume with respect to diameter.

3.5 VERTICAL TUBULAR REACTOR (VTR)

To ensure the availability of a sufficient quantity of samples for porosimetry analyses, calcination and carbonation experiments of dolomite were conducted in a vertical, electrically heated, and temperature-controlled VTR, Figure 21.

Figure 21 – Schematic of VTR setup used in this work: 1 - Nitrogen and Carbon Dioxide gas cylinders; 2 - Flow controllers; 3 - Gas entrance valve; 4 - Crucible containing sample; 5 - Thermocouple; 6 - Exhaust valve; 7 - Acquisition and control software.

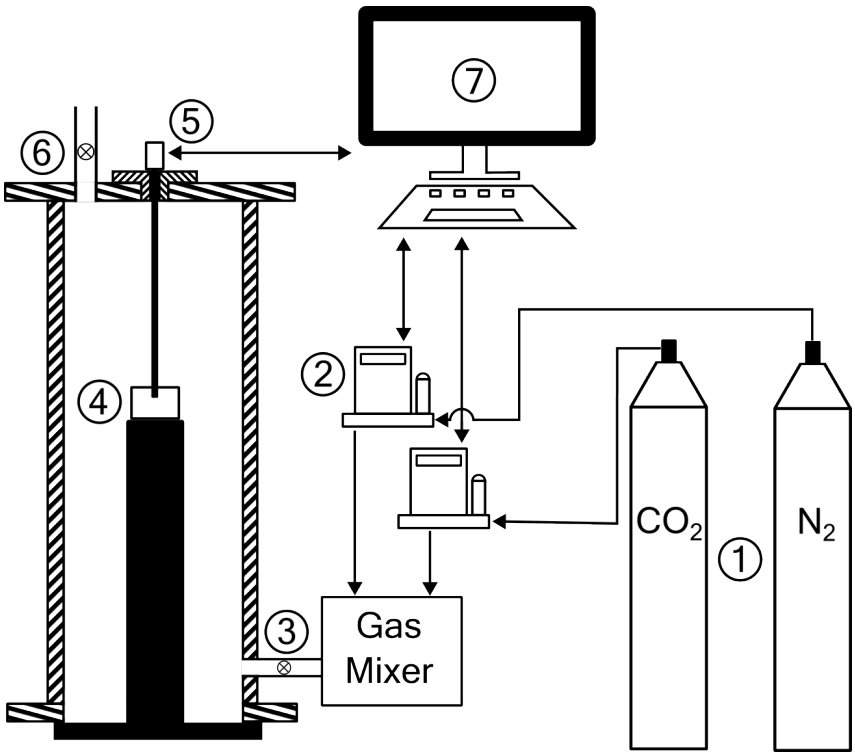

Source: Author

Considering the larger volume of the reactor, a total gas flow rate of 300 mL/min was employed, using a larger crucible (⌀ 35 mm × 2.5 mm) and an increased sample mass of (3.0 ± 0.1) g, while maintaining the same gas-phase composition (96% N_2–4.0% CO_2). All other experimental conditions were identical to those used in the TGA measurements.

For the carbonation experiments, raw dolomite samples were placed in the furnace and heated at a rate of 10 °C/min under a N_2 flow of 300 mL/min. Once the target temperature of 850 °C was reached, the samples were cooled at a controlled rate of 10 °C/min to 580 °C. At this point, CO_2 was introduced at a flow rate of 12 mL/min (Aalborg GF C 17), and the N_2 flow was reduced to 288 mL/min (Aalborg G19618C), thereby preserving the overall flow and gas composition. The samples were carbonated for eight different residence times: 0, 2.5, 5, 7.5, 10, 15, 30, and 60 min.

3.6 EFFECT OF COMPACTION AND PORE-BLOCKAGE IN CO_2 CAPTURE

3.6.1 Compaction effect Assessment

Samples with (12.0±0.5) mg were introduced on the TGA for a single loop of CaL. Parameters are set to heating rate of 10 °C/min up to 900 °C for calcination reaction while in 100 % air atmosphere, followed by a controlled cooling to 550 °C. After equilibrating on temperature, the atmosphere was changed to 50% CO_2 balance air and an isotherm of 10 min is followed, in this way no effect of CO_2 concentration would be seen. A plot is generated to examine the relationship between carbon mass capture and the mean particle size of the sample.

For this analysis (6.0±0.05) g of sample were placed on aluminum crucible and pre-treated in oven for at least 24 h at 290 °C before measuring surface area. This step was necessary to reduce amount of particle, oil, and general substance that would be extracted and cleaned during degasification step. After pre-treatment, samples were let to cool down inside a desiccator and directed to ASAP 2020 equipment for analysis of BET area.

3.6.2 Pore-blockage in CO_2 capture

3.6.2.1 Pore distribution deformation analysis

The initial pore distribution curve is analyzed to enhance the understanding and characterization of the pore distribution during the carbonation process. This curve demonstrates nearly symmetrical characteristics and approximates a Gaussian distribution, albeit not precisely because of its positivity. The parameters are $\mu \approx 52$ (cm^3/gÅ) and $\sigma \approx 29$ (cm^3/gÅ), reflecting the distribution of pores across the surface of the material. The processing of the material across varying time scales results in the loss of symmetry, with larger pores being occupied initially (as will be discussed further). This evolution is assessed by analyzing each curve, from 2.5 to 60 min, as a normalized probability density function of the pore availability on the surface. This analysis employs the KL divergence, defined as $D_{KL}\{P|Q\} = \int_{\varkappa} p(x) \log \frac{p(x)}{q(x)} dx$. In this analysis, $q(x)$ represents the curve with no carbonation while the other functions are denoted as $p(x)$ in this equation (COVER; THOMAS, 2006).

The KL is a fundamental concept in information theory and statistics that quantifies how much one probability distribution P (typically representing the true or observed distribution) differs from another distribution Q (often representing a model or approximation). A higher KL divergence indicates that the two probability density functions are increasingly dissimilar. In the extreme case where PDFs do not overlap, that is, Q assigns zero probability to events that have positive probability under P—the KL divergence becomes infinite. This measure is essential for evaluating probabilistic models and understanding how much a model deviates from the true distribution over time or as the data evolve. Quantifies the inefficiency or information loss incurred when using Q to approximate P.

3.6.2.2 Pore blockage modeling

The Beta distribution was selected to model the observed experimental data due to its exceptional flexibility. This probability distribution is well-suited for a wide range of data shapes, from symmetrical to highly skewed profiles, which are frequently encountered in empirical measurements. In its standard form (with a location parameter of zero and a scale parameter of one), the distribution is mathematically defined by its Probability Density Function (PDF) as:

$$f(x;\alpha,\beta) = \frac{\Gamma(\alpha+\beta)x^{\alpha-1}(1-x)^{\beta-1}}{\Gamma(\alpha)\Gamma(\beta)}$$

In this equation, $f(x)$ represents the probability density at a given value x, defined for $0 < x < 1$. The function is characterized by two positive shape parameters: α (alpha) and β (beta). α influences the distribution's behavior near the upper bound (x=1), pulling density toward that side. β influences the distribution's behavior near the lower bound (x=0), pulling density toward that side. Together, the ratio and magnitude of α and β dictate the curve's overall form, determining its modality (e.g., unimodal, U-shaped, uniform), skewness (left, right, or symmetric), and tail behavior. The term $B(\alpha,\beta)$ refers to the Beta function, which is defined using the Gamma function as $B(\alpha,\beta) = \frac{\Gamma(\alpha)\Gamma(\beta)}{\Gamma(\alpha+\beta)}$. This term serves as a normalization constant, ensuring the total area under the probability density curve sums to one.

Prior to fitting, the raw experimental data, typically represented as counts or frequencies within specific bins, underwent a normalization process. This involved dividing the observed counts by the product of the total number of experimental observations and the width of each data bin. This crucial step converts the raw frequencies into a probability density function, ensuring that the total area under the empirical data histogram integrates to unity, a fundamental requirement for comparison with theoretical probability distributions. It is also important to highlight only pore with diameter smaller than 100 Å were used in this analysis, due to it semblances with a density distribution and to the fact that it presents the most affected area during pore blockage.

The fitting process involved an optimization algorithm, specifically the *curve_fit* function from Python's *scipy.optimize* library, which iteratively adjusts these parameters to best match the theoretical PDF to our normalized experimental data. After the optimal parameters were determined, the resulting fitted probability density function was then denormalized. This denormalization step involved multiplying the fitted PDF values by the same total number of experimental observations and bin width used during the initial normalization. This converts the fitted probability density back into the scale of the original frequency or count data, allowing for direct comparison and visualization against the raw experimental histogram. Being this multiplication identified as "weight".

The *scipy.stats.beta* function works with 4 parameters, α, β, loc, and scale, where α, β are the shape parameters while loc and scale are used to shift and/or scale the distribution.

Denormalization is also necessary to use the model back to original magnitude, which is this case the variable named "weight" is used. After fitting all data, for each parameter (α, β, loc, scale, and weight), an curve fit is used in order to generate a model in function of carbonation time. A final correlation is presented which estimates dV/dD Pore Volume in $cm^3/g{\cdot}Å$ as function of pore diameter and carbonation time. This correlation is though to be an simple approximate description of pore blockage in limestone rocks, specially related to rate of pore blockage, which would need a larger dataset including different sorbents in order to be largely used.

3.7 STUDY OF CALCIUM LOOPING BY THERMOGRAVIMETRY

3.7.1 Partial cycle optimization of Calcium Looping experiments

CO_2 capture by dolomite increases with residence time and temperature up to a certain threshold. Above a critical temperature, the process is dominated by calcination reactions (BLAMEY *et al.*, 2010a), while the effect of residence time approaches saturation. Under these conditions, further optimization based solely on residence time and temperature is not feasible, since the maximum CO_2 uptake is attained at the highest practicable values of both parameters. Consequently, an additional independent variable must be introduced in order to assess the CO_2 capture performance as a function of this newly defined parameter.

Figure 22 shows an example of the behavior of a carbonation reaction for an evaluated sample. It is possible to observe that carbonation has three well-defined regions. The methodology proposes that the mass capture-to-energy ratio used in regions I and II should be greater than that in region III.

Figure 22 – Brazilian dolomite representation of the three stages of carbon capture – Region I representing the fast chemical reaction, region II is saturation and transition to region III where diffusion takes over the process

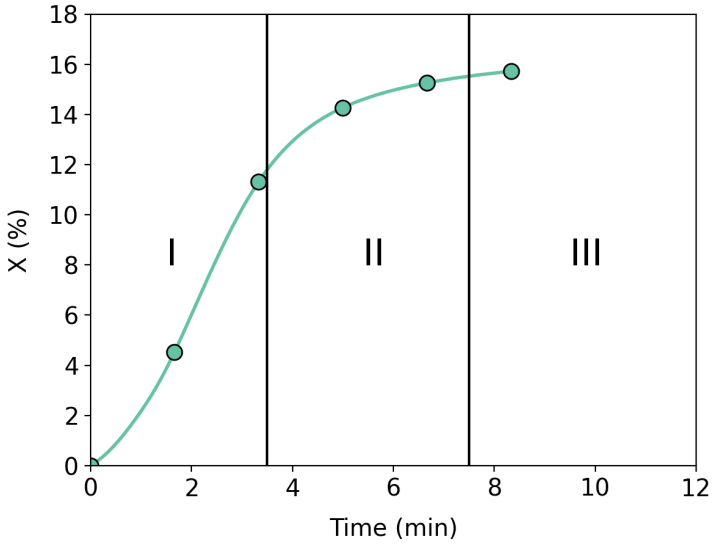

Source: Author

In this context, this methodology proposes to interrupt the cycle around region II to investigate a optimization region when investigating the CO_2 mass captured and energy spent in the process.

Dolomite samples with masses of (10.0 ± 0.5) mg were employed, this being the maximum amount that permits a single-layer distribution at the bottom of the crucible and ensures that all particles remain in contact with the reactant gas. The samples were calcined up to 800 °C at a heating rate of 10 °C/min in a synthetic air atmosphere flowing at 100 mL/min. The calcination temperature was selected as the minimum value required to guarantee 100% conversion of $CaCO_3$, while simultaneously minimizing sintering and other high-temperature calcination effects on CO_2 capture performance (CHARITOS *et al.*, 2010; DUELLI *et al.*, 2015b). Following calcination, the samples were cooled at a controlled rate of 10 °C/min to their respective carbonation temperatures. Subsequently, the reaction atmosphere was switched to a gas mixture containing 4.0 % CO_2 balanced with synthetic air. The tests were carried out for the residence times defined in the experimental design matrix (Table 5).

The calcined mass (m_{calc}) and carbonated mass (m_{carb}) were obtained from the TGA weight signal, as shown in Figure 23. Subsequently, the mass of captured CO_2 ($CO_{2\ cap}$) was determined using Equation (3.4).

$$CO_{2\ cap} = m_{carb} - m_{calc} \tag{3.4}$$

The total energy spent (E_{sp}) in the process of each experiment was calculated by integrating the signal of instantaneous energy spent by the reactor along the process, i.e. from the beginning of calcination to the end of carbonation. In order to avoid the magnification effect produced by different magnitudes of E_{sp} (kJ) and $CO_2 cap$ (mg), both equations were normalized by their maximum value as presented in Equation (3.5) and Equation (3.6), respectively.

$$E_{sp,n} = \frac{E_{sp}}{E_{sp,max}} \tag{3.5}$$

$$CO_{2\ cap,n} = \frac{CO_{2\ cap}}{CO_{2\ cap,max}} \tag{3.6}$$

A response variable IEC was determined as in Equation (3.7), which calculates the ratio between $E_{sp,n}$ and $CO_{2\ cap,n}$. Index of Capture Efficiency (IEC) is then used as response, which relates CO_2 mass capture by the system and the furnace energy spent during the test.

$$IEC = \frac{CO_{2\ cap,n}}{E_{sp,n}} \tag{3.7}$$

In practical applications, the IEC quantifies the energetic efficiency of CO_2 capture. This parameter specifies the amount of CO_2 removed per unit of energy input and thus constitutes a direct indicator of the relationship between performance and energy cost of the process. Elevated IEC values reflect enhanced efficiency, i.e., increased CO_2 capture at a lower relative energy expenditure, whereas reduced IEC values indicate a decline in efficiency, potentially arising from sorbent degradation, diminished reactivity over multiple cycles, or non-optimal operating

conditions.

Figure 23 – CaL cycle of the Brazilian dolomite used to show m_{calc}, m_{carb}, and residence time (t). Calcination temperature: 800 °C, Carbonation temperature: 550 °C, heating rate of 10 °C/min, residence time of 10 min and atmosphere: 100 mL/min - 4.0 %CO_2 balance synthetic air for carbonation

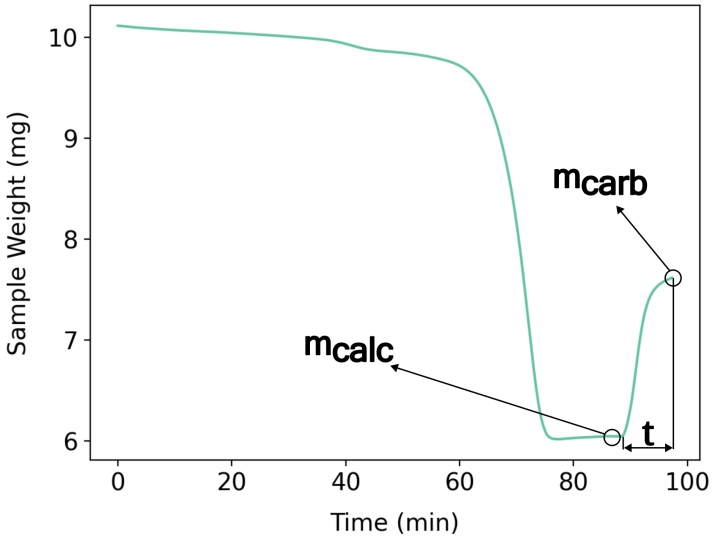

Source: Author

3.7.2 The rotatable central composite design (RDCD) model

A rotatable central composite design (RCCD) was employed, as it allows a reduction in the number of experimental runs required for two factors. The independent variables were residence time (min, as shown in Figure 23) and process temperature (T/°C), which were coded as x_1 and x_2, respectively, as described in Equation (3.8). These factors were selected based on their documented influence on the efficiency of the CaL reaction and on overall energy consumption, given that the furnace constituted the principal source of energy demand in the system.

In the RCCD 2^k design (where k represents the number of factors), two factors were considered (RCCD 2^2) and investigated at five levels to optimize the response variables of interest. In this methodology, the coded levels comprise: a central level (0)—with a minimum of three replicates to estimate experimental variability; low and high levels corresponding to the factorial points (-1; +1), associated with the rotation of the factors; and low and high axial levels, or axial points ($-\sqrt{2}$; $+\sqrt{2}$), employed to characterize the curvature of the response surface. For practical reasons and to facilitate experimental implementation and analysis, the axial point values were approximated to -1.41 and +1.41, thus yielding integer temperature values rather than fractional ones. The corresponding coding scheme is presented in Table 5.

The RCCD planning matrix was established for the region related to the carbonation reaction, based on preliminary experiments conducted to assess the behavior of the dolomite sample

during calcination and subsequent carbonation. This region is characterized by a transition in the dominant reaction mechanism: initially, the entire external surface reacts with CO_2 to form $CaCO_3$, after which the process proceeds under a regime controlled by the diffusion of CO_2 into the particle core, which remains predominantly composed of CaO (ROUCHON; FAVERGEON; PIJOLAT, 2013).

Table 5 – RCCD matrix used in optimization tests presenting the two investigated parameters (carbonation time and carbonation temperature) and their codification

Test	x_1	x_2	t (min)	T (°C)
1	-1	-1	5	400
2	+1	-1	10	400
3	-1	+1	5	550
4	+1	+1	10	550
5	0	0	7.5	475
6	0	0	7.5	475
7	0	0	7.5	475
8	0	0	7.5	475
9	-1.41	0	4	475
10	+1.41	0	11	475
11	0	-1.41	7.5	370
12	0	+1.41	7.5	580

Source: Author

After performing the tests, a generic quadratic model is adjusted according to these data, as in Equation (3.8).

$$y = b_0 + b_1 x_1 + b_2 x_2 + b_3 x_2^2 + b_4 x_2^2 + b_5 x_1 x_2 \tag{3.8}$$

To find model adjustment constants, the level matrix is written as in Equation (3.9), where b_0, b_1, b_2, b_{11}, b_{22} and b_{12} are the constants adjusted experimentally according to RCCD levels and response variables.

$$\mathbf{X} = \begin{bmatrix} x_{11} & x_{21} & x_{11}^2 & x_{21}^2 & x_{11} \times x_{21} \\ x_{12} & x_{22} & x_{12}^2 & x_{22}^2 & x_{12} \times x_{22} \\ \vdots & \vdots & \vdots & \vdots & \vdots \\ x_{1n} & x_{2n} & x_{1n}^2 & x_{2n}^2 & x_{1n} \times x_{2n} \end{bmatrix} \tag{3.9}$$

Where **X** is the planning matrix comprising time and temperature variables, i.e. the main planning matrix of the curve region defined by the rotational design. The response vector **z** is also found in Equation (3.10).

$$\mathbf{z} = \begin{bmatrix} y_1 \\ y_2 \\ \vdots \\ y_n \end{bmatrix} \tag{3.10}$$

Thus, it is possible to calculate the adjustment coefficients of Equation (3.8) using Equation (3.11) where y_1, y_2 and y_n are the response variables.

$$b = (\mathbf{X}^T\mathbf{X})^{-1}\mathbf{X}^T\mathbf{z} \tag{3.11}$$

Where *b* are the coefficients of Equation (3.8).

A response surface is generated the moment the optimization methodology was determined. The response surface aims to show the energy mapping of the whole process, highlighting the difference in the effect of the two process variables.

The analysis of variance (ANOVA) was used to verify the statistical significance of process parameters for the calcium looping process.

3.7.3 Multicycle path analysis

Samples showing a distinct behavior and/or great performance in the RCCD model were selected to investigate the effect of residence time and carbonation temperature on multicycles of CaL. The ratio between the total mass CO_2 captured, $\sum(m_{carb} - m_{calc})$ as illustrated in Figure 24, and the energy spent in the process was calculated according to Equation (3.12) not taking into account the first cycle of each test due to their high variability.

Thus, it is possible to evaluate the optimization process effect in the performance decay and how energy consumption affects this analysis for a higher number of cycles.

$$y_{10,c} = \frac{\sum(m_{carb} - m_{calc})}{\sum E_{\,sp}} = \frac{\sum CO_{2\,cap,n}}{\sum E_{\,sp,n}} \tag{3.12}$$

Repeating the methodology of the RCCD tests, results of $CO_{2\,cap}$ and $E_{\,sp}$ were normalized by their maximum value before analyzing its ratio.

Multicycle tests were conducted using the previous experimental setup. After the first cycle, the atmosphere was switched to synthetic air, and temperature was again raised to 800 °C at a rate of 20 °C/min to reduce the total time amount spent during the tests, followed by going through the carbonation stage once more. A total of ten complete calcination/carbonation cycles were performed.

3.8 STUDY OF CALCIUM LOOPING BY FLUIDIZED BED REACTOR

3.8.1 Experimental setup

The reactor used for the fluidized experiments is a DIFB system, Figure 25.

The reactor consists of two identical fluidized beds acting as calciner (right) and carbonator (left). Central reactors are built around a stainless steel (AISI 316) tube with 40 mm internal diameter and 1.5 mm of wall thickness. Heating is provided by electrical semi-cylindrical heated elements insulted by mineral wool and covered with aluminum metal sheets. Each reactor is

composed by: an individual heating system, a plenum with its perforated plate, a fluidized section, thermal insulation and a filtration system.

Figure 24 – CaL multi-cycle of the Brazilian dolomite used to show m_{calc}, m_{carb}, and the first cycle magnitude difference. Calcination temperature: 800 °C, Carbonation temperature: 580 °C, heating rate of 20 °C/min, residence time of 7.5 min and atmosphere: 100 mL/min - 4.0%CO_2 balance synthetic air for carbonation

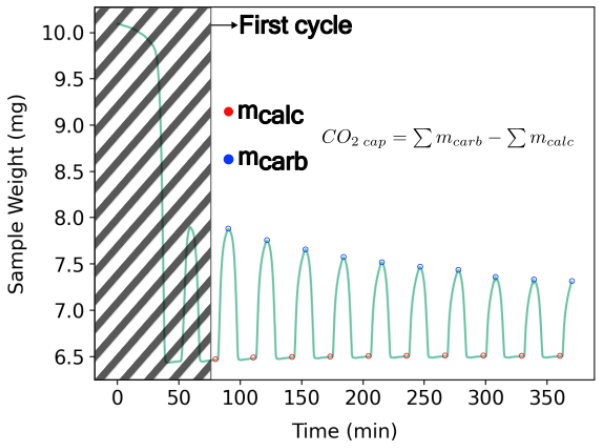

Source: Author

The plenum serves the purpose of pre-heating and mixing the gas, prior to the entry in fluidized section. This sections is filled with metallic fins to obtain a well-mixed flow through a height of 0.66 m. Gases are forced from the bottom of this section through a 10 mm hole, using a Bronkhorst mass flow controller that fixes the flux at the inlet to obtain the desired gaseous composition.

The Fluidized section is composed of a 1 m tube connected to the plenum at the bottom by a flange which contains a perforated plate with 55 holes, 0.5 mm diameters disposed in a triangular pitch. The perforated plate accelerates the gas to fluidized the bed and distributes the flow evenly to the reactor.

The filtration section receive the flue gases at the top end of the fluidization section, through a valve system, which capture elutriated fines. This section uses sintered steel filters to collect the fines with efficiency >99% for >10 μm particles.

The most important data in this setup is the CO_2 concentration acquisition. Both reactors are connected to a sample outlet gas where a Nondispersive infrared sensor (NDIR) analyser measures the gases concentration. The data is saved in equipments logger which is processed after test is finished.

Dolomite samples are loaded into the reactors through cylindrical steel hoppers, positioned laterally connected to each reactor. After each cycle, the material is discharged in an inox steel tank at the end of a vertical central duct, connected to the reactors through a 3-way valve.

Both reactors work independently in batch mode, and they are connected to each other by a duct (internal diameter 10 mm) partially immersed in the bed and enabling fast pneumatic

transport of solids between the two reactors. This setups allows for the reactor not in operation to be set in a "resting" state, conserving temperature homogenization and saving cost in expensive gas as N_2 and CO_2 by using air when not in use.

Figure 25 – Photo of the DIFB system in operation at University of Naples

Source: Author

Figure 26 presents the three valves system which allow the transfer of sorbent from the calciner to the carbonator and vice versa:

- Valve 1, placed above each reactor, allows the gas delivery to filtration system;
- Valve 2 allows the passage of the material between the reactors;
- The central valve 3, a 3-way T valve, defines the transfer direction of the material.

The reactor in which the reaction takes place is called working bed, while the other one is called receiving bed, their role is alternated in each calcination/carbonation stage. The whole process is constituted by 3 steps:

- Working Stage: Reaction occurs in this stage; valves 1 are open in order to allow the delivery of gases to the filtration system and to the analyzer, while valves 2 are closed;
- Transport Stage: it is the step of the material transfer from one reactor to the other. Valve 1 from the working bed is closed to prevent the gas passage to the vent and generate the overpressure for transport, while valves 2 are both open, together with valve 3 to facilitate the passage of sorbent.
- Discharging stage: valve 1 is closed, valves 2 and 3 are open, the latter oriented in such a way that the bed material flows only from the working bed to the container located at the end of the central duct.

Figure 26 – Transport system of DIFB: 1 - Valve to filtration system; 2 - Transport valve between reactors; 3 - T valve controlling discharge to container

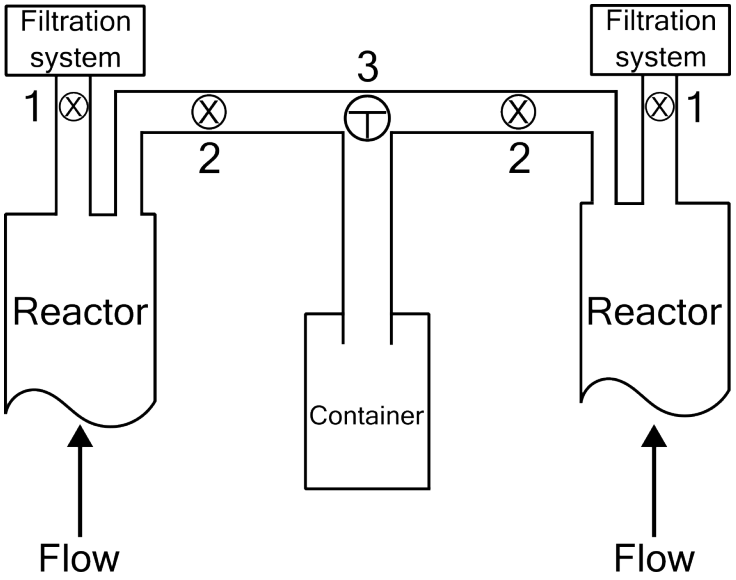

Source: Author

3.8.2 Experimental preparation

First step for this setup is the cleaning of both reactors and transport system. This step is conducted by disassembling the filtration system and transport ducts from both reactors for manual cleaning. Both reactors are vacuumed until all residual bed content is removed. Bed is ready for resembling while bed content is sieved to separate elutriate from filler material.

Fluidized bed filler material chosen is silica sand, with particle size ranging between 850-1000 μm. A higher particle size is chosen to facilitate sieving of sand and dolomite after test. Filler material have a important role in this process, while reaction takes place the sand behaves as fluidization/thermal ballast material to limit both temperature fluctuations (chemical reactions and reactor temperature variations). Sand proved to be chemically inert and with negligible

contribution to attrition/fragmentation of the sorbent (COPPOLA *et al.*, 2023), being usage of sand as bed material a common practice in CaL research (LAURO *et al.*, 2023; TREGAMBI *et al.*, 2023; WANG *et al.*, 2023).

After the preparation, the calciner is loaded with 150 g of sand, while the carbonator with 100 g; 20 g of sorbent, sieved in the range 400-600 μm, are fed at the beginning of the experiment to the calciner.

A single test consists of 10 complete cycles of calcination/carbonation, plus an 11th calcination stage (resulting in 21 total stages) to obtain the exhausted sorbent in its calcined form. The duration of each stage is 10 min, a time long enough to observe completion of the reactions. Hence, a complete carbonation/calcination cycle takes place in 20 min.

Experiments followed different carbonation temperatures and velocities according to a RCCD described in section 3.8.4. The carbonator bed is fluidized with 4.0%vol. CO_2 as previous TGA experiment, and the remaining volume balanced by air to simulate the reducing conditions of natural gas combustion gasifier-carbonator.

Both beds started fluidizing at a superficial velocity equal to 0.5 m/s, twice the minimum fluidization velocity. This value optimizes the segregation between sorbent and bed material (silica sand), which is crucial to have a good pneumatic transport of the sorbent between the two reactors, and to minimize sand transport (COPPOLA *et al.*, 2023).

3.8.3 Carbon capture tests

Before a test, both reactors undergo a preset procedure. Calciner is pre-heated to 940 °C while fluidization velocity is set to 0.5 m/s with an atmosphere of 70% CO_2 balance air until steady state is reached. For the carbonator, temperature and velocity were set to a condition from one of the test in Table 6 with an atmosphere of 4.0% CO_2 until steady state.

After steady state on both reactors were reached, gas analyzer (VARIOluxx - Portable stack gas emission analyser) is started recording and 20 g of dolomite is added to the calciner. Both carbonation and calcination will have a residence time of 10 min, which after this point the sorbent is transferred from one reactor to another. During the transferring, independent of the reactor or the velocity, the fluidization velocity was set to 0.6 m/s to have an efficient transfer between reactors. After 10 full cycles, samples are calcinated for 10 min and then discharged to let cool down in ambient temperature.

The signal output of CO_2 capture was filtered and organized by individual cycle. Each cycle consist of a complete carbonation reaction (achieving 99% conversion of CaO particles, including diffusion carbonation stage), Figure 27, where each test have 10 values of CO_2 capture capacity (ξ).

The specific ξ can then be evaluated by integrating each individual cycle profile, Figure 27, by assessing the sum of the ratio between the mass of CO_2 captured in every cycle and the initial

mass of sorbent (m_0):

$$\xi = \frac{\int_0^t \left[W_{CO_2}^{in} - W_{CO_2}^{out}(t)\right] dt}{m_0} \tag{3.13}$$

where $W_{CO_2}^{in}$ is the CO_2 mass flow rate at the carbonator inlet and $W_{CO_2}^{out}$ is the CO_2 mass flow rate at its outlet. This equation can be further expanded to:

$$\xi = \left(\int_{t_0}^{t_f} \frac{C(t)}{100} \cdot Q \, dt\right) \cdot \frac{P \cdot M_{CO_2}}{R \cdot T \cdot m_0} \tag{3.14}$$

where C(t) is the CO_2 concentration (%, as depicted in Figure 27,) t_0 and t_f are beginning and ending time of carbonation (s), respectively, Q is the volumetric flow rate in liters per second (L/s), P_{atm} is the pressure in atmospheres (atm), M_{CO_2} is the molar mass of CO_2 (44 g/mol), R is the gas constant (0.08206 L·atm/mol·K), and T is the absolute temperature in Kelvin (K).

Figure 27 – Curve example showing the first cycle of an DIFB test (600 °C and 0.3 m/s) % of CO_2 present in reactor atmosphere by time

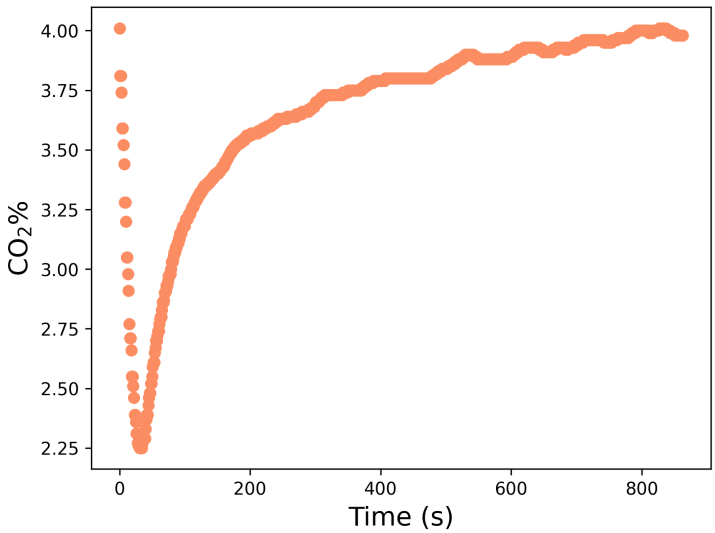

Source: Author

For this specific dolomite, due also to the high elutriation observed, m_0 will be taken as the retrieved mass sample after the test (around 60% of initial sample mass).

For a realistic representation of this sorbent performance in operation, the carbon capacity (Equation 3.13), was chosen using the mean of the last five cycle where deactivation effect as illustrated in Figure 28.

$$\xi_{mean} = \frac{(\xi_6, \xi_7, \xi_8, \xi_9, \xi_{10})}{5} \tag{3.15}$$

The response ξ_{mean} was fitted to a second order model as described in section 3.8.4.1.

Figure 28 – Curve of degradation for 675 °C and 0.5 m/s presenting experimental data and calculated value of mean capture capacity (ξ_{mean})

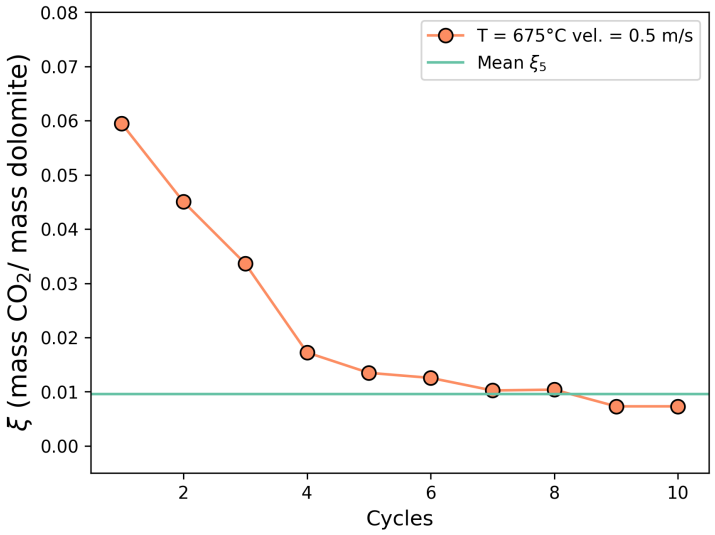

Source: Author

3.8.4 Investigation of temperature and velocity on carbon capture

This methodology propose using a RCCD to investigate the effect of fluidization velocity and carbonation temperature on ξ. For two unique parameters, Table 6 presents the recommended design with 8 unique experiments (4 from 2^2 design and 4 extrapolation, 2 per parameter) and 4 replicates on central point, making a total of 12 experiments (MONTGOMERY, 2013; RODRIGUES; IEMMA, 2005).

Table 6 – RCCD matrix for two parameters, fluidization velocity and carbonation temperature, used in the DIFB system: actual values and codification

Test	Velocity (m/s)	Temperature (°C)	x_1	x_2
1	0.30	600	-1	-1
2	0.70	600	1	-1
3	0.30	750	-1	1
4	0.50	750	0	1
5	0.50	675	0	0
6	0.50	675	0	0
7	0.50	675	0	0
8	0.23	675	-1.41	0
9	0.78	675	1.41	0
10	0.50	570	0	-1.41
11	0.50	780	0	1.41

Source: Author

3.8.4.1 Second order model and surface response method

As previous presented in section 3.7.2, the same methodology was applied to the DIFB system.

3.8.4.2 Elutriation parameters

Attrition inside fluidized bed reactors can be divided in two main categories: surface wear and impact damage. First case is caused by the abrasion of particles in movements constantly in contact with each other. The second is due to the high velocity impact some particle are subject to (SCALA; MONTAGNARO; SALATINO, 2007).

When dealing with full-scale reactors, the fragmentation due to the impact of high velocity on the structure of the bed is a main concern, which leads to coarse and fine particulates (COPPOLA *et al.*, 2020; MASSA *et al.*, 2024; XIAO; GRACE; LIM, 2014). For the experimental setup used in this work, each reactor also contains a filter in their outlet responsible for collecting the fines that are generated during the test. Figure 29 illustrates the filtration system used in the setup.

Figure 29 – Filtration system schematic from DIFB: 1 - Fluidized bed; 2 - Sorbent transport Valve; 3 - T valve; 4 - Filtration Cup; 5 - Filtration element; 6 - Gas outlet;

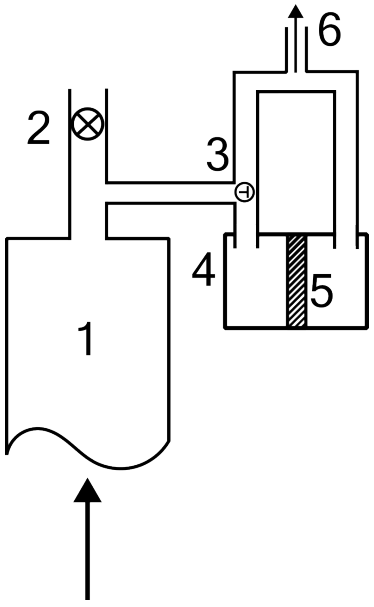

Source: Author

The dolomite used presented a high fragmentation, specially for the first two cycles. In this situation, two filter elements were used in the first two calcination an carbonation cycle, being the first filter changed after 4 min of calcination or carbonation reaction.

Each filter element is weighted before and after the test and elutriate mass is recorded, being possible to evaluate elutriate fines of carbonation and calcination in each cycle.

The sample attrition rate has been determined by collecting the fine particles captured in the filters. The elutriation have been evaluated considering the specific elutriation velocity (E(t),

Equation 3.16) at the end of each stage. E(t) is defined as the net mass of sorbent fines collected over a carbonation or a calcination stage (Δm_{el}), divided by the initial mass of sorbent (m_0) and by the duration of the cycle (Δt):

$$E(t) = \frac{\Delta m_{el}}{m_0 \Delta t} \tag{3.16}$$

Δm_{el} is determined by measuring the weight of the filter before and after each carbonation or calcination; Δt is the test time which will be fixed at 10 min. The average specific elutriation velocity ($\overline{E}(t)$, Equation 3.17) is defined as an arithmetical mean:

$$\overline{E}(t) = \frac{\sum_{i=1}^{n} E(t)}{n} \tag{3.17}$$

where n is the sum of the number of carbonation (10) and calcination (11) cycles occurring during the whole process, hence n=21.

The elutriated fragment fraction (f_{ff}) is defined as the ratio of the net mass of elutriate by initial sample mass:

$$f_{ff} = \frac{\Delta m_{el}}{m_0} \tag{3.18}$$

Accordingly, an average fraction of elutriated fragments ($\overline{f}_{ff}$) can be defined for every test:

$$\overline{f}_{ff} = \frac{\sum_{i=1}^{n} f_{ff}}{n} \tag{3.19}$$

3.8.5 Impact test

The high velocity condition usually applied to real scale reactors could not be met in the DIFB setup due to its small flow velocity used in lab scale reactors; in this sense, the effect of the impact had to be evaluated elsewhere.

Figure 30 presents the setup used to simulate the effect of the impact on bed on ambient temperature (COPPOLA *et al.*, 2020; COPPOLA *et al.*, 2023b; MASSA *et al.*, 2024; SCALA; MONTAGNARO; SALATINO, 2007). For this setup, after CaL tests (calcined and cooled in ambient temperature) samples were sieved and 1.2 g, with a mean diameter of 400 μm, were sent to the impact test. Each impact test condition have five different velocities (17, 24, 31, 38 and 45 m/s), totalizing five samples per carbonation condition.

After testing, samples are sieved again to investigate the PSD effect of impact. After this step the fragmentation index (f (-)), which represents the fragmentation intensity of each sample where higher value of f indicates higher amount of fragments bellow 400 μm in this case, is calculated as suggested by SCALA; MONTAGNARO; SALATINO (SCALA; MONTAGNARO; SALATINO, 2007), in Equation 3.20.

$$f = \frac{m_{355-0\mu m}}{m_{impact}} \tag{3.20}$$

Each f curve was then fitted into a first order linear model, Equation 3.21, where m is the angular coefficient, x the velocity in m/s and b is the linear coefficient. m presents f inclination indicated the fragmentation intensity and was choose as the response for a RCCD model. Where the minimum response, lower inclination, indicates the best condition fragmentation wise. In this context, a RCCD model auxiliate the discussion trying to find the minimum m measured.

$$f = mx + b \tag{3.21}$$

Figure 30 – Impact test apparatus: (1) gas flow meter, (2 and 4) lock hopper valves, (3) hopper, (5) feeding tube, (6) eductor tube, (7) target plate, (8) collection chamber, (9) cellulose filter, (10) gas flow metering valve

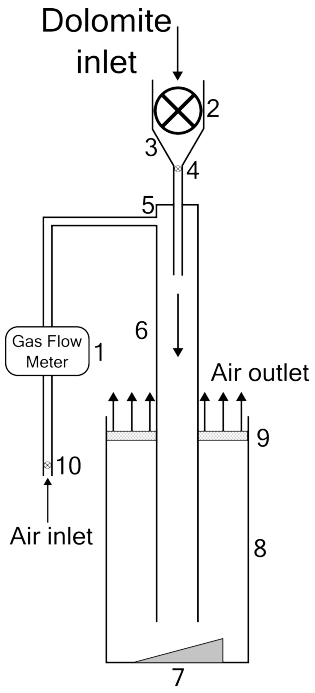

Source: Adapted from (SCALA; MONTAGNARO; SALATINO, 2007)

4 RESULTS AND DISCUSSION

This chapter presents the results of the conducted tests and investigations, examines their relationship to the existing body of literature, and highlights the principal findings and their implications.

4.1 MATERIAL CHARACTERIZATION

4.1.1 Particle size distribution

Table 7 present sample weight used for estimation of particle distribution with mean value and standard deviation.

Table 7 – Dolomite samples mass after quarting including mean value and standard deviation

Sample n°	1	2	3	4	5	6	7	mean	std
DOL mass (g)	53.54	52.73	49.98	50.52	52.77	47.26	49.69	50.93	2.05

Source: Author

Figure 31 presents the particle size distribution. The relatively high mass fraction in the >1000 μm class indicates that large sieves would more accurately resolve this portion of the material. The 925–137.5 μm size range exhibits both low and relatively uniform uncertainty, as well as a moderately homogeneous mass distribution. In contrast, the greater uncertainty observed in the smaller particle-size fractions indicates that this dolomite contains a significant proportion of fine material that passes through the smallest sieve used. Microscopic measurement results are shown in Figure Figure 32. Although both methods have intrinsic limitations, the microscopy-based analysis incorporates a substantially larger number of measurements, yielding a more robust and consistent estimate of variability. The results of measuring using a microscope are presented in Figure 32. Although both techniques exhibit inherent limitations, the microscopy-based analysis involves a substantially larger number of samples, which results in a more stable and consistent estimate of variability. It can be observed that the width of the confidence intervals decreases with decreasing particle size, which can be attributed to the higher number of particles present in the smaller size fractions.

A first-order linear regression model (Equation 4.1) was fitted to the data to adjust the sieve analysis results toward a more realistic representation. In this model, $\mathrm{d}_m p$ is the mean particle size (μm) and $\mathrm{d}_m s$ is the mean particle size measured by the current and superior sieve.

$$d_{mp} = 0.882 \cdot d_{ms} + 52.97 \tag{4.1}$$

Figure 31 – Particle size distribution for dolomite samples, presenting sample mass held in sieves by diameter in µm

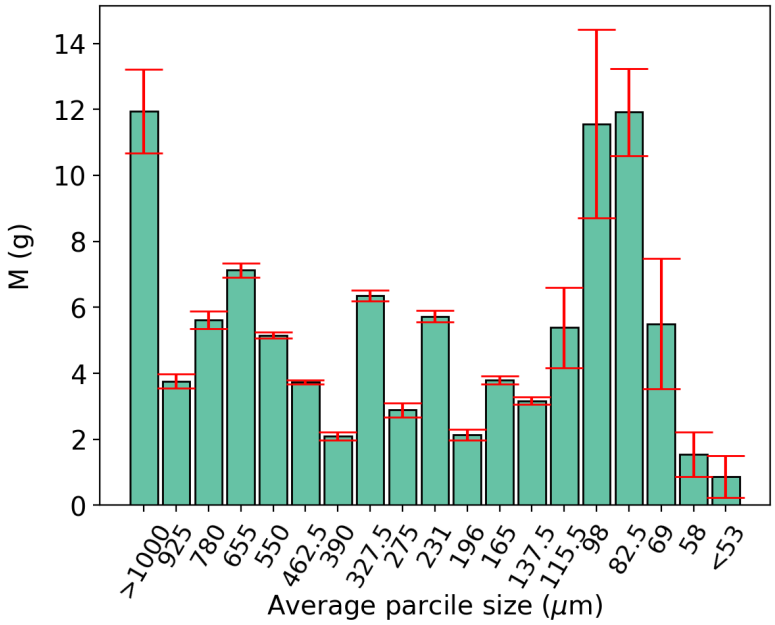

Source: Author

Figure 32 – Sample particle size correlation – measured in sieves and in microscope

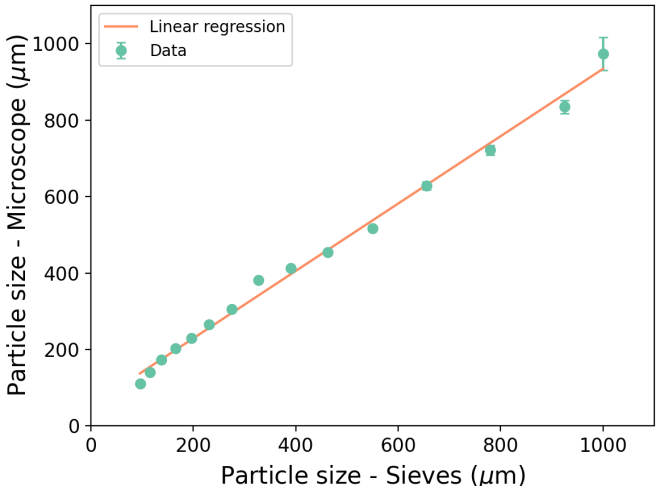

Source: Author

This correlation and adjustment are only valid for this specific set of sieves and sample, being its use limited for other configurations. The adjusted data from Figure 31 to the correlation is presented in the Table 8.

Figure 32 shows a linear model that provides a good fit to the observed correlation. Some sieves, due to wear and prolonged use, exhibit a more uniform effective aperture than others, which accounts for the discrepancies observed at the 350 µm size, for example. In addition, the

Table 8 – Adjust particle size by using the proposed correlation – Equation 4.1

Original	<1000	925	780	655	550	462.5	390	327.5
Correlation	934.5	868.4	740.6	630.4	537.8	460.7	396.8	341.7
Original	275	231	196	165	137.5	115.5	96	
Correlation	295.4	256.6	225.8	198.4	174.2	154.8	137.6	

Source: Author

particles possess heterogeneous geometries, which may facilitate their passage through specific sieve size classes. The reduction in the width of the confidence interval is again attributed to the increased number of particles included in the microscope-based analysis.

Figure 33 – Circularity by particle size measured in microscope

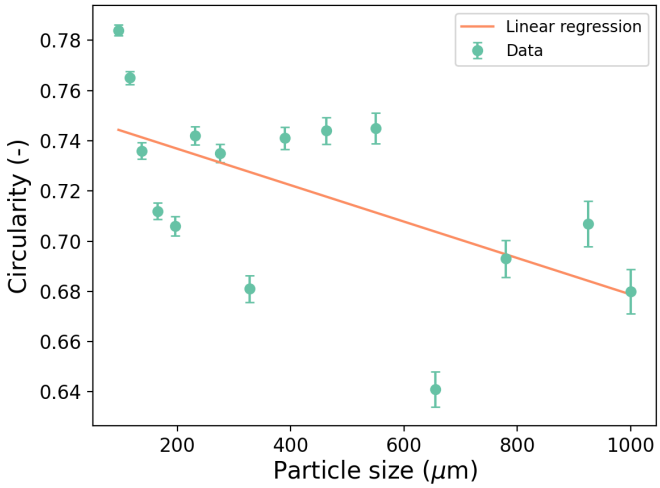

Source: Author

Figure 33 compares the circularity data with the correlation proposed in Equation 4.2 and reveals a pronounced lack of fit with the experimental measurements. This discrepancy suggests that the dependence of circularity on particle size exhibits a more complex behaviour than that captured by the proposed model. Analogously to the analysis performed for the mean diameter, a first-order linear regression model was fitted to the circularity data, as expressed in Equation 4.2, where ϕ is the particle mean circularity (-).

$$\phi = -7.25e^{-5} \cdot d_{ms} + 0.7513 \tag{4.2}$$

4.1.2 Composition analysis

Table 9 presents XRF analysis for the initial sample. It can be seen, as expected of a dolomite, a higher content of MgO (21.632%) and an unexpected amount of SiO_2 (26.977%).

Table 9 – XRF analysis showing percentage composition by elements and oxides

Elements	100 wt%	Oxides	100 wt%
Mg	17.224	MgO	21.632
Si	18.145	SiO_2	26.977
S	0.912	SO_3	1.473
Ca	57.589	CaO	45.719
Mn	0.841	MnO	0.533
Fe	3.603	Fe_2O_3	2.518
Sr	0.283	SrO	0.160
In	1.402	In_2O_3	0.988

Source: Author

The Brazilian dolomite sample exhibits three macroscopically distinguishable rock colors within its formation which are readily observable to the naked eye. To further investigate this heterogeneity, a XRF analysis was performed. Figure 34 presents the XRF-derived oxide composition, expressed as weight percentage, for the white, gray, and dark gray fractions of the sample. As shown in Figure 34, the dark gray particles are characterized by a significantly higher SiO_2 content, indicating that the majority of the silica present in the sample originates from this fraction.

Figure 34 – XRF results showing the oxide composition (in wt%) of white, gray, and dark gray particles.

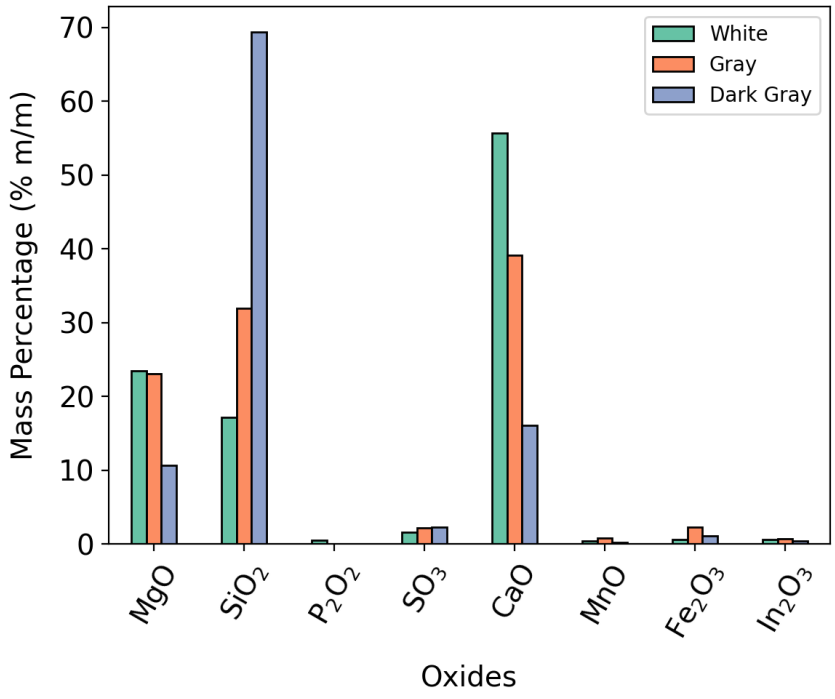

Source: Author

4.2 EFFECT OF CO_2 CONCENTRATION IN CALCINATION AND CARBONATION REACTION ATMOSPHERE

4.2.1 Effect of CO_2 concentration on calcination

Figure 35 presents the effect of CO_2 atmosphere in the calcination reaction. A clear effect in the calcination reaction can be seen with the CO_2 increase. Increasing CO_2 concentration shifts mass decomposition to the right past the 36 min mark. This shift is attributed to high Mg content which makes the calcination have an in between reaction (ÁVILA *et al.*, 2012b), Equation 4.3, due to stable form of $CaMg(CO_3)_2$.

$$\begin{aligned} \mathrm{CaMg(CO_3)_2} &\longrightarrow \mathrm{CaCO_3 + MgO + CO_2} \\ &\longrightarrow \mathrm{CaO + MgO + 2\,CO_2} \end{aligned} \tag{4.3}$$

Figure 35 – Calcination effect for atmosphere with 5, 10, 20, and 30% CO_2. Intervals from 5 to 30% are $\pm$ 0.14, $\pm$ 0.23, $\pm$ 0.22, $\pm$ 0.02, respectively

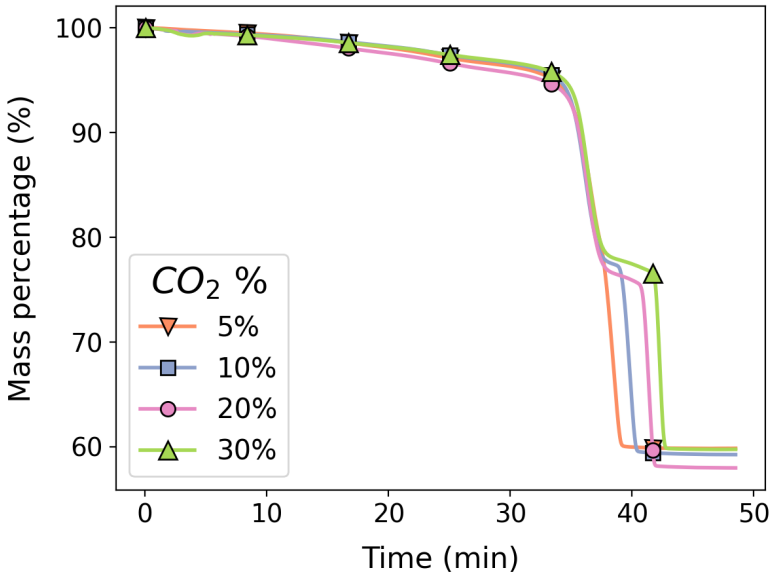

Source: Author

4.2.2 Effect of CO_2 concentration on carbonation

Figure 36 presents the effect of CO_2 concentration on carbonation reaction. A variability is observed at the onset of the carbonation front, which can once again be attributed to sample heterogeneity, a factor that is difficult to reproduce reliably at the milligram scale.

Figure 37 provides a more detailed view of the carbonation process. The primary difference observed is the change in slope, which increases with higher CO_2 concentrations. However, the total mass of CO_2 captured exhibits little to no variation, provided that sufficient time is allowed for the reaction to reach completion.

Figure 36 – Carbonation effect test for atmosphere ranging from 5-30% CO_2

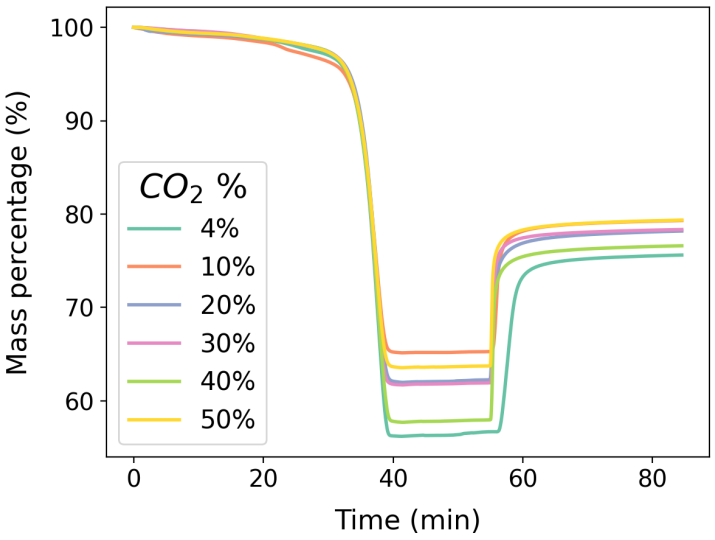

Source: Author

Figure 37 – Carbonation effect test excluding calcination, comparison for atmosphere from 5-50% CO_2 concentration

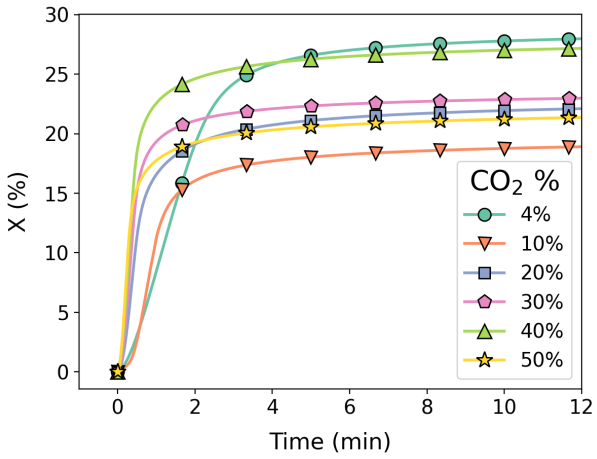

Source: Author

4.3 EFFECT OF COMPACTION AND PORE-BLOCKAGE IN CO_2 CAPTURE

4.3.1 Compaction effect assessment

Increasing the mass of sorbent within a fixed-bed configuration promotes bed compaction. As particle size decreases, particles are able to pack more efficiently, occupying the interstitial voids between them. However, when a large number of particles are densely packed, an effective loss of accessible surface area may occur, which in turn reduces the carbon capture capacity of the CaL system.

Figure 38a illustrates an approximately linear increase in surface area as a function of

the initial particle size within the regime where compaction effects are negligible or absent. Although the surface area initially increases with particle size, the data reveal a pronounced decrease beyond 170 µm, followed by a further decline until a plateau is attained.

The larger deviations observed at higher particle sizes are attributed to the intrinsic heterogeneity of the samples. Figure 34 indicates that, aside from minor variations in the concentrations of the other oxides, the most significant changes occur in the SiO_2 and CaO contents. Specifically, the SiO_2 content increases with progressive darkening of the color, whereas the CaO content exhibits an inverse trend. The darkening of the material is primarily associated with the reduction in CaO, which is characteristically bright white, while SiO_2 is essentially transparent and therefore contributes less directly to lightening the color.

To the hypothesized compaction effect, Figure 38b reports the evolution of surface area as a function of particle size. The results indicate that the surface area increases as particle size decreases. This relationship implies that smaller particles are expected to exhibit higher conversion due to their larger specific surface area. Nevertheless, as illustrated in Figure 38a, the conversion actually decreases with increasing particle size, revealing an unanticipated reduction in performance. This behavior is ascribed to enhanced bed compaction, which reduces the effective surface area available for interaction with CO_2.

Figure 38 – Compaction effect in dolomite samples

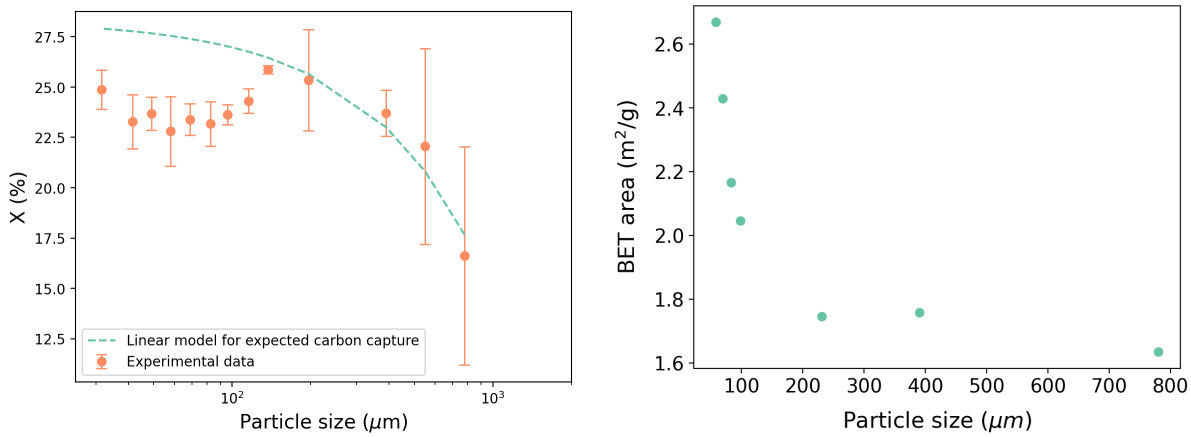

(a) CO_2 capture conversion by particle size compaction effect on TGA analysis

(b) Dolomite particle surface area measured by porosimetry

Source: Author.

Figure 39 presents carbonation curves of Figure 38a tests. It can be seen a very homogeneous pattern between fast and slow phase carbonation where fluctuations on total CO_2 mass captured is attributed to composition heterogeneity and compaction effect.

In fluidized-bed systems, a reduction in particle size enhances CO_2 capture efficiency as a result of the increased specific surface area available for gas–solid contact. Although a similar trend may initially apply to fixed-bed systems, progressive particle size reduction is expected to

promote bed compaction, which in turn can hinder gas flow and mass transfer, ultimately leading to a decrease in the stability and effectiveness of the carbon capture process.

Figure 39 – Compaction effect on carbonation reaction analysis in TGA

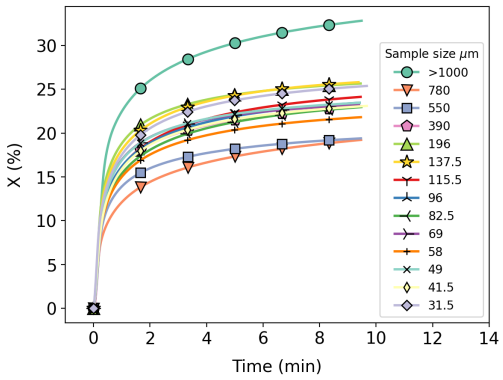

Source: Author

4.3.1.1 Compaction effect on calcination temperature

The processing history of limestone significantly influences its behavior during carbon capture applications (BENITEZ-GUERRERO *et al.*, 2018; SÁNCHEZ-JIMÉNEZ *et al.*, 2016). Valverde *et al.* ((VALVERDE; SANCHEZ-JIMENEZ; PEREZ-MAQUEDA, 2014b)) investigated the impact of limestone pre-treatment on calcium looping (CaL) performance and reported that milled limestone exhibits superior behavior during the slow carbonation phase when compared with annealed and untreated samples. They also demonstrated that a high density of defects reduces the energy required to achieve limestone calcination. A similar trend was observed in the present work (see Figure 40), where the calcination temperature decreased with decreasing particle size. However, this effect may also be attributed to enhanced heat transfer mechanisms associated with the use of smaller particles.

4.3.2 Effect of compaction and pore-blockage in CO_2 capture

4.3.2.1 Capture capacity assessment

After obtaining the partially carbonated samples in the VTR reactor, the process was evaluated by thermogravimetric analysis, considering different carbonation times (TOLEDO *et al.*, 2025). The first step was to assess how carbonation time impacted the conversion of sorbents. Figure 41 presents the conversion up to 20 min for each sample. An expressive decline can be seen from a total calcined sample (0 min) to the next sample, a carbonation time of 2.5 min. This result was expected, as the majority of fast carbonation reactions occur within the first few minutes of the process (GRASA; ABANADES, 2006). The following carbonation times continue to behave as expected, the total capture capacity is reduced, the initial capture is reduced, and the results show a really long diffusion phase, especially for $\geq$ 30 min results.

Figure 40 – Calcination temperature reduction with smaller particle size observed in TGA

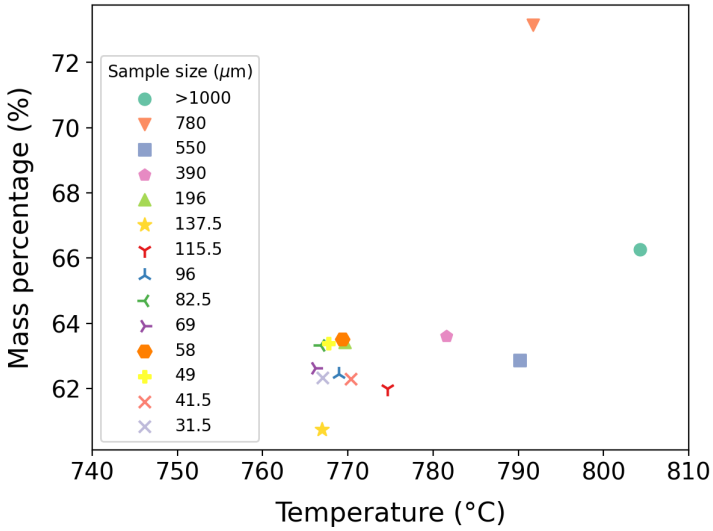

Source: Author

Figure 41 – TGA results of conversion (X) as a function of time (t) for dolomite samples with an average particle size of 462.5 μm in 4.0%CO_2-N_2 atmosphere at temperatures of 580 °C for calcined, 2.5, 5, 7.5, 10, 30 and 60 min of carbonation in the VTR

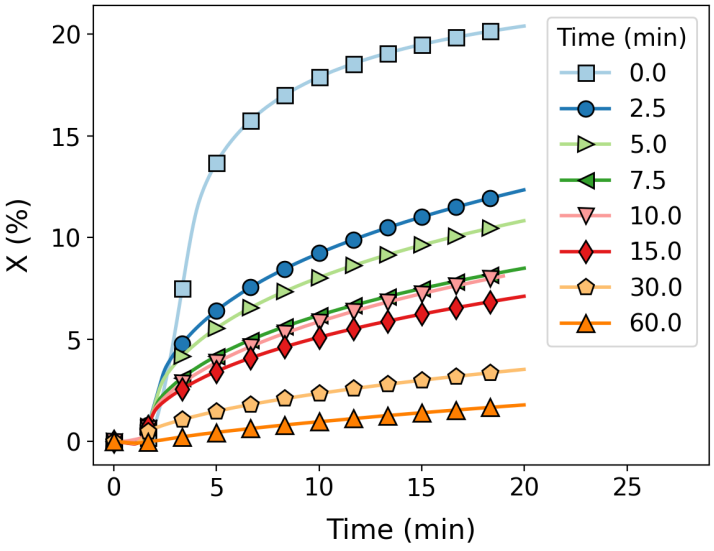

Source: Author

With the exception of 60 min sample, all tests seem to present a fast phase reaction. According to the noncarbonated curve (0 min), no sample should have a fast phase reaction past the 7 min mark; however, up to 15 min, even though smaller when increasing carbonation time, samples presented a fast phase. This observation might be related to a thermal shock caused by the abrupt moving of the sample at the end of the test to ambient air (MANOVIC; ANTHONY, 2008).

4.3.2.2 Pore blockage by CO_2 capture

After the TGA tests carried out to evaluate the preparation process of the calcined and carbonated samples at different times, nitrogen adsorption porosimetry tests were performed. These tests were conducted in duplicate.

Porosimetry techniques can be used to determine pore size and distribution, as well as the specific surface area. These results enable the correlation of the dolomite carbonation reaction's efficiency with the changes in its physical characteristics throughout the reactive process.

Figure 42 shows the adsorption and desorption isotherms obtained for a raw dolomite sample, a calcined dolomite sample, and a partially carbonated dolomite sample (carbonation time: 30 min), under the experimental conditions used in this study. These samples are representative, as the same behavior was observed for the other samples under similar reaction conditions.

Figure 42 – Adsorption and desorption isotherms for dolomite samples with in their raw, calcined and partly carbonated conditions (30 min)

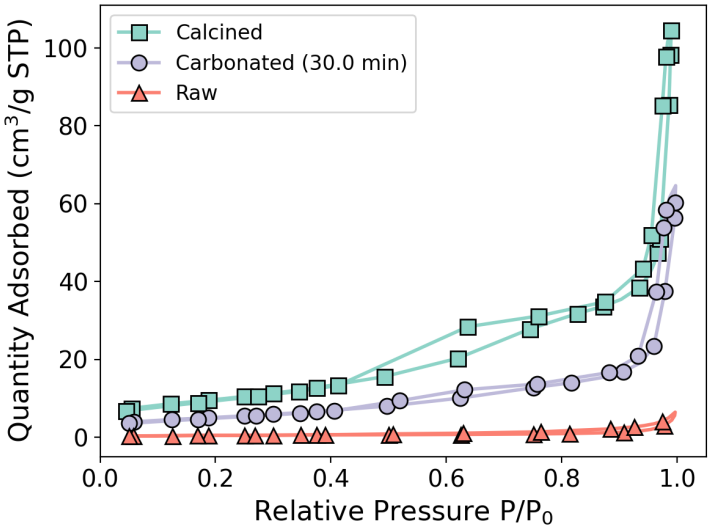

Source: Author

According to IUPAC recommendations, physisorption isotherms were initially classified into six types (SING, 1982) and later revised and updated (THOMMES *et al.*, 2015). Based on this classification, it is observed that the adsorption and desorption isotherms obtained for the analyzed samples (Figure 42) exhibit similar profiles, corresponding to type V, with the presence of hysteresis. This behavior is characteristic of mesoporous and macroporous materials and the hysteresis corresponds to type H3 (THOMMES *et al.*, 2015), which, according to IUPAC, is associated with aggregates of particles containing slit-shaped pores (ROUQUEROL; ROUQUEROL; SING, 1999).

Table 10 presents the mean values and standard deviations for the physical characteristics of all samples used in this study. Shown are the values of specific surface area determined by the Brunauer-Emmett-Teller method (S_{BET}), average pore volume from adsorption/desorption steps

(VP.Ads/VP.Ds), and average pore diameter from adsorption/desorption steps (DP.Ads/DP.Ds), both calculated according to the Barrett-Joyner-Halenda (BJH) method.

Table 10 – Mean values and standard deviations obtained by N_2 adsorption porosimetry for dolomite samples in their raw, calcined, and carbonated forms at different exposure times

Sample Units		S_{BET} (m^2/g)	VP_{BJH}.Ads (cm^3/g)	VP_{BJH}.Ds (cm^3/g)	DP_{BJH}.Ads (Å)	DP_{BJH}.Ds (Å)
Raw		1.59±0.00	0.06±0.05	0.01±0.00	261.92±27.10	162.95±0.81
Calcined		36.74±1.04	0.16±0.00	0.16±0.00	139.59±3.74	103.68±3.43
Carbonated	2.5 min	35.50±1.28	0.15±0.00	0.15±0.00	142.41±4.48	116.11±3.45
	5 min	31.87±0.00	0.14±0.00	0.14±0.00	140.97±0.00	120.77±0.00
	7.5 min	27.27±3.54	0.12±0.00	0.12±0.00	151.36±20.85	123.03±13.67
	10 min	26.93±2.95	0.13±0.01	0.13±0.01	170.84±6.79	132.91±1.35
	15 min	22.98±1.45	0.10±0.01	0.10±0.01	164.29±5.79	129.42±0.44
	30 min	13.50±1.82	0.08±0.00	0.08±0.00	241.38±31.85	192.29±23.23
	60 min	8.73±1.03	0.06±0.01	0.06±0.01	284.13±45.16	253.21±33.58

Source: Author

As shown in Table 10, raw dolomite exhibits low S_{BET} and VP_{BJH} values due to its low porosity, along with a high DP_{BJH} value. After calcination, there is a significant increase in S_{BET}, accompanied by a higher VP_{BJH} and a reduction in DP_{BJH}, indicating the formation of a more porous structure as a result of CO_2 release. As carbonation time increases, S_{BET} and VP_{BJH} show a decreasing trend due to the progressive blockage caused by the reaction products, which hinders the access of N_2 to the internal regions. DP_{BJH} displays the opposite behavior, possibly associated with the collapse of the fine-pore network and the predominance of macropores resulting from coalescence or selective pore blockage (BORGWARDT, 1989a).

For a better understanding of the carbonation process behavior in the parameters presented in Table 10, the corresponding results are shown in Figure 43. In the cases of VP_{BJH} and DP_{BJH}, only the values obtained in the desorption step are considered, since this is recognized as the most stable condition (LOWELL; SHIELDS, 2013).

It should be noted that when multiple curves are used for pore-blocking analysis, due to the heterogeneity of the limestone sample, dispersion of the results increases, making the analysis more challenging. In addition, a change in mechanism with exposure time has been observed, as reported in previous studies (ÁVILA *et al.*, 2012a; MORTARI; AVILA; CRNKOVIC, 2013). Therefore, in this study, differentiated increments were applied to evaluate the different phases of the carbonation process, which are identified as Phase I, Phase II, and Phase III, as shown in Figure 43.

In the initial stage (Phase I), increments of 2.5 min were applied to ensure a higher temporal resolution and allow for a detailed identification of the fast-reaction behavior. At this stage, the

pores are widely available, favoring the rapid formation of carbonate, predominantly controlled by surface chemical kinetics (BORGWARDT, 1989a). This behavior corresponds to the so-called fast carbonation phase, associated with gas-solid interface reactions (GRASA; ABANADES, 2006).

Figure 43 – Pore-blocking behavior evidenced by the effect on: (a) S_{BET}, (b) VP_{BJH}, and (c) DP_{BJH}

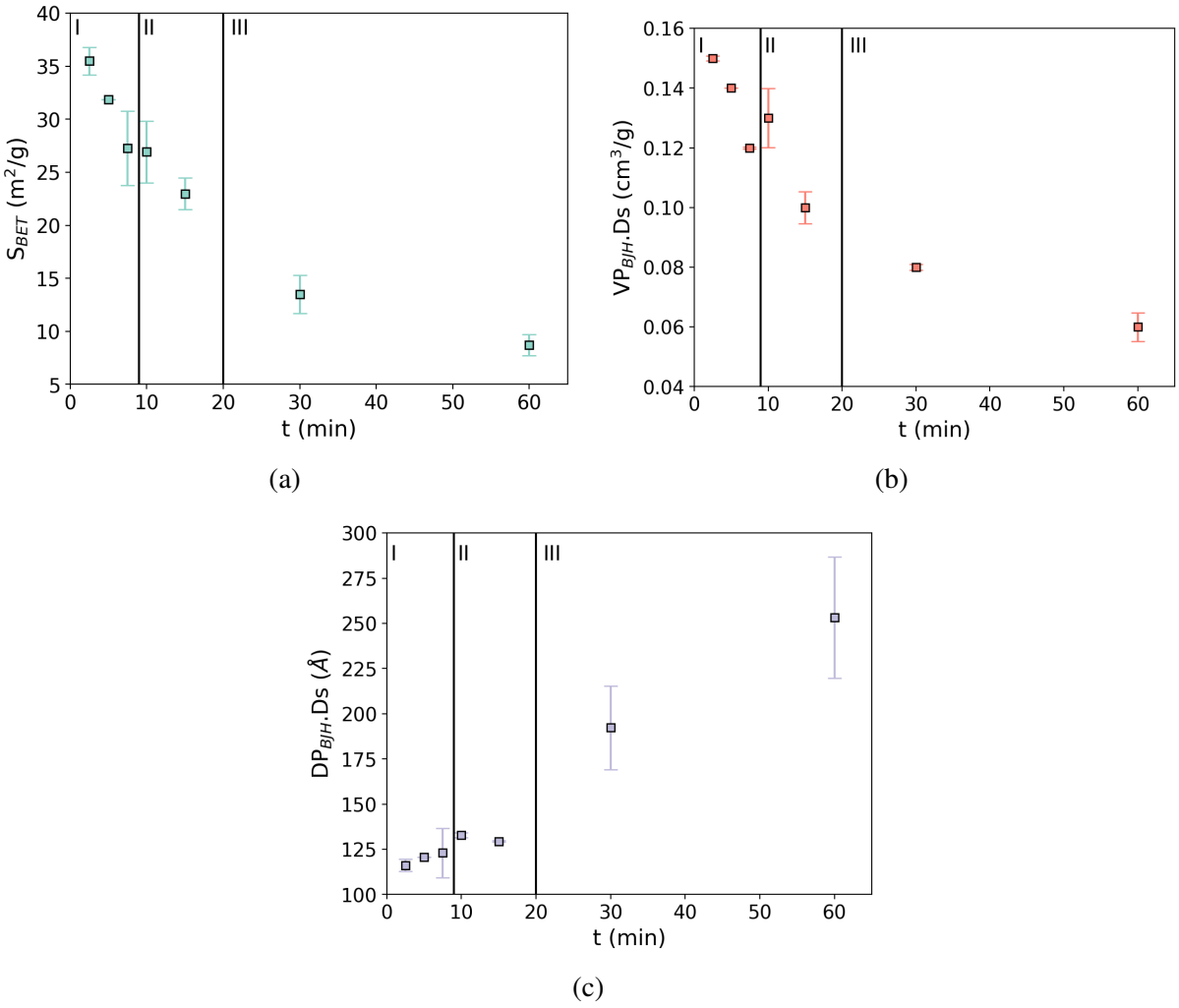

Source: Author

In the subsequent phase (Phase II), 5-minute time increments were employed to enable monitoring of the transition between the kinetic and diffusion-controlled regimes. This adjustment in temporal spacing prevents redundancy in the dataset in regions where changes in the measured response are no longer sharp (GRASA; ABANADES, 2006).

Finally (Phase III), increments of 30 min were applied, a stage in which the reaction rate is significantly reduced and becomes controlled by diffusional mechanisms, associated with the progressive pore blockage. At this point, the reaction's evolution is slow and tends toward an asymptotic regime (BORGWARDT, 1989a).

The BJH method provides data on the pore size distribution by analyzing the desorption and adsorption N_2 isotherms, which is suitable for evaluating mesoporous structures. BJH analysis was used to investigate the progressive blockage of mesopores over time, with the aim of better understanding which pores were closed, the rate at which this occurred, and the underlying mechanisms. Figure 44 presents previous TGA samples in N_2 porosimetry. Two sets of experiments can be seen: Figure 44a presents the results of the higher volume value, and Figure 44b the lower replicate. Even though shape of the curves is consistent for most cases, magnitude of volume tends to differ specially for 7.5, 10, and 60 min samples. This variation is attributed to the heterogeneity of the material, indicating that some particles exhibit a lower pore volume, which is directly related to the morphological structure of the sample (ÁVILA *et al.*, 2012a).

As expected, increasing carbonation time leads to progressive pore blockage. Between 0.0 and 10 min, pore blockage appears to progress uniformly, resembling an exponential decay behavior. From 15 min onward, however, blockage becomes increasingly selective toward the larger pore classes (30–100 Å), resulting in a discernible shift in the pore size distribution toward smaller diameters. Even after 60 min of carbonation, complete pore blockage is not observed—many larger pores remain open, and a measurable volume is still present in the smallest pores when compared to raw dolomite. This observation is consistent with Figure 41, which shows that CO_2 diffusion continues to increase, indicating that the carbonation process is still ongoing.

Figure 44 – Porosimetry pore volume ($cm^3/g{\cdot}Å$) distribution results for 0, 2.5, 5, 7.5, 10, 15, 30, and 60 min of carbonation as a function of time (t). Markers represents original experimental data points while lines represent spline interpolated values: a) Data set with higher volume results; b) Data set with lower volume results;

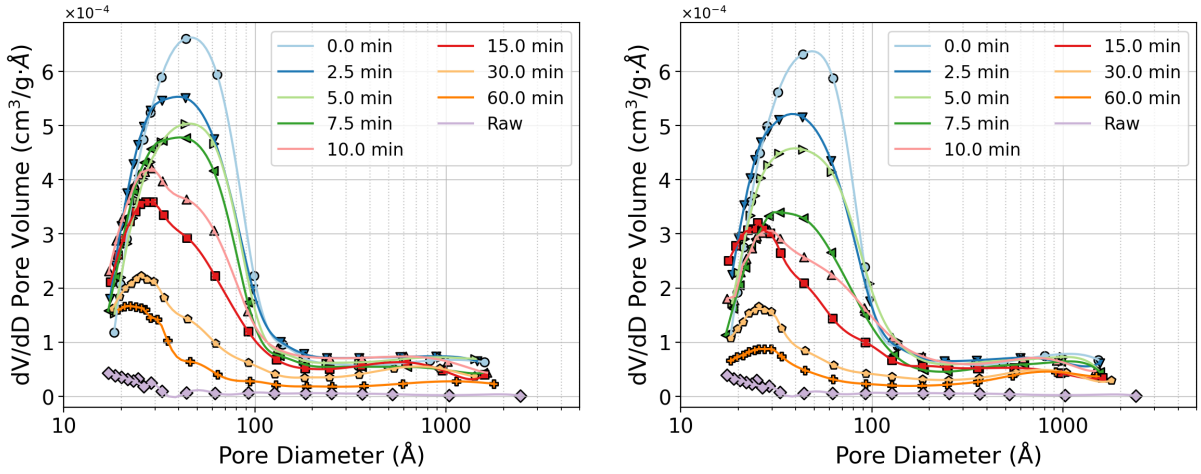

Source: Author

For this dolomite, it can seem that most of the volume of the pores is concentrated in the

range of 17 to 150 Å, with a small portion of the volume in larger pores in the range of 500 to 2000 Å. Compared to similar studies on dolomites reported in the literature, Figure 44 exhibits a markedly different behavior, characterized by smaller pore sizes and a lower pore volume across the measured range (LAURO *et al.*, 2021; SCALTSOYIANNES *et al.*, 2021; TEIXEIRA *et al.*, 2021). Figure 45 shows a comparison of their studies with experimental test with no carbonation.

Figure 45 – BJH pore size distributions of calcined dolomites from the literature (LAURO *et al.*, 2021; SCALTSOYIANNES *et al.*, 2021; TEIXEIRA *et al.*, 2021) compared with the experimental data of this work.

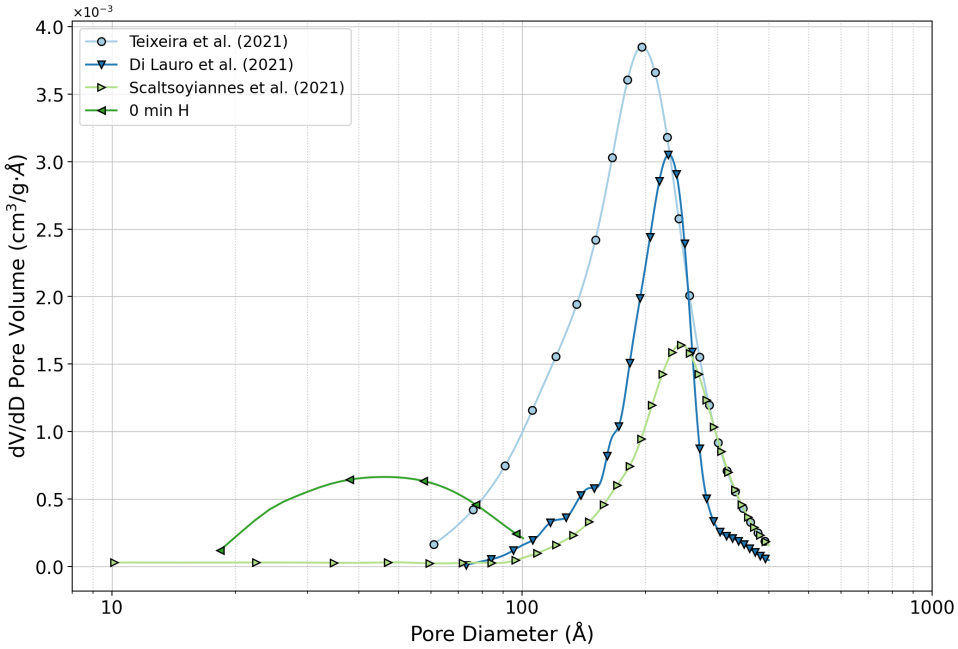

Source: Author

The work of Scaltsoyiannes *et al.* (2021) shows BJH results of calcined dolomite (Ca: 25.86 wt%, Mg: 9.70 wt%, O: 17.03 wt%, LOI:47.03 wt%) within the pore diameter range of 100-500 Å, which is much higher compared to the one used in this work. It is important to note that their carbonation was done in a fluidized bed, which might have affected the pore distribution.

Sun *et al.* (2018) reported that lower mean pore sizes are generally associated with higher carbon capture capacity and improved resistance to decay. In contrast, the present sorbent—despite exhibiting the smallest pore size distribution among those reported in the literature—showed poor performance in both capture capacity and decay resistance (TOLEDO *et al.*, 2025). Di Lauro *et al.* (2021) investigated dolomite for CaL, reporting both higher CO_2 capture capacity and greater pore volume within the 80–500 Å range, assuming the same dolomite source as in their related work (MARROCCOLI *et al.*, 2022). Teixeira et. al. (2021) also reported both higher carbon capacity and pore volume within a pore range of 60-1000 Å.

It is worth noting that the studies by Scaltsoyiannes *et al.* (2021), Di Lauro *et al.* (2021), and Teixeira *et al.* (2021) reported relatively consistent pore diameter distributions and pore volume magnitudes, even though the sorbents originated from different regions. In addition, these works

reported a limited SiO_2 content in their sorbents (up to 0.09 wt% SiO_2). These findings strength our past work conclusion regarding SiO_2 presence in dolomite for CaL, which not only affect carbon capacity but also seems to alters pore structure reducing its volume and limiting pore distribution range (BORGWARDT, 1989b; MANOVIC *et al.*, 2009; TOLEDO *et al.*, 2025).

Although further studies are required to confirm this observation, the results suggest that carbon capture performance may be influenced by the total pore volume available within preferential size ranges. Previous reports have indicated that dolomites with smaller minimum pore sizes (60 Å and 80 Å, respectively) exhibit better resistance to decay (SUN *et al.*, 2018); however, this trend could not be confirmed, as the 17–100 Å distribution observed in this work did not show improved resistance to decay. These results indicate that pore size alone does not have a direct relationship with decay resistance, suggesting that additional parameters play a controlling role and warrant further investigation.

4.3.2.3 Pore distribution deformation analysis

Figure 46 presents a fresh carbonation sample alongside with sum of pore volume and pore distribution deformation over carbonation time. Total pore volume present a inverted exponential curve, reducing pore volume rapidly for the first 15 min and then slowly decreasing. A expected behavior that agree with carbonation reactions phases. In both Figure 46a and Figure 46b at 5 min mark it is possible to observe a step change of angle which marks precisely with the end of fast phase carbonation. The deformation curve present a stable distribution (very stable for Figure 46a) and a abrupt change of angle, which further agree with the previous statement. Being Figure 46b related to Figure 44b and presenting smaller volume, a faster change of phase is expected and might explain the difference between both distribution. This analysis indicates that the end of fast phase reaction for this setup occurs between 5-7.5 min of carbonation and fast reaction phase duration is directly proportional to pore volume in 30-100 Å range of pore diameter. This affirmation is further reinforced as increasing pore distribution deformation continue to occur and little effect is observed in capture capacity. Indicating that major loss in efficiency is caused by the closure of 30-100 Å pores.

4.3.3 Pore blockage correlation

Figure 47 provides a direct fit of the data shown in 44a. This was accomplished using a nonlinear least-squares optimization via the *curve_fit* function in conjunction with the *beta.pdf* probability density function. The resulting fit for carbonation times between 0 and 60 min is assessed based on the R^2 value, which quantifies the model's quality of fit. The Beta PDF provides a satisfactory fit to the observed data, showing R^2 higher than 90% for every carbonation time. While the preferential closure effect on pore diameters induces a noticeable deformation in the model's shape, the overall representation of the data remains robust. Table 11 presents the parameters used in both Figure 44a and Figure 44b datasets, referenced as H and S, respectively.

Figure 46 – A three y axis plot presenting: Total pore volume ($cm^3/g \cdot Å$), fresh dolomite sample (X%), and pore distribution deformation (-) over carbonation time. a) Data set with higher volume results (H); b) Data set with lower volume results (S);

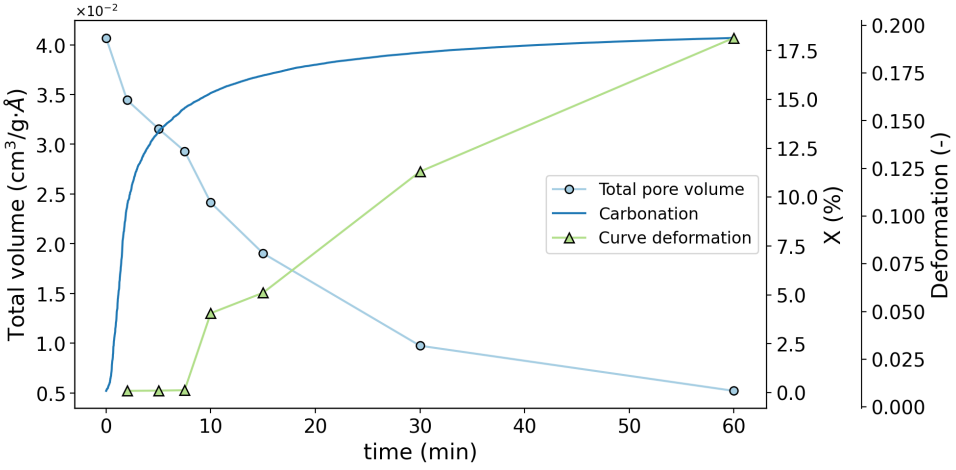

(a)

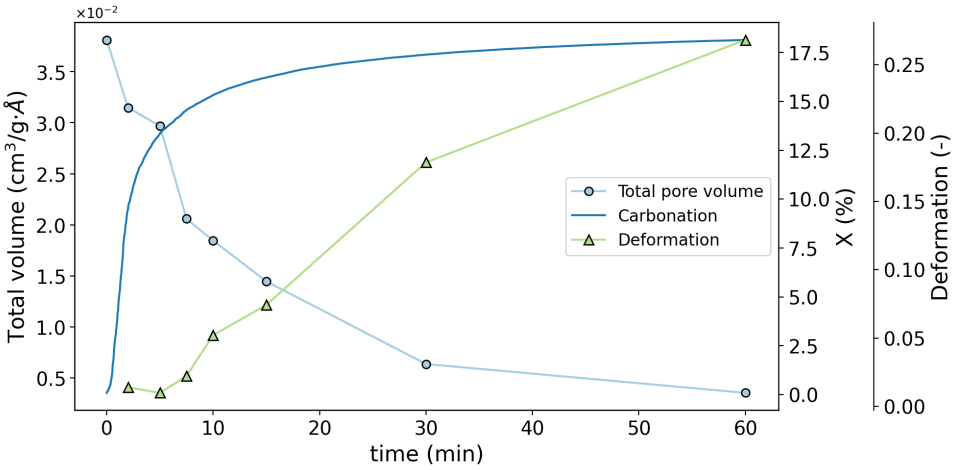

(b)

Source: Author

Figure 48 presents the parameters in graphical form, together with the selected fitting expressions. The parameter α exhibited a decaying exponential trend, asymptotically approaching 1. This behavior suggests a stronger influence of pore closure at larger diameters, since α governs the upper end of the probability density function ($x = 1$). When $\alpha = 1$, the probability contribution associated with this parameter becomes constant, which may indicate the cessation of the mechanism controlling large-pore blockage. Notably, α stabilizes at around 40 min of carbonation, consistent with the TGA curve in Figure 46. This alignment suggests that the mechanism responsible for closing the larger pores may be completed by this time. Beyond 40 min, another mechanism likely dominates, as CO_2 uptake continues up to 60 min according to both the TGA results and the behavior of β.

Figure 47 – Beta PDF distribution fittings to Figure 44a data showing spline model in markers, and Beta function in lines.

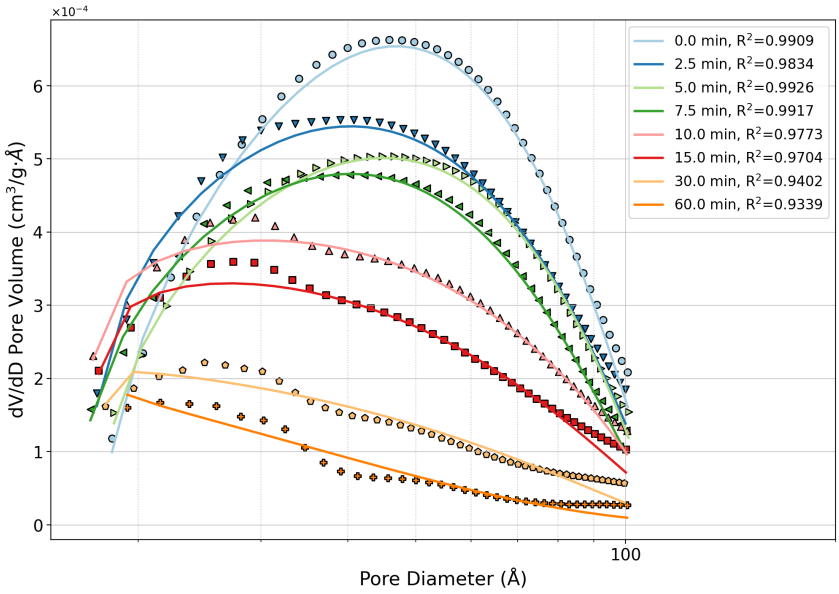

Source: Author

Table 11 – Beta PDF distribution fitted to both Figure 44a and Figure 44b data showing R^2 as fitting performance and shape (α, β) and scale (weight) parameters.

Reference	R^2	α	β	weight
0 min H	0.9909	1.5446	2.2909	0.0410
2 min H	0.9834	1.3599	2.1696	0.0348
5 min H	0.9926	1.4451	2.1166	0.0318
7.5 min H	0.9917	1.4303	2.3615	0.0296
10 min H	0.9773	1.1526	1.9801	0.0245
15 min H	0.9704	1.1309	2.3571	0.0194
30 min H	0.9402	1.0160	2.3875	0.0099
60 min H	0.9334	0.9724	6.3457	0.0054
0 min S	0.9942	1.6058	2.3521	0.0384
2 min S	0.9867	1.3126	2.1250	0.0319
5 min S	0.9714	1.2864	1.7690	0.0300
7.5 min S	0.9141	1.2334	2.1279	0.0208
10 min S	0.8473	1.0795	1.4747	0.0188
15 min S	0.9296	1.0102	2.2645	0.0148
30 min S	0.8736	1.0207	3.0478	0.0065
60 min S	0.8991	1.0161	3.1486	0.0036

Source: Author

In contrast to α, the parameter β exhibited a semi-steady value between 0 and 10 min, followed by a steady increase. Since β governs the left-hand side of the PDF, values greater than 1 shift the distribution toward smaller diameters, as the mean pore size follows:

$$\mathbb{E}[D] = \frac{\alpha}{\alpha + \beta}$$

This shift corresponds to the peak displacement observed from 10 min onward in Figure 44. The continuous increase of β suggests that CO_2 capture remains active, although driven by a different mechanism.

Figure 48 – Shape and scale parameters from beta PDF fitting with exponential and linear models: (a) α (exponential); (b) β (linear); (c) $s(t)$ = weight × scale (exponential).

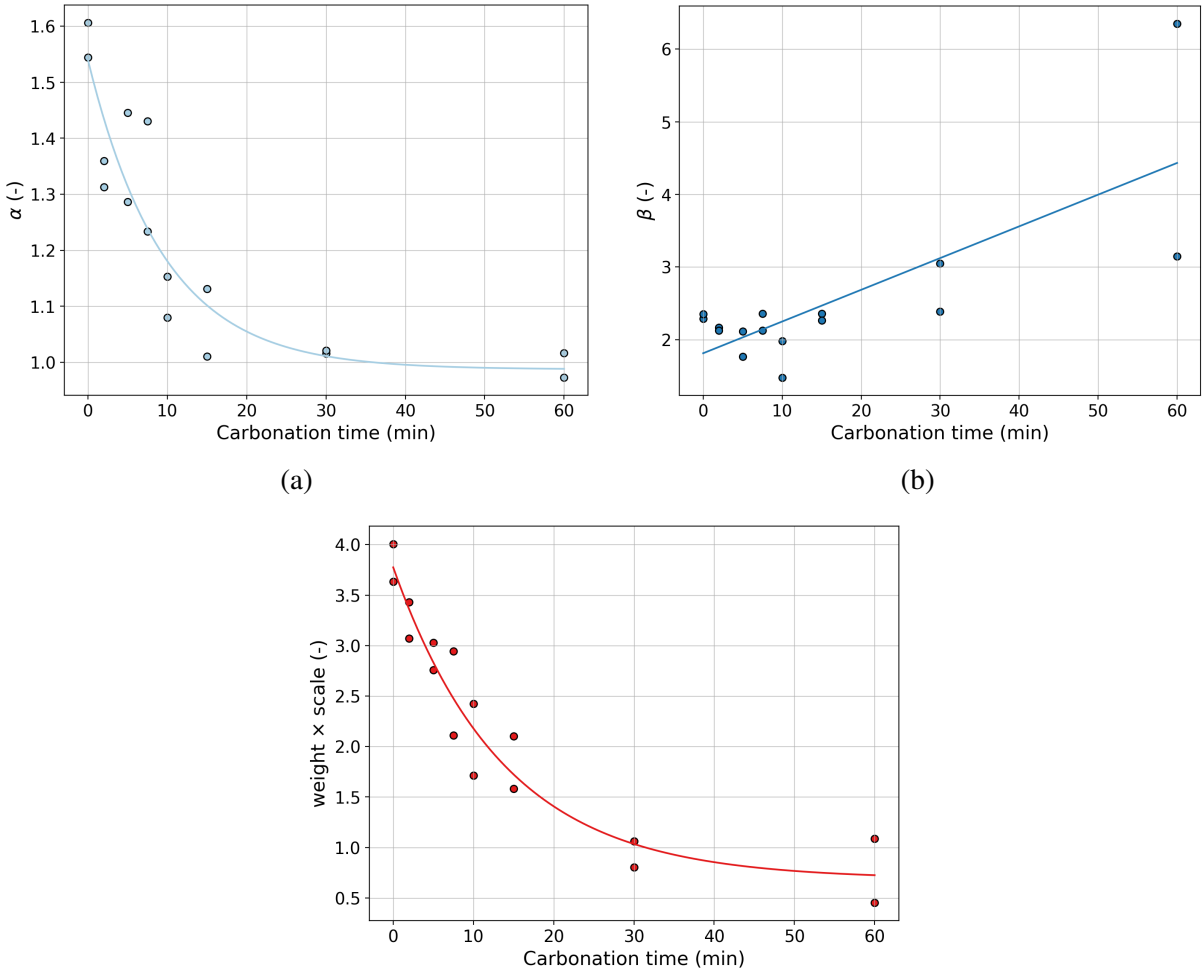

Source: Author

Both the 'loc' and 'scale' parameters represent the distribution's position and scaling factor. Since these values provide limited insight into the phenomenon, they are not displayed; however, their mean values are 17.8 and 108.6, respectively.

The s(t) function (weight × scale) reflects how the height of the distribution decreases, which can be interpreted as the rate of pore closure. This decaying exponential trend aligns with the TGA and pore volume curves in Figure 46. The sharp pore volume loss observed up to 7.5 min—highlighted by the KL curve—corresponds to the region of highest capture performance for this dolomite, where pores between 35 and 75 Å contribute most significantly. Understanding why pores in this range preferentially close, what controls their total available volume, and how

to extend this range could be crucial for enhancing sorbent performance in CaL.

The parameters equations from Figure 48 can be found on Table 12 and if we arrange the proposed equations for α, β, and s(t) into the beta PDF function, we have Equation 4.4, where D is the pore diameter in Å and t the carbonation time in min.

Table 12 – Parameters expression to be used with the proposed correlation, Equation 4.4.

Parameter	Expression
β(t)	0.0436t + 1.814
α(t)	0.552exp(-0.105t) + 0.987
s(t)	3.09exp(-0.073t) + 0.686

Source: Author

$$f(D;t) = s(t)\frac{\Gamma(\alpha(t)+\beta(t))D^{\alpha(t)-1}(1-D)^{\beta(t)-1}}{\Gamma(\alpha(t))\Gamma(\beta(t))}, \quad 15 < D < 100\ \text{Å}, t \geq 0\ \text{min} \tag{4.4}$$

Figure 49 shows the pore blockage correlation fitted to the data from Figure 46a. As expected, the predictive performance is reduced, since the correlation was intended only as an approximate representation of the blockage rate. Nevertheless, it provides a useful reference for analyzing this dolomite.

Figure 49 – Correlation distribution fittings to Figure 44a data showing spline model in markers, and the new correlation in lines.

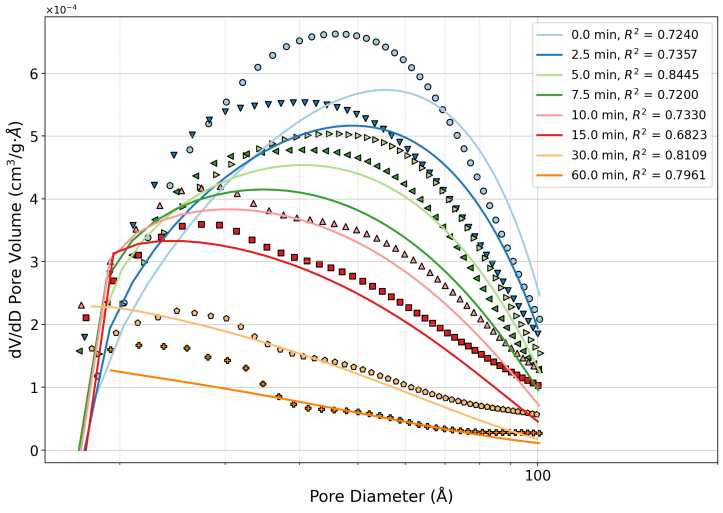

Source: Author

4.4.1 RCCD response variables

Response variables were energy spent (E_{sp}) and mass of CO_2 captured ($CO_{2\,cap}$), and those obtained from the RCCD model are shown in Table 13. It can be observed that shorter residence times (t) and lower temperatures (T) indicate less energy consumption, as expected. $CO_{2\,cap}$ was greater for TGA-4, TGA-5, TGA-10 and TGA-12, reaching 1.72, 1.44, 1.43, and 1.51, respectively. The ratio between $CO_{2\,cap,n}$ and $E_{sp,n}$ was consistent with the results presented above, and higher values were also found for TGA-4, TGA-5, TGA-10 and TGA-12, and their IEC was 1.01, 0.88, 0.83 and 0.89, respectively. On other hand, TGA-1, TGA-2 and TGA-11 had low $CO_{2\,cap}$ and IEC values. From Table 13, it is possible to generate a response surface model

Table 13 – Optimization TGA-RCCD experimental results showing initial parameters: time and temperature, and experimental results: calcined mass (m_{calc}), carbonated mass after calcination (m_{carb}), mass of CO_2 ($CO_{2\,cap}$), energy spent (E_{sp}), normalized mass of CO_2 ($CO_{2\,cap,n}$), normalized ($E_{sp,n}$), and ratio of normalized CO_2 by energy spent (IEC)

Test name Unit	t [min]	T [°C]	m_{calc} [mg]	m_{carb} [mg]	$CO_{2\,cap}$ [mg]	E_{sp} [kJ]	$CO_{2\,cap,n}$ [-]	$E_{sp,n}$ [-]	IEC [-]
TGA-1	5	400	6.10	6.45	0.35	8.04	0.20	0.93	0.22
TGA-2	10	400	6.04	6.53	0.49	8.26	0.28	0.96	0.29
TGA-3	5	550	6.04	6.99	0.95	8.16	0.55	0.95	0.58
TGA-4	10	550	5.90	7.62	1.72	8.52	1.00	0.99	1.01
TGA-5	7.5	475	5.87	7.31	1.44	8.26	0.84	0.96	0.88
TGA-6	7.5	475	5.87	7.18	1.31	8.29	0.76	0.96	0.79
TGA-7	7.5	475	6.11	7.33	1.22	8.35	0.71	0.97	0.73
TGA-8	7.5	475	5.82	7.19	1.37	8.29	0.80	0.96	0.83
TGA-9	4	475	6.82	7.66	0.84	8.03	0.49	0.93	0.53
TGA-10	11	475	6.26	7.69	1.43	8.60	0.83	1.00	0.83
TGA-11	7.5	370	6.33	6.66	0.33	8.14	0.19	0.95	0.20
TGA-12	7.5	580	6.05	7.56	1.51	8.50	0.88	0.99	0.89

Source: Author

as presented in the methodology, while Table 14 present the experimental interval. Equation (4.5) describes its results in which t is a variable representing residence time (t/min) and carbonation temperature (T/°C).

$$IEC = -6.49 + 2.67E^{-2}t + 2.61E^{-2}T - 1.39E^{-2}t^2 - 2.77E^{-5}T^2 + 4.80E^{-4}tT \quad (4.5)$$

Figure 50 and Figure 51 present the response surface plots and contour lines related to Equation (4.5), respectively. It is possible to observe a curved response surface, indicating a region of maximum response for IEC. The contour lines allow identifying the peak region with

Table 14 – Uncertainty interval for each measured response variable

Parameter	Accuracy
$E_{\,sp}$ [kJ]	$\pm$ 0.05
$CO_{2\ cap}$ [mg]	$\pm$ 0.13
$E_{\,sp,n}$ [-]	$\pm$ 0.01
$CO_{2\ cap,n}$ [-]	$\pm$ 0.08
IEC [-]	$\pm$ 0.09

Source: Author

greater precision, which is located between 7.3 to 11 min and between temperatures of 490 to 580 °C.

Figure 50 – Response surface plot of IEC experimental data by time and temperature, based on Equation (4.5).

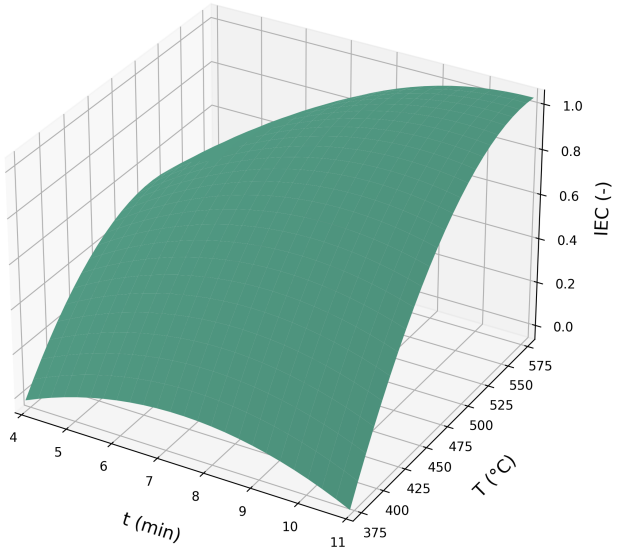

Source: Author

Concerning response variable, IEC, had excellent performance on TGA-4, TGA-5, TGA-10, and TGA-12, as it can be seen on Table 13. However, as shown in Table 14, tests have equivalent efficiency by adding estimated accuracy intervals. Such deviation is expected since the sample has open particle size in a wide particle size range. This hinders the replication of the same distribution using a small 10 mg alumina crucible. This phenomenon is observed at central points of the experimental design where IEC, for example, varies from 0.73 to 0.88. Furthermore, the sample consists of three original rock types with distinct compositions, as shown in Figure 34,

which presents XRF analysis results for white, gray, and dark gray particles. These particles visually correspond to three different rock colors observed at larger particle sizes.

Thus, although care was taken to ensure that particle size distribution was represented within the crucible, it is unlikely that the chemical composition of each test could be replicated according to Figure 34. Despite the variability presented, the sample in question simulates a real use of dolomite in application.

Figure 51 – Response surface plot contour lines of IEC experimental data by time and temperature, based on Equation (4.5).

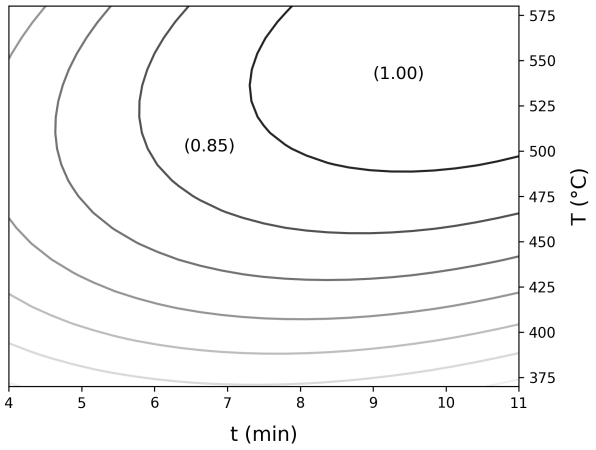

Source: Author

Table 15 present ANOVA results, which revealed that the quadratic model was statistically significant (p = 0.001), with T showing the strongest effect (F = 41.91, p < 0.001). Both linear and quadratic terms for temperature (T, T^2) were highly significant (F = 41.91 and 32.93 respectively, $p \leq 0.001$), t and its quadratic term demonstrated to be significant as well, but having weaker effects (F = 14.98, p = 0.008 and F = 10.23, p = 0.019). The time-temperature interaction (t×T) was marginally significant (F = 7.08, p = 0.038). The lack-of-fit test (p = 0.423) confirmed the model adequately fit the experimental data. Table 15 shows the ANOVA results for the IEC model, from Equation (4.5).

Despite the extrapolation experiments ($\pm$ 1.4) used in RCCD, it was impossible to cross the upper limit of carbonation so that calcination reaction becomes predominant, and a reduction in capture efficiency was expected for carbonation temperature, since different particle sizes should have different calcination temperatures (VALVERDE; SANCHEZ-JIMENEZ; PEREZ-MAQUEDA, 2014b). The use of the proposed model is limited to temperatures outside the evaluated ranges, especially higher ones.

Variability in composition and particle size distribution might not have been fully captured by replicates at central points. Open particle size samples are challenging to represent small quantities accurately, as required by instruments such as thermogravimetric balances. To address this issue, a new investigation is proposed by using a system capable of handling larger sample

masses, combined with the quartering method and an increased number of replicates.

Table 15 – ANOVA analysis of Equation (4.5)

Source	DF	Adj. SS	F-value	p-value
Model	5	0.4905	21.47	0.001
Linear	2	0.2605	28.45	0.001
t	1	0.0686	14.98	0.008
T	1	0.1919	41.91	0.001
Square	2	0.1976	21.58	0.002
t^2	1	0.0469	10.23	0.019
T^2	1	0.1508	32.93	0.001
2-Way Int.	1	0.0324	7.08	0.038
$t \cdot T$	1	0.0324	7.08	0.038
Error	6	0.0275	-	-
Lack-of-Fit	3	0.0154	1.28	0.423
Pure Error	3	0.0121	-	-
Total	11	0.5190	-	-

Source: Author

4.4.2 Multi-cycle calcination–carbonation process

Table 16 shows the results achieved from those presented in Table 13 for the multi-cycle path condition. It is possible to observe that the best responses were found at higher temperatures.

Table 16 – RCCD results for tests TGA-2, TGA-4, TGA-5, TGA-10 and TGA-12 from Table 13 for 10 cycles of carbonation

t [min]	T [°C]	$CO_2 cap$ [mg]	E_{sp} [kJ]	$CO_{2\ cap,n}$ [-]	$E_{sp,n}$ [-]	$IEC_{10,c}$ [-]
10	400	3.42	45.93	0.35	1.00	0.35
7.5	475	6.44	39.91	0.66	0.87	0.76
11	475	6.42	43.15	0.66	0.94	0.70
10	550	9.80	37.97	1.00	0.83	1.20
7.5	580	9.61	33.48	0.98	0.73	1.34

Source: Author

Figure 52a shows TGA-2 for the cycle condition presenting a slight initial capture of around 0.4 (mg) and similar degradation behavior of other conditions. The tests at 370 and 400 °C are unsuitable for real-world applications due to its extremely low mass capture. Figure 52a supports this observation, showing that despite having achieved low capture capacity, the deactivation effect remains significant, even at reduced temperatures. This effect alone rules out

the possibility of improving the number of cycles through reduced temperatures, which might have been beneficial considering the emissions associated with transporting make-up dolomite. Instead, the findings suggest that operating conditions with higher capture capacities and shorter residence times could be more emission-efficient, even if they increase the material make-up ratio. However, confirming this hypothesis would require further investigation on a large-scale fluidized bed considering factors such as particle fragmentation and the net emissions of the process.

Figure 52 – 10 cycle reaction at 400 °C, 550 °C and 580 °C at a given carbonation time: (a) Test TGA-1 was carbonated at 400 °C for 10 min; (b) Test TGA-4 was carbonated at 550 °C for 10 min; (c) Test TGA-12 was carbonated at 580 °C and residence time of 7.5 min

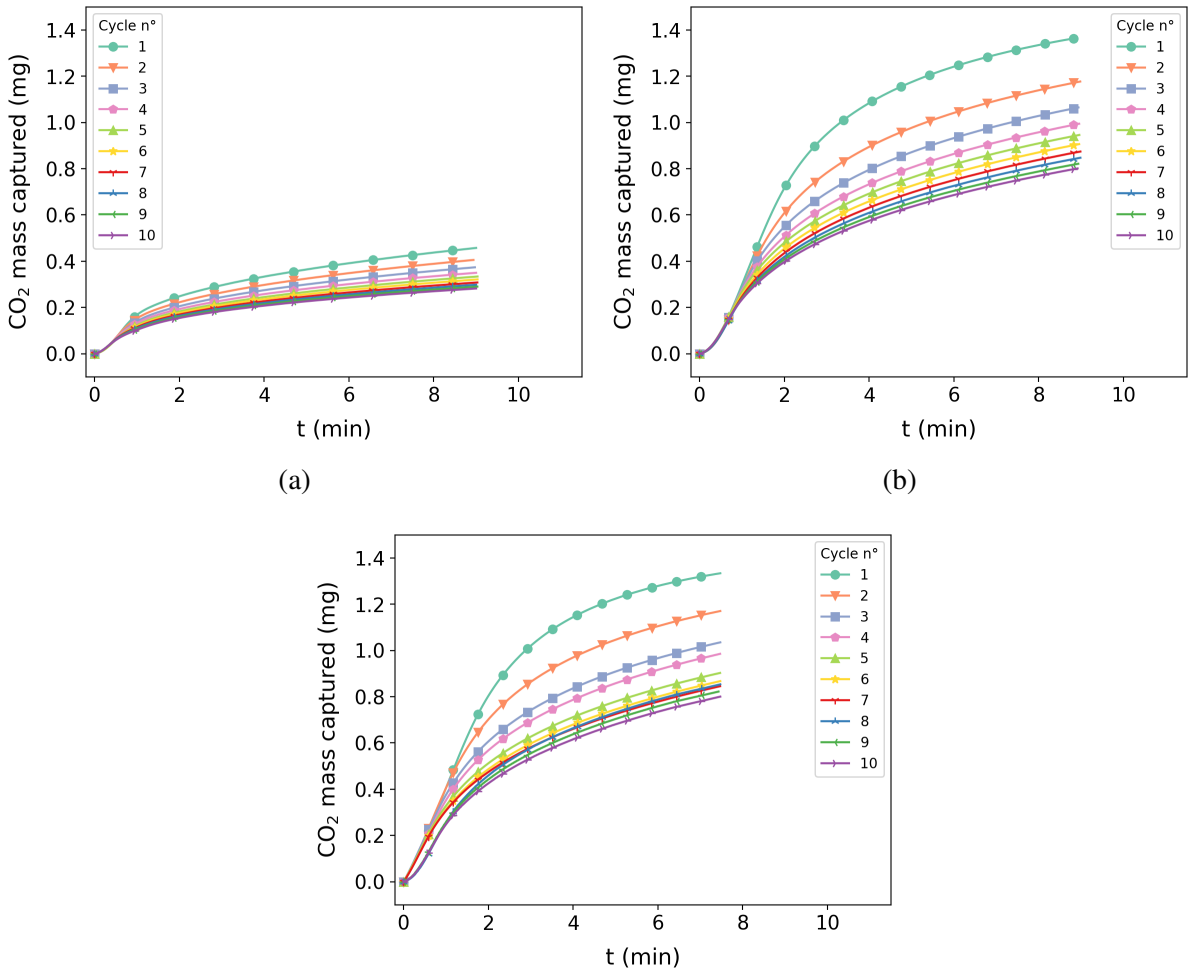

Source: Author

Figure 53c shows an intact surface with few temperature cycling marks resembling natural dolomite (MEDINA-CARRASCO; VALVERDE, 2022; SÁNCHEZ-JIMÉNEZ *et al.*, 2016; SU *et al.*, 2019), which might indicate that larger particle was unable to react due to a low temperature. This mechanism is attributed to the amount of defects associated with smaller

particle size which reduces the temperature necessary for the reaction (VALVERDE; SANCHEZ-JIMENEZ; PEREZ-MAQUEDA, 2014b), i.e. carbonation. When dealing with open partible size samples in calcium looping, it seems pertinent to maintain a carbonation temperature high enough to allow most particles to react.

Figures 54a and 54b present the cycles for TGA-5 and TGA-10, respectively. It is possible to observe in both images that there was great capture performance in the first cycle and loss of efficiency in the following cycles with a slight difference on the degradation pattern during each cycle. 475 °C samples show similar capture performance and energy efficiency, as in Figure 54. Figures 54a and 54b show the cycles for TGA-5 and TGA-10, respectively. In both figures, a high capture performance is observed in the first cycle, followed by a decline in efficiency in subsequent cycles, with only minor differences in the degradation pattern between cycles. The samples at 475 °C exhibit comparable CO_2 capture capacity and energy efficiency, as shown in Figure 54. Overall, the cycling behavior is consistent in terms of both total CO_2 captured and the degree of performance deterioration over successive cycles.

Figure 52b and Figure 52c shows TGA-4 and TGA-12, respectively. It can be observed a similar performance with mass capture above 1.2 (mg) for both tests. A similar pattern of degradation can be seen with a slight difference on test 12 after the fifth cycle.

Figure 54 – 10 cycle reaction of 475 °C samples: (a) Test TGA-5 for carbonation at 475 °C and residence time of 7.5 min; (b) Test TGA-10 for carbonation at 475 °C and residence time of 11 min

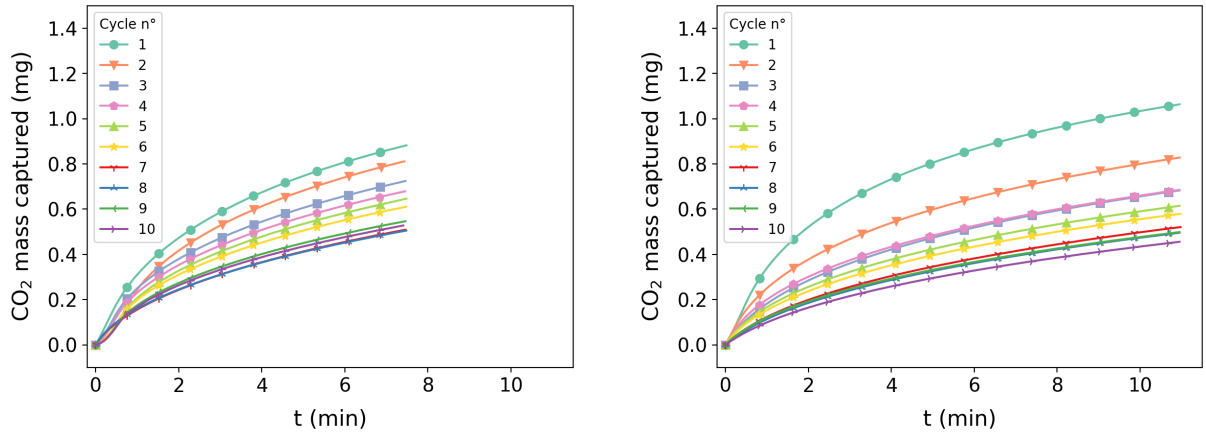

(a) (b)

Source: Author

The morphological structures of dolomite were investigated using TGA-2, TGA-4, TGA-5, TGA-10 and TGA-12 shown in Table 15, respectively. Figure 53 depicts SEM images of multi-cycle tests at 5000x magnification.

Samples at 580 °C and 550 °C showed the best $CO_2 cap$ results which, given the uncertainties, present the same $CO_2 cap$ value and energy efficiency for the RCCD experiments, respectively. The surface shown by Figure 53e has a uneven appearance without sharp corners, unlike other

Figure 53 – SEM images of all multi-cycle samples: (a) TGA 5 – 475 °C and 7.5 min; (b) TGA 10 – 475 °C and 11 min; (c) TGA 2 – 400 °C and 10 min; (d) TGA 4 – 550 °C and 10 min; (e) TGA 12 – 580 °C and 7.5 min

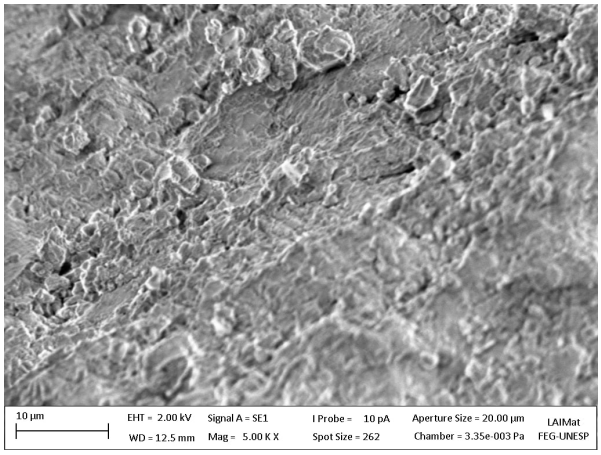

(a)

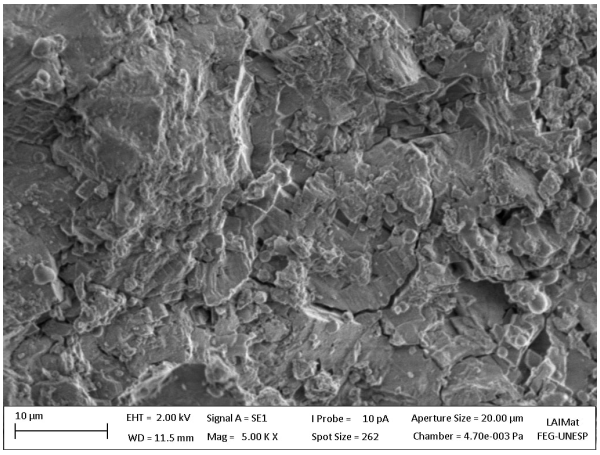

(b)

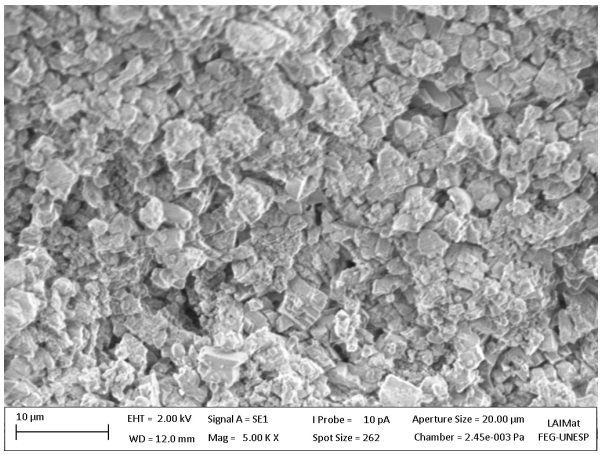

(c)

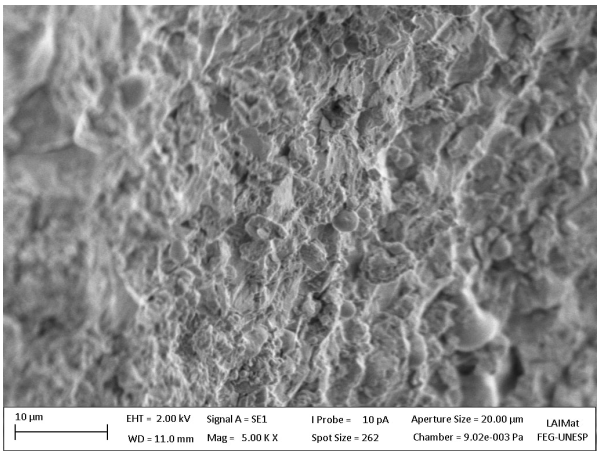

(d)

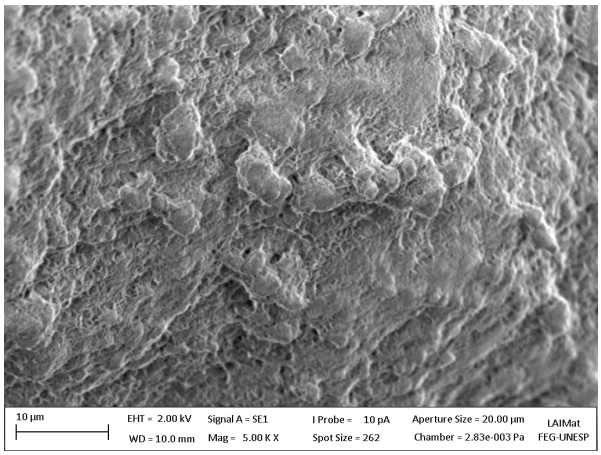

(e)

Source: Author

images. If compared to Figure 53d, the surface of Figure 52c shows fewer irregularities, appearing to be more deteriorated. Sample at 580 ºC with 10 cycles was the only one showing signs of sintering by a visual analysis.

The degradation curves corresponding to tests in Table 16 are shown in Figure 55. All tests exhibit a decay in efficiency, regardless of time and temperature differences.

When analyzed solely by CO_2cap, Figure 55 exhibits a characteristic decay curve of deactivating limestone/dolomite, which is consistent with findings in literature (CONTE *et al.*, 2023; VALVERDE; SANCHEZ-JIMENEZ; PEREZ-MAQUEDA, 2014; VALVERDE; SANCHEZ-JIMENEZ; PÉREZ-MAQUEDA, 2015), including studies conducted on setups of different scales (COPPOLA *et al.*, 2013a). Temperature appears to influence degradation, as lower-temperature curves exhibit a smoother transition from the initial high-capacity cycle to a steady deactivated state. However, this effect is negligible compared to the overall loss of capture capacity due to temperature differences. Notably, even at the 10th cycle, higher-temperature conditions still achieve greater capture efficiency than the first cycle under lower-temperature conditions.

Figure 55 – Deactivation curves presenting CO_2 mass capture in mg by cycle number. Corresponding to the tests presented in Table 16

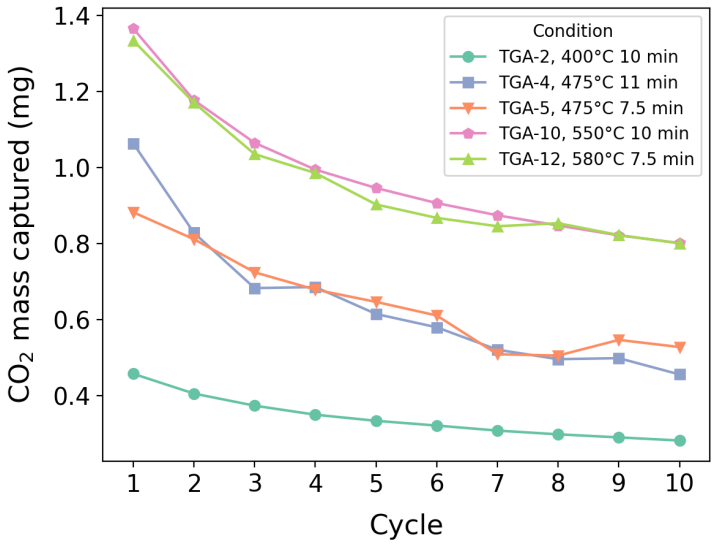

Source: Author

These results, along with Table 16, suggest that while an optimal zone may have been identified in the initial analysis, a multi-cycle perspective indicates that the most effective strategy for CO_2 capture is to operate at the highest possible temperature without inducing calcination. However, such a conclusion requires validation in larger-scale setups, as the shape of the deactivation curve may be influenced by increased carbon capture as well as elutriation and fragmentation effects due to fluidization (COPPOLA *et al.*, 2013; COPPOLA *et al.*, 2020).

Regarding residence time, longer residence makes a relevant impact in the total energy spent when compared to temperature, and this impact is related to the carbonation reaction. This result

emphasizes that residence time must be found using others means (PEREJÓN *et al.*, 2016). Although increasing residence time enhances the efficiency of carbon capture following the fast reaction phase, the most efficient conditions appear to result from an optimal combination of carbonation temperature and residence time. Both parameters influence surface degradation and elutriation (CHARITOS *et al.*, 2010; DUELLI *et al.*, 2015b; TREGAMBI *et al.*, 2018), which in turn impacts the requirement for the make-up material in the reactor, contributing to additional emissions from its transport and preparation.

One factor contributing to a high value of IEC for elevated temperatures in this experimental configuration is the fact that the majority of process energy was spent in the calcination stage. Thus, the energy required to heat up to 800 °C from 580 °C is lower than those in other conditions, therefore it has the lowest energy consumption among all conditions. This suggests the need to repeat this analysis on dual fluidized beds, which are commonly used configurations in calcium looping plants.

4.5 STUDY OF CALCIUM LOOPING WITH A FLUIDIZED BED REACTOR

The experimental campaign was completed successfully, despite delays associated with the certification procedures required for accessing and operating the facility where the DIFB was installed. The material sample exhibited extensive fragmentation under all tested conditions, which compromised several components of the planned methodology. During the first cycle of each calcination, the filters were frequently completely or partially obstructed, even when multiple filters were employed, rendering it impossible to retain the entirety of the elutriated material. It was reported that the observed degree of fragmentation was unprecedented in prior investigations.

Table 17 presents the RCCD (rotatable central composite design) associated with the carbon capture configuration proposed in the methodology. Due to complications from Brazilian dolomite behaviour, one central point was omitted, thereby reducing the number of replicated runs from the original four to three. In Table 17, m_0 denotes the initial sample mass, whereas $m_{f,s}$ represents the sieved sample mass measured after the experimental cycles.

The measurement uncertainty is presented in Table 18, which indicates a high degree of consistency in the experimental data. The most favorable operating condition identified was DIFB-8, characterized by the lowest gas velocity tested (0.23 m/s) and a central-point temperature of 675 °C. Under this condition, the response value was more than twice that obtained for the next best condition. Although this result is robust, the higher capture efficiency is also attributable to the reduced gas flow velocity, which provides a longer residence time for the gas to react with the sorbent.

No carbonation was observed under any of the conditions at 750 °C and above. This behavior can be attributed to the combined effects of pressure and elevated temperature, which shift the thermodynamic equilibrium toward the calcination reaction (BLAMEY *et al.*, 2010a). Test

DFIB-11 was not conducted due to the unavailability of the equipment during the experimental campaign. In this case, the initial and final masses were estimated by linear regression based on the available experimental data.

Table 17 – Experimental results data for DIFB equipment presenting parameters: Velocity and temperature, and results: Carbon capacity (ξ, Equation 3.13), initial mass (m_0) and spent mass after cycle ($m_{f,s}$)

Test name	Velocity (m/s)	Temp. (°C)	m_0	$m_{f,s}$	ξ_{mean}
DIFB-1	0.30	600	19.8833	8.6723	0.0067
DIFB-2	0.70	600	20.0000	8.5008	0.0092
DIFB-3	0.30	750	20.0000	9.1199	0.0000
DIFB-4	0.50	750	21.6500	10.8000	0.0000
DIFB-5	0.50	675	20.0000	8.7381	0.0113
DIFB-6	0.50	675	22.8489	9.4662	0.0106
DIFB-7	0.50	675	21.0000	12.8500	0.0096
DIFB-8	0.23	675	20.2500	6.1300	0.0177
DIFB-9	0.78	675	19.9000	10.2500	0.0116
DIFB-10	0.50	570	20.0300	11.7592	0.0083
DIFB-11	0.50	780	21.8290*	10.8570*	0.0000

*Note: estimated values

Source: Author

Table 18 – Interval measurement for ξ_{mean} in Table 17

Test	ξ_{mean}
DIFB-5	0.0113
DIFB-6	0.0106
DIFB-7	0.0096
Std	0.0007
Mean	0.0105
interval	0.0015

Source: Author

Figure 56 presents degradation curves of all tested samples for 10 cycles. The shape of the decay in carbon capture curve is a typical CaL curve with high values of ξ for the first and second cycle, followed by a characteristic decay and stabilization.

Dolomite are reported to have a less step curve of decay, associated with their higher cycle capacity (COPPOLA *et al.*, 2012a; COPPOLA *et al.*, 2013a; COPPOLA; SCALA; SALATINO, 2018), however this sorbent showed a limestone like behavior. If compared to other studies, the best ξ of first cycles found in this study is 0.09 while for limestone in similar conditions and same setup this value could reach up to 0.21 (COPPOLA *et al.*, 2013a). A pondering point in

this analysis is the calcination time applied (10 min), according to Figure 57, a time longer than 10 min would be necessary to complete the calcination reaction. However, considering tests wore conducted in a fluidized bed which has a higher heat and mass transfer and samples were dropped directly at temperature of 940 °C instead of a heating ramp, 10 min might have been enough time for complete calcination.

While this is expected, as Mg and Si contents do not contribute to carbon capture, the stabilization is reached in about five cycles for both dolomite and limestone. In this experiment, the measured values were approximately 50% lower than those reported for limestones in comparable studies (COPPOLA *et al.*, 2013a). Dolomites are find to be more resistant to abrasion and elutriation inside the reactor due to Mg content acting as reinforcing structure which hold the fragments longer if compared to limestone (which presents Ca content usually higher than 95%) (VALVERDE; SANCHEZ-JIMENEZ; PÉREZ-MAQUEDA, 2015). However, no such affect in deactivation was observed in this investigation.

Figure 56 – Experimental results of DFIB system for RCCD planning presenting degradation curves from Table 17 tests: Carbonation temperature 570-780 °C, Fluidization velocity 0.23-0.78 m/s, sample mass of 20 g

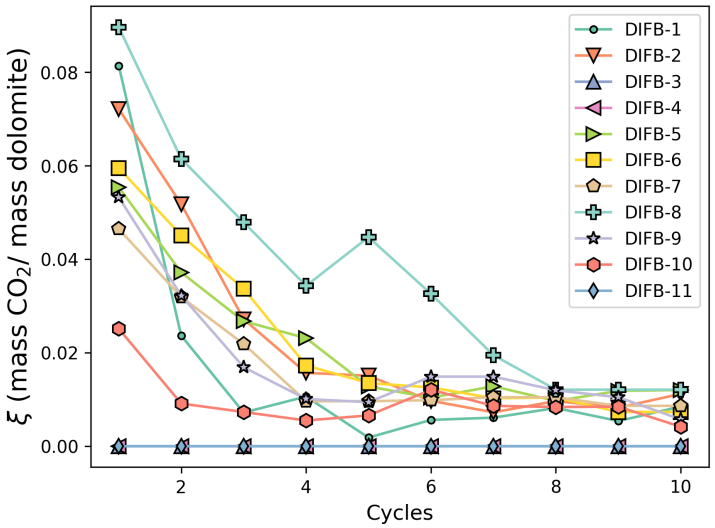

Source: Author

Coppola (2013b) investigated dolomite using the same experimental setup and comparable operating conditions, including identical fluidization velocities and sample mass, with the main differences being the higher CO_2 concentration in the carbonation atmosphere and the elevated temperature. In their study, Coppola (2013b) reported a higher ξ in the first cycle, which is consistent with the use of a 15% CO_2 atmosphere. Figure 37 demonstrates that the influence of the CO_2 partial pressure on CO_2 capture is pronounced for limestone, whereas it appears to be negligible for dolomite. This behavior may be attributed to the higher temperature (1000 °C for calcination) employed in their methodology, which likely caused degradation of the particle

surface and consequently reduced its CO_2 capture capacity. At lower calcination temperatures, dolomite would be expected to exhibit performance more comparable to that of limestone.

Figure 57 – Calcination of a fresh dolomite with mean diameter of 500 μm under atmosphere of 30%air-70%CO_2, ramp rate of 20 °C min to 940 °C and isothermal of 1 h

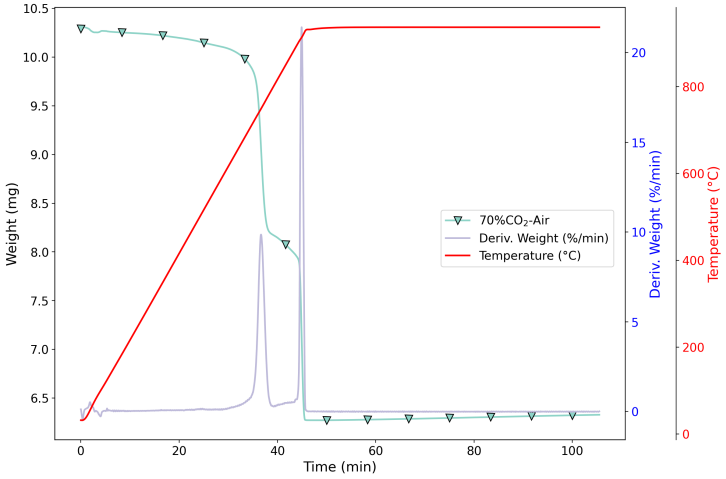

Source: Author

The degradation curve difference between this sorbent to Coppola (2013b) work is very particular. While Coppola (2013b) show an almost linear decrease of its ξ, the sorbent used in this work behaves almost as a limestone presenting a characteristic decay curve. When comparing both sorbents, Coppola *et al.* (2013b) reported the following oxide composition for one material: CaO = 31.80 %, MgO = 20.90 %, SiO_2 = 0.91 %, Fe_2O_3 = 0.25 %, Al_2O_3 = 0.22 %, TiO_2 = 0.02 %, and loss on ignition (LOI) = 45.12 %. In contrast, the relatively higher SiO_2 content observed in the dolomite (DOL) sample may have contributed to the enhanced abrasion resistance documented in other dolomite-based sorbents reported in the literature.

During the experimental runs, it was observed that operational temperatures of 750 °C and above exceed the thermodynamic equilibrium threshold for the carbonation reaction, causing a shift in the dominant reaction pathway from carbonation ($CaO + CO_2 \rightarrow CaCO_3$) to calcination ($CaCO_3 \rightarrow CaO + CO_2$). At these elevated temperatures, the sorbent does not effectively capture CO2 via carbonation. Although minor mass upetake was detecte during the transfer of solids between reactors, this transient "capture" is attributable to a temporary drop in material temperature during the forced transport rather than sustainable carbonation. Specifically, initial CO_2 uptake occurred only until the particles contacted the carbonator and subsequently ceased as their temperature increased back towards the target carbonation setpoint. Under these conditions, the overall CO_2 capture as considered negligible, since the reaction regime corresponded to calcination rather than to effective carbonation.

Figure 58 presents a 3D surface plot of the design, which exhibits a characteristic saddle-shaped topology. This morphology indicates the absence of a single, well-defined global

maximum or minimum. Instead, two distinct regions with comparatively higher response values are observed, thereby complicating the optimization procedure.

A valley can be discerned between intermediate fluidization velocities, suggesting enhanced performance at both relatively low and very high velocities, with lower velocities yielding more favorable results than higher ones. In contrast, the temperature exhibits a monotonic increase, reaching a maximum for each fluidization velocity.

It is important to emphasize that, although the model predicts a gradual decrease in performance after this maximum is reached, such behavior does not accurately represent the actual physical system. Once the maximum carbonation temperature is attained, the dominant reaction mechanism shifts from carbonation to calcination, rendering further carbonation impossible. This phenomenon is associated with abrupt changes in system behavior that are not adequately captured by the continuous empirical or semi-empirical equations employed in the model.

Figure 58 – Response surface plot of ξ_{mean} experimental data by fluidization velocity and temperature, based on Equation (4.6)

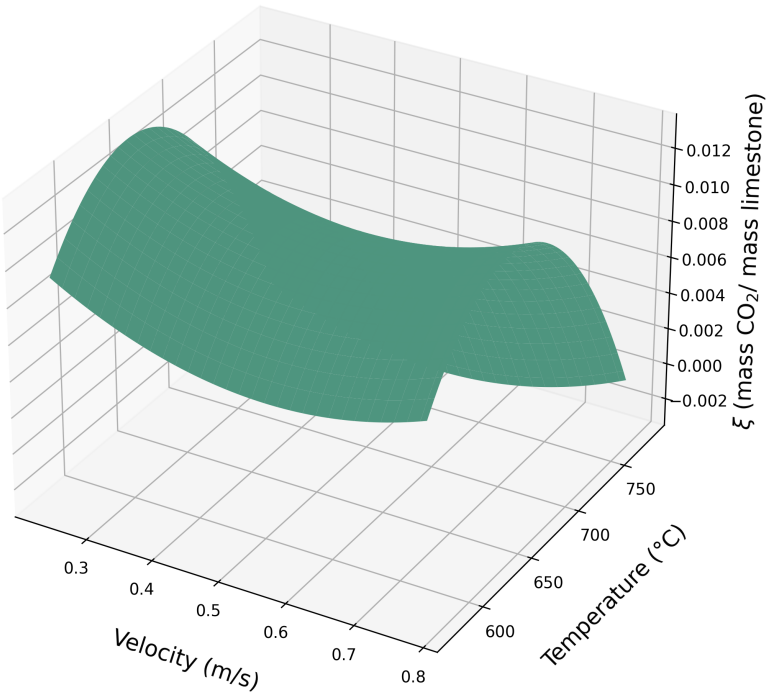

Source: Author

Figure 59 displays a contour map of the surface plot, where the presence of two local maxima can be more clearly distinguished: one on the left, highlighted in solid black, corresponding to lower velocities, and a second on the right, associated with higher velocities, indicating a

renewed increase in capture efficiency. If the fluidization velocity were to continue increasing, it could potentially exceed the lower local maximum. However, the maximum velocity employed in these experiments is constrained by the operational limits of the experimental setup.

Figure 59 – Response surface contour plot of ξ_{mean} experimental data by fluidization velocity and temperature, based on Equation (4.6)

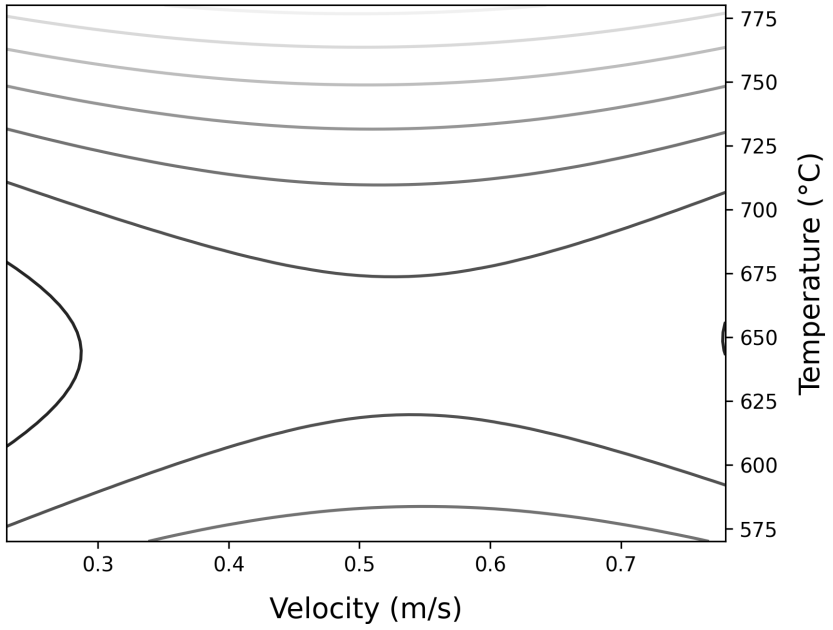

Source: Author

Equation 4.6 presents the model that describes this design:

$$\xi_{mean} = -3.11E^{-1} - 4.04E^{-2}v + 1.03E^{-3}T + 2.80E^{-2}v^2 - 8.01E^{-7}T^2 + 1.60E^{-5}vT \quad (4.6)$$

The response variable ξ_{mean} was modeled using a second-order polynomial in order to analyze the influence of Velocity and Temperature. Nevertheless, the underlying process exhibits a pronounced transition between calcination and carbonation, leading to a reduction of ξ_{mean} to zero at elevated temperatures. This discontinuous behavior introduces a level of complexity that cannot be adequately represented by a quadratic function, thereby limiting the quality of the fit in these regions. Despite this limitation, the quadratic model was retained in its conventional form to preserve simplicity and facilitate interpretability.

The ANOVA results, presented in Table 19, show that the model explains a substantial portion of the response variability, with an R^2 of 0.7598 and an adjusted R^2 of 0.5196. Temperature emerged as the most influential factor, with both its linear (p = 0.0509) and quadratic (p = 0.0470) terms being statistically significant. Other terms—including Velocity, its square, and the interaction between Velocity and Temperature—were not significant (p > 0.5). Despite capturing key trends, the model exhibited a significant lack-of-fit (p = 0.0281), likely due to its inability to represent the sharp transitions in the system where ξ_{mean} approaches zero.

Table 19 – ANOVA table and lack-of-fit test for the regression model of Equation 4.6

Source	DF	Sum of Squares	F-value	p-value
Velocity	1	7.03e–06	0.4535	0.5306
Temperature	1	1.01e–04	6.5289	0.0509
Velocity^2	1	6.36e–06	0.4103	0.5500
Temperature^2	1	1.07e–04	6.8701	0.0470
Vel. · Temp.	1	1.41e–07	0.0091	0.9276
Residual	5	7.75e–05	–	–
Lack-of-Fit	3	0.0001	34.7334	0.0281
Pure Error	2	0.0000	–	–

Source: Author

In general, for saddle plots such as the one discussed, a broader exploration of the parameter space or the inclusion of additional variables is required to further refine the system analysis. Given that the current range of variables has been comprehensively explored within the constraints of the experimental setup, incorporating alternative or additional parameters—such as fragmentation intensity—may enable the identification of a more pronounced global maximum in the response surface.

Although the present experimental design could be enhanced, the results obtained here nonetheless allow for robust conclusions regarding the sorbent's performance and its potential future applications. The overall viability of calcium looping is mostly dependent on carbon capture efficiency, resistance to elutriation, and sorbent deactivation behavior. In this study, the observed deactivation curve profile together with the relatively low CO_2 capture efficiency constitute significant limitations that challenge the justification for scaling up this specific configuration and sorbent.

While the calcination temperature applied (940 °C) was relatively high and likely contributed to reduced capture capacity, these operating conditions were selected based on previous studies that reported improved performance under similar settings. The present findings therefore raise new research questions, including: (i) what is the role of silica in determining CO_2 capture efficiency and elutriation behavior, and (ii) how would lower calciner temperatures influence the overall performance and economic feasibility of industrial-scale CaL systems?

Addressing these questions is essential for guiding future decisions regarding the deployment and optimization of CaL technology within the Brazilian context.

4.5.1 Elutriation investigation

All PSDs from Table 17 are shown in Figure 60. During the experimental campaign, it was observed that a substantial fraction of the elutriated material was not retained by the filters and was instead lost through the exhaust gas stream. The experimental procedure was therefore

modified in three occasions: initially by employing two filters per cycle for the first two cycles, and subsequently by introducing a reactor-cleaning step prior to each test. These methodological adjustments had a pronounced influence on the results, introducing variability that hinders the establishment of robust assumptions. Nevertheless, following the final adjustment of the methodology, it is still possible to qualitatively compare the results and derive meaningful conclusions.

Figure 60 – Mass fraction analysis presenting the experimental particle size distribution (PSD) of DIFB samples after testing. The image displays the absolute mass fraction of each individual sample as a function of particle diameter

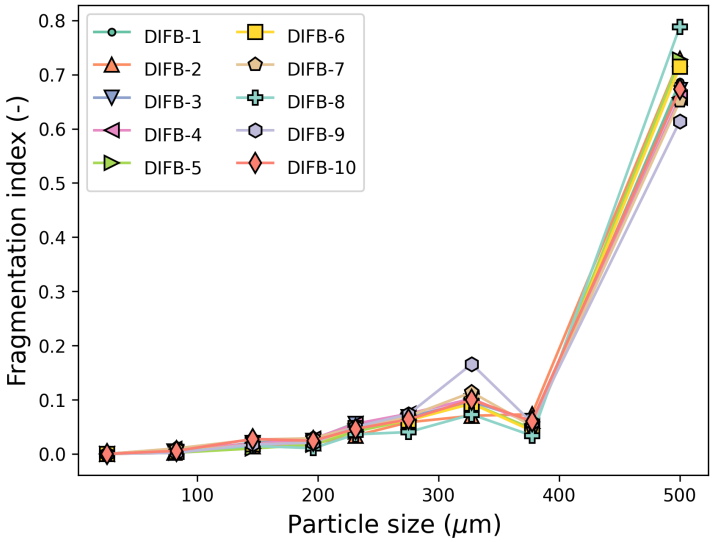

Source: Author

From Figure 60, it is possible to observe the impact of fluidization velocity on elutriation. At the highest velocity investigated (0.78 m/s), extensive fragmentation of larger particles was observed. For particles smaller than 250 μm, variation in the RCCD did not produce a discernible effect, suggesting that temperature and gas velocity are the dominant variables governing the behavior of the finest elutriated fraction (< 50 μm), which could not be recovered. In contrast, the experiment performed at the lowest velocity (0.23 m/s) exhibited the least susceptibility to elutriation. Overall, a difference of approximately 20% in elutriated mass was measured between the tested conditions.

When evaluating the effect of temperature, no clear conclusion can be established, as the influence of velocity appears to predominate. In light of the variability observed among replicates, it is not possible to assert a definitive temperature effect. Nonetheless, a tendency indicating the presence of two distinct groups, corresponding to the highest and lowest temperature extremes, can be discerned.

Figure 61 confirms the later statement as a large portion of the sample mass is missing from finer diameters. As shown in Table 17, a large portion of sample mass is loss during the experiments. Even if particles captures by filter are added, most of test lost at least 50% of its

mass. Those particle would ideally being retained in filter and results should show an relevant increase in mass fraction as particle diameter decreases.

Figure 61 – Mass fraction analysis presenting the experimental cumulative particle size distribution (PSD) of DIFB samples after testing. The image displays the absolute mass fraction of each individual sample as a function of particle diameter

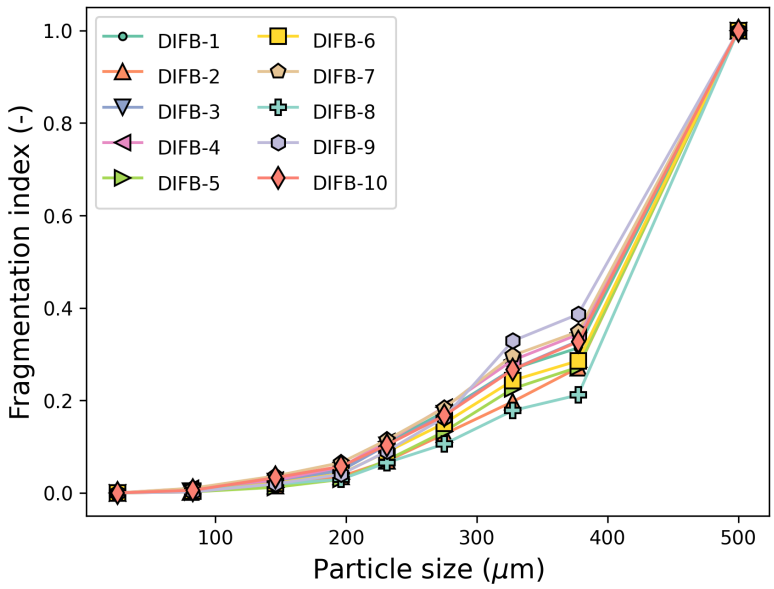

Source: Author

Figure 62 presents the average elutriation values for each test, with the exception of the 780 ºC experiment, which is not included due to experimental complications. In test DIFB-6, two filters were employed per reaction cycle, resulting in a total of 42 filters per run. The data indicate that the filters were ineffective at retaining the fines, primarily due to the small particle size. Tests DIFB-1, DIFB-2, DIFB-3, DIFB-4, and DIFB-5 were conducted using the initial methodology (a single filter per cycle, without cleaning), whereas DIFB-6 represents a unique case. Tests DIFB-7, DIFB-8, DIFB-9, and DIFB-10 were performed subsequently, following the protocol described in Section 3.8.4.2, in which two filters were used for the first two cycles and the reactor was cleaned after each test. Because replicates were carried out under different methodological conditions, they are not directly comparable in this analysis.

First five tests (DIFB-1, DIFB-2, DIFB-3, DIFB-4 and DIFB-5) had a critical problem where fine elutriate was accumulating inside the system after each test and would aggravate the blocking of filters, interfere in carbon capture and transport of particle. After further analysis, methodology was changed and last four tests (DIFB-7, DIFB-8, DIFB-9, DIFB-10) met the expectation. The test which least suffered from elutriation was the one with the lower fluidization velocity, being also the highest related to higher velocity. This figure reinforce the point of fluidization velocity making the most impact on elutriation if compared to temperature, specially when comparing DIFB-10 and DIFB-5, DIFB-6, and DIFB-7 tests.

Figure 62 – Experimental data from DFIB elutriation tests showing the average elutriation time per test. Elutriation refers specifically to carbonation fines from the tests listed in Table 17

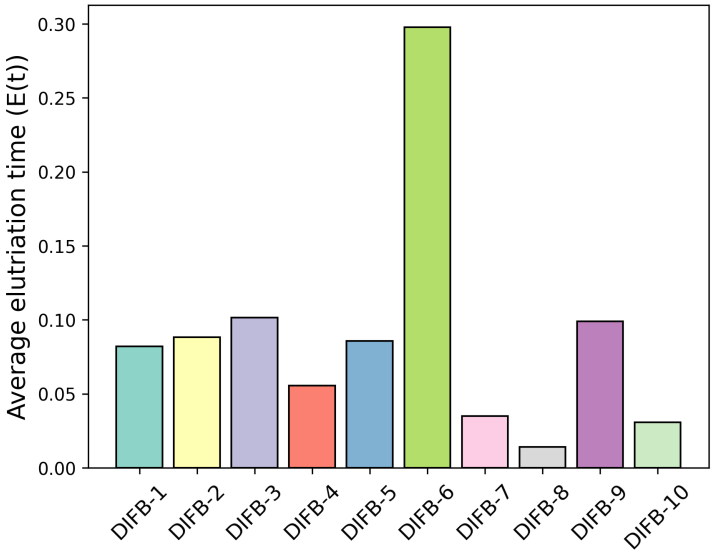

Source: Author

Based on the mean particle elutriation (including calcination) presented in Figure 63, test DIFB-6 indicates higher elutriation during carbonation compared to calcination. This suggests that filter obstruction is likely related to elutriation occurring in the carbonation step.

Figure 63 – Experimental data from DFIB elutriation tests showing the average elutriation time per test. Elutriation refers to both calcination and carbonation fines from the tests listed in Table 17

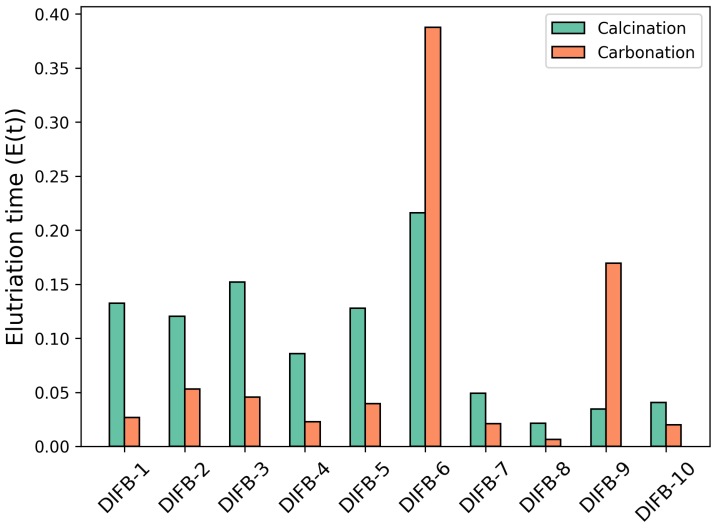

Source: Author

While test DIFB-9, previous reactor cleaned, might have been affected by high fluidization

velocity. When confronting with previous work in this experimental setup (COPPOLA *et al.*, 2012a; COPPOLA *et al.*, 2013a; COPPOLA; SCALA; SALATINO, 2018) a higher carbonation E(t) is expected, however it largely depends on the sorbent used (COPPOLA; SCALA; SALATINO, 2018). This outcome reinforces the prior discussion concerning SiO_2 content, indicating its potential impact on overall fragmentation.

4.5.2 Impact test

The impact test results are presented in Figure 64, where the fragmentation index (f) is plotted as a function of impact velocity. The slope of each curve represents the rate of particle production, with a steeper slope indicating a higher fragmentation rate. Although no curve fitting has been applied, the data indicate that elevated temperatures are associated with steeper gradients, suggesting an enhanced generation of particles under higher thermal conditions.

The proximity of the data points in Figure 64 makes it challenging to draw clear conclusions. To address this, Figure 65 displays a fitted curve based on Equation 3.20, which helps clarify the trends. The fitted results reveal two distinct behaviors: one associated with high temperatures and the other with low velocities. Notably, tests conducted at 750 °C and velocities below 0.3 m/s exhibit a marked increase in slope, indicating intensified fragmentation under these specific conditions.

Figure 64 – Estimated fragmentation index (f) as a function of fluidization velocity for DIFB tests conducted using the impact test equipment

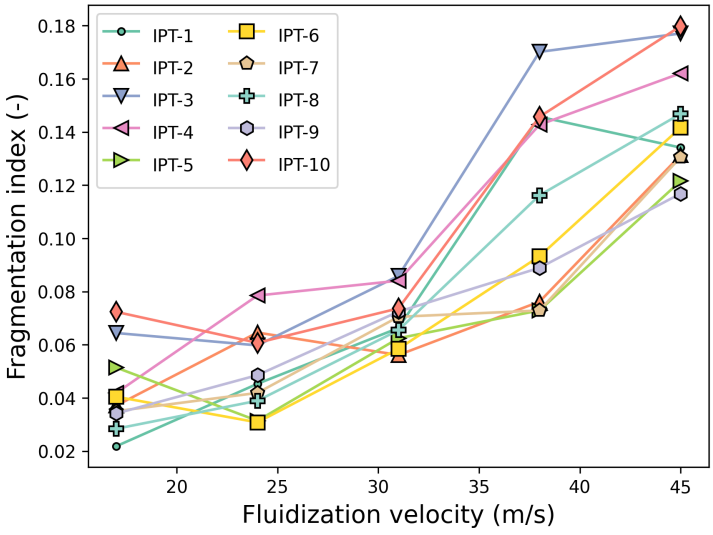

Source: Author

Table 20 present results for each inclination showed on Figure 65. It can be seen the best result are presented in test IPT-5, IPT-2 and IPT-9, with angular coefficient of 0.002597, 0.002856 and 0.002939, respectively. Table 21 show the interval based on the three central points. Interval points showed good dispersion leading to high confidence interval.

Figure 65 – Interpolated fragmentation index (f) curves according to according to Equation 3.21 as a function of fluidization velocity for DIFB tests conducted using the impact test equipment

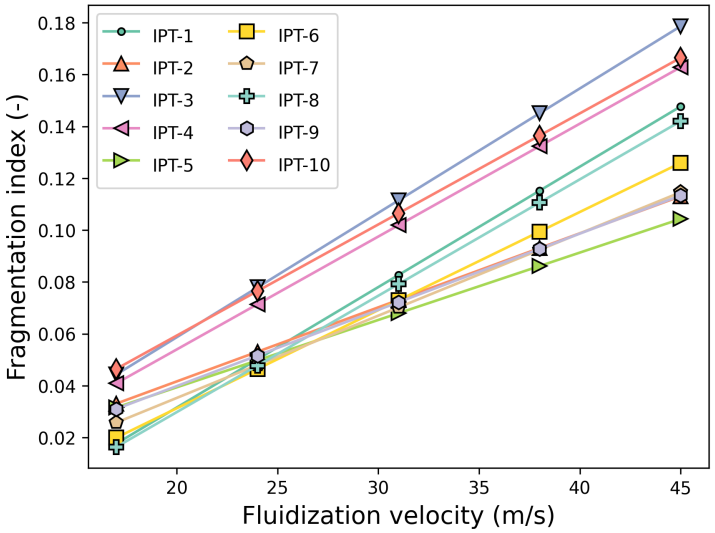

Source: Author

Table 20 – Modeling results data for impact test equipment presenting parameters: fluidization velocity and temperature, and results: m_{impact}

Test name	Velocity (m/s)	Temp. (°C)	m_{impact}
IPT-1	0.30	600	0.004643
IPT-2	0.70	600	0.002856
IPT-3	0.30	750	0.004795
IPT-4	0.50	750	0.004352
IPT-5	0.50	675	0.002597
IPT-6	0.50	675	0.003784
IPT-7	0.50	675	0.003172
IPT-8	0.23	675	0.004487
IPT-9	0.78	675	0.002939
IPT-10	0.50	570	0.004284

Source: Author

Equation 4.7 presents the model based on Table 21 for response as angular coefficient m_{impact} according to Equation 3.21.

$$m_{impact} = 7.38E^{-2} - 2.48E^{-2}v - 1.94E^{-4}T + 6.40e^{-3}v^2 + 1.39E^{-7}T^2 + 2.32E^{-5}vT \quad (4.7)$$

Figure 66 and Figure 67 show surface plots of the impact test results. Both figures highlight a region of low fragmentation occurring at higher velocities (above 0.6 m/s) and temperatures between 580–680 °C. This suggests that, within these conditions, the fragmentation is minimized

in the experimental tests.

Figure 66 – Response surface plot of fragmentation index (f) experimental data by fluidization velocity and temperature, based on Equation (3.21)

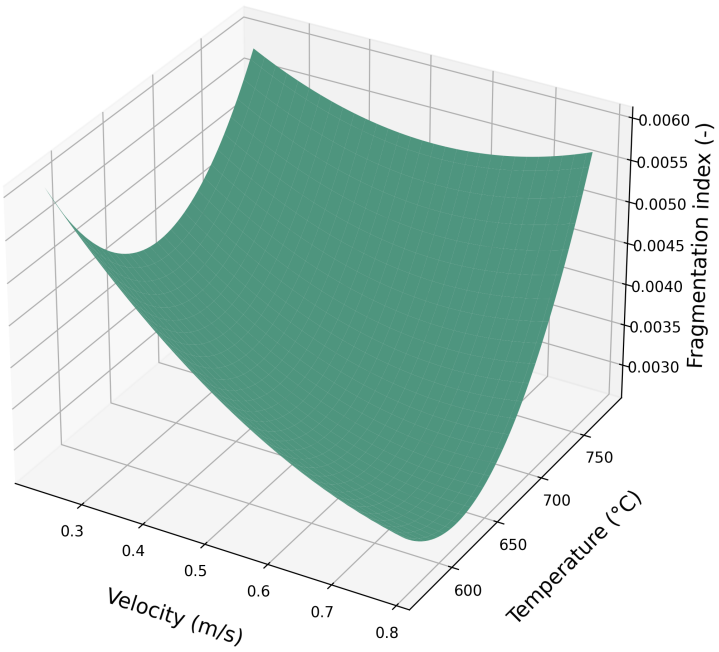

Source: Author

Table 21 – Impact test interval measurements

Test	m_{impact}
IPT-5	0.002597
IPT-6	0.003784
IPT-7	0.003172
Std	0.000485
Mean	0.003184
interval	0.001204

Source: Author

The ANOVA analysis returns once more Temperature and Temperature^2 as statistically significant effects (p = 0.0455 and p = 0.0361, respectively), reinforcing the importance of both linear and nonlinear temperature behavior. All other terms, including Velocity and its

interaction with Temperature, were not significant ($p > 0.14$). The model passed the lack-of-fit test ($p = 0.9522$), confirming its adequacy. Despite the small scale of the sum of squares—likely a result of transformation—the model effectively captures the main response trends with no indication of overfitting or missing structure. In contrast to the carbon capture capacity analysis,

Figure 67 – Response surface contour plot of fragmentation index (f) experimental data by fluidization velocity and temperature, based on Equation (3.21)

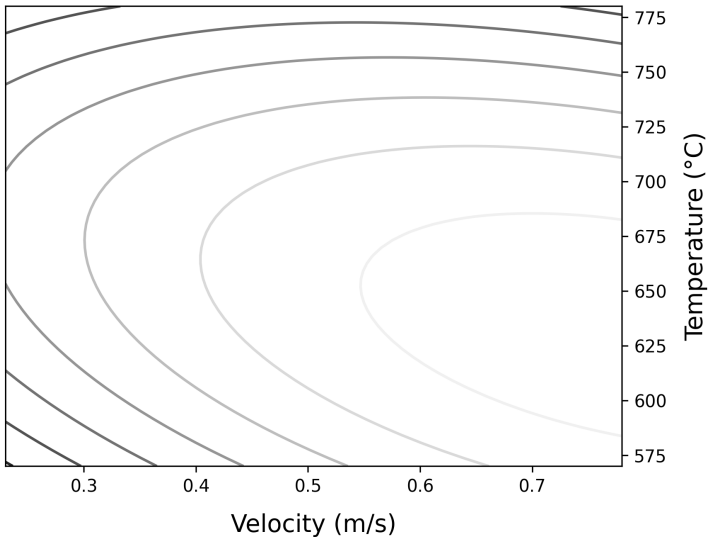

Source: Author

this surface plot reveals a clear and simultaneous influence of both parameters. The observed reduction in fragmentation at higher temperatures can be attributed to sintering phenomena and particle fragilization, which is consistent with the expected behavior. These results suggest that operation under a higher fluidization regime during carbonation, despite the associated increase in fragmentation, ultimately contributed to the preservation of sorbent particles. It is plausible that elevated fluidization velocities promoted the removal of fragile external layers by attrition or chipping, thereby exposing a mechanically more robust surface for the subsequent impact tests. When these particles are subjected to impact loading, the presence of such fragile surface layers is likely to result in lower impact resistance (SCALA; MONTAGNARO; SALATINO, 2006; SCALA; MONTAGNARO; SALATINO, 2007).

On the other hand, the apparent trend whereby higher velocities are associated with reduced fragmentation may be misleading. At lower velocities, particles tend to absorb a greater amount of energy, resulting in an increase in their temperature. As previously discussed, elevated particle temperatures are known to promote degradation, which could account for the enhanced fragmentation observed at lower velocities. Although this result does suggest a positive indication for high-velocity operation it must be confirmed through experiments employing pre-heated fluidization gas in combination with higher gas velocities.

Table 22 – ANOVA table and lack-of-fit test for the regression model (Equation 3.21)

Source	DF	Sum of Squares	F-value	p-value
Velocity	1	6.09×10^{-7}	3.293	0.144
Temperature	1	1.52×10^{-6}	8.231	0.046
Velocity^2	1	3.32×10^{-7}	1.793	0.252
Temperature^2	1	1.78×10^{-6}	9.631	0.036
Vel. $\times$ Temp.	1	2.50×10^{-7}	1.354	0.309
Residual	4	7.40×10^{-7}	–	–
Lack-of-Fit	2	0	0.050	0.952
Pure Error	2	0	–	–

Source: Author

4.5.3 Model validation

Both Equations 4.6 and 4.7 were evaluated under a test condition that lies within the experimental range but was not included in the original design matrix. These tests were conducted at a carbonation temperature of 600 °C, a fluidization velocity of 0.5 m/s, and the same impact test velocities used previously, as summarized in Table 23. Within the experimental uncertainty, the model predictions are consistent with the measured data.

It should be emphasized, however, that the model for ξ_{mean} is only valid within the range of operating conditions for which carbonation effectively occurs. In particular, for T > 750 °C the model may yield non-zero values, but such outputs must be disregarded because they fall outside the validated parameter space and do not represent the actual behavior of the system. Aside from this limitation, the models exhibit satisfactory predictive capability, indicating good reproducibility and reliability in describing the system response.

Table 23 – Test and validation of carbon capacity (ξ_{mean}, Equation 4.6) fragmentation index model (, Equation 3.21) using a new test. New test conditions: T = 600 °C and v = 0.5 m/s

Parameter	Predicted	Experimental
ξ_{mean}	0.009240	0.010778
m_{impact}	0.004642	0.003582

Source: Author

4.6 EXPERIMENTAL COMPARISON TGA-DIFB

TGA's and a DIFB setup are mechanically different setups, where TGA's behaves as fixed bed reactor while DIFB have a fluidization velocity which comes with different dynamic of

reaction. In order to compare both studies, results both from TGA and DIFB were converted to ξ, Figure 68.

Although both tests exhibit a similar decay profile, the DIFB results are consistently lower than those of the TGA. Additionally, while the TGA tests show a continuous degradation per cycle over time, the DIFB sample displays an abrupt drop after the third cycle. This results is expected as, differently from TGA, DIFB have additional decay inducing parameters as attrition and fragmentation, being this increased decay after few cycles in accordance with the expected behavior.

Figure 68 – Results comparison between experimental carbon capacity (ξ) by cycle in both TGA and DIFB.

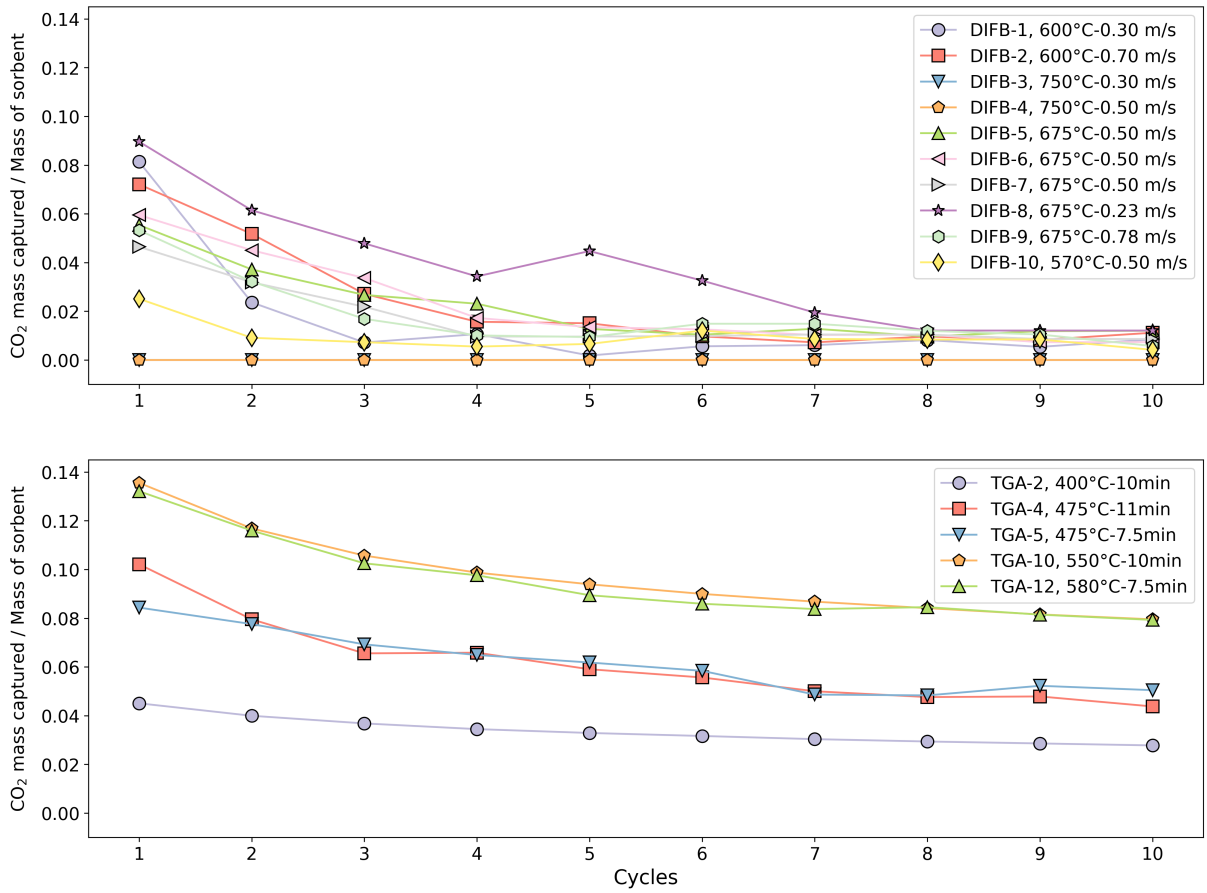

Source: Author

The lower ξ values observed in the DIFB tests are unexpected, as a higher ξ was anticipated based on the inherent advantages of fluidized bed systems, including their superior heat and mass transfer efficiency and the larger sample size employed. However, it appears that the operating conditions in the calciner—discussed in Section 4.5—may have significantly influenced the results, potentially offsetting the expected performance benefits.

Despite the discussion regarding DIFB tests, condition applied in this setup are a better

representation of reality of CaL process. DIFB results have shown a lower ξ, however regarding its utilization with natural gas power plants conditions it showed characteristic performance of CaL as in any other plant, as coal for example, being difficulties found in this work related mostly to the sorbent rather than low CO_2 concentration.

4.7 OVERALL TECHNICAL ASSESSMENT AND APPLICABILITY OF THE CALCIUM LOOPING PROCESS

Based on the experimental data, this thesis establishes that laboratory-scale investigations can define rigorous operational parameters and evaluate the technical feasibility of the calcium looping (CaL) process employing Brazilian dolomite as a CO_2 sorbent under conditions that simulate flue gas from natural gas-fired power generation.

N_2 adsorption porosimetry combined with statistical pore blockage modeling elucidated the mechanistic drivers of sorbent performance degradation, revealing a critical pore size domain (30–100 Å) that governs both initial CO_2 uptake efficacy and the evolution of cyclic deactivation. These findings indicate that the technical viability of calcium looping with Brazilian dolomite is determined not only by process operating parameters but also by the intrinsic pore architecture and mineralogical makeup of the sorbent, thereby underscoring the importance of targeted sorbent selection and/or structural modification for scale-up and long-term implementation

Thermogravimetric analysis (TGA) experiments demonstrated that, even at low CO_2 concentrations characteristic of natural gas flue gas streams, Brazilian dolomite exhibits substantial CO_2 capture potential provided that the carbonation temperature and solid residence time are maintained within appropriate operational windows. Application of a rotatable central composite design (RCCD) statistical model identified carbonation temperature as the primary operational parameter influencing process performance, with a more pronounced effect on overall capture efficiency than residence time, consistent with results reported in the literature for similar CaL systems. These findings facilitated the derivation of quantitative operational criteria that optimize the trade-off between energy consumption, sorbent capture capacity, and surface stability over cyclic operation.

Bench-scale dual interconnected fluidized bed (DIFB) experiments indicated that, while fluidized bed reactors more closely emulate the industrial configuration of the CaL process, geometric and dynamic scale-up introduces additional sorbent degradation mechanisms—specifically elutriation, particle fragmentation, and thermal stress–induced deterioration—that significantly impair sorbent performance. These reduced CO_2 capture efficiencies observed in the DIFB configuration were attributed not to the low CO_2 concentrations per se, but to the inherent mechanical and thermal limitations of Brazilian dolomite subjected to the intensive hydrodynamic and thermal environment of the fluidized system, particularly under the specific calciner configuration employed.

Comparative analysis between TGA and DIFB, using the dimensionless variable ξ, indicated

that while TGA provides essential information on reaction kinetics, cyclic stability, and degradation trends, the DIFB configuration is indispensable for assessing operational feasibility, as it incorporates hydrodynamic and mechanical effects absent in fixed-bed systems. In this regard, laboratory-scale studies proved to be complementary, enabling more realistic extrapolations toward industrial application.

Therefore, it can be verified that laboratory-scale experimental studies provide a consistent and reliable basis to define operational criteria, identify sorbent-related limitations, and demonstrate the technical feasibility of the calcium looping process in conditions typical of natural gas–fired power plants, while simultaneously revealing the challenges associated with the industrial application of Brazilian dolomite. Collectively, these findings establish a solid technical foundation for future pilot studies and for the development of strategies aimed at improving sorbent performance, strengthening the relevance of calcium looping as a viable CO_2 capture technology within the Brazilian energy matrix.

5 CONCLUSION

A Brazilian dolomite was evaluated in both TGA and DIFB systems under a simulated natural gas exhaust atmosphere, with particular emphasis on its overall performance, technological feasibility, and the influence of gas velocity and temperature on process behavior. The TGA results indicated that optimization of the CaL process using this dolomite in low CO_2-concentration flue gas—characteristic of natural gas-fired thermoelectric power plants—exhibits substantial potential for efficient CO_2 capture within Brazil's power generation mix. Nonetheless, the findings strongly indicate the need for further investigations in fluidized bed reactors to evaluate the sorbent's performance at a larger and more industrially representative scale. Such studies would enable a more accurate assessment of energy consumption, sorbent elutriation, and sintering phenomena, all of which can critically affect the long-term cyclic stability and overall effectiveness of the capture process.

The fluidized bed investigation was carried out in a reference laboratory in Naples, Italy, to evaluate the performance of the sorbent. During testing in the DIFB configuration, the dolomite exhibited an unexpectedly high degree of elutriation even at relatively low gas velocities, which directly impaired the CO_2 capture performance, yielding a maximum value on the order of 0.0177 kg CO_2/kg $CaCO_3$ under the most favorable operating conditions. Consistent with previous studies, the scale-up of the system introduced additional challenges for the sorbent, indicating that this material may not be suitable for conventional CaL configurations, particularly for the specific calciner design employed in this work.

Although several limitations were identified in this study regarding performance under large-scale operating conditions, these constraints are attributable exclusively to the sorbent employed. When assessing the overall behavior, the tests conducted under a simulated natural-gas-derived flue gas were consistent with expectations for a typical CaL process, exhibiting only a slightly reduced, if any, CO_2 capture efficiency.

All key phenomena reported in previous CaL investigations were also observed in this work, including: a successful and reversible carbonation–calcination cycling; a decline in capture efficiency over repeated cycles, following the characteristic deactivation profile; and the occurrence of sorbent elutriation.

From this perspective, it is possible to conclude that:

1. Initial material characterization revealed an elevated SiO_2 content, a feature not commonly reported in existing literature. Particle size exerted a measurable influence on the calcination behavior, with smaller particles lowering the temperature required to achieve complete calcination. The CO_2 concentration affected both calcination and carbonation reactions, indicating that the gaseous atmosphere is a critical parameter in the kinetic and mechanistic analysis of these processes.

BJH analysis indicated a unimodal pore size distribution in the range of 17–150 Å, with the lower bound of the pore size notably smaller than those reported in other studies, which typically describe larger minimum pore diameters. As carbonation proceeded, progressive pore closure was observed: initially, a relatively uniform reduction in pore volume occurred across the entire diameter range up to approximately 10 min, followed by preferential closure of pores in the 30–100 Å interval. This led to a shift of the distribution toward smaller pores, with larger pores being more readily occluded.

When characterization data are compared across different experimental scales, the results suggest that sorbent performance and behavior can be predicted on the basis of chemical composition, crystalline structure, and pore size distribution. Although additional experimental validation is required to robustly confirm this hypothesis, the capacity to forecast sorbent behavior and performance constitutes a promising strategy for reducing development costs in carbon capture technologies.

2. Carbonation temperature is identified as the most critical parameter governing the process. When comparing temperature and carbonation time based on TGA experiments, it is observed that, even after accounting for the energy consumption during the process, temperature remains the dominant factor influencing carbon capture efficiency, as higher temperatures yield superior energy performance under the investigated conditions.

   From the RCCD design, the optimal operating conditions were determined to be 580 °C for 7.5 min (IEC = 0.89), 550 °C for 10 min (IEC = 1.01), and 475 °C for both 11 min (IEC = 0.83) and 7.5 min (IEC = 0.88). Among these, less surface damage was observed at 475 °C compared with 580 °C and 550 °C. Nevertheless, in multi-cycle tests, superior performance was obtained at 580 °C for 7.5 min and 550 °C for 10 min, with $\mathrm{IEC}_{10,c}$ values of 1.34 and 1.20, respectively, corresponding to an improvement of approximately 40

   Within this framework, the best overall performance was achieved at 580 °C for 7.5 min, which exhibited a lower E_{sp} (33.48 kJ) and a CO_2cap value comparable to that obtained at 550 °C. However, for scale-up purposes, the condition of 550 °C for 10 min appears more suitable, as it provided robust performance (E_{sp} = 37.97 kJ and CO_2cap = 9.80 mg) without any observable signs of sintering on the sorbent surface. This latter aspect is particularly relevant for enhancing process feasibility in a fluidized bed system.

3. In the analysis of the interaction between temperature and fluidization velocity, temperature appears to exert a predominant influence, largely independent of the fluidization velocity. According to the RCDD results, the optimal operating window corresponds to the highest attainable carbonation temperature that does not yet trigger the onset of calcination. The saddle-shaped response surface obtained from the RCCD further indicates that additional

factors may be affecting the system response, thereby underscoring the necessity for a more comprehensive exploration of the parameter space.

The observed lack of fit is attributed to the abrupt transition between the carbonation and calcination regimes, a phenomenon that cannot be adequately represented by a second-order polynomial model. Nevertheless, within the investigated domain that excludes the transition to calcination (570 °C < T < 675 °C and 0.23 m/s < v < 0.78 m/s), the model exhibits good agreement with the experimental observations. For example, it yields values of 0.009240 (experimental) and 0.010778 (predicted) for ξ_{mean}.

4. TGA experiments indicate that the capture capacity declines sharply within the first 2.5 min of carbonation, confirming that the majority of the fast reaction occurs at the early stages; this observation is further corroborated by DIFB tests. Contrary to the expectation that no fast reaction phase should remain after 7 min, samples carbonated for up to 15 min still exhibit signatures of it, possibly due to thermal shock effects associated with rapid transfer between the VTR and ambient conditions. In contrast, longer carbonation times are characterized by extended diffusion-controlled phases and a concomitant reduction in overall performance.

   Pore-structure deformation analysis demonstrates that the fast carbonation phase terminates between 5 and 7.5 min, and its duration is directly proportional to the initial pore volume in the 30–100 Å range. The loss of efficiency is primarily attributed to the closure of these pores, as additional pore blockage at later stages exerts only a minor influence on CO_2 capture.

   The evaluation of the Beta probability density function (PDF) parameters, α and β, suggests a two-step pore closure mechanism. The presence of SiO_2 appears to adversely affect the pore structure by decreasing the total pore volume and constraining the formation or preservation of smaller pores. Overall, these findings indicate that factors beyond the sorbent pore size distribution and SiO_2 content influence the resistance to performance decay and therefore warrant further investigation.

5. Residence time has a substantial impact on the overall energy consumption where 3.5 min per cycle had and increase of 8% of total energy spent during the 475 °C multi-cycle tests, underscoring the importance of identifying an optimal balance to maximize net carbon capture efficiency;

6. At smaller scales, the variability in chemical composition and particle size associated with the selected Brazilian dolomite was critically important, as it posed challenges to experimental reproducibility. Tests employing this dolomite should preferably be conducted within narrow particle size fractions and with larger sample masses. Although DIFB tests were performed using both a restricted particle size range and an increased

sample mass, the variability in the results remained high, underscoring the necessity of conducting replicate experiments when using this material.

7. The DIFB system was not able to retain the entirety of the fine particles using the current experimental methodology. The requirement to employ two filters per experiment proved to be labor-intensive, thereby underscoring the need for the development of a more efficient and robust solution. Elevated temperatures (> 475 °C) exerted a pronounced influence on the surface degradation of the dolomite, whereas the influence of residence time was comparatively negligible. In accordance with the impact test design, the optimal operating window for minimizing elutriation lies between 580 °C and 680 °C at fluidization velocities exceeding 0.55 m/s.

8. The deactivation curves obtained in DIFB exhibit a performance trend characteristic of limestone, which may be partially attributable to temperature-induced degradation. Most samples reached their deactivated state by the fifth cycle, a behavior that is not typically observed for dolomite. In contrast, TGA measurements did not attain a clear deactivation point even after ten cycles, thereby supporting the hypothesis that temperature degradation plays a significant role in the observed behavior. Moreover, the deactivation curves measured in the TGA do not indicate any interaction between partial carbonation and variations in deactivation performance when compared with data reported in the literature, as all tested conditions followed the expected decay-curve profile. Nevertheless, a more detailed investigation directly comparing complete and partial carbonation is required to rigorously validate this hypothesis.

5.1 FUTURE WORKS

Although the feasibility of operating the calciner at lower temperatures was confirmed and the life cycle assessment yielded promising results, the investigated dolomite exhibited a significantly high elutriation rate during the experimental tests. The main working hypothesis attributes this behavior to the silica content, which may induce increased brittleness in the sorbent structure rather than the reinforcing effect typically associated with magnesium. Further phase characterization, particularly by X-ray diffraction, is required to clarify the role of silica within the crystalline structure. In addition, when the pore size distribution of this Brazilian dolomite is compared with those of other dolomites reported in the literature, it exhibits an excessively broad distribution, without a pronounced peak and outside the pore size range considered most effective for carbon capture. In this context, the evaluation of alternative sorbent materials emerges as a relevant and necessary step toward mitigating elutriation-related limitations.

A logical next step of this analysis would be the mapping of limestone mines in Brazil and their spatial proximity to natural gas power plants. Building on the findings of this work, the geological formations could be analyzed to identify and select the most promising limestone

sources based on their likely chemical and mineralogical composition. Subsequent characterization analyses should then be performed to establish a ranking of limestone candidates for calcium looping applications in Brazil. Further studies should also incorporate life cycle assessments considering transport distances to existing power plants, as well as an evaluation of the technical and economic feasibility of implementing a pilot-scale calcium looping facility in Brazil.

Brazil has shown increasing interest in supplying its energy matrix to data processing activities, which is expected to significantly raise electricity demand. At the same time, climate-change-driven variability in rainfall regimes poses challenges to the reliability of hydropower generation, thereby increasing the reliance on natural gas power plants. This trend reinforces the urgency of advancing research on carbon capture technologies to non-renewable energy sores such as power plants. As a carbon capture–based approach, it is imperative to rigorously assess the emission efficiency of the process. In this thesis, such evaluation was achievable only at lab scale; therefore, further investigation using larger scales, such as DIFB systems, is essential and should be pursued.

BIBLIOGRAPHY

ACHARYA, B.; DUTTA, A.; BASU, P. Circulating-fluidized-bed-based calcium-looping gasifier: experimental studies on the calcination–carbonation cycle. **Industrial & engineering chemistry research**, Washington, v. 51, n. 25, p. 8652–8660, 2012. Available from: https://doi.org/10.1021/ie300629a. Acessed in: 27 Mar. 2026.

ALFONSO, S.; GESTO, M.; SADOUL, B. Temperature increase and its effects on fish stress physiology in the context of global warming. **Journal of Fish Biology**, Hoboken, v. 98, n. 6, p. 1496–1508, 2021. Available from: https://doi.org/10.1111/jfb.14599. Acessed in: 27 Mar. 2026.

ALLEN, T. **Particle size measurement**. London: Chapman & Hall, 1997.

ALONSO, M. *et al.* Measuring attrition properties of calcium looping materials in a 30 kw pilot plant. **Powder Technology**, Amsterdam, v. 336, p. 273–281, 2018. Available from: https://doi.org/10.1016/j.powtec.2018.06.011. Acessed in: 27 Mar. 2026.

ALONSO, M. *et al.* Biomass combustion with in situ CO_2 capture by CAO in a 300 kwth circulating fluidized bed facility. **International Journal of Greenhouse Gas Control**, Amsterdam, v. 29, p. 142–152, 2014. Available from: https://doi.org/10.1016/j.ijggc.2014.08.002. Acessed in: 27 Mar. 2026.

ALVAREZ, D.; ABANADES, J. C. Determination of the critical product layer thickness in the reaction of CAO with CO_2. **Industrial & engineering chemistry research**, Washington, v. 44, n. 15, p. 5608–5615, 2005. Available from: https://doi.org/10.1021/ie050305s. Acessed in: 27 Mar. 2026.

AMGHAR, N. *et al.* Influence of long-term CAO storage conditions on the calcium looping thermochemical reactivity. **Energy & Fuels**, Washington, v. 37, n. 21, p. 16904–16914, 2023. Available from: https://doi.org/10.1021/acs.energyfuels.3c02652. Acessed in: 27 Mar. 2026.

AMROLLAHI, Z.; ERTESVÅG, I. S.; BOLLAND, O. Thermodynamic analysis on post-combustion CO_2 capture of natural-gas-fired power plant. **International Journal of Greenhouse Gas Control**, Miami, v. 5, n. 3, p. 422–426, 2011. Available from: https://doi.org/10.1016/j.ijggc.2010.09.004. Acessed in: 27 Mar. 2026.

ANTZARA, A. N. *et al.* In-depth evaluation of a ZRO_2 promoted CAO-based CO_2 sorbent in fluidized bed reactor tests. **Chemical Engineering Journal**, Amsterdam, v. 333, p. 697–711, 2018. Available from: https://doi.org/10.1016/j.cej.2017.09.192. Acessed in: 27 Mar. 2026.

ARCE, G. L. *et al.* Influence of physicochemical properties of brazilian serpentinites on the leaching process for indirect CO_2 mineral carbonation. **Hydrometallurgy**, Basel, v. 169, p. 142–151, 2017. Available from: https://doi.org/10.1016/j.hydromet.2017.01.003. Acessed in: 27 Mar. 2026.

ARIAS, B. *et al.* Calcium looping performance under extreme oxy-fuel combustion conditions in the calciner. **Fuel**, Amsterdam, v. 222, p. 711–717, 2018. Available from: https://doi.org/10.1016/j.fuel.2018.02.163. Acessed in: 27 Mar. 2026.

ARIAS, B. *et al.* Operating experience in la pereda 1.7 MW th calcium looping pilot. **Energy Procedia**, Amsterdam, v. 114, p. 149–157, 07 2017. Available from: https://doi.org/10.1016/j.egypro.2017.03.1157. Acessed in: 27 Mar. 2026.

ASIEDU-BOATENG, P. *et al.* Attrition characteristics of limestone in gas-solid fluidized beds. **Powder Technology**, Amsterdam, v. 419, p. 118342, 2023. Available from: https://doi.org/10.1016/j.powtec.2023.118342. Acessed in: 27 Mar. 2026.

ÁVILA, I.; CRNKOVIC, P. M.; MILIOLI, F. E. Determinação dos parâmetros de arrhenius da reação de sorção do dióxido de enxofre por calcário. **Química Nova**, São Paulo, v. 30, p. 1275–1281, 2007. Available from: https://doi.org/10.1590/S0100-40422007000500041. Acessed in: 27 Mar. 2026.

ÁVILA, I. *et al.* Investigation of the pore blockage of a brazilian dolomite during the sulfation reaction. **Applied surface science**, Amsterdam, v. 258, n. 8, p. 3532–3539, 2012. Available from: https://doi.org/10.1016/j.apsusc.2011.11.108. Acessed in: 27 Mar. 2026.

ÁVILA, I. *et al.* Thermal decomposition kinetics of brazilian limestones: effect of CO_2 partial pressure. **Environmental technology**, England, v. 33, n. 10, p. 1175–1182, 2012. Available from: https://doi.org/10.1080/09593330.2011.618930. Acessed in: 27 Mar. 2026.

BAHIA STATE FEDERATION OF INDUSTRIES (FIEB). **Federação das Indústrias do Estado da Bahia**. 2024. Available from: https://www.fieb.org.br/wp-content/uploads/2021/01/Estudo-de-Petroleo-e-Gas_id_411__x1a669897e2e141888c87d9fa0b7a3dd9_08052019101642_.pdf. Accessed in: 24 Apr. 2024.

BAKER, E. The calcium oxide–carbon dioxide system in the pressure range 1—300 atmospheres. **Journal of the Chemical Society (Resumed)**, London, p. 464–470, 1962. Available from: https://doi.org/10.1039/JR9620000464. Acessed in: 27 Mar. 2026.

BENITEZ-GUERRERO, M. *et al.* Effect of milling mechanism on the CO_2 capture performance of limestone in the calcium looping process. **Chemical Engineering Journal**, Amsterdam, v. 346, p. 549–556, 2018. Available from: https://doi.org/10.1016/j.cej.2018.03.146. Acessed in: 27 Mar. 2026.

BLAMEY, J. *et al.* CO_2 capture by calcium aluminate pellets in a small fluidized bed. **Fuel Processing Technology**, Perth, v. 142, p. 100–106, 2016. Available from: https://doi.org/10.1016/j.fuproc.2015.09.015. Acessed in: 27 Mar. 2026.

BLAMEY, J. *et al.* The calcium looping cycle for large-scale co_2 capture. **Progress in Energy and Combustion Science**, Amsterdam, v. 36, n. 2, p. 260–279, 2010. Available from: https://doi.org/10.1016/j.pecs.2009.10.001. Acessed in: 27 Mar. 2026.

BLAMEY, J. *et al.* The use of the calcium looping cycle for post-combustion co_2 capture. **Progress in Energy and Combustion Science**, Oxford, v. 36, n. 2, p. 260–279, 2010. Available from: https://doi.org/10.1016/j.pecs.2009.10.001. Acessed in: 27 Mar. 2026.

BLAMEY, J. *et al.* Mechanism of particle breakage during reactivation of CAO-based sorbents for CO_2 capture. **Energy & fuels**, Lakewood, v. 24, n. 8, p. 4605–4616, 2010. Available from: https://doi.org/10.1021/ef100476d. Acessed in: 27 Mar. 2026.

BLAMEY, J. *et al.* Reactivation of a CAO-based sorbent for CO_2 capture from stationary sources. **Proceedings of the Combustion Institute**, Pittsburgh, v. 33, n. 2, p. 2673–2681, 2011. Available from: https://doi.org/10.1016/j.proci.2010.07.052. Acessed in: 27 Mar. 2026.

BORGWARDT, R. H. Calcium oxide sintering in atmospheres containing water and carbon dioxide. **Industrial & Engineering Chemistry Research**, Washington, v. 28, n. 4, p. 493–500, 1989. Available from: https://doi.org/10.1021/ie00088a019. Acessed in: 27 Mar. 2026.

BORGWARDT, R. H. Sintering of nascent calcium oxide. **Chemical Engineering Science**, Amsterdam, v. 44, n. 1, p. 53–60, 1989. Available from: https://doi.org/10.1016/0009-2509(89)85232-7. Acessed in: 27 Mar. 2026.

BORGWARDT, R. H.; BRUCE, K. R. Effect of specific surface area on the reactivity of CAO with SO_2. **AIChE journal**, Dongguan, v. 32, n. 2, p. 239–246, 1986. Available from: https://doi.org/10.1002/aic.690320210. Acessed in: 27 Mar. 2026.

BRAZIL NATIONAL AGENCY OF PETROLEUM, NATURAL GAS AND BIOFUELS (ANP). **Boletim mensal da produção de petróleo e gás natural**. 2024. Available from: https://www.gov.br/anp/pt-br/centrais-de-conteudo/publicacoes/boletins-anp/boletins/boletim-mensal-da-producao-de-petroleo-e-gas-natural. Accessed in: 22 Apr. 2024.

BRAZIL NATIONAL AGENCY OF PETROLEUM, NATURAL GAS AND BIOFUELS (ANP). **Produção do Pré-sal**. 2024. Available from: https://www.presalpetroleo.gov.br/bacia-de-santos/. Accessed in: 22 Apr. 2024.

BRAZILIAN DEVELOPMENT BANK (BNDES). **GÁS PARA O DESENVOLVIMENTO: Perspectivas de oferta e demanda no mercado de gás natural do Brasil**. 2021. Available from: https://web.bndes.gov.br/bib/jspui/bitstream/1408/20581/1/Relatorio_Gas_Desenvolvimento%20Final.pdf. Accessed in: 11 Apr. 2024.

CAMPANARI, S.; MANZOLINI, G.; CHIESA, P. Using mcfc for high efficiency CO_2 capture from natural gas combined cycles: Comparison of internal and external reforming. **Applied energy**, England, v. 112, p. 772–783, 2013. Available from: https://doi.org/10.1016/j.apenergy.2013.01.045. Acessed in: 27 Mar. 2026.

CHAI, S. *et al.* Simultaneous NO/CO_2 removal performance using ce-doped CAO in calcium looping process: Experimental and dft studies. **Journal of Environmental Chemical Engineering**, Amsterdam, v. 10, n. 5, p. 108236, 2022. Available from: https://doi.org/10.1016/j.jece.2022.108236. Acessed in: 27 Mar. 2026.

CHAMPAGNE, S. *et al.* The effect of steam addition to the calciner in a calcium looping pilot plant. **Powder technology**, Schofield, v. 290, p. 114–123, 2016. Available from: https://doi.org/10.1016/j.powtec.2015.07.039. Acessed in: 27 Mar. 2026.

CHANG, C.-S. *et al.* Effect of limestone type and grind on so2 scrubber performance. the cost-reduction effect of finer limestone grinding on so2 scrubber efficiency can be very considerable. **Environmental Progress**, Austin, v. 1, n. 1, p. 59–65, 1982. Available from: https://doi.org/10.1002/ep.670010114. Acessed in: 27 Mar. 2026.

CHARITOS, A. *et al.* Parametric investigation of the calcium looping process for CO_2 capture in a 10 kwth dual fluidized bed. **International Journal of Greenhouse Gas Control**, Amsterdam, v. 4, n. 5, p. 776–784, 2010. Available from: https://doi.org/10.1016/j.ijggc.2010.04.009. Acessed in: 27 Mar. 2026.

CHEN, L. *et al.* The combined effect of SO_2 and H_2O on CO_2 capture performance by calcium looping. **Journal of CO_2 Utilization**, Amsterdam, v. 54, p. 101798, 2021. Available from: https://doi.org/10.1016/j.jcou.2021.101798. Acessed in: 27 Mar. 2026.

CLEANKER. **CLEAN clinKER production by Calcium looping process**. 2017. Available from: https://cordis.europa.eu/project/id/764816. Accessed in: 26 Jul. 2022.

CLEVER PROJECT. **Creating Legitimate Emission Factors for Verified GHG Emission Reductions in Transport**. 2024. Available from: https://cordis.europa.eu/project/id/101146908. Accessed in: 11 Jun. 2024.

COLORADO, A.; HERRERA, B.; AMELL, A. Performance of a flameless combustion furnace using biogas and natural gas. **Bioresource technology**, Hong Kong, v. 101, n. 7, p. 2443–2449, 2010. Available from: https://doi.org/10.1016/j.biortech.2009.11.003. Acessed in: 27 Mar. 2026.

CONTE, S. L. *et al.* Calcium looping for thermochemical storage: assessment of intrinsic reaction rate and estimate of kinetic/transport parameters for synthetic cao/mayenite particles from tga data. **Industrial & Engineering Chemistry Research**, Washington, v. 62, n. 41, p. 16647–16659, 2023. Available from: https://doi.org/10.1021/acs.iecr.3c01820. Acessed in: 27 Mar. 2026.

COPPOLA, A. *et al.* The combined effect of H_2O and SO_2 on CO_2 uptake and sorbent attrition during fluidised bed calcium looping. **Proceedings of the Combustion Institute**, Pittsburgh, v. 37, n. 4, p. 4379–4387, 2019. Available from: https://doi.org/10.1016/j.proci.2018.08.013. Acessed in: 27 Mar. 2026.

COPPOLA, A. *et al.* Effect of steam on the performance of Ca-based sorbents in calcium looping processes. **Powder Technology**, Amsterdam, v. 316, p. 578–584, 2017. Available from: https://doi.org/10.1016/j.powtec.2016.11.062. Acessed in: 27 Mar. 2026.

COPPOLA, A. *et al.* Analysis of the behaviour of limestone sorbents for sorption-enhanced gasification in dual interconnected fluidised bed reactor. **Fuel**, Amsterdam, v. 340, p. 127594, 2023. Available from: https://doi.org/10.1016/j.fuel.2023.127594. Acessed in: 27 Mar. 2026.

COPPOLA, A. *et al.* Analysis of the behaviour of limestone sorbents for sorption-enhanced gasification in dual interconnected fluidised bed reactor. **Fuel**, Amsterdam, v. 340, p. 127594, 2023. Available from: https://doi.org/10.1016/j.fuel.2023.127594. Acessed in: 27 Mar. 2026.

COPPOLA, A. *et al.* Attrition of limestone during fluidized bed calcium looping cycles for co2 capture. **Combustion science and technology**, Philadelphia, v. 184, n. 7-8, p. 929–941, 2012. Available from: https://doi.org/10.1080/00102202.2012.663986. Acessed in: 27 Mar. 2026.

COPPOLA, A. *et al.* Fluidized bed calcium looping: The effect of SO_2 on sorbent attrition and CO_2 capture capacity. **Chemical Engineering Journal**, Amsterdam, v. 207, p. 445–449, 2012. Available from: https://doi.org/10.1016/j.cej.2012.06.149. Acessed in: 27 Mar. 2026.

COPPOLA, A. *et al.* Impact fragmentation of limestone-based sorbents for calcium looping: The effect of steam and sulphur dioxide. **Fuel Processing Technology**, Amsterdam, v. 208, p. 106499, 2020. Available from: https://doi.org/10.1016/j.fuproc.2020.106499. Acessed in: 27 Mar. 2026.

COPPOLA, A. *et al.* Reactivation by steam hydration of sorbents for fluidized-bed calcium looping. **Energy & Fuels**, Washington, v. 29, n. 7, p. 4436–4446, 2015. Available from: https://doi.org/10.1021/acs.energyfuels.5b00413. Acessed in: 27 Mar. 2026.

COPPOLA, A. *et al.* Hydration-induced reactivation of spent sorbents for fluidized bed calcium looping (double looping). **Fuel processing technology**, Amsterdam, v. 120, p. 71–78, 2014. Available from: https://doi.org/10.1016/j.fuproc.2013.12.004. Acessed in: 27 Mar. 2026.

COPPOLA, A. *et al.* Performance of limestone-based sorbent for sorption-enhanced gasification in dual interconnected fluidized bed reactors. **AIChE Journal**, Amsterdam, v. 69, n. 1, p. e17588, 2023. Available from: https://doi.org/10.1002/aic.17588. Acessed in: 27 Mar. 2026.

COPPOLA, A. *et al.* A twin-bed test reactor for characterization of calcium looping sorbents. **Powder Technology**, Amsterdam, v. 316, p. 585–591, 2017. Available from: https://doi.org/10.1016/j.powtec.2016.11.067. Acessed in: 27 Mar. 2026.

COPPOLA, A. *et al.* Performance of natural sorbents during calcium looping cycles: a comparison between fluidized bed and thermo-gravimetric tests. **Energy & fuels**, Washington, v. 27, n. 10, p. 6048–6054, 2013. Available from: https://doi.org/10.1021/ef401876q. Acessed in: 27 Mar. 2026.

COPPOLA, A.; SCALA, F.; SALATINO, P. Characterization of calcium looping sorbents with a novel twin bed reactor. **Fuel Processing Technology**, Amsterdam, v. 172, p. 49–54, 2018. Available from: https://doi.org/10.1016/j.fuproc.2017.11.019. Acessed in: 27 Mar. 2026.

COPPOLA, A. *et al.* Fluidized bed calcium looping cycles for CO_2 capture under oxy-firing calcination conditions: Part 1. assessment of six limestones. **Chemical Engineering Journal**, Amsterdam, v. 231, p. 537–543, 2013. Available from: https://doi.org/10.1016/j.cej.2013.07.113. Acessed in: 27 Mar. 2026.

COPPOLA, A. *et al.* Fluidized bed calcium looping cycles for CO_2 capture under oxy-firing calcination conditions: Part 2. assessment of dolomite vs. limestone. **Chemical engineering journal**, Amsterdam, v. 231, p. 544–549, 2013. Available from: https://doi.org/10.1016/j.cej.2013.07.112. Acessed in: 27 Mar. 2026.

COSENSE4CLIMATE PROJECT. **Compressed Sensing for Climate: A Novel Approach to Localize, Quantify and Characterize Urban Greenhouse Gas Emitters**. 2024. Available from: https://cordis.europa.eu/project/id/101146908. Accessed in: 11 Jun. 2024.

COTTON, A.; PATCHIGOLLA, K.; OAKEY, J. Hydrodynamic characteristics of a pilot-scale cold model of a CO_2 capture fluidised bed reactor. **Powder technology**, Amsterdam, v. 235, p. 1060–1069, 2013. Available from: https://doi.org/10.1016/j.powtec.2012.10.011. Acessed in: 27 Mar. 2026.

COVER, T. M.; THOMAS, J. A. **Elements of Information Theory**. 2. ed. New York: Wiley, 2006.

DEAN, C. C. *et al.* The calcium looping cycle for CO_2 capture from power generation, cement manufacture and hydrogen production. **Chemical Engineering Research and Design**, Pittsburgh, v. 89, n. 6, p. 836–855, 2011. Available from: https://doi.org/10.1016/j.cherd.2010.10.013. Acessed in: 27 Mar. 2026.

DÍAZ-HERRERA, P. R. *et al.* Capture level design for a natural gas combined cycle with post-combustion CO_2 capture using novel configurations. **Energy**, Amsterdam, v. 193, p. 116769, 2020. Available from: https://doi.org/10.1016/j.energy.2019.116769. Acessed in: 27 Mar. 2026.

DIEGO, M.; ARIAS, B. Impact of load changes on the carbonator reactor of a 1.7 MWth calcium looping pilot plant. **Fuel Processing Technology**, Amsterdam, v. 200, p. 106307, 2020. Available from: https://doi.org/10.1016/j.fuproc.2019.106307. Acessed in: 27 Mar. 2026.

DIEGO, M.; ARIAS, B. Impact of load changes on the carbonator reactor of a 1.7 MWth calcium looping pilot plant. **Fuel Processing Technology**, v. 200, p. 106307, 2020. Available from: https://doi.org/10.1016/j.fuproc.2019.106307. Acessed in: 27 Mar. 2026.

DIETER, H. *et al.* Development of the calcium looping CO_2 capture technology from lab to pilot scale at ifk, university of stuttgart. **Fuel**, Amsterdam, v. 127, p. 23–37, 2014. Available from: DevelopmentofthecalciumloopingCO2capturetechnologyfromlabtopilotscaleatIFK, UniversityofStuttgart. Acessed in: 27 Mar. 2026.

DONG, J. *et al.* Effect of steam addition during carbonation, calcination or hydration on re-activation of CAO sorbent for CO_2 capture. **Journal of CO_2 Utilization**, Amsterdam, v. 39, p. 101167, 2020. Available from: https://doi.org/10.1016/j.jcou.2020.101167. Acessed in: 27 Mar. 2026.

DUELLI, G. *et al.* Characterization of the oxy-fired regenerator at a 10 kwth dual fluidized bed calcium looping facility. **Applied Thermal Engineering**, England, v. 74, p. 54–60, 2015. Available from: https://doi.org/10.1016/j.applthermaleng.2014.03.042. Acessed in: 27 Mar. 2026.

DUELLI, G. *et al.* Investigations at a 10 kwth calcium looping dual fluidized bed facility: Limestone calcination and CO_2 capture under high CO_2 and water vapor atmosphere. **International Journal of Greenhouse Gas Control**, Amsterdam, v. 33, p. 103–112, 2015. Available from: https://doi.org/10.1016/j.ijggc.2014.12.006. Acessed in: 27 Mar. 2026.

DUHOUX, B. *et al.* Simulation of a calcium looping CO_2 capture process for pressurized fluidized bed combustion. **The Canadian Journal of Chemical Engineering**, Ottawa, v. 98, n. 1, p. 75–83, 2020. Available from: https://doi.org/10.1002/cjce.23569. Acessed in: 27 Mar. 2026.

DUTTA, R.; NORD, L. O.; BOLLAND, O. Selection and design of post-combustion CO_2 capture process for 600 mw natural gas fueled thermal power plant based on operability. **Energy**, Amsterdam, v. 121, p. 643–656, 2017. Available from: https://doi.org/10.1016/j.energy.2017.01.053. Acessed in: 27 Mar. 2026.

EPE. **Empresa de Pesquisa Energética - Relatório síntese**. 2024. Available from: https://www.epe.gov.br/sites-pt/publicacoes-dados-abertos/publicacoes/PublicacoesArquivos/publicacao-45/topico-79/Relat%C3%B3rio%20Final%20do%20PDE%202024.pdf. Accessed in: 11 Apr. 2024.

ERANS, M.; MANOVIC, V.; ANTHONY, E. J. Calcium looping sorbents for CO_2 capture. **Applied Energy**, Islandia, v. 180, p. 722–742, 2016. Available from: https://doi.org/10.1016/j.apenergy.2016.07.074. Acessed in: 27 Mar. 2026.

FILONCHYK, M. *et al.* Greenhouse gases emissions and global climate change: Examining the influence of CO_2, CH_4, and N_2O. **Science of The Total Environment**, Amsterdam, v. 935, p. 173359, 2024. ISSN 0048-9697. Available from: https://www.sciencedirect.com/science/article/pii/S004896972403506X. Acessed in: 27 Mar. 2026.

FRIEDMAN, J.; LI, H. Natural gas combustion in a fluidized bed heat-treating furnace. **Combustion science and technology**, Philadelphia, v. 177, n. 11, p. 2211–2241, 2005. Available from: https://doi.org/10.1080/00102200500240844. Acessed in: 27 Mar. 2026.

GEOLOGICAL SURVEY OF BRAZIL (SGB/CPRM). **Mapa de Recursos do Estado de São Paulo**. 2006. Available from: https://rigeo.sgb.gov.br/handle/doc/2966. Accessed in: 13 Jun. 2024.

GONZÁLEZ, B.; KOKOT-BLAMEY, J.; FENNELL, P. Enhancement of CAO-based sorbent for CO_2 capture through doping with seawater. **Greenhouse Gases: Science and Technology**, London, v. 10, n. 5, p. 878–883, 2020. Available from: https://doi.org/10.1002/ghg.2013. Acessed in: 27 Mar. 2026.

GRASA, G. S.; ABANADES, J. C. CO_2 capture capacity of CaO in long series of carbonation/calcination cycles. **Industrial & Engineering Chemistry Research**, Washington, v. 45, n. 26, p. 8846–8851, 2006. Available from: https://doi.org/10.1021/ie0606946. Acessed in: 27 Mar. 2026.

GUPTA, V.; FUERSTENAU, D.; MIKA, T. An investigation of sieving in the presence of attrition. **Powder Technology**, Dongguan, v. 11, n. 3, p. 257–271, 1975. Available from: https://doi.org/10.1016/0032-5910(75)80052-0. Acessed in: 27 Mar. 2026.

HAAF, M. *et al.* CO_2 capture from waste-to-energy plants: Techno-economic assessment of novel integration concepts of calcium looping technology. **Resources, Conservation and Recycling**, Amsterdam, v. 162, p. 104973, 2020. Available from: https://doi.org/10.1016/j.resconrec.2020.104973. Acessed in: 27 Mar. 2026.

HAAF, M. *et al.* Operation of a 1 MWth calcium looping pilot plant firing waste-derived fuels in the calciner. **Powder technology**, Amsterdam, v. 372, p. 267–274, 2020. Available from: https://doi.org/10.1016/j.powtec.2020.05.074. Acessed in: 27 Mar. 2026.

HASHEMI, S. M.; ZHOU, R.; MAHINPEY, N. Evaluation of mgo- and $cazro_3$-promoted CAO-based pellets produced via solution combustion synthesis. **Chemical Engineering Journal**, Amsterdam, v. 450, p. 138274, 2022. ISSN 1385-8947. Available from: https://www.sciencedirect.com/science/article/pii/S1385894722037573. Acessed in: 27 Mar. 2026.

HAWTHORNE, C. *et al.* CO_2 capture with CAO in a 200 kwth dual fluidized bed pilot plant. **Energy Procedia**, Beirut, v. 4, p. 441–448, 2011. Available from: https://doi.org/10.1016/j.egypro.2011.01.073. Acessed in: 27 Mar. 2026.

HILZ, J. *et al.* Scale-up of the carbonate looping process to a 20 MWth pilot plant based on long-term pilot tests. **International Journal of Greenhouse Gas Control**, Amsterdam, v. 88, p. 332–341, 2019. Available from: https://doi.org/10.1016/j.ijggc.2019.04.026. Acessed in: 27 Mar. 2026.

HILZ, J. *et al.* Long-term pilot testing of the carbonate looping process in 1 MWth scale. **Fuel**, Amsterdam, v. 210, p. 892–899, 2017. Available from: https://doi.org/10.1016/j.fuel.2017.08.105. Acessed in: 27 Mar. 2026.

HILZ, J. *et al.* Investigation of the fuel influence on the carbonate looping process in 1 MWth scale. **Fuel Processing Technology**, Amsterdam, v. 169, p. 170–177, 2018. Available from: https://doi.org/10.1016/j.fuproc.2017.09.016. Acessed in: 27 Mar. 2026.

HOFMANN, C. *et al.* Enhancement of a 300 kwth pilot plant for testing the indirectly heated carbonate looping process for CO_2 capture from lime and cement industry. **Experimental Thermal and Fluid Science**, Basel, v. 151, p. 111091, 2024. Available from: https://doi.org/10.3390/pr12091926. Acessed in: 27 Mar. 2026.

HOMSY, S. L. *et al.* Calcium looping: On the positive influence of SO_2 and the negative influence of H_2O on CO_2 capture by metamorphosed limestone-derived sorbents. **ACS omega**, Washington, v. 5, n. 50, p. 32318–32333, 2020. Available from: https://doi.org/10.1021/acsomega.0c04157. Acessed in: 27 Mar. 2026.

HU, Y.; AHN, H. Process integration of a calcium-looping process with a natural gas combined cycle power plant for CO_2 capture and its improvement by exhaust gas recirculation. **Applied Energy**, Porto, v. 187, p. 480–488, 2017. Available from: https://doi.org/10.1016/j.apenergy.2016.11.014. Acessed in: 27 Mar. 2026.

HUGHES, R. W. *et al.* Changes in limestone sorbent morphology during CAO-$CACO_3$ looping at pilot scale. **Chemical Engineering & Technology: Industrial Chemistry-Plant Equipment-Process Engineering-Biotechnology**, Weinheim, v. 32, n. 3, p. 425–434, 2009. Available from: https://doi.org/10.1002/ceat.200800590. Acessed in: 27 Mar. 2026.

INTERNATIONAL ENERGY AGENCY (IEA). **World Energy Outlook 2023**. 2023. Available from: https://www.iea.org/reports/world-energy-outlook-2023. Accessed in: 11 Jun. 2024.

ISIAKA, I. O.; NDUKWE, K. O.; CHIBUIKE, U. S. Mean sea level: The effect of the rise in the environment. **Journal of Geoinformatics & Environmental Research (JGIER)**, Duhok, v. 2, n. 2, 2021. Available from: https://jastt.org/index.php/jasttpath/article/view/178. Acessed in: 27 Mar. 2026.

JAYARATHNA, C. K. *et al.* Improved multi-stage cross-flow fluidized bed classifier. **Powder technology**, Amsterdam, v. 342, p. 621–629, 2019. Available from: https://doi.org/10.1016/j.powtec.2018.10.026. Acessed in: 27 Mar. 2026.

KHILYUK, L. F. *et al.* Typical composition of natural gases. In: KHILYUK, L. F. *et al.* (Ed.). **Gas Migration**. Houston: Gulf Professional Publishing, 2000. p. 238–247. Accessed in: 26 Mar. 2026. Available from: https://www.sciencedirect.com/science/article/pii/B9780884154303500173.

KONG, P. *et al.* Insight into the deactivation mechanism of CAO-based CO_2 sorbent under in-situ coal combustion. **Separation and Purification Technology**, Amsterdam, v. 346, p. 127529, 2024. Available from: https://doi.org/10.1016/j.seppur.2024.127529. Acessed in: 27 Mar. 2026.

LAMB, W. F. *et al.* A review of trends and drivers of greenhouse gas emissions by sector from 1990 to 2018. **Environmental research letters**, Bristol, v. 16, n. 7, p. 073005, 2021. Available from: https://iopscience.iop.org/article/10.1088/1748-9326/abee4e/meta. Acessed in: 27 Mar. 2026.

LAURO, F. D. *et al.* Improving the performance of calcium looping for solar thermochemical energy storage and CO_2 capture. **Fuel**, Amsterdam, v. 298, p. 120791, 2021. Available from: https://doi.org/10.1016/j.fuel.2021.120791. Acessed in: 27 Mar. 2026.

LAURO, F. D. *et al.* Influence of fluidised bed inventory on the performance of limestone sorbent in calcium looping for thermochemical energy storage. **Energies**, Basel, v. 16, n. 19, p. 6942, 2023. Available from: https://doi.org/10.3390/en16196942. Acessed in: 27 Mar. 2026.

LEE, H.; ROMERO, J. (Ed.). **Summary for Policymakers. In: Climate Change 2023: Synthesis Report. Contribution of Working Groups I, II and III to the Sixth Assessment Report of the Intergovernmental Panel on Climate Change**. Geneva: Intergovernmental Panel on Climate Change (IPCC), 2023. Available from: https://doi.org/10.59327/IPCC/AR6-9789291691647.001. Accessed in: 24 Apr. 2024.

LESCHONSKI, K. Sieve analysis, the cinderella of particle size analysis methods? **Powder Technology**, Dongguan, v. 24, n. 2, p. 115–124, 1979. Available from: https://doi.org/10.1016/0032-5910(79)87027-8. Acessed in: 27 Mar. 2026.

LI, D.; WANG, Y.; LI, Z. Limestone calcination kinetics in microfluidized bed thermogravimetric analysis (mfb-tga) for calcium looping. **Catalysts**, Basel, v. 12, n. 12, p. 1661, 2022. Available from: https://doi.org/10.3390/catal12121661. Acessed in: 27 Mar. 2026.

LOTT, P. *et al.* Exhaust gas after-treatment of lean-burn natural gas engines–from fundamentals to application. **Applied Catalysis B: Environmental**, v. 330, p. 123241, 2023. Available from: https://doi.org/10.1016/j.apcatb.2023.123241. Accessed in: Mar. 27, 2026.

LOWE, C.; GREENAWAY, M. Compaction processes in granular beds composed of different particle sizes. **Journal of applied physics**, Melville, v. 98, n. 12, 2005. Available from: https://doi.org/10.1063/1.2149167. Acessed in: 27 Mar. 2026.

LOWELL, S.; SHIELDS, J. E. **Powder Surface Area and Porosity**. 2. ed. Dordrecht: Springer, 2013.

LU, D. Y.; HUGHES, R. W.; ANTHONY, E. J. Ca-based sorbent looping combustion for CO_2 capture in pilot-scale dual fluidized beds. **Fuel Processing Technology**, Amsterdam, v. 89, n. 12, p. 1386–1395, 2008. Available from: https://doi.org/10.1016/j.fuproc.2008.06.011. Acessed in: 27 Mar. 2026.

LUO, S. *et al.* Effect of particle size on pyrolysis of single-component municipal solid waste in fixed bed reactor. **International journal of hydrogen energy**, Miami, v. 35, n. 1, p. 93–97, 2010. Available from: https://doi.org/10.1016/j.ijhydene.2009.10.048. Acessed in: 27 Mar. 2026.

LUZ, A. B. d.; SAMPAIO, J. A.; FRANÇA, S. C. A. **Tratamento de minérios**. 5. ed. Rio de Janeiro: CETEM/MCT, 2010.

LYSIKOV, A. I.; SALANOV, A. N.; OKUNEV, A. G. Change of CO_2 carrying capacity of CAO in isothermal recarbonation- decomposition cycles. **Industrial & engineering chemistry research**, Washington, v. 46, n. 13, p. 4633–4638, 2007. Available from: https://doi.org/10.1021/ie0702328. Acessed in: 27 Mar. 2026.

MA, Z. *et al.* Calcium looping heat storage performance and mechanical property of CAO-based pellets under fluidization. **Chinese Journal of Chemical Engineering**, Beijing, v. 36, p.

170–180, 2021. Available from: https://doi.org/10.1016/j.cjche.2020.10.002. Acessed in: 27 Mar. 2026.

MANOVIC, V.; ANTHONY, E. J. Thermal activation of CaO-based sorbent and self-reactivation during CO_2 capture looping cycles. **Environmental science & technology**, Washington, v. 42, n. 11, p. 4170–4174, 2008. Available from: https://doi.org/10.1021/es800152s. Acessed in: 27 Mar. 2026.

MANOVIC, V. *et al.* Influence of calcination conditions on carrying capacity of CAO-based sorbent in CO_2 looping cycles. **Fuel**, Amsterdam, v. 88, n. 10, p. 1893–1900, 2009. Available from: https://doi.org/10.1016/j.fuel.2009.04.012. Acessed in: 27 Mar. 2026.

MARROCCOLI, M. *et al.* Dolomite-based binders manufactured using concentrated solar energy in a fluidised bed reactor. **Solar Energy**, Amsterdam, v. 232, p. 471–482, 2022. Available from: https://doi.org/10.1016/j.solener.2022.01.007. Acessed in: 27 Mar. 2026.

MASSA, F. *et al.* Investigating the behavior of six limestones in presence of steam in dual interconnected fluidized beds, under operating conditions relevant for sorption-enhanced gasification. **Powder Technology**, Amsterdam, v. 438, p. 119597, 2024. Available from: https://doi.org/10.1016/j.powtec.2024.119597. Acessed in: 27 Mar. 2026.

MEDINA-CARRASCO, S.; VALVERDE, J. M. The calcium looping process for energy storage: Insights from in situ xrd analysis. **Chemical Engineering Journal**, Amsterdam, v. 429, p. 132244, 2022. Available from: https://doi.org/10.1016/j.cej.2021.132244. Acessed in: 27 Mar. 2026.

MIGUEL, P. A. C. *et al.* **Metodologia de pesquisa em engenharia de produção e gestão de operações**. 2010. Available from: Undergraduate Thesis (Bachelor in Production Engineering) – University of São Paulo, São Paulo. Accessed in: Jun. 30, 2024.

MIKHAYLOV, A. *et al.* Global climate change and greenhouse effect. **Entrepreneurship and Sustainability Issues**, Kaunas, Lithuania, v. 7, n. 4, p. 2897–2911, 2020. Available from: https://doi.org/10.9770/jesi.2020.7.4(46). Accessed in: 27 Mar. 2026.

MOGHTADERI, B.; SEYFAEE, A. A multi-scale experimental study on calcium-looping for thermochemical energy storage using the CO_2 captured from power generation systems. **Journal of Energy Storage**, Amsterdam, v. 86, p. 111400, 2024. ISSN 2352-152X. Available from: https://www.sciencedirect.com/science/article/pii/S2352152X2400985X. Acessed in: 27 Mar. 2026.

MOKHOV, I. Climate change: Causes, risks, consequences, and problems of adaptation and regulation. **Herald of the Russian Academy of Sciences**, Moscow, v. 92, n. 1, p. 1–11, 2022. Available from: https://link.springer.com/article/10.1134/S101933162201004X. Acessed in: 27 Mar. 2026.

MONTGOMERY, D. C. **Design and Analysis of Experiments**. 8. ed. Hoboken, NJ: Wiley, 2013.

MONTGOMERY, D. C. **Design and Analysis of Experiments**. 9. ed. Hoboken, NJ: Wiley, 2017.

MOORE, S.; CRISTINA, C.; KULAY, L. Effect of the implementation of carbon capture systems on the environmental, energy and economic performance of the brazilian electricity matrix. **Energies**, Basel, v. 12, n. 2, p. 331, 2019. Available from: https://doi.org/10.3390/en12020331. Acessed in: 27 Mar. 2026.

MORTARI, D. A.; AVILA, I.; CRNKOVIC, P. M. Response surface methodology applied to the evaluation of the SO_2 sorption process in two brazilian limestones. **Energy & Fuels**, Washington, v. 27, n. 6, p. 2890–2898, 2013. Available from: https://doi.org/10.1021/ef400049z. Acessed in: 27 Mar. 2026.

MUGWANYA, M. *et al.* Anthropogenic temperature fluctuations and their effect on aquaculture: A comprehensive review. **Aquaculture and Fisheries**, Shanghai, v. 7, n. 3, p. 223–243, 2022. ISSN 2468-550X. Available from: https://www.sciencedirect.com/science/article/pii/S2468550X21001611. Acessed in: 27 Mar. 2026.

NATURAL RESOURCES CANADA. **Carbon capture, utilization, and storage (CCUS)**. 2022. Available from: https://www.nrcan.gc.ca/our-natural-resources/energy-sources-distribution/carbon-capture-utilization-and-storage/4275. Accessed in: 27 Jul. 2022.

PAPALAS, T. *et al.* Experimental investigation of integrated CO_2 capture and conversion to syngas via calcium looping coupled with dry reforming of CH_4. **Chemical Engineering Journal**, Lausanne, p. 149866, 2024. Available from: https://doi.org/10.1016/j.cej.2024.149866. Acessed in: 27 Mar. 2026.

PATANKAR, A. N.; MANDAL, G. The packing of solid particles: a review. **Transactions of the Indian Ceramic Society**, Varanasi, v. 39, n. 4, p. 109–119, 1980. Available from: https://doi.org/10.1080/0371750X.1980.10840732. Acessed in: 27 Mar. 2026.

PENG, W.; XU, Z.; ZHAO, H. Batch fluidized bed test of sats-derived CAO/TiO_2–Al_2O_3 sorbent for calcium looping. **Fuel**, Amsterdam, v. 170, p. 226–234, 2016. Available from: https://doi.org/10.1016/j.fuel.2015.12.004. Acessed in: 27 Mar. 2026.

PEREJÓN, A. *et al.* Magnesium calcites for CO_2 capture and thermochemical energy storage using the calcium-looping process. **Environmental Research**, Beijing, v. 246, p. 118119, 2024. Available from: https://doi.org/10.1016/j.envres.2024.118119. Acessed in: 27 Mar. 2026.

PEREJÓN, A. *et al.* On the relevant role of solids residence time on their CO_2 capture performance in the calcium looping technology. **Energy**, Amsterdam, v. 113, p. 160–171, 2016. Available from: https://doi.org/10.1016/j.energy.2016.07.028. Acessed in: 27 Mar. 2026.

PILLAI, B. B. K. *et al.* A novel calcium looping–integrated ngcc power plant configuration for carbon capture and utilization—comprehensive performance analysis. **International Journal of Energy Research**, Amsterdam, v. 46, n. 2, p. 900–922, 2022. Available from: https://doi.org/10.1002/er.7212. Acessed in: 27 Mar. 2026.

QURESHI, Y.; ALI, U.; SHER, F. Part load operation of natural gas fired power plant with CO_2 capture system for selective exhaust gas recirculation. **Applied Thermal Engineering**, Amesterdam, v. 190, p. 116808, 2021. Available from: https://doi.org/10.1016/j.applthermaleng.2021.116808. Acessed in: 27 Mar. 2026.

RAMEZANI, M. *et al.* Application of a novel calcium looping process for production of heat and carbon dioxide enrichment of greenhouses. **Energy Conversion and Management**, Amsterdam,

v. 103, p. 129–138, 2015. Available from: https://doi.org/10.1016/j.enconman.2015.06.044. Acessed in: 27 Mar. 2026.

RIDHA, F. N. *et al.* Attrition of CAO-based pellets in a 0.1 MWth dual fluidized bed pilot plant for post-combustion CO_2 capture. **Powder Technology**, Amsterdam, v. 291, p. 60–65, 2016. Available from: https://doi.org/10.1016/j.powtec.2015.11.065. Acessed in: 27 Mar. 2026.

RILEY, G. An examination of the separation of differently shaped particles. **Powder Technology**, Dongguan, v. 2, n. 6, p. 315–319, 1969. Available from: https://doi.org/10.1016/0032-5910(69)80022-7. Acessed in: 27 Mar. 2026.

RIO DE JANEIRO STATE FEDERATION OF INDUSTRIES (FIRJAN). **Federação das Indústrias do Estado do Rio de Janeiro**. 2024. Available from: https://www.firjan.com.br/lumis/portal/file/fileDownload.jsp?fileId=2C908A8A7D159ABE017D6D4AE7CF2987. Accessed in: 24 Apr. 2024.

RODRIGUES, M. I.; IEMMA, A. F. **Planejamento de experimentos & otimização de processos: uma estratégia sequencial de planejamentos**. 1. ed. Campinas: Casa do Pão, 2005.

RODRÍGUEZ, N.; ALONSO, M.; ABANADES, J. Experimental investigation of a circulating fluidized-bed reactor to capture CO_2 with CAO. **AIChE Journal**, New York, v. 57, n. 5, p. 1356–1366, 2011. Available from: https://doi.org/10.1002/aic.12337. Acessed in: 27 Mar. 2026.

ROUCHON, L.; FAVERGEON, L.; PIJOLAT, M. Analysis of the kinetic slowing down during carbonation of CAO by CO_2. **Journal of Thermal Analysis and Calorimetry**, Dordrecht, v. 113, n. 3, p. 1145–1155, 2013. Available from: https://link.springer.com/article/10.1007/s10973-013-2950-5. Acessed in: 27 Mar. 2026.

ROUQUEROL, F.; ROUQUEROL, J.; SING, K. Assessment of mesoporosity. **Adsorption by powders and porous solids**, Amsterdam, p. 191–217, 1999. Available from: https://doi.org/10.1016/B978-0-12-598920-6.X5000-3. Acessed in: 27 Mar. 2026.

SALAUDEEN, S. A. *et al.* Eggshell as a potential co2 sorbent in the calcium looping gasification of biomass. **Waste Management**, Amsterdam, v. 80, p. 274–284, 2018. Available from: https://doi.org/10.1016/j.wasman.2018.09.027. Acessed in: 27 Mar. 2026.

SÁNCHEZ-JIMÉNEZ, P. E. *et al.* Influence of ball milling on CAO crystal growth during limestone and dolomite calcination: effect on CO_2 capture at calcium looping conditions. **Crystal Growth & Design**, Washington, v. 16, n. 12, p. 7025–7036, 2016. Available from: https://doi.org/10.1021/acs.cgd.6b01228. Acessed in: 27 Mar. 2026.

SCALA, F.; MONTAGNARO, F.; SALATINO, P. Limestone attrition by impact loading during fluidized bed combustion. In: **Proceedings of the 29th Meeting of the Italian Section of the Combustion Institute**. Pisa, Italy: The Combustion Institute, 2006. p. 8–10. Available from: https://www.combustion-institute.it/proceedings/proc2006/documenti/Papers/10-08-scala-066.pdf. Accessed in: 27 Mar. 2026.

SCALA, F.; MONTAGNARO, F.; SALATINO, P. Attrition of limestone by impact loading in fluidized beds. **Energy & fuels**, Washington, v. 21, n. 5, p. 2566–2572, 2007. Available from: https://doi.org/10.1021/ef0700580. Acessed in: 27 Mar. 2026.

SCALTSOYIANNES, A. *et al.* Towards a generalized carbonation kinetic model for CaO-based materials using a modified random pore model. **Chemical Engineering Journal**, Amsterdam, v. 407, p. 127207, 2021. Available from: https://doi.org/10.1016/j.cej.2020.127207. Acessed in: 27 Mar. 2026.

SCHAKEL, W. *et al.* Impact of fuel selection on the environmental performance of post-combustion calcium looping applied to a cement plant. **Applied Energy**, Amsterdam, v. 210, p. 75–87, 2018. Available from: https://doi.org/10.1016/j.apenergy.2017.10.123. Acessed in: 27 Mar. 2026.

SHAH, I. H. *et al.* Comprehensive review: Effects of climate change and greenhouse gases emission relevance to environmental stress on horticultural crops and management. **Journal of Environmental Management**, Amsterdam, v. 351, p. 119978, 2024. ISSN 0301-4797. Available from: https://www.sciencedirect.com/science/article/pii/S0301479723027664. Acessed in: 27 Mar. 2026.

SHIMIZU, T. *et al.* A twin fluid-bed reactor for removal of CO_2 from combustion processes. **Chemical Engineering Research and Design**, London, v. 77, n. 1, p. 62–68, 1999. ISSN 0263-8762. Available from: https://doi.org/10.1205/026387699525882. Acessed in: 27 Mar. 2026.

SING, K. S. Reporting physisorption data for gas/solid systems with special reference to the determination of surface area and porosity (provisional). **Pure and applied chemistry**, Berlin, v. 54, n. 11, p. 2201–2218, 1982. Available from: https://doi.org/10.1351/pac198254112201. Acessed in: 27 Mar. 2026.

SIPÖCZ, N.; TOBIESEN, F. A. Natural gas combined cycle power plants with CO_2 capture–opportunities to reduce cost. **International Journal of Greenhouse Gas Control**, Amsterdam, v. 7, p. 98–106, 2012. Available from: https://doi.org/10.1016/j.ijggc.2012.01.003. Acessed in: 27 Mar. 2026.

SOCRATCES. **SOlar Calcium-looping integRAtion for Thermo-Chemical Energy Storage**. 2018. Available from: https://cordis.europa.eu/project/id/727348. Accessed in: 26 Jul. 2022.

STANDISH, N. The kinetics of batch sieving. **Powder Technology**, Dongguan, v. 41, n. 1, p. 57–67, 1985. Available from: https://doi.org/10.1016/0032-5910(85)85075-0. Acessed in: 27 Mar. 2026.

STIPS, A. *et al.* On the causal structure between CO_2 and global temperature. **Scientific reports**, London, v. 6, n. 1, p. 21691, 2016. Available from: https://www.nature.com/articles/srep21691. Acessed in: 27 Mar. 2026.

STRAUSS, B. H. *et al.* Unprecedented threats to cities from multi-century sea level rise. **Environmental Research Letters**, Bristol, v. 16, n. 11, p. 114015, 2021. Available from: https://iopscience.iop.org/article/10.1088/1748-9326/ac2e6b?trk=public_post_comment-text. Acessed in: 27 Mar. 2026.

SU, C.; DUAN, L.; ANTHONY, E. J. CO_2 capture and attrition performance of competitive eco-friendly calcium-based pellets in fluidized bed. **Greenhouse Gases: Science and Technology**, London, v. 8, n. 6, p. 1124–1133, 2018. Available from: https://doi.org/10.1002/ghg.1825. Acessed in: 27 Mar. 2026.

SU, Y. *et al.* Novel method for regeneration/reactivation of spent dolomite-based sorbents from calcium looping cycles. **Chemical Engineering Journal**, Amsterdam, v. 360, p. 148–156, 2019. Available from: https://doi.org/10.1016/j.cej.2018.11.095. Acessed in: 27 Mar. 2026.

SUN, J. *et al.* Stabilized CO_2 capture performance of wet mechanically activated dolomite. **Fuel**, Amsterdam, v. 222, p. 334–342, 2018. Available from: https://doi.org/10.1016/j.fuel.2018.02.162. Acessed in: 27 Mar. 2026.

SYMONDS, R. T. *et al.* CO_2 capture performance of CAO–based pellets in a 0.1 MWth pilot-scale calcium looping system. **Powder Technology**, Amsterdam, v. 290, p. 124–131, 2016. Available from: https://doi.org/10.1016/j.powtec.2015.08.044. Acessed in: 27 Mar. 2026.

SYMONDS, R. T. *et al.* Pilot-scale study of CO_2 capture by CAO-based sorbents in the presence of steam and SO_2. **Industrial & engineering chemistry research**, Washington, v. 51, n. 21, p. 7177–7184, 2012. Available from: https://doi.org/10.1021/ie2030129. Acessed in: 27 Mar. 2026.

SãO PAULO STATE PUBLIC UTILITIES REGULATORY AGENCY (ARSESP). **Agência Reguladora de Serviços Públicos do Estado de São Paulo**. 2023. Available from: https://www.arsesp.sp.gov.br/Paginas/gas/gas-canalizado.aspx. Accessed in: 24 Apr. 2024.

TAN, Y. *et al.* Conventional and optimized testing facilities of calcium looping process for CO_2 capture: A systematic review. **Fuel**, Amsterdam, v. 358, p. 130337, 2024. Available from: https://doi.org/10.1016/j.fuel.2023.130337. Acessed in: 27 Mar. 2026.

TEIXEIRA, G. *et al.* Gasification of char from wood pellets and from wood chips: Textural properties and thermochemical conversion along a continuous fixed bed. **Fuel**, Amsterdam, v. 102, p. 514–524, 2012. Available from: https://doi.org/10.1016/j.fuel.2012.05.039. Acessed in: 27 Mar. 2026.

TEIXEIRA, P. *et al.* Blending wastes of marble powder and dolomite sorbents for calcium-looping CO_2 capture under realistic industrial calcination conditions. **Materials**, Basel, v. 14, n. 16, p. 4379, 2021. Available from: https://doi.org/10.3390/ma14164379. Acessed in: 27 Mar. 2026.

THOMMES, M. *et al.* Physisorption of gases, with special reference to the evaluation of surface area and pore size distribution (iupac technical report). **Pure and applied chemistry**, Berlin, v. 87, n. 9-10, p. 1051–1069, 2015. Available from: https://doi.org/10.1515/pac-2014-1117. Acessed in: 27 Mar. 2026.

TOLEDO, R. C. *et al.* Experimental development of calcium looping carbon capture processes: an overview of opportunities and challenges. **Energies**, basel, v. 16, n. 9, p. 3623, 2023. Available from: https://doi.org/10.3390/en16093623. Acessed in: 27 Mar. 2026.

TOLEDO, R. C. *et al.* Efficiency and energy consumption of partial carbonation process for CO_2 capture from natural gas combustion. **Energies**, Basel, v. 18, n. 9, p. 2285, 2025. Available from: https://doi.org/10.3390/en18092285. Acessed in: 27 Mar. 2026.

TOLMASQUIM, M. T. *et al.* **The Brazilian Commitment to Combating Climate Change**. Brasília, 2021. Available from: https://www.epe.gov.br/sites-en/publicacoes-dados-abertos/publicacoes/PublicacoesArquivos/publicacao-181/NT%20COP%2021%20-English.pdf. Accessed in: 27 Mar. 2026.

TREGAMBI, C. *et al.* Solar-driven calcium looping in fluidized beds for thermochemical energy storage. **Chemical Engineering Journal**, Amsterdam, v. 466, p. 142708, 2023. Available from: https://doi.org/10.1016/j.cej.2023.142708. Acessed in: 27 Mar. 2026.

TREGAMBI, C. *et al.* An experimental characterization of calcium looping integrated with concentrated solar power. **Chemical Engineering Journal**, Amsterdam, v. 331, p. 794–802, 2018. Available from: https://doi.org/10.1016/j.cej.2017.08.068. Acessed in: 27 Mar. 2026.

TSAI, D. *et al.* **Análise das Emissões de Gases de Efeito Estufa e suas Implicações para as Metas Climáticas do Brasil: 1970–2022**. São Paulo, 2023. Available from: https://oc.eco.br/wp-content/uploads/2023/11/Relatorio-SEEG_gases-estufa_2023FINAL.pdf. Accessed in: 27 Mar. 2026.

VALVERDE, J.; SANCHEZ-JIMENEZ, P.; PEREZ-MAQUEDA, L. Calcium-looping for post-combustion CO_2 capture. on the adverse effect of sorbent regeneration under CO_2. **Applied Energy**, Amsterdam, v. 126, p. 161–171, 2014. ISSN 0306-2619. Available from: https://doi.org/10.1016/j.apenergy.2014.03.081. Acessed in: 27 Mar. 2026.

VALVERDE, J.; SANCHEZ-JIMENEZ, P.; PEREZ-MAQUEDA, L. A. Relevant influence of limestone crystallinity on CO_2 capture in the ca-looping technology at realistic calcination conditions. **Environmental Science & Technology**, Washington, v. 48, n. 16, p. 9882–9889, 2014. Available from: https://doi.org/10.1021/es5014505. Acessed in: 27 Mar. 2026.

VALVERDE, J.; SANCHEZ-JIMENEZ, P.; PÉREZ-MAQUEDA, L. A. Ca-looping for postcombustion CO_2 capture: A comparative analysis on the performances of dolomite and limestone. **Applied Energy**, Amsterdam, v. 138, p. 202–215, 2015. Available from: https://doi.org/10.1016/j.apenergy.2014.10.087. Acessed in: 27 Mar. 2026.

VALVERDE, J.; SANCHEZ-JIMENEZ, P. E.; PEREZ-MAQUEDA, L. A. Calcium-looping for post-combustion co2 capture. on the adverse effect of sorbent regeneration under co2. **Applied energy**, Amsterdam, v. 126, p. 161–171, 2014. Available from: https://doi.org/10.1016/j.apenergy.2014.03.081. Acessed in: 27 Mar. 2026.

VALVERDE, J. M. *et al.* Constant rate thermal analysis for enhancing the long-term co2 capture of cao at ca-looping conditions. **Applied energy**, New York, v. 108, p. 108–120, 2013. Available from: https://doi.org/10.1016/j.apenergy.2013.03.013. Acessed in: 27 Mar. 2026.

VOGE, H. H.; MORGAN, C. Z. Effect of catalyst particle size on selectivity in butene dehydrogenation. **Industrial & Engineering Chemistry Process Design and Development**, Washington, v. 11, n. 3, p. 454–457, 1972. Available from: https://pubs.acs.org/doi/pdf/10.1021/i260043a022?casa_token=EqKtlIVEqk0AAAAA:R3bcEYF4TJ7w_7SlpQ38G-lnXbomlQmDIWQ1wEhQgN8DgH7MSUgi_rwtowJguKxkHTKSj-c3Mn5wmYI0. Acessed in: 27 Mar. 2026.

WANG, F. *et al.* Investigations on biomass gasification of compact-fast dual fluidized bed calcium looping. **Journal of Cleaner Production**, Amsterdam, v. 405, p. 137065, 2023. Available from: https://doi.org/10.1016/j.jclepro.2023.137065. Acessed in: 27 Mar. 2026.

WEBB, P.; ORR, C. Analytical methods in fine particle technology, micromeritics instrument corp. **Norcros. Stud in Surf Sci and Catal**, p. 273–280, 01 1997. Acessed in: 27 Mar. 2026.

WEBER, M.; MORAN, R. F. weber1938precise. **Ind. Eng. Chem. Anal. Ed**, Saltvile, v. 10, n. 4, p. 180–184, 1938. Available from: https://pubs.acs.org/doi/pdf/10.1021/ac50120a003?casa_token=shfqE1DF4DsAAAAA:PIhvEMiwhMU3GIlzt5rpk-VtdGu5dWxSGrdidAExYWyFsemNKXu0BjNJ6rVtEpIrnihPPNJzpL09GJz_. Acessed in: 27 Mar. 2026.

WERTHER, J. Fluidized-bed reactors. **Ullmann's encyclopedia of industrial chemistry**, Hoboken, 2000. Available from: https://doi.org/10.1002/14356007.b04_239.pub2. Acessed in: 27 Mar. 2026.

XIAO, G.; GRACE, J. R.; LIM, C. J. Evolution of limestone particle size distribution in an air-jet attrition apparatus. **Industrial & Engineering Chemistry Research**, Washington, v. 53, n. 41, p. 15845–15851, 2014. Available from: https://doi.org/10.1021/ie501745h. Acessed in: 27 Mar. 2026.

YUAN, Y. L. . Y.; ZHAO, J. Development on thermochemical energy storage based on CaO-based materials: A review. **Bioscience Journal**, Basel, n. 4, p. 24, 2018. Available from: https://www.mdpi.com/2071-1050/10/8/2660. Acessed in: 27 Mar. 2026.

ZHANG, W. *et al.* Attrition behavior of calcium-based waste during co_2 capture cycles using calcium looping in a fluidized bed reactor. **Chemical Engineering Research and Design**, London, v. 109, p. 806–815, 2016. Available from: https://doi.org/10.1016/j.cherd.2016.02.018. Acessed in: 27 Mar. 2026.

APPENDIX A – EVALUATION OF SIEVING ON CALCIUM CARBONATE SAMPLES

LITERATURE REVIEW

Soil sample sieving by batch sieving is a complex procedure with many divergences and problem with repeatability (LESCHONSKI, 1979; STANDISH, 1985). As reported by STANDISH (1985) in his empirical study, to have a minimum level of credibility it is necessary to have a standard procedure. According to Standish, the influential parameters to measure uncertainty are: incorrect material preparation, mix of untested and tested samples, tests under humid weather, entrance motor voltage fluctuation, and sieves alignment during tests. LESCHONSKI (1979), classify the sieving process as not ideal due to the differences in construction between sieves with a identical cloth mesh. Even for standard sieves, a calibration must be conducted to results being reproducible. Leschonski shows that results deviations may be solved with a calibration, even for distinct methods of sieving i.e. rectangular and circular shaped sieves.

Sieve mesh blockage

STANDISH (1985) verified the mesh obstruction effect during sieving. This event takes place when a non-homogeneous particle have part of its body stuck in a mesh opening. Standish verified the obstruction event over time and noticed that it might happen in different ways. A particle can be stuck at any given moment permanently, it can be stuck only for a short or long period of time, and it can be cycle process of it being stuck in a opening, free itself and being stuck again somewhere else. Two key parameters are reported: sieve mesh with openings too close to the material diameter showed higher obstruction rate, and a higher density of particles of higher diameter showed reduction on obstruction rate.

Sieving time

The sieving curves, Figure 69 shows a well developed characteristic consisted by a first stage fast sieving, region (I), due to high particle number which are smaller than the mesh size, followed by a efficiency reduction (region (II)) until the final stage is reached in which the efficiency is small and constant (STANDISH, 1985). On the final stage (III), LESCHONSKI (1979), shows that particle have the approximate size of the sieve mesh. Standish reported sieving efficiency higher than 95% for sieving time of 1000 s (16,5 min). Despite the loss of precision owing to smaller sample sizes, the sieving time is stated to be shorter (WEBER; MORAN, 1938).

WEBER; MORAN (1938) emphasize the value of time in the sieving process, particularly for irregular and small samples. It does, however, suggest that a very long sieving time causes the medium-sized particles to flow through the bigger openings in the sieve, affecting the value

Figure 69 – Three part sieving behaviour

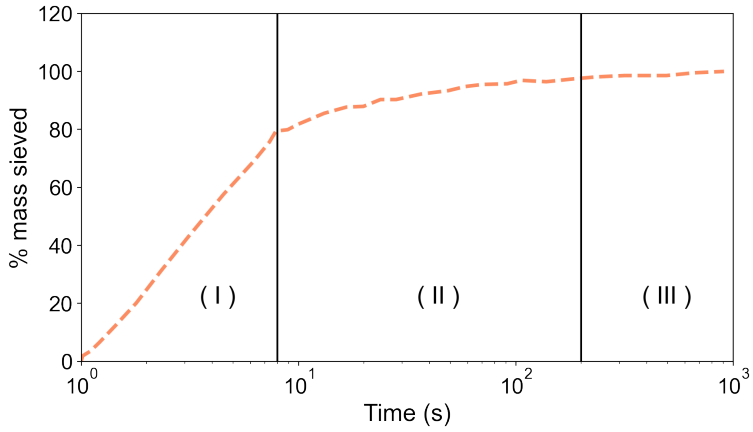

Source: Adapted from (LESCHONSKI, 1979)

of the result. It advises that the samples be sieved minute by minute, and that the sieving period be optimized when the sieve with the highest weight of samples begins to alter its constant mass for the following minutes.

LESCHONSKI (1979) explains how sieve construction affects sieving time. Putting aside the effects of locking and blockage. Smaller particles pass through the perforations with relative ease. Because of the non-homogeneity of the holes in the sieve itself, the diameter will be regulated by the larger holes when the process reaches its final step. When taking the effects of obstruction, it becomes considerably more difficult to estimate the behavior of the sieve's diameter and, as a result, the required sieving time. LESCHONSKI (1979) employs a more exact reference than time in the calibration chapter.

The bottom weight was verified, and the process was ended if the mass value did not vary by more than 0.1%/min. RILEY (1969) employed the previous methodology, referring to a more reliable process than the predetermined sieving time. Following that, the sieve was tapped to ensure that any mass that passed through it would pass if the sieving period was increased.

RILEY (1969) verified the effect of particles geometries in the sieving time, Figure 70 shows sieving time of spheres (25 ASTM), cylinders (25 ASTM), flakes (25ASTM), irregular (25 ASTM) and irregular (ASTM 12).The experiment showed irregular particles need a longer sieving time compared to samples with standard shapes. Flocculate shaped particles also needed more time to be sieved compared to spherical and cylindrical shapes. Riley justifies the fact by the friction of the particles during sieving.

GUPTA; FUERSTENAU; MIKA (1975) verified the effect of time and attrition of the particles on the effectiveness of the sieving process. The deformation of the particles was verified for longer sieving times, causing particles with sharp corners to have rounded ends.

Figure 71 show how sieving is affect by % of mass higher than the current sieve.

Figure 70 – Particle geometry effect on sieving time

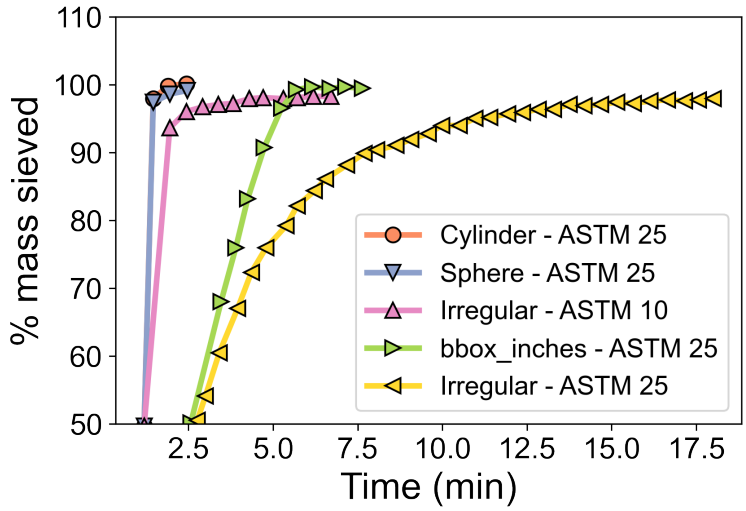

Source: Adapted from (RILEY, 1969)

Figure 71 – Effect of sieving time by mass percentage higher than the sieve.

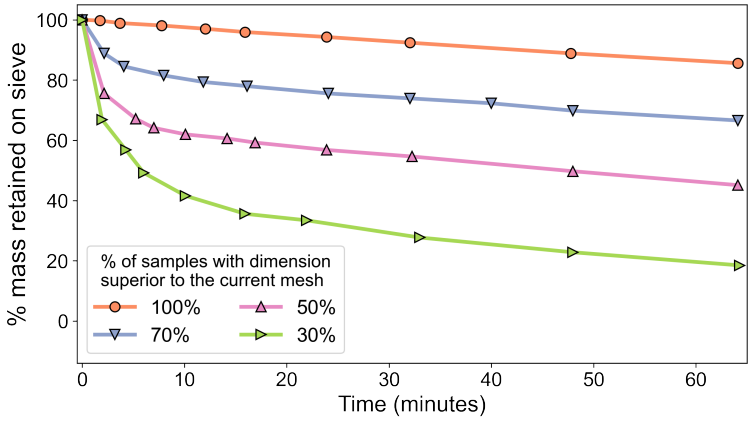

Source: some source

Sample mass

The standard amount of mass used for each test have been different proposed by authors. RILEY (1969) used samples of 50 g in their analysis, while WEBER; MORAN (1938) recommend sample with 100 g for the practicality of working with percentages, however author indicate an optimal ratio of sample size and sieving time could be used. GUPTA; FUERSTENAU; MIKA (1975) and ALLEN (1997) used the density of the material and estimated an amount that would be enough to cover the surface of the mesh (50-70g, for their material).

EXPERIMENTAL

Sample were weighted (SHIMADZU - BL3200H) and dried individually following ABNT - NBR 6457 standard for “Amostras de solo - Preparação para ensaios de compactação e ensaios de caracterização” where it describes the importance of previously drying soil sample before sieving. Drying was conducted on a controlled stove (Quimis ™ model 03117M-33) where two times were investigated, 2 e 24 h, with a isothermal temperature of 100 °C. After this step, samples were left on dissecant for 30 min while they return to ambient temperature. Samples were weighted again and humidity was calculated.

To avoid error caused by material segregation a homogenizing step following by an operation of quarting can be applied. The quarting process Figure 72 is used to reduce sample weight from its original size to the desired size without losing the original distribution of particles (LUZ; SAMPAIO; FRANÇA, 2010). Quarting procedure was followed as instructed on standard ABNT

Figure 72 – Quarted sample

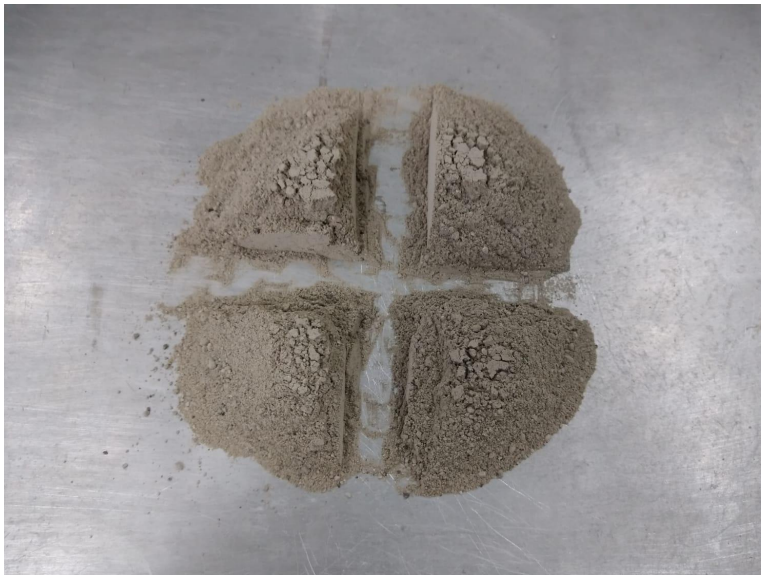

Source: Author

NBR 10007 for sampling of solid waste which shows the process of diving original sample in four equal parts after a pre-homogenization, being two parts taken as a new sample and the rest stored. Every stored part is mixed and can be used again as original sample.

The sample weight used on siever was decided based on Table 24 which is a recommendation based on material density (ALLEN, 1997). Sieving test were conducted on a Bertel siever which can hold up to six sieves and a end recipient, Figure 73. For this analysis the following mean granulometry was chosen: 390 (355 μm < φ < 425 μm), 462.5 (425 μm < φ < 500 μm), 550 (500 μm < φ < 600 μm), 655 (600 μm < φ < 710 μm), 780 (710 μm < φ < 850 μm). The siever allows for time control and intensity(0-100%). For this experiments were used sieving time of 3-15 min and intensity of 20%-80%. To reduce uncertainty, sieves were kept on initial mesh

Table 24 – Amount of mass to sieve based on density

Density[g× cm^3]	Sample mass [g]
1.5	25
1.5-3.0	50
+3	100

Source: (ALLEN, 1997)

Figure 73 – Bertel siever

Source: Author

orientation during all analyzing being handle by a single operator.

The design method chosen was the 2^k complete factorial design. The variable k refers to number of parameters investigated, which in this analysis were used: analysis Drying time, vibration intensity and sieving time. For three different factors, a number of eight experiments were conducted.

Factorial design works with two levels for each parameter, being coded as "-" and "+" for low and high level, respectively (MONTGOMERY, 2017). Table 25 show factors and levels, every experiment was repeat three times to verify repeatability. Table 26 shows how the levels will be used to calculate factor effect, being the effect calculated by the sum of positive level minus the sum of negative levels divided by the sum of possible levels.

$$A = \frac{\text{(sum of + levels) - (sum of - levels)}}{4} \tag{A.1}$$

To verify relevancy of effect it is applied a significance test (T) which is a comparison between test and t student table, where T is result of effect divided by experimental error and student's t

Table 25 – Parameters names and their description

Parameter	Coded Parameter	Negative level (-)	Positive level (+)
Drying time (h)	A	2	24
Vibration intensity (%)	B	20	80
Sieving time	C	3	15

Source: Author

Table 26 – 2^k design

Sample	A	B	C	AB	AC	BC	ABC	effect
1	-	-	-	+	+	+	-	-1
2	+	-	-	-	-	+	+	A
3	-	+	-	-	+	-	+	B
4	+	+	-	+	-	-	-	C
5	-	-	+	+	-	-	+	AB
6	+	-	+	-	+	-	-	AC
7	-	+	+	-	-	+	-	BC
8	+	+	+	+	+	+	+	ABC

Source: Author

value for the number of experiments and 95% of confidence (2.31, which will be called critical t). In this test, any value for T below critical t is given as non relevant. The results can be seen on Table 28.

The experimental error is measured by variance (s^2), Equation A.2

$$s^2 = \frac{\sum(x_i - \mu)^2}{n - 1} \tag{A.2}$$

where x_i is the measure, μ the mean and n the number of test. Table 27 show the experiments conducted and their replicates with every condition described. Samples that showed mass percentage higher than 60% have intensity parameter set to 80%. Also, the s2 showed higher values for intensity values of 20% for 75% of the samples. This points to a non uniformity of sieving in samples with lower intensity setting. Table 28 shows factor effects and their combinations (A, B, C, AB, AC, BC, and ABC) estimated from sieving process. Results present only one significant effect from all parameter involved. After this analysis it is possible to conclude that only Vibration intensity is a relevant factor for sieving on this setup. Even though humidity play a role in sieving as pointed by the standard used, no influence could be found on this analysis. Further analysis will be conducted taking theses parameters into account.

Table 27 – Results of 2^k design.

Sample	Drying time (h)	Vibration intensity (%)	Sieving time (min)	% of mass replicates 1	2	3	Mean	s^2
1	2	20	3	55.2	60.6	58.7	58.2	7.5
2	24	20	3	58.1	54.5	51.5	54.7	11.1
3	2	80	3	61.7	61.0	61.8	61.5	0.2
4	24	80	3	60.2	60.1	61.2	60.5	0.3
5	2	20	15	55.8	58.1	59.7	57.9	3.7
6	24	20	15	56.1	56.3	55.7	56.0	0.1
7	2	80	15	62.3	61.6	61.9	62.0	0.1
8	24	80	15	61.8	61.2	61.9	61.6	0.1

Source: Author

Table 28 – Relevancy test.

Parameter order	Parameter	Effect	Relevancy
	A	-1.68	not relevant
1°	B	4.72	relevant
	C	0.65	not relevant
	AB	1.00	not relevant
2°	BC	0.12	not relevant
	AC	0.59	not relevant
3°	ABC	-0.26	not relevant

Source: Author

Elutriation effect by long sieving time

Figure 74 shows mass percentage by mean granulometry for four different sieving times (15, 30, 45, and 60 min). A linear nature is observed for the finer sieves (355 μm – 600 μm) pointing to a homogeneous distribution for this granulometry, which is not observed for the rest of the tests. A small elutriation effect can be observed with the reduction of sieves diameter. Even though the effect is noticed, evaluation for higher time (45 min) indicated only a small influence of elutriation effect. This analysis leads to the conclusion that negligible elutriation effect is taking place while analyzing granulometry distribution.

SAMPLE GRANULOMETRY CHARACTERIZATION

Limestone material is derived from rocks that are crushed to a range of different granulometry. It is is important to work with a really predictable material where all ranges of granulometry is known because some application might have difficulties with finer or bigger particles. Also, when using this material it is important to know what is the mass percentage that will be used from the batch.

Figure 74 – Elutriation effect on long sieving time

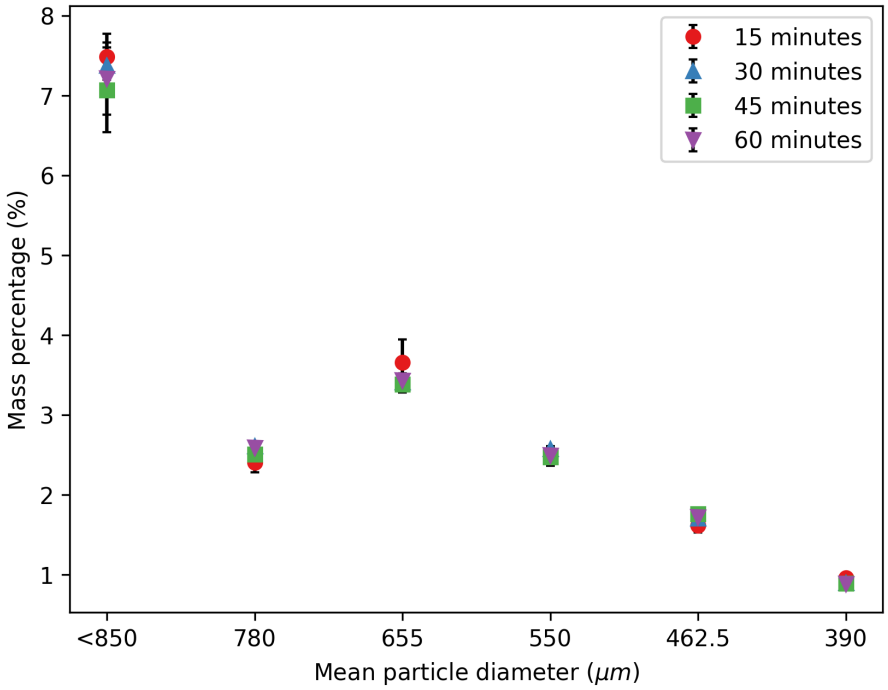

Source: Author

Sample characterization was conducted using best practices already states on standard ABNT-NBR 6457 and ABNT NBR 10007 also applying the knowledge acquired from results of Appendix A.

Sample were quarted from original sample size down to 50 g as stated in Table 24 ready for sieving. A total number of seven sample were used to calculate ranges of granulometry to avoid errors as discussed on Appendix A.

Sieves were set on the siever, Figure 73, and sample were add on the first sieve. Sample were set for the maximum intensity available and the lid closed. Samples were then passed through set of sieves until no mass could be register on a sieve or all available sieves were used. The sieves available for use on the lab are ASTM 18, 20, 25, 30, 35, 40, 45, 50, 60, 80, 100, 120, 140, 170, 200, 230 and <270. Which correspond to a diameter of particles that can be understood as the mean diameter of current sieve and previous sieve based on aperture size of the sieves. Sieves can also be identified by their mean diameter of particle which for the available sieves is in µm: >1000, 925, 780, 625, 550, 462.5, 390, 327.5, 275, 231, 196, 165, 137.5, 115.5, 98, 82.5, 69, 58, and <53, respectively.

After each set of sieve, limestone retained on sieves were weighted and stored on a specific recipient. These granulometry were later used to further analysis.

APPENDIX B – EXPERIMENTAL DATA

In this chapter, references are made to experimental data that, for clarity and brevity, are not presented in table format within the main body of the thesis.

Table 29 – Mass distributiom, average mass and standard deviation of sieved dolomitic sample. Reference to Figure 31

Average particle size μ m	Replicate-1 m	Replicate-2 m	Replicate-3 m	Replicate-4 m	Replicate-5 m	Replicate-6 m	Replicate-7 m	Mean m	St.dev m
> 1000 (top sieve)	12.10	13.90	10.90	13.80	11.90	9.90	11.10	11.94	1.38
925	3.60	4.10	3.60	4.10	3.80	3.50	3.60	3.76	0.23
780	5.40	5.70	5.20	5.90	5.60	5.40	6.10	5.61	0.29
655	7.30	7.50	7.10	7.30	7.00	6.90	6.80	7.13	0.23
550	5.20	5.20	5.20	5.00	5.30	5.20	5.00	5.16	0.10
462.5	3.80	3.80	3.70	3.70	3.70	3.80	3.60	3.73	0.07
390	2.00	2.00	2.30	2.10	2.00	2.00	2.30	2.10	0.13
327.5	6.70	6.20	6.40	6.20	6.20	6.50	6.30	6.36	0.18
275	3.40	2.80	2.90	2.60	2.90	2.90	2.70	2.89	0.24
231	5.60	5.70	5.80	5.40	5.90	6.00	5.70	5.73	0.18
196	2.30	1.90	2.30	2.00	2.00	2.40	2.10	2.14	0.18
165	3.80	3.70	3.90	3.60	3.70	4.00	3.90	3.80	0.13
137.5	3.20	2.90	3.30	3.10	3.30	3.20	3.20	3.17	0.13
115.5	4.60	6.00	4.70	4.30	6.30	3.90	7.90	5.39	1.31
98	12.90	14.50	11.70	12.60	11.30	4.40	13.50	11.56	3.09
82.5	11.90	10.00	13.00	11.70	12.00	14.50	10.30	11.91	1.42
69	4.80	3.10	6.40	4.70	5.20	10.20	4.10	5.50	2.13
58	1.00	0.80	1.20	1.10	1.90	3.10	1.70	1.54	0.73
< 53 (bottom)	0.80	0.30	0.40	0.70	0.10	2.10	1.70	0.87	0.69

Source: Author

Table 30 – Average particle diameter (d) and standard deviation (σ_d) for each particle size. Reference to Figure 32

Particle Size (μm)	Diameter d (μm)	Std. dev. σ_d (μm)
1000	974.01	43.22
925	834.94	16.87
780	722.13	12.63
655	628.83	10.35
550	516.53	7.71
462.5	455.08	5.97
390	412.67	4.66
327.5	380.97	4.50
275	304.96	2.62
231	265.80	2.46
196	229.67	1.97
165	203.57	1.51
137.5	173.05	1.42
115.5	140.16	0.82
96	111.02	0.61

Source: Author

Table 31 – Average particle circularity (ϕ) and standard deviation (σ_ϕ) for each particle size. Reference to Figure 33

Particle size (μm)	Circularity (ϕ)	Std. dev. $\sigma_p hi$
1000	0.680	0.0088
925	0.707	0.0090
780	0.693	0.0074
655	0.641	0.0070
550	0.745	0.0061
462.5	0.744	0.0053
390	0.741	0.0045
327.5	0.681	0.0052
275	0.735	0.0036
231	0.742	0.0037
196	0.706	0.0038
165	0.712	0.0033
137.5	0.736	0.0034
115.5	0.765	0.0026
96	0.784	0.0022

Source: Author

Table 32 – Oxide composition of particle color fractions (%). Reference to Figure 34

Oxide	White	Gray	Dark Gray
MgO	23.465	23.024	10.597
SiO_2	17.192	31.963	69.360
P_2O_5	0.535	0.000	0.000
SO_3	1.594	2.142	2.286
CaO	55.635	39.123	16.093
MnO	0.378	0.834	0.188
Fe_2O_3	0.596	2.223	1.093
In_2O_3	0.604	0.694	0.385

Source: Author

Table 33 – Compacting TGA data from Figure 38a

Particle size (μm)	Mean value	Interval
780	16.616	5.412
550	22.054	4.855
390	23.710	1.147
196	25.340	2.518
137.5	25.866	0.190
115.5	24.312	0.600
96	23.629	0.500
82.5	23.170	1.103
69	23.390	0.780
58	22.798	1.735
49	23.676	0.822
41.5	23.282	1.352
31.5	24.871	0.970

Source: Author

Table 34 – BET surface area as a function of particle size Figure 38b

Particle size (μm)	BET surface area (m^2/g)
780	1.6346
390	1.7575
231	1.7460
98	2.0453
82.5	2.1658
69	2.4295
58	2.6694

Source: Author

Table 35 – CO_2 mass captured (mg) over 10 carbonation–calcination cycles under different temperature and duration conditions. Reference to Figure 55

Cycle	400°C 10 min	475°C 7.5 min	475°C 11 min	550°C 10 min	580°C 7.5 min
1	0.457	1.063	0.882	1.365	1.334
2	0.405	0.828	0.811	1.177	1.170
3	0.373	0.683	0.724	1.065	1.035
4	0.350	0.685	0.679	0.994	0.985
5	0.334	0.615	0.646	0.946	0.903
6	0.321	0.580	0.611	0.906	0.867
7	0.308	0.521	0.509	0.874	0.845
8	0.298	0.496	0.505	0.847	0.853
9	0.290	0.498	0.546	0.821	0.822
10	0.282	0.456	0.528	0.801	0.800

Source: Author

Table 36 – Capture ratio ξ_{mean} (mass CO_2/mass dolomite) over ten cycles for each DIFB test run. Reference to Figure 56

Cycle	DIFB-1	DIFB-2	DIFB-3	DIFB-4	DIFB-5	DIFB-6	DIFB-7	DIFB-8	DIFB-9	DIFB-10	DIFB-11
1	0.081	0.072	0.000	0.000	0.055	0.066	0.046	0.090	0.053	0.025	0.000
2	0.024	0.052	0.000	0.000	0.037	0.050	0.032	0.061	0.032	0.009	0.000
3	0.007	0.027	0.000	0.000	0.027	0.037	0.022	0.048	0.017	0.007	0.000
4	0.011	0.016	0.000	0.000	0.023	0.019	0.010	0.034	0.010	0.005	0.000
5	0.002	0.015	0.000	0.000	0.013	0.015	0.010	0.045	0.009	0.007	0.000
6	0.006	0.010	0.000	0.000	0.010	0.014	0.010	0.033	0.015	0.012	0.000
7	0.006	0.007	0.000	0.000	0.013	0.011	0.010	0.019	0.015	0.009	0.000
8	0.008	0.010	0.000	0.000	0.010	0.012	0.008	0.012	0.012	0.008	0.000
9	0.005	0.008	0.000	0.000	0.012	0.008	0.009	0.012	0.010	0.008	0.000
10	0.008	0.011	0.000	0.000	0.012	0.008	0.009	0.012	0.006	0.004	0.000

Source: Author

Table 37 – Particle size distribution (PSD) and fragmentation index fraction for DIFB samples. Reference to Figure 60

P. S. (μm)	DIFB-1	DIFB-2	DIFB-3	DIFB-4	DIFB-5	DIFB-6	DIFB-7	DIFB-8	DIFB-9	DIFB-10
25	0.0000	0.0000	0.0000	0.0000	0.0000	0.0000	0.0000	0.0000	0.0000	0.0000
81	0.0033	0.0019	0.0042	0.0093	0.0021	0.0034	0.0101	0.0041	0.0020	0.0055
146	0.0206	0.0142	0.0200	0.0185	0.0100	0.0175	0.0265	0.0147	0.0176	0.0275
196	0.0268	0.0191	0.0239	0.0278	0.0170	0.0206	0.0288	0.0104	0.0205	0.0243
231	0.0568	0.0336	0.0550	0.0556	0.0413	0.0471	0.0490	0.0360	0.0498	0.0461
275	0.0677	0.0583	0.0682	0.0741	0.0620	0.0618	0.0693	0.0402	0.0732	0.0636
327.5	0.0927	0.0703	0.0965	0.1019	0.0930	0.0928	0.1136	0.0726	0.1659	0.0998
377.5	0.0458	0.0732	0.0607	0.0556	0.0465	0.0425	0.0514	0.0336	0.0576	0.0601
500	0.6863	0.7293	0.6715	0.6574	0.7280	0.7143	0.6514	0.7883	0.6137	0.6730

Source: Author

Table 38 – Cumulative Fragmentation Index at Particle Sizes for DIFB Samples. Reference to Figure 61

P. S. (μm)	DIFB-1	DIFB-2	DIFB-3	DIFB-4	DIFB-5	DIFB-6	DIFB-7	DIFB-8	DIFB-9	DIFB-10
25	0.0000	0.0000	0.0000	0.0000	0.0000	0.0000	0.0000	0.0000	0.0000	0.0000
81	0.0033	0.0019	0.0042	0.0093	0.0021	0.0034	0.0101	0.0041	0.0020	0.0055
146	0.0239	0.0161	0.0242	0.0278	0.0121	0.0209	0.0366	0.0188	0.0195	0.0330
196	0.0507	0.0352	0.0481	0.0556	0.0291	0.0415	0.0654	0.0293	0.0400	0.0574
231	0.1075	0.0688	0.1030	0.1111	0.0705	0.0886	0.1144	0.0653	0.0898	0.1034
275	0.1752	0.1271	0.1713	0.1852	0.1325	0.1504	0.1837	0.1055	0.1629	0.1670
327.5	0.2679	0.1974	0.2678	0.2870	0.2255	0.2433	0.2973	0.1781	0.3288	0.2668
377.5	0.3137	0.2707	0.3285	0.3426	0.2720	0.2857	0.3486	0.2117	0.3863	0.3270
500	1.0000	1.0000	1.0000	1.0000	1.0000	1.0000	1.0000	1.0000	1.0000	1.0000

Source: Author

Table 39 – Average elutriation time (E(t)) for each DIFB condition. Reference to Figure 62

Test name	Average E(t)
DIFB-1	0.082
DIFB-2	0.088
DIFB-3	0.101
DIFB-4	0.056
DIFB-5	0.086
DIFB-6	0.298
DIFB-7	0.035
DIFB-8	0.014
DIFB-9	0.099
DIFB-10	0.031

Source: Author

Table 40 – Elutriation Time (E(t)) for Calcination and Carbonation. Reference to Figure 63

Sample	Calcination	Carbonation
DIFB-1	0.1324	0.0266
DIFB-2	0.1204	0.0530
DIFB-3	0.1522	0.0457
DIFB-4	0.0857	0.0226
DIFB-5	0.1276	0.0396
DIFB-6	0.2160	0.3876
DIFB-7	0.0491	0.0211
DIFB-8	0.0215	0.0063
DIFB-9	0.0347	0.1695
DIFB-10	0.0406	0.0198

Source: Author

Table 41 – Fragmentation index f values for different IPT samples and particle sizes. Reference to Figure 64

Imp. vel. (m/s)	IPT-1	IPT-2	IPT-3	IPT-4	IPT-5	IPT-6	IPT-7	IPT-8	IPT-9	IPT-10
17	0.03505	0.02844	0.03418	0.07238	0.02188	0.03715	0.06443	0.04191	0.05143	0.04046
24	0.04192	0.03896	0.04858	0.06075	0.04533	0.06461	0.05978	0.07852	0.03144	0.03083
31	0.07052	0.06549	0.07245	0.07370	0.06631	0.05616	0.08590	0.08411	0.06247	0.05847
38	0.07291	0.11623	0.08894	0.14575	0.14575	0.07621	0.17016	0.14275	0.07292	0.09328
45	0.13056	0.14685	0.11686	0.17980	0.13417	0.13130	0.17708	0.16213	0.12158	0.14167

Source: Author

APPENDIX C – SCIENTIFIC PUBLICATIONS ORIGINATING FROM THIS THESIS

PUBLICATIONS IN INTERNATIONAL SCIENTIFIC JOURNALS

- TOLEDO, R. C.; ARCE, G. L.; CARVALHO JR., J. A.; ÁVILA, I. Experimental development of calcium looping carbon capture processes: an overview of opportunities and challenges. Energies, Basel, v. 16, n. 9, p. 3623, 2023. DOI: 10.3390/en16093623.
- TOLEDO, R. C.; MORAES, C. L. de; THANGARASU, V.; CARVALHO JR., J. A. de; ÁVILA, I. Efficiency and energy consumption of partial carbonation process for CO_2 capture from natural gas combustion. Energies, Basel, v. 18, n. 9, p. 2285, 2025. DOI: 10.3390/en18092285.

PUBLICATIONS IN UNDER REVIEW IN INTERNATIONAL SCIENTIFIC JOURNALS

- TOLEDO, R. C.; PSWARAYI, T.; Valim, D.; CARVALHO JR., J. A.; Maciel, C. D; ÁVILA, I. CO2-Induced Pore Blocking in Dolomite During the Carbonation Stage of the Calcium Looping Process. Green Carbon.

FULL PAPERS PUBLISHED IN CONFERENCE PROCEEDINGS

- MORAES, C. L. ; TOLEDO, R. C. ; AVILA, I. . Otimização energética do processo calcium looping em atmosfera de queima de gás natural. In: Congresso Nacional de Estudantes de Engenharia Mecânica, 2024, Uberaba. XXX Congresso Nacional de Estudantes de Engenharia Mecânica, 2024.
- FORTES, T. M. ; TOLEDO, R. C. ; AVILA, I. . AVALIAÇÃO DO PENEIRAMENTO DE AMOSTRAS DE CALCÁRIO PARA APLICAÇÃO EM LEITO FLUIDIZADO. In: Congresso Nacional de Estudantes de Engenharia Mecânica, 2022, Santa Maria. CREEM 2022 - XXVIII Congresso Nacional de Estudantes de Engenharia Mecânica, 2022. v. 1.
- TOLEDO, R. C.; CARVALHO JUNIOR, J. A. ; AVILA, I. . Calcium looping em leitos fluidizados: Identificando as principais publicações. In: VI Workshop da Pós-graduação em Engenharia, 2022, Guaratinguetá. VI Workshop da Pós-graduação em Engenharia, 2022. v. 1.

APPENDIX D – CURRICULUM

Identification	
	Rubens Coutinho Toledo 25/06/1994
Nationality	Brazilian
Name for citations	Toledo, Rubens Coutinho; Toledo, R. C.
Lattes CV	https://lattes.cnpq.br/6754257943749374
ORCID	https://orcid.org/0000-0002-9682-3102
Other identifier	-
Academic Background	
2019–2021	Postgraduate program in mechanical engineer, Thermal and fluids science – EESC/USP
2012–2018	Bachelor's degree Mechanical Engineer – Federal University of Mato Grosso
Bibliographic Production	
TOLEDO, R. C.; ARCE, G. L.; CARVALHO JR., J. A.; ÁVILA, I. Experimental development of calcium looping carbon capture processes: an overview of opportunities and challenges. Energies, Basel, v. 16, n. 9, p. 3623, 2023. DOI: 10.3390/en16093623. TOLEDO, R. C.; MORAES, C. L. de; THANGARASU, V.; CARVALHO JR., J. A. de; ÁVILA, I. Efficiency and energy consumption of partial carbonation process for CO_2 capture from natural gas combustion. Energies, Basel, v. 18, n. 9, p. 2285, 2025. DOI: 10.3390/en18092285.	
Scientific Events	
VI Workshop da Pós-Graduação em Engenharia. Calcium looping em leitos fluidizados: Identificando as principais publicações. 2022. (Simpósio).	